A search for dark galaxies through the AGES

by

Robbie Richard Auld

A thesis submitted to

Cardiff University

for the degree of

Doctor of Philosophy

May 2007

ProQuest LLC
789 East Eisenhower Parkway
P.O. Box 1346
Ann Arbor, MI 48106-1346

ACKNOWLEDGMENTS

Jane, for all your support and love during our difficult time apart, thank you. You have always been there for me, thank you so much. And thank you for being so patient with me during my lengthy writing-up period. I love you.

Mum and Dad, thanks for all your love and 'where's the thesis?' support.

Thanks also to Jon and Erwin for your guidance, advice and free drinks throughout the three years. Without your support and tutelage I would not have made it this far. I feel privileged to have worked with you both and hope that this thesis does you both justice.

Thanks to the other members of the group; Diego, Luca, Marco, Mike, Rhodri, Rhys, Rory, Sabina & Sarah for some very entertaining group meetings and discussions. Thanks also to my officemates, Simon, Luca and Rory for enduring my endless questions and terrible jokes.

Finally, thanks to everyone else who've helped me enjoy my time in the department (and in the pub); James, Bruce, Mike Z., Gustav, Tim, Rich, Pete, Rhianne, Dave, Dimitris and everyone else.

This research makes use of data taken with the 305 m radio telescope at Arecibo, Puerto Rico. The Arecibo Observatory is part of the National Astronomy and Ionoshpere Centre, which is operated by Cornell University under a cooperative agreement with the National Science Foundation.

This research makes use of data taken with The Australian Telescope Compact Array. The Compact Array is part of the Australian Telescope National Facility (ATNF). ATNF is funded by the Commonwealth of Asutralia for operations as a national facility managed by CSIRO.

This research makes use of the NASA/IPAC Extragalactic Database (NED) which is operated by the Jet Propulsion Laboratory, California Institute of Technology, under contract with the National Aeronautics and Space Administration.

This research also makes use of data products from the Two Micron All Sky Survey, which is a joint project of the University of Massachusetts and the Infrared Processing and Analysis Center/California Institute of Technology, funded by the National Aeronautics and Space Administration and the National Science Foundation.

ABSTRACT

The work I have performed for this thesis covers a number of different areas of astronomy. My work on the LSBs is an in-depth exploration of the gas morphology and kinematics of these unusual objects. The focus is on the star forming abilities of the galaxy sample, but the H I observations also reveal a rich variety of gas morphology and motion, which are not necessarily apparent at other wavelengths. As well as being LSB, they are neutral gas-rich objects. As such they are more suited to being detected by H I surveys than by optical surveys.

The Arecibo Galaxy Environment Survey (AGES) is a survey that expects to detect a large number of this type of galaxy and a large proportion of the thesis has been dedicated to my involvement with the survey. This has included designing and implementing the observing strategy, testing the data reduction pipeline, producing the final data, testing their quality and examining the efficiency of the survey detection methods. I have demonstrated some uses the AGES data can be put to; from discovering hitherto undetected galaxies, through measuring the cosmic distribution of neutral hydrogen, to evaluating the cosmic significance of dark galaxies. The last point forms the central theme throughout the thesis.

Of the 69 detections made by AGES in the first two datacubes, 55 do not have previous H I measurements and 26 are previously uncatalogued. An H I mass function (HIMF) was produced from the first galaxies detected by AGES. The best fit line to the data was a Schechter function with the parameters: $\alpha = -1.28 \pm 0.17$, $\Phi_* = 0.0076 \pm 0.0027$ and $M_* = 7.7 \pm 1.8 \times 10^9$ $M_\odot$. Using the HIMF the calculated value for the space density of neutral hydrogen was found to be $\rho_{HI} = 7.5^{0.6}_{0.3} \times 10^7 M_\odot$ Mpc^{-3}, which is consistent with previous measurements. The overall contribution of H I to the Universal energy density was calculated from this value and found to be $\Omega_{HI} = 4.1^{1.8}_{1.6} \times 10^{-4}$, confirming previous measurements of this value.

Assuming the two candidates are indeed optically dark, based on this value the contribution of dark galaxies was calculated to be 4% to their respective mass bins, and less than 0.5% overall. The number density was found to be $n_{dark} \sim 6.6 \times 10^{-4}$ Mpc^{-3}. Hence it would appear that dark galaxies are not numerous enough nor of substantial mass to be able to account for the 'missing mass' or to be able to fully represent the high number of dark matter haloes produced by CDM simulations.

Contents

List of Figures

List of Tables

Chapter 1

Introduction

1.1 General Properties of the Universe

It is probably best to put dark galaxies into context by first describing some fundamental aspects of the Universe in which they are thought to exist. Their existence could explain some shortcomings of the widely accepted cosmological concordance model and so establishing the existence of a population of dark galaxies is of great importance. I then move on to describing the mechanisms by which dark galaxies could exist. This explains how dark galaxies can be considered extreme versions of low surface brightness galaxies and a brief history of searching for low surface brightness galaxies is given. This will naturally lead on to a discussion of H I surveys and their rôle in the search for dark galaxies.

We now live in cosmologically enlightened times. We know this because cosmologists tell us so, but how has cosmology arrived at such a confident claim? It is a story that has been 80 years in the making and is by no means complete. When

Georges Lemaître first proposed the idea that the Universe had a finite age, and had grown from a very small, hot, dense state, it was based on largely theoretical grounds, from solutions to Einstein's equations for General Relativity. This idea is what came to be known as the Big Bang theory. Einstein had proposed that the Universe is a dynamically stable system that is not expanding nor contracting. The redshift work of Hubble and Slipher (Slipher, 1913; Hubble, 1929) led to the inference that the Universe is expanding and the rejection of Einstein's Static Universe principle.

Other Cosmological models were also proposed between 1920 and 1950 (e.g. Zwicky, 1929; Milne, 1935; Hoyle, 1948). The discovery of the Cosmic Microwave Background, Penzias & Wilson (1965), provided the strongest evidence in favour of the Big Bang and caused the majority of cosmologists to abandon other theories.

Measurements of the motions of galaxies in clusters (Zwicky, 1937) had revealed that the galaxies themselves were moving much faster than predicted. This had two interpretations: either there is more matter than can be traced by visible light alone, or Newton's theory of gravity is incorrect at these large distance and mass scales. The scientific community by and large could not accept the latter. The only other alternative was that there must be a new type of matter unlike anything that was known, that could only interact gravitationally, without emitting or absorbing radiation – Dark Matter. In later years Dark Matter was also mentioned as a possible explanation of the discrepancy between the mass of the Universe as measured from luminous material (Hubble, 1926; Whitford, 1954) to that predicted by simple calculations based on an expanding Universe (e.g. Sandage, 1961).

Throughout the 1970s, astronomers studied the gas content of spiral galaxies through the use of the 21-cm spectral line of hydrogen. The large extent of the gas

suggested that there might be a lot of baryonic mass that does not emit at optical wavelengths and so had gone undetected. However another startling result came from studying the rotation of the gas within these galaxies. Newtonian gravity predicts that the gas in the outer reaches of galaxies should follow Keplerian orbits, where the rotational velocity V follows a $r^{-0.5}$ dependence and r is the distance from the centre of the galaxy. The observations showed that V is actually constant in the outer reaches of the galaxies, suggesting that the mass is actually increasing linearly with radius. Once again, the validity of Newtonian gravity was thrown into doubt, but could be rescued if one invoked the same Dark Matter that was responsible for the motions of cluster galaxies.

Early estimates on the amount of Dark Matter present in the universe varied wildly. By the 1980s, observational astronomers had converged on a value for the matter energy density, Ω_m of roughly 20 % of the Universal energy budget, with Dark Matter dominating over the baryonic matter by a factor of ten. Yet there was still no theory to explain the apparent energy shortfall.

As instruments became more sensitive and sophisticated, astronomers began to peer further and further into the universe, and everywhere they looked they saw evidence of Dark Matter on galaxy scales and larger. Large area optical surveys (e.g. the CfA redshift survey, Huchra et al. 1983) were painting a picture of a web-like universe consisting of vast filaments and walls of galaxies and equally vast, empty regions, i.e. voids (e.g. Geller & Huchra, 1989). Without the gravitational influence of the Dark Matter it is impossible to create these huge structures within the lifetime of the Universe.

Despite the adoption of a Universe dominated by Dark Matter, at the turn of the 1980s the Big Bang model still had its flaws. The Inflationary Scenario (Guth,

1981) was very successful in addressing many of the issues (the Horizon problem, the Flatness problem, magnetic monopoles to name but a few) and was incorporated into the model. In this scenario the Universe underwent a period of intense exponential expansion very early on. Primordial temperature fluctuations were quickly blown up to cosmological scales which would go on to produce the seeds of the large scale structure seen in galaxy redshift surveys. Any residual curvature in space-time would be smoothed out by the rapid expansion producing the flat, Euclidean Universe that is measured today. However, at the time of Inflation's inception, no temperature fluctuations had been observed in the CMB. The flatness of the Universe introduced a further problem: the matter energy density was still only about a quarter of that required to produce a flat Universe.

Throughout the next 20 years astronomy instrumentation improved and computing power became cheaper. Orbiting telescopes, uninhibited by the Earth's atmosphere, began to play a major rôle in astronomy. The COBE experiment (Smoot et al. 1992) revealed not only that the Universe is flat but also discovered the minor temperature fluctuations in the CMB predicted by Inflation.

Ground-based galaxy redshift surveys (the 2dF Galaxy Redshift Survey, Colless et al. 2001; the Sloan Digital Sky Survey – SDSS, Stoughton et al. 2002; the 6dF Galaxy Redshift Survey, Jones et al. 2004) built on the work of the CfA redshift survey, providing redshift data for 100,000s of galaxies and quasars, revealing more large-scale filaments and superclusters. Gravitational lensing studies using Hubble Space Telescope, and high resolution radio interferometers provided a means of estimating galaxy and cluster masses independently of the light. The results of these studies have added to the growing support of Dark Matter on the scales of galaxies and clusters. The energy density fraction of Dark Matter (~ 0.24) still fell far short of the value required for a flat universe. Although many cosmologists still adhered

to an Einstein-de Sitter model of the Universe in which $\Omega_m = 1$, speculation was growing that there was an as-yet unmeasured contributor to the Universal energy budget akin to the Cosmological Constant first proposed by Einstein.

Results from the Supernova Cosmology Project (Perlmutter et al. 1999) and the High-z Supernovae Search Team (Reiss et al. 1998) first discovered that supernovae at high redshift were dimmer than expected. This was interpreted as the first evidence of a non-zero Cosmological Constant, and it's measured value was sufficient to close the gap between the matter energy density and the critical value. This mysterious new energy form has been christened Dark Energy and it is causing the expansion of the Universe to accelerate.

More recently WMAP (Bennett et al. 2003) has mapped the CMB over the entire sky but with higher resolution than COBE. By combining the results of this survey with all the previous studies mentioned above, the WMAP team were able to derive an accurate set of cosmological parameters given different assumed cosmological models. These derived values have been measured to an astonishing degree of precision and it is this that has heralded the self-proclaimed era of 'Precision Cosmology' and has established what we now accept as the Concordance Model, or Λ-CDM model, which constitutes the following:

- The Universe violently came into existence when it expanded from an extremely small, dense, hot state. This is known as the Big Bang.
- At a very early stage in the Universe's existence it underwent a period of exponential expansion, known as the Inflationary Period.
- The universe then carried on expanding and is still expanding today.
- The geometry of the Universe is Euclidean, which requires a specific energy

budget. The energy budget consists of:

- 73.2 % Dark Energy
- 22.2 % Cold Dark Matter
- 4.6 % Baryonic Matter

Despite this being the self-proclaimed age of precision cosmology little is known of the nature of what makes up the majority of the Universe. Let us discuss what is known of Dark Matter and in particular, Cold Dark Matter.

1.2 Cold Dark Matter

There is a wealth of indirect evidence for Dark Matter: motions of galaxies in clusters (Zwicky, 1929), galaxy rotation curves (e.g. Rubin & Ford, 1970; Roberts & Rots, 1973; Gottesman & Davies, 1970; Rubin, Thonnard & Ford, 1978), gravitational lensing (Sanders, van Albada & Oosterloo, 1984; Lacey & Ostriker, 1985; Trimble, 1987), CMB anisotropy measurements (Smoot et al. 1992; Bennett et al. 2003), and most recently observations of the Bullet cluster (Clowe, 2006). Two forms of Dark Matter are already known: baryonic (e.g. non-luminous gas, brown dwarfs) and non-baryonic (e.g. neutrinos and black holes) however, these forms are considered to make up a small fraction of the matter energy component. The rest must consist of an exotic form of matter. By its nature Dark Matter is difficult to observe directly, nevertheless in the recent years several experiments have begun with the aim of directly detecting Dark Matter. Although some of these experiments have been running for two years or more, there has not been a convincing detection yet.

Most of the exploration of the different forms Dark Matter might take has been the result of large cosmological simulations. Results from CMB experiments and galaxy redshift surveys provide two very useful sanity check points: they show what the Universe looked like very soon after it came into existence and what it looks like now. Any cosmological simulation can assume any model so long as these two criteria are met. Computing the various forces acting on individual particles, applying those forces and repeating the steps over a simulated evolution of 10^{10} years is computationally intensive. It is no surprise that availability and cheapness of computing power has played a large part in the development of numerical simulations. Whereas only a few years ago a Universe of a few million particles was about the limit of simulations (Moore et al. 1999), it is now possible to work with simulated Universes of up to 10^{10} particles (Springel et al. 2005).

For a decade or so the favoured form of Dark Matter has been Cold Dark Matter. The particles that comprise this type are long-lived, non-relativistic and collisionless. They must be long lived, because the Universe is still feeling their effects in the present epoch. The importance of travelling at non-relativistic speeds contributes to their ability to be able to cluster immediately after the Universe became matter-dominated. Collision-less means that they they exert no pressure on each other or on baryons, hence they can only interact gravitationally.

As the Universe expanded and cooled, matter began to condense into defined structures. The smallest objects in Universe were the first to form. These in turn would coalesce and form larger structures, which in turn would merge and form larger structures and so on. This is what we have come to know as hierarchical structure formation. Simulations using Cold Dark Matter have been extremely successful in reproducing the the large-scale structure distribution that is observed in galaxy-redshift surveys, within the given lifetime of the Universe. Below the

scale of galaxy clusters the simulations are less successful. Two problems persist to this day: at the sub-kiloparsec scale, high-resolution observations of the cores of nearby low surface brightness galaxies have revealed that the central density profile of Dark Matter is a lot flatter than predicted (de Blok & Bosma, 2002). Such a profile is usually referred to as having a core rather than a cusp. The other problem exists at the mass level of Milky Way sized galaxies. The simulations predict that there should be a large population of dozens or even hundreds of associated dwarf galaxies (Klypin, 1998; Moore, 1999). This is in stark contrast to the Local Group where the known population of dwarf galaxies is around 14 or 15 per large Milky Way-sized galaxy.

The issue of cores versus cusps for Dark Matter haloes has been hotly debated by theorists and observers. The theorists initially claimed that uncertainties that arise from observing techniques could account for the observed flattening of the Dark Matter profile in the inner parts of the galaxies. The work of de Blok & Bosma (2002) showed a population of 65 galaxies all of which had high resolution Hα spectra in which effects such as beam smearing and slit alignment had been accounted for. Their results clearly show that the Dark Matter halo is significantly flatter in the inner kiloparsec of low surface brightness systems. This particular problem is unlikely to be definitively resolved until numerical simulations can attain sufficient spatial resolution at the sub-kiloparsec scale.

The other issue of numbers of Dark Matter haloes surrounding Galactic-sized haloes has a number of possible solutions: not all Dark Matter haloes contain baryons; the haloes are populated with galaxies that are too faint to detect with current methods; the haloes are populated with baryons in the form of gas, but the gas has not formed stars and has, thus far, avoided detection; or the model on which the simulations are based is incorrect.

Could there be a class of object too faint or diffuse that could comprise the missing satellite population? Low Surface Brightness Galaxies (LSBs) are particularly difficult to detect by usual methods due to their extremely diffuse nature. As a result their numbers were vastly underestimated until the 1980s and 1990s when detailed surveys were commissioned specifically aimed at detecting LSBs. Could these constitute the missing population, as suggested by Dalcanton et al. (1997)?

Briggs (1997) concluded that our knowledge of the local Universe is remarkably complete and that new, more sensitive surveys are discovering more distant LSB galaxies. This suggested that LSBs were unlikely to constitute the missing dark matter haloes. In the last few years, however, the number of companions to our Milky Way has nearly doubled thanks to the introduction of new techniques such as detecting stellar over-densities in sky surveys such as the SDSS (e.g. Willman et al. 2005) or 2MASS (Martin et al. 2004). All the objects found were among the lowest luminosity and lowest surface brightness systems ever found. Even with the success of this new method the number of satellites around the Milky Way is still far short of the 150 or so predicted by the simulations.

Another solution is that the population of missing satellite haloes is not luminous. If the haloes do not contain baryons, as suggested by Benson (2001), then the satellites will be impossible to detect by current methods. Their presence may be detectable by gravitational lensing, but that would require much more sensitive techniques than are presently available. If it transpires that the decay of Dark Matter particles yields detectable electromagnetic emission (Bertone, Sigl & Silk, 2001), then this would provide another way in which such a population may be detected.

Without modifying the model, the other option left open is that the satellite haloes

contain baryons that have not formed stars for some reason. At one time, it was thought that High Velocity Clouds could fit this criterion. These are low column density, small mass ($< 10^6$ $M_\odot$) clouds of neutral hydrogen that have been detected via their H I signature. They are called high velocity because their measured velocities relative to the Local Standard of Rest (LSR) are much higher than the gas that rotates in the plane of the Galaxy. Some of these clouds are extremely extended forming filaments and web-like structures that cover the entire sky.

The debate has rested on whether the HVC population is bound to the Galaxy or whether they lie at extragalactic distances. At moderate distances they would harbour huge amounts of baryons and dark matter, but without primary distance measurements it was impossible to judge how close to the Galaxy these objects were. With the detection of individual HVCs bound to other galaxies (e.g. Braun & Thilker, 2004; Westmeier, Braun & Thilker, 2005; Miller & Bregman, 2005) it was realised that HVCs must also be bound to the Milky Way and no more than 50 kpc from the Galaxy. The proximity of the HVCs enabled upper limits to be placed on the dynamical mass of these systems. These in turn have revealed that HVCs are not Dark Matter dominated and hence they can't represent the missing Dark Matter satellite population. It is still unclear where these objects fit into the picture of galaxy evolution. While some believe they are the leftover building blocks of hierarchical structure formation, others believe they represent clouds of neutral gas that have been ejected by Galactic Fountains (Shapiro & Field, 1976) which are now raining back down on to the disk.

Another way of creating baryon-bearing Dark Matter haloes is by suppressing the star formation processes within them. Currently there are two schools of thought for achieving this: the baryons are heated at some time in the Universe's past and

have not had sufficient opportunity to cool and condense into stars in the present day; the baryons retain enough centrifugal force during condensation to balance gravitational instabilities which would lead to star formation.

Photo-ionisation is a popular method of heating baryonic matter. And there is evidence to suggest that there was a time in the Universe's past, subsequent to the time of recombination, when it underwent a period of ionisation. This 'Epoch of Reionisation' as it has come to be known is still not well constrained.

The source of the ionising flux is Lyman-α photons from the Inter-Galactic Medium (IGM). However the origin of these photons is still debated. While most authors agree that important rôles are played by stellar winds from the first generation of massive stars, the subsequent supernovae and Active Galactic Nuclei (AGN), there is still disagreement on the amount of energy contributed by each.

By changing the time at which this era of reionisation occurred, it is possible to account for different structure formation scenarios. For instance using the WMAP year 1 results places $z_{ion} \sim 17$. With such a high value, baryons within dwarf galaxy DM haloes should have had sufficient time to condense and form stars. If all DM haloes are populated with baryons, the number of observed companion galaxies to the Milky Way and Andromeda should be much higher. However with the WMAP year 3 results, $z_{ion} \sim 10$, making it possible for ionised structures to survive to the present day, embedded within some of the DM haloes surrounding the Milky Way (Macciò, 2006). While the simulations predict the number of luminous galaxy companions to the Milky Way which is consistent with the observed numbers, evidence of these DM dominated, ionised structures remains to be found. It is unlikely that this will be directly observed in emission any time soon, since the signature of the haloes containing ionised material would be diffuse and of low

luminosity.

The rate of gas accretion on to a galaxy depends on the temperature of the IGM gas falling into the halo. As the gas falls into the halo potential, shock-heating will also take place. The subsequent cooling of baryons within the halo is crucial in defining whether or not stars will form in the gas. Macciò (2006) attempts to model this cooling, but unfortunately it is complex, depending on metallicity and gas density which also evolve with time. This, combined with the fact that observations of the Epoch of Reionisation are limited to a handful of galaxies at $z \sim 5$ and quasars at $z \sim 6$, the interpretation of the results of Macciò (2006) is limited.

The other method of preventing star formation is to somehow counteract the gravitational forces responsible for the collapse of the gas into stars, while accepting that some of the gas in the halo has cooled sufficiently to the levels required for star formation (<20 K). At this level it is quite possible that a significant amount of the hydrogen is in neutral form and so would be detectable by the 21cm spectral line emission. The resulting object would contain baryons, dark matter but no stars – a 'Dark Galaxy'. The issue then becomes what mechanisms are available that can balance gravity. As this is central to the thesis, this will now be considered in more detail.

1.3 Star Formation Thresholds

1.3.1 The Toomre-Q Criterion

At its most basic, star formation results from gravitational collapse of a gas cloud. The first person to attempt to quantify the conditions for star formation was Jeans (1928). He first defined a length scale for an isothermal gas cloud of a given mass, the Jeans Length, beyond which the cloud would be unstable to its own self-gravity and would collapse. Jeans' work has been at the heart of star formation theories ever since.

Jeans' originally considered a 3-D cloud, however galactic gas and the stellar population of spiral galaxies is confined to a disk. It was then a natural progression to apply Jeans' stability criterion to a disk and explore the impact of rotation, shear, density waves etc. Two important papers on this subject are Toomre (1964) and Goldreich & Lynden-Bell (1965).

Toomre was exploring, analytically, the ability of stars to cluster together under the influence of spiral density waves. He considered a mini-disk of stars embedded within the rotating galactic stellar disc and investigated what would happen if the mini-disc underwent a small perturbation. His major result was to calculate to what extent rotation could balance the self-gravitation of the mini-disc. His result is expressed here in terms of the stellar surface density:

$$\Sigma_{crit} = \frac{\sigma_* \kappa}{3.36G} \tag{1.1}$$

where Σ_{crit} is the critical stellar surface density, σ_* is the velocity dispersion of the stars, κ is the epicyclic frequency (see Appendix A.1) and G is the gravitational

constant. κ is a term which is dependent on the rotation of the stars, thus:

$$\kappa^2 = 2\left(\frac{V^2}{R^2} + \frac{V\mathrm{d}v}{R\mathrm{d}R}\right) \tag{1.2}$$

The importance of Eqn. 1.1 is that if the local stellar surface density rises above Σ_{crit} the region becomes unstable and will undergo gravitational collapse.

Goldreich & Lynden-Bell (1965) independently developed the equivalent relation for a thin gaseous disk. The analysis gave a very similar result to Toomre (1964) only differing by 7 percent:

$$\Sigma_{crit} = \frac{c_s\kappa}{\pi G} \tag{1.3}$$

Here, Σ_{crit} is the critical *gas* surface density and c_s is the local gas sound speed.

The analyses of Toomre and Goldreich & Lynden-Bell gave rise to a different interpretation than that of the 3-D Jeans model: if the size of the perturbation in some local region is too small, the self-gravitation is too weak to overcome the local gas pressure. If the perturbation is too large, then rotation balances the self-gravitation.

The results from these analyses provided the basis for the first observational test (Quirk, 1972) of what has come to be known as the Toomre-Q criterion. H I spectral line data from several nearby, large, spiral galaxies provided all the necessary information to be able to examine the radial dependence of the Toomre criterion. κ was deduced from the rotation curves, Σ was simply measured directly from the data and the sound speed c_s is set equivalent to the 1-D velocity dispersion of the gas.

For most of the galaxies, beyond the extent of the stellar disk, the gas in the disk

did fall below the critical surface density threshold described by the Toomre-Q. The one discrepant result came from the highly inclined galaxy M 101. The high inclination angle increases the uncertainty in the surface density measurements and the rotation velocity estimation.

In the intervening years the Toomre-Q criterion has come under greater scrutiny (Kennicutt, 1989; van der Hulst, 1993; van Zee, 1997; Martin & Kennicutt, 2001, de Blok & Walter 2006) and while it has been refined (e.g. Fall & Efstathiou, 1980; Kennicutt, 1989; Martin & Kennicutt 2001) it remains basically the same. Kennicutt (1989) studied 15 galaxies and found a sharp decrease in the star formation rate when the surface density dropped below two thirds of the critical value. Hence Kennicutt introduced a factor, $\alpha_Q \equiv Q^{-1}$, to match the observations to the theory. The introduction of α_Q is not just a 'fudge factor' to force the results to match the theory. It's physical significance is in accounting for the oversimplifications involved with assuming an infinitely thin, purely gaseous disk. Kennicutt & Martin (2001) built on the work of Kennicutt (1989) and studied over 30 nearby spiral galaxies. They concluded that the Toomre-Q was still a valid star formation threshold criterion, and refined the value of, α_Q to 0.69.

This result was largely consistent with the findings of van der Hulst et al. (1993). They studied a sample of LSBs and found that the gas surface density profiles consistently fell below the critical surface density profile prescribed by Kennicutt (1989). This was used as an explanation as to why LSBs have fewer stars despite their 'normal' gas repositories. It was simply that the surface density of the gas was not sufficiently high to become unstable. This, however, was a global statement and did not address how, at local scales, stars could be forming.

The criterion is not universally successful, nor has it been without its opponents.

Kennicutt (1989) noted that for two of his lower luminosity galaxies, the gas surface density fell *below* the critical threshold for much of their star-forming disks. For a star formation threshold theory to be successful it must work for all types of galaxy without exception. The Toomre-Q criterion ignores the influence that shear has in stabilising the gas in a differentially rotating disk. A natural progression was to then examine the effect of shear.

1.3.2 The Shear-modified Toomre-Q

Dwarf Irregular galaxies (dIrrs) are low-luminosity, gas-rich, low-mass systems. Generally they have rotation curves that rise slower than larger-mass systems and peak at lower velocities (Simpson & Gottesman, 2000). Their lack of spiral structure is an indication that they are not subject to spiral density waves that help shape spiral galaxies. As such the gas should be less stable in dIrrs than in larger galaxies, so it must be supported by some other means, such as shear, to explain the lack of star formation.

The local shear rate is described by the equation:

$$A = -\frac{1}{2} R \frac{d\Omega}{dR} \tag{1.4}$$

where, $\Omega = \frac{V}{R}$, is the angular speed. If R is replaced by the distance of the Sun from the Galactic centre, and Ω is replaced by the Sun's angular speed, A is simply equal to Oort's constant.

Following Elmegreen (1993) shearing perturbations grow with a characteristic time of:

$$t_{sh} = \frac{c_s}{\pi G \Sigma} \tag{1.5}$$

If this time is longer than the dynamical timescale of a perturbation the region will be unstable and collapse leading to star formation. This leads to a modification of the Toomre-Q:

$$Q_{shr} = \frac{c_s A}{G\Sigma} \tag{1.6}$$

Hunter, Elmegreen & Baker (1998) studied several different star formation model criteria in a limited sample of 15 irregular galaxies. When the Toomre-Q is used, they found a value of $\alpha_Q = 0.25$ for their sample, compared to $\alpha_Q = 0.69$ as found by Kennicutt for his sample of spirals. Surprisingly a smaller value of α suggests that the gas in irregulars is *more* stable than in spirals, or possibly that the Toomre-Q is not as applicable to irregular galaxies as it is to spirals. Toomre or Quirk only considered thin, pure gas or thin, purely stellar disks. Hunter, Elmegreen & Baker (1998) extended their analysis to include thick gas disks with an embedded stellar component, 3-D systems with dark matter, thermal impact on the gas, and shear regulated star formation. In fact all the processes listed produced unacceptable values for α, apart from shear. However, none of the models was successful in predicting at what radius star formation ends. They do make the comment however that the gas column density at the radius where H II regions are no longer observed is always $\sim 3 M_\odot$ pc^{-2}. This suggests that there is a star formation threshold based on the column density of the gas alone.

1.3.3 Constant H I star formation threshold

Simpson & Gottesman (2000) take a different view to star formation in dIrrs to that of Hunter, Elmegreen & Baker (1998). While they concede that dIrrs have slowly rising rotation curves, the shape of the curves indicate that most dIrrs rotate as solid bodies. They inferred from this that neither density waves nor shear could

promote stability in these systems and that the most likely cause was simply that the observed H I surface density was below the canonical value of $\Sigma_{HI} = 10^{21}$ cm^{-2}.

This was not a new idea – the thought that a critical surface density of H I for star formation that is apparently independent of rotation was first suggested by Gallagher & Hunter (1984). Data from spiral and irregular galaxies available at the time provided empirical evidence that there was a sharp cutoff in Hα emission and hence in recent massive star formation at around 5×10^{20} cm^{-2}. Further studies (e.g. Skillman & Bothun, 1986; Skillman, 1987; Guiderdoni, 1987; de Blok & McGaugh, 1996) all led to a similar conclusion although the measured critical values vary between (2.6–10) $\times$ 10^{20} cm^{-2}.

A physical mechanism that could give rise to a constant critical gas surface density was first suggested by the modelling of Elmegreen & Parravano (1994). They first argue against the Toomre-Q criterion as prescribed by Kennicutt (1989) claiming that Q should be self-regulated by feedback processes. These processes would conspire to keep Q between 1–2 throughout the *entire* galactic disk, not just in the inner parts of the galaxy.

Instead they claim that the star forming potential of the ISM is governed by the pressure of the ISM, irrespective of the source of the pressure. When the pressure is sufficiently great, the density increases to such a point that the gas can cool efficiently. Eventually the thermal temperature of the gas will be sufficiently low that star formation can occur. Hence the only requirement for a potential star forming region is that the ambient temperature of its gas be low enough that any pressure perturbation (as a result of rotation, shear, shock, turbulence etc.) will cause the gas density to rise and induce collapse.

They allow their gas to have varied metallicities and subject it to different radiation fields and ionising fluxes. For each combination they calculate the minimum pressure and corresponding density that can sustain the two thermal phases (cold, T $\sim 10^2$ K and warm T $\sim 10^4$ K) necessary for star formation. They show that low equilibrium temperatures require moderately high pressures. The gas in the outer parts of galaxies cannot cool and form cold, dense clouds since the pressure here is too low and hence the star formation in these regions is low. They observe that there is a corresponding increase in Q at the edge of the stellar disk, but that this is coincidental, and only affects strongly self-gravitating clouds and regions inside spiral arms.

The discoveries of Elmegreen & Parravano (1994) laid the foundations for the modelling of Schaye (2004). Schaye modelled both HSBs and LSBs embedded within Dark Matter haloes. The gaseous disks were self-gravitating, contained metals and dust, and were exposed to ionising UV radiation.

His particular focus was on the behaviour of the gas sound speed, c_s, as a function of radius. Previous studies of the Toomre criterion had assumed a constant value of c_s, although not necessarily the same value (e.g. Hunter, Elmegreen & Baker (1998) use $c_s = 9$ km s^{-1}). Ferguson et al. (1998) disputed this assumption. They traced c_s using the 1-D velocity dispersion of the gas and included its radial variation in their calculations of the critical gas column density. The analysis is limited to one galaxy (NGC 6946) due to the high inclination of the other galaxies. They find that using a constant c_S is incompatible with the recovered value of α. To recover the stability criterion, either α must be higher, or c_s must be higher in the outer parts of the disk.

Schaye recognised from the Elmegreen & Parravano (1994) models that the abrupt

change in temperature associated with moving from one phase to the other must also affect the sound speed. Hence the phase transition must have important implications for disk stability. His modelling shows that the change from the warm phase to the cold phase happens abruptly. This swift phase transition is accompanied by a corresponding drop in the sound speed.

This has great impact on the Toomre-Q criterion. Since κ in Eqn. 1.3 is varying smoothly over this regime, a sharp drop in c_s will cause a corresponding drop in Q and the gas then becomes unstable. Since the temperature change is responsible for the change in the sound speed, it is the phase transition that influences Q and not vice versa. This is emphasised in Fig. 3 of Schaye (2004).

One of the most important results is that he predicts a critical H I surface density, $\Sigma_{HI} = 3\text{–}10 \times 10^{20}$ cm^{-2} (2.4–8 M$_\odot$pc^{-2}) below which star formation is unlikely to occur. This critical surface density is insensitive to the galactic rotation.

Star formation thresholds are vitally important to the discussion on Dark Galaxies. If there exists a population of objects that consist solely of gas and Dark Matter, then the gas must be gravitationally stable. For this to occur, requires different scenarios depending on which criterion is considered. To investigate which criterion should be adopted, a study of LSBs will prove to be vital, since they represent a class of objects in which the criteria for star formation are only just met. Since observations of LSBs are subject to subtle selection effects, their impact is now discussed.

1.4 Selection Effects

The existence of massive galaxies with low surface brightness were first formally postulated by Zwicky (1957) and investigated later by Arp (1965). They both recognised that galaxy catalogues (at that time limited to optical surveys) used various selection criteria (e.g. size, magnitude) to distinguish galaxies from stars and that these criteria were biased against both finding compact bright galaxies and large dim galaxies. Such biases are known as selection effects and it is impossible to say anything about the size and distribution of the LSB population without quantifying these effects.

Freeman (1970) compared the surface photometry for 36 disk galaxies. For 28 of his sample, the B-band central surface brightness, μ_{0B} corrected for inclination, was nearly constant: $\mu_{B0} = 21.65 \pm 0.30$ mag arcsec^{-1}. His sample spanned a magnitude range of $\sim$5 so the result seemed even more astonishing. This finding came to be known as 'Freeman's Law' and was adopted by many as proof that the LSB population was insignificant. In his final conclusions though, Freeman himself questions what process could possibly produce such a narrow surface brightness distribution.

The question went unanswered for several years until a paper by Disney (1976). In this brief paper, Disney presented a method of quantifying the selection effects present in surveys. He proposed that galaxy selection from optical surveys was based on isophotal diameter. Disney estimated the surface brightness limit of the emulsions typical of surveys at the time ($\mu_B \sim 24$ mags arcsec^{-1}) and applied the size selection criterion to objects of different surface brightness. With this information he was able to estimate the volume over which galaxies of different surface brightness could be seen - the *visibility function.*

The visibility function peaked at a central surface brightness value of $\mu_{B0} = 21.83$ mags arcsec^{-1} for spirals. This was very close to the observed peak in the surface brightness distribution, $\mu_{B0} = 21.65$ mags arcsec^{-1}, that Freeman found. Disney also applied his analysis to the work of Fish (1964) who had found a similar result for ellipticals. This time the visibility function peaked at $\mu_{B0} = 15.31$ mags arcsec^{-1} compared with Fish's value of $\mu_{B0} = 14.8$ mags arcsec^{-1}. This method of selection naturally excluded LSBs since only a small proportion of their disk would be above the isophotal limit. Similarly very compact HSBs have small isophotal diameters, so they would also be excluded from the catalogue. Disney deduced that there was probably a large population of LSBs in the local universe that had gone undiscovered.

Disney's deductions were not met with universal enthusiasm. Kormendy (1977) offered an alternative explanation of Freeman's law. He suggested that the fitting process that was used to estimate the central surface brightness gave rise to the peak in the surface brightness distribution. Shostak (1977) analysed four separate H I surveys of the nearby universe and declared that there were no new H I sources that were unambiguously extragalactic. Freeman himself raised several objections to Disney's assertions (Freeman, 1978).

Disney & Phillips (1983) revised the visibility function to account for limiting luminosity L as well as limiting size R_L. Each imposed its own limitation on the visibility function, the overall limit being the lesser of the two functions at any given surface brightness. Disney had already shown that the visibility function for a size-limited catalogue was highly peaked. They argued that there would be two effects acting on the measured luminosity: for galaxies of a given luminosity, most of the light from LSBs would fall below the detection limit, hence the luminosity would be erroneously low. Similarly for very compact HSBs, the plate would saturate

again lowering the measured value of the luminosity. So the visibility function for luminosity was also peaked. The visibility functions, V_L, V_θ calculated from the distance limits of Disney and Phillips (1983) are:

$$V_L \equiv \Omega d_L^3 = \Omega \frac{L_{ap}}{L_T}^{1.5} 10^{0.6(m-M+5)} \tag{1.7}$$

for the magnitude limited catalogue, and:

$$V_\theta \equiv \Omega d_\theta^3 = \Omega \frac{R_{ap}}{R_L}^3 \frac{10^{0.6(m-M+5)}}{(\theta\sqrt{\pi})^3} \tag{1.8}$$

for the size limited catalogue. Where Ω is the solid angle covered by the catalogue, M is the absolute magnitude, m is the apparent magnitude, θ is the angular size limit of the catalogue. The ratio $\frac{L_{ap}}{L_T}$ is given by the equation:

$$\frac{L_{ap}}{L_T} = X - [1 + 0.4ln10(\mu_L - \mu_0)]10^{-0.4(\mu_L - \mu_0)} \tag{1.9}$$

where $X = 1$ for unsaturated images and $X = (1 + s + 0.5s^2)e^{-s}$ for saturated images, where $s \equiv 0.4ln10(\mu_L - \mu_0 - 2.5log_{10}N)$. μ_L is the limiting surface brightness of the catalogue, μ_0 is the central surface brightness. The ratio $\frac{R_{ap}}{R_T}$ is given by the equation:

$$\frac{R_{ap}}{R_T} = \left(\frac{0.4ln10}{\sqrt{2}}\right)(\mu_L - \mu_0)10^{-0.2(\mu_L - \mu_0)} \tag{1.10}$$

The combination of the two visibility functions causes the range of μ_0 to be limited even further.

1.4.1 Low Surface Brightness Galaxies

Disney & Phillips (1983) sparked renewed interest in LSBs as different groups went in search of Disney's 'crouching giants' - massive LSBs. Their potential cosmological importance at the time is obvious since a large population of these objects could possibly account for a substantial amount of Dark Matter. Following a survey of field galaxies, van der Kruit (1987) claimed that Freeman's law was correct and could not be explained by the surface brightness selection effects of Disney & Phillips (1983). Selecting only galaxies whose $\mu_J = 26.5$ mags arcsec^{-2} isophote was larger than $\theta = 120''$, he did not find any galaxies that were not already listed in the UGC (Nilson, 1973). By just selecting spirals of type Sc or earlier, the surface brightness distribution was found to peak at $\mu_0 = 21.5 \pm 0.4$ mags arcsec^{-2}.

Re-analysis of the data by Davies et al. (1994) examined the completeness of van der Kruit's surface brightness bins using the $< V/V_{max} >$ criterion. For a complete sample one would expect $< V/V_{max} >= 0.5$, yet for $\mu_{B0} > 22.3$ mags arcsec^{-2} Davies et al. found the value nearer 0.35, indicating that the survey was incomplete for LSBs. He also assumed that the maximum visible distances defined by the magnitude limit and the size limit were the same, so he normalised the visibility curves. This produced an artificially low surface brightness limit, which implied unrealistic limits on the response of the photographic emulsion.

There was a large number of surveys, catalogues and detailed observations of LSBs throughout the 1980s and 1990s (e.g. Longmore *et al.* 1982; Binggeli *et al.* 1985; Phillipps *et al.* 1987; Impey, Bothun & Malin, 1988; Ferguson & Sandage 1988; Schombert *et al.* 1992; van der Hulst et al. 1993; de Blok, van der Hulst & Bothun, 1995). The first giant low surface brightness galaxy, Malin 1, was not discovered

until 1987 (Bothun *et al.* 1987). Instead of turning up a large population of large-mass LSBs, these early surveys typically discovered large numbers of late-type spiral and irregular galaxies with low surface brightnesses. The general properties of this galaxy class are: central surface brightnesses $\mu_{0B} \gtrsim 23.0$ mag arcsec^{-2}, luminosities in the range $-13 \lesssim M_B \lesssim -19$ (Impey *et al.* 1996), blue colours $B - V \sim 0.5$ (Schombert *et al.* 1992), gas rich disks (gas fraction $\sim$ 0.5–1.0) (Schombert *et al.* 1992), metallicities [O/H] $\lesssim$ 0.3 solar (McGaugh, 1994) and low star formation rates ~ 0.1 M$_\odot$yr^{-1} (van den Hoek *et al.* 2000). In comparison HSBs have luminosities in the range $-17 \lesssim M_B \lesssim -21$, central surface brightnesses $19.6 \lesssim \mu_{0B} \lesssim 23.0$ mag arcsec^{-2}, typical colours ($B - V \sim 0.8$), gas fractions $\sim$ 0.1, metallicities ($0.5 \lesssim$ [O/H] $\lesssim 1.0$ solar) and star formation rates ~ 1 M$_\odot$yr^{-1}. While making such comparisons can be useful, it should be noted that the division between LSB and HSB is somewhat artificial since all galaxies form a continuum. Most late-type LSBs are dark matter dominated at all radii (de Blok & McGaugh, 1997), making them ideal test beds for Cold Dark Matter models, galaxy evolution theories and in particular, star formation theories.

In two important works, McGaugh (1999) and O'Neil & Bothun (2000) collated the work of several LSB surveys and examined the visibility corrected surface brightness distribution down to $\mu_{B0} = 25$ mag arcsec^{-2}. They both show that beyond the Freeman value, the surface brightness distribution is relatively flat. De Jong & Lacey (1999) however disagree with these analyses, stating that the visibility function is more complicated than a simple relation between the volume and the surface brightness. There do seem to be significant differences at the HSB end implying that there may well be other factors influencing galaxy selection from optical surveys. Since LSBs are rich in H I and H I emission takes place in the radio part of the spectrum, one would expect that a survey designed specifically to detect

this gas signature would avoid the selection effects experienced in the optical and detect many LSBs. As will be shown, this is true to some extent, but inevitably different selection effects are introduced, which must also be quantified.

1.5 H I Surveys

In previous sections the importance of H I has been emphasised in the context of star formation, galaxy dynamics and also as a means of avoiding the complicated selection effects of galaxy catalogues based on optical astronomy. It is not surprising then that there have been a number of H I surveys in the last thirty years. The H I line emits in the radio part of the spectrum, hence it is necessary to have some understanding of radio astronomy.

1.5.1 Radio Astronomy

Until the twentieth century astronomers were limited to the optical waveband, due to the limitations of technology of the receivers (the eye or photographic plates). With the recognition by Jansky in 1931 that there are radio sources that must be extra-terrestrial, a new window was opened up with which to observe the cosmos. Unlike optical radiation, radio waves are not attenuated by gas or dust extinction and so provide a unique probe of the Universe.

The flux density of radio waves, S_ν, that is measured by a radio telescope is defined as the intensity of the source, I_ν integrated over some solid angle:

$$S_\nu = \int_\Omega I_\nu \, d\Omega \qquad (Wm^{-2}Hz^{-1}) \tag{1.11}$$

For convenience, the intensity of a source is usually expressed in terms of the brightness temperature, T_b. This is the temperature of a theoretical black body that would produce the measured intensity at the observed frequency. In the Rayleigh-Jeans approximation for long wavelengths (valid for radio wavelengths), the Planck function for black body radiation reduces to:

$$B_\nu \equiv I_\nu = \frac{2kT_b}{\lambda^2} \tag{1.12}$$

Hence integrating Eq. 1.12 over the entire solid angle of the object that falls within the telescope beam yields:

$$S_\nu = \frac{2kT_b}{\lambda^2} \int_\Omega f(\Omega) d\Omega \tag{1.13}$$

where $f(\Omega)$ is the telescope beam. This fundamental equation directly relates the flux received from the object to one of its most important thermodynamic properties.

1.5.2 The 21-cm line of hydrogen

Astronomers have used spectral lines as an astronomical tool since the 19th century. It was then recognised that dark lines in the solar spectrum were a direct result of absorption of light by different atomic species in the Sun's atmosphere. This made it possible to probe the chemical makeup of the Sun and has since been one of the most powerful means of measuring chemical abundances throughout the Universe. One of the most important spectral line discoveries of the 20th century was that of the 21-cm spectral line of atomic hydrogen (Ewen & Purcell, 1951).

The 21-cm line arises from a hyperfine transition in the neutral hydrogen atom.

There are two possible spin states that the proton and electron can occupy. When the proton and the electron spin vectors are parallel the atom is in a slightly higher energy state than when they are aligned anti-parallel ($\Delta E \sim 5.9 \times 10^{-6} eV$). When the transition occurs a photon is emitted of wavelength $\sim$ 21 cm giving the line its characteristic name.

The chance of the transition occurring spontaneously is very small ($A_{10} = 2.85 \times 10^{-15} s^{-1}$ equivalent to a half-life of 11 million years). Collisions in a typical ISM occur on the timescale of hundreds of years. Since relatively few of these collisions will result in the emission or absorption of a photon, the relative populations of the hyperfine levels can be considered to be determined by collisions.

By combining aspects of quantum theory and theory of radio astronomy two useful equations can be derived. The first provides a means of measuring the H I column density of an astronomical object from measurements of its H I flux, defined in Eqn. 1.13:

$$\int_{v_1}^{v_2} N_H(v) \ dv = 1.835 \times 10^{18} \int_{v_1}^{v_2} T_b(v) \ dv. \tag{1.14}$$

This equation is vital for constructing column density maps, such as those presented in Chapter 4. The second equation allows an estimation of the H I mass of an object from its integrated H I emission:

$$M_{HI} = 2.36 \times 10^5 D^2 \int_{v_1}^{v_2} S \ dv \tag{1.15}$$

where D is the assumed distance to the object measured in Mpc. Knowledge of the spatial distribution of H I objects of different mass, can put tight constraints on cosmological models. The most common way of representing this distribution

is through the H I Mass Function.

1.5.3 The H I Mass Function

The H I mass function (HIMF) is the H I equivalent of the luminosity function, and is simply a measure of space density of galaxies of a given H I mass. The contribution of each mass bin to the Universal density of H I, ρ_{HI} is found from the product of the HIMF with each mass bin. The contribution of H I to the Universal energy budget, Ω_{HI}, can then be found by comparing ρ_{HI} to the critical energy density of the Universe. The HIMF provides a powerful tool for putting constraints on the amount of neutral gas in the Universe which can then be compared to predictions from numerical simulations.

It is usually modelled as a Schechter function (Schechter, 1976), as is the Luminosity Function:

$$\Phi\left(\frac{M_{HI}}{M^*_{HI}}\right) d\left(\frac{M_{HI}}{M^*_{HI}}\right) = \Phi^* \left(\frac{M_{HI}}{M^*_{HI}}\right)^{-\alpha} e^{\left(\frac{M_{HI}}{M^*_{HI}}\right)} \; d\left(\frac{M_{HI}}{M^*_{HI}}\right) \qquad (1.16)$$

where α represents the slope of the function at the low-mass end, M^*_{HI} defines the characteristic mass of the 'knee' of the function, and Φ^* is a normalising factor, representing the space density at M^*_{HI}. Currently accepted values from HIPASS are $\log M^*_{HI} = 9.8 \pm 0.03 M_\odot$ and $\Phi^* = 0.006 \pm 0.014 Mpc^{-3}$. The low-mass end of the HIMF has been of considerable interest in recent years following Schneider, Spitzak & Rosenberg (1998) who found tenuous evidence of an upturn below $M_{HI} = 10^8 M_\odot$. Of the methods of deriving the HIMF, the most common is generally known as the $1/V_{TOT}$ or $1/V_{max}$ approach (Schmidt, 1968). The technique assumes that the source distribution is uniform, thus the expected mean for the

ratio of the volume, V, over which an object was detected to the maximum volume, V_{max}, over which it could be detected is a half.

There are other, complementary methods of deriving the HIMF using maximum likelihood techniques. The maximum likelihood technique (Sandage, Tammann & Yahil, 1979) was the first of these to be developed and most subsequent techniques are based on this original method. One of the drawbacks of the technique is that it assumes some functional form for the true distribution. In this case a Schechter function is usually assumed. To avoid this assumption the Stepwise Maximum Likelihood technique was invented (SWML: Efstathiou, Ellis & Peterson, 1988). The different methods have their various benefits and limitations. as outlined below.

The $1/V_{TOT}$ method requires detailed knowledge of the survey sensitivity over the entire survey volume. This is needed to calculate the volume over which an object has been detected. In contrast SWML requires only the maximum distance to which an object might be detected at the position it was detected. This is a simpler approach if the survey sensitivity is a complicated function of position.

Since $1/V_{TOT}$ is based on the assumption of a uniform distribution, it can be affected by large-scale structure. SWML is designed to be insensitive to large-scale structure, but unfortunately this assumes that the HIMF is the same everywhere. A more recent method, developed for HIPASS, uses the 2-D SWML technique (Zwaan et al. 2003). This method draws on the best parts of the SWML method but assumes no knowledge of the functional form of the mass function. However, the 2-D SWML technique does not perform well when the completeness is low, tending to overestimate the populations in these bins. Hence the lowest S/N sources must be rejected from the sample.

One of the drawbacks for both of the SWML approaches is that the normalisation of the function has to be estimated from constraints that are placed on the data. If the survey in question has complex positional and distance dependencies, then these constraints are not easily adapted to the H I data. The $1/V_{TOT}$ method has the benefit that the normalisation is determined directly. In either case the overall shape of the function is not affected by the normalisation, so α should be independent of the method used.

Due to the statistical nature of the HIMF, it is vital to have as large a sample of galaxies as possible for putting tight constraints on the HIMF function parameters. The different methods employed for collecting such samples now comes under scrutiny.

1.5.4 Single Beam H I Surveys

Until recently, radio telescopes did not share the ability of optical telescopes to be able to image large areas of sky instantaneously. Instead radio receivers have been limited to individual detectors mounted at the focal point of the dish. This effectively means that radio telescopes produce pencil beams on the sky making them more suitable to pointed observations than large area surveys, which would consume large amounts of valuable telescope time.

Initially H I targets were selected from optical surveys, subjecting any analyses to optical selections effects. In order to search for a population of LSBs it is vital to avoid these effects. This required observations of random, large areas of the sky. The pencil-beam nature of radio observations made large H I surveys impractical, nevertheless several surveys were conducted between the end of the 1970s and 2000.

Minchin (2000) lists those H I surveys that have been important in the context of LSB surveys. These include: Shostak (1977), Henning (1995), the Arecibo H I Strip Survey (AHISS – Zwaan et al. 1997), the Arecibo Slice Survey (Schneider, Spitzak & Rosenberg, 1998) and the Arecibo Dual Beam Survey (Rosenberg & Schneider, 2000).

The final product of H I observing is a spectrum, and the bandwidth of this spectrum governs the distance out into the Universe the survey extends. Galaxies with a large H I mass produce larger H I signals. However, move the galaxy to a greater distance, D and the integrated flux will drop off as D^{-2}. Eventually there will be a point where the signal will be indistinguishable from the noise in the spectrum, and the galaxy will become undetectable. Naturally large H I galaxies will be observable over a much bigger volume than their smaller cousins. In order to compare the sensitivity of different surveys it is often useful to define a standard galaxy and calculate the volume in which it would be detected. The standard galaxy used in Minchin (2000) is one with M=M^*_{HI} with a velocity width of $\Delta V = 200$ km s^{-1}.

The early surveys suffered not only from low sensitivity but also from small survey area and the survey sensitivity was often a complicated function of spatial dependencies. For instance, Shostak (1977) combines H I emission data from different surveys with H I absorption studies. If one calculates the expected H I column density limits for each of the datasets, they clearly lie above the column densities regularly observed in LSB galaxies. It is not surprising then that he did not find a missing population of LSBs. Subsequent surveys such as Henning (1995) and AHISS, addressed the issues of low sensitivity and survey area. The sensitivity of these surveys, however, is complicated and uncertain (Spitzak, Schneider & Rosenberg, 1998) affecting the calculated survey volumes.

The Arecibo Slice Survey was the first blind H I survey that had high, uniform sensitivity over a relatively large survey area. One of the major results of this survey was a previously undetected upturn in the HIMF at the lowest masses. This suggested that the space density of H I might not be dominated by $M_{HI} > M^*_{HI}$ galaxies after all.

The ADBS (Rosenberg & Schneider, 2000) provided the largest area (430 sq. deg.) H I survey before the introduction of multibeam surveys. Technically this survey should be considered a multibeam survey since they used two line feeds simultaneously. The increase in survey area greatly increased the chances of detecting low-mass objects. Sure enough they detected 7 galaxies with a $M_{HI} < 10^8 M_\odot$. The optical data of these objects revealed they were previously uncatalogued LSBs, adding to the evidence from the Arecibo Slice that there was a population of low-mass LSB objects that was being missed by optical surveys, but being detected by H I surveys.

The surveys mentioned above produced a total of 17 potential dark galaxies. After follow-up observations were conducted, this number shrank to zero. From AHISS, it was concluded that there were no galaxies with a column density lower than $N_{HI} = 10^{19.7} cm^{-2}$. This limit was well above the column density limit for the survey ($N_{HI} = 10^{19} cm^{-2}$) suggesting there was a fundamental limit on the minimum column density of H I for galaxies. This column density limit is well below the lower limit predicted by Schaye (2004) for a star formation threshold. But it also illustrates how difficult it is for galaxies to remain dark.

The largest single restraint on these early surveys was the volume of space they probed. It was simply too expensive in terms of telescope time to cover large areas of sky at the sensitivity limits required. Clearly a new approach was needed and

this led to the development of multibeam systems for radio telescopes.

1.5.5 Multibeam H I Surveys

Placing more feed horns in the focal plane of the telescope increases the instantaneous field of view of the telescope. A greater field of view means that the telescope can survey the same amount of sky as a single beam dish but in a fraction of the time. With the advent of multibeam focal arrays for large telescopes, large area H I surveys have now become a viable option.

The first such multibeam was designed for the Parkes 64 m dish and the resulting survey was the H I Parkes All Sky Survey (HIPASS, Barnes et al. 2001). As the name suggests HIPASS covered the entire southern sky to a declination of +2°. The 64 MHz bandpass available at the telescope enabled a velocity coverage of $-1000 \leq cz \leq 12700$ km s^{-1}. The mass and column density sensitivity (M_{HI} limit $= 8.5 \times 10^5 M_\odot d^2_{Mpc}$, n_{HI} limit$= 7.8 \times 10^18$ cm^{-2}, $\Delta v = 200$ km s^{-1}) is comparable to the previous surveys mentioned above, but the massive increase in survey area increases the survey volume to 1.17×10^6 Mpc^3, for an M^*_{HI} galaxy – 200 times greater than the ADBS. This makes it possible to discover large numbers of low mass objects, helping to constrain the low-mass end of the HIMF.

Early results from HIPASS (Kilborn, Webster & Staveley-Smith, 1999) found 263 H I galaxies, three of which had a H I mass below $10^8 M_\odot$. Their HIMF didn't show the same dramatic upturn at the low-mass end as found by Schneider & Rosenberg (2000). Instead they measured $\alpha = -1.32$ and $M^* = 10^{9.5} M_\odot$, which is only slightly steeper at the low mass end than the HIMF of Zwaan et al. (1997). Their derived value for the local mass density of neutral gas ($\Omega_g = 1.88 \times 10^{-4} h_{75}^{-1}$) was slightly

lower than that of Zwaan et al. (1997) and similar to that predicted from optically selected surveys. However a conservative flux limit was used in this early paper since knowledge of the sensitivity of the survey was limited at the time.

Once HIPASS had been complete, a catalogue was collated of 1000 galaxies with the brightest H I peak flux densities (Bright Galaxy Catalogue; BGC, Koribalski et al. 2004). The catalogue provided for the first time, a view of the large scale structure in the local universe that was unhindered by extinction from our own Galaxy, and exposed several new features.

Zwaan et al. (2003) measured the HIMF for the BGC and found no upturn in the HIMF at low masses. The specific measured values were $\alpha = -1.30 \pm 0.08$ and $log\mathrm{M}^{*}_{HI} = 9.79 \pm 0.06$. Since the sample is so large, they were also able to explore how the HIMF changes with morphological type and surface brightness. There is a general trend of the low-mass slope steepening with later type galaxies. They compare this result to the optical luminosity function (Marzke et al. 1998) and find a similar trend, so the low-mass end of the HIMF and the low-luminosity end of the luminosity function are both dominated by late type galaxies. It should be noted though, that the small number of H I detected E/S0 galaxies (43) makes a mass function for these galaxies of marginal significance and the Schechter function provides a poor fit to the data. In the context of surface brightness related variations of the HIMF, they find that LSBs also dominate the low-mass end of the HIMF. Their contribution to the overall H I mass density is nevertheless small, no more than 15 % based on the Schechter fits.

The full HIPASS catalogue (HICAT, Meyer et al. 2004) consists of 4315 H I selected galaxies. Zwaan et al. (2005) constructed the HIMF from the final list which contains 4010 objects after rejecting those objects for which the calculated

completeness is low. This leaves 44 objects in the mass range 10^7–$10^8 M_\odot$. The overall HIMF is identical within the errors to that of Zwaan et al. (2003) with values of $\alpha = -1.37 \pm 0.03$ and $log M^*_{HI} = 9.80 \pm 0.03$.

An interesting discovery is that they detect an environmental dependence of the slope of the HIMF. This effect was originally measured by Rosenberg & Schneider (2002). The difference in α was fairly dramatic when they compared the HIMF of the Virgo Cluster ($\alpha = -1.2$) to that of the field ($\alpha = -1.5$). Zwaan et al. (2005), using a more statistically complete sample, found the *opposite* trend; α steepens from ~ -1.2 to ~ -1.5 as galaxy density increases. They defined the local galaxy density using a 'number of nearest neighbours' technique and by varying this number were able to investigate the change of α with distance. Interestingly they reveal that the largest dependence of α on environment happens on the largest scales; it is not limited to galaxy-galaxy interactions.

HIPASS data has also been used to explore and catalogue High Velocity Clouds and extended H I structures in the Local Group (Putman et al. 2002, 2003), to study the kinematics of the Milky Way-Magellanic system (Putman et al. 1998), to analyse diffuse Galactic H II regions through radio recombination lines of hydrogen (Auld, 2003), and to measure the H I properties of cluster galaxies (Waugh et al. 2002; Davies et al. 2004).

In addition to HIPASS, a second, deeper survey was commissioned to study the ZOA – HIZOA. The results of HIZOA (Henning et al. 2000) have helped build a more complete view of large scale structure behind the Milky Way, and have proved vital in studying the Local Velocity Field. A study of the data from the Great Attractor region ($300° < l < 332°$) helped substantiate the massive cluster A3627 as the core of the Great Attractor (Juraszek et al. 2000). This data also

supported the view that the Great Attractor is actually a wall like structure of which A3627 forms a part. Recently Donley et al. (2006) have reported the discovery of a Malin 1 sized H I galaxy in the ZOA which is only the fourth such object found to date.

Another survey using the multibeam instrument at Parkes that benefited from going deeper is HIDEEP (Minchin et al. 2003), which was dedicated to a study of the Centaurus region. The population of H I objects they discovered did not differ significantly from those found in the shallower surveys, suggesting that the shallower surveys mentioned above are not missing a significant fraction of low column density objects.

The sister survey to HIPASS is the H I Jodrell All Sky Survey (HIJASS, Lang et al. 2003) using a separate multibeam system on the 76 m Lovell telescope at Jodrell Bank, UK. This survey was designed to have very similar sensitivity and resolution and, combined with the HIPASS, would have provided an almost uniform dataset covering the entire sky. Although 220 objects were discovered in the first 1115 sq. deg., the survey was plagued by local sources of RFI which rendered the velocity region 4500–7500 km s^{-1}unusable. Due to this restriction the survey was cut short. It is hoped that this survey will be completed in the near future either using the Lovell or even the Bonn 100m dish which is about to receive its own multibeam instrument.

An extension to the HIJASS data was performed on the Virgo Cluster (VIRGOH I, Davies et al. 2004). This survey was deeper than HIJASS by a factor of three and revealed four objects with no apparent optical counterparts in the Digital Sky Survey (Djorgovski et al. 1992). One object was rejected as RFI upon follow up observations with the Arecibo 305m dish and from analysis of HIPASS data. Deep

optical follow up using the Isaac Newton Telescope revealed that two of the remaining objects have LSB counterparts, but the final object, VIRGOH121 remained dark down to a limiting surface brightness of $\mu_R \sim 27.5$. Could VIRGOH121 be representative of a population of dark, massive objects? If so how large is this population and why have these objects not turned up in previous H I surveys?

Minchin et al. (2005) explain that there are three criteria that a H I survey should meet if objects such as this are to be detected:

- they should be blind, i.e. not targeted at previously identified optical galaxies
- they should be capable of detecting a galaxy with a 200 km s^{-1}velocity width down to a limiting column density of $5 \times 10^{19} cm^{-2}$
- they should be accompanied by a program of optical observations down to deep isophotal limits to identify all possible optical counterparts

The final point should be expanded to include optical spectral measurements of all presumed optical counterparts to avoid misidentification of spatially aligned objects that may be at different redshifts.

Of the above criteria AHISS, HIDEEP and VIRGOHI fulfil all three criteria. The fact that AHISS and HIDEEP did not detect objects similar to VIRGOHI21 immediately suggests that such a population cannot be large. Combining the volume probed by all three surveys, Minchin et al. calculate that the contribution to the Universal mass density of these objects is no more than 1%.

Future surveys (e.g The Arecibo Galaxy Environment Survey: AGES and the ALFA Legacy Fast All-sky survey: ALFALFA; both described in chapter 3) will also have to meet these criteria if the true extent of the dark population is to be

discovered. However the claim that VIRGOHI21 is a dark galaxy has been met with mixed opinion. Doyle et al. (2005) argue against a dark galaxy population based on observational evidence. Taylor & Webster (2006) argue against a dark galaxy population from a theoretical viewpoint. Both papers are considered in more detail in the next section.

A further argument against VIRGOHI21 being a dark galaxy is that it has been incorrectly classed. Indeed VIRGOHI21 does seem to form part of a tidal stream of gas linked to the nearby one-armed spiral galaxy NGC 4254. This stream resembles other H I streams that have been detected in the Virgo Cluster such as that of Osterloo & van Gorkom (2005) which have been linked to mechanisms such as ram-pressure stripping or tidal interactions.

One-armed spiral galaxies are indeed thought to be the result of close encounters with other galaxies (Karachentsev, 2006). Many in the astronomical community have argued that this evidence is sufficient to disregard VIRGOHI21 as simply the result of a recent interaction. If so where is the interacting body? Vollmer, Huchtmeier & van Driel (2005) have conducted numerical simulations of galaxy-galaxy interactions and the morphology of NGC 4254 requires an interacting body of mass $\sim 10^{11} M_{\odot}$. There are no other objects within the region that could have played a part in the interaction apart from VIRGOHI21 itself, which happens to be the correct mass for such an interaction (Minchin et al. 2007).

Bekki, Koribalski & Kilborn (2005) have also argued against the dark galaxy nature of VIRGOHI21 from a theoretical point of view. They simulated galaxy-galaxy interactions and studied the kinematics and location of the gas following the interactions. The simulations are very successful at reproducing either the observed structure and kinematics of VIRGOHI21 and provide evidence against it being a

dark galaxy. But again, their results are dependent on having a second body to interact with NGC 4254 and there isn't one within the region.

However recent observations using the Arecibo 305m dish have revealed a northern extension to VIRGOHI21 (Giovanelli et al. 2007) and it is not yet possible to reproduce this structure numerically (Hibbard, private communication), but this feature is typical of close galaxy encounters which often produce leading and trailing streams. This seems to imply that VIRGOHI21 is indeed the interacting body in question.

The attention now turns to the history of dark galaxies to find out where this unusual class originated and whether or not they are viable in the concordance model as it is understood today.

1.6 Dark Galaxies

Dark Galaxies were first postulated in the context of gravitational lens studies, whereby the lensing object could not be identified in optical data (e.g. Weedman et al. 1982; Djorgovski & Spinrad, 1984; Hawkins et al. 1997). Despite their intriguing impact on these studies no-one had proposed how these galaxies could exist. The possible origin of Dark Galaxies was only first discussed in 1997 (Jimenez et al., 1997). In their analysis, the stability of the gas to gravitational collapse was discussed in the context of the Toomre-Q criterion (Toomre, 1964; Quirk, 1972). In this view, dark galaxies can be considered the ultimate LSBs – the gas column density has remained so low in the system that it has been unable to form stars at all. They predict that a population of dark galaxies could exist and that deep H I surveys of voids should detect this population. Verde, Oh & Jimenez (2002)

expanded the analysis of Jimenez et al. (1997) for a ΛCDM scenario. They also conclude that it is possible for a dark galaxy population to exist until the present epoch as galaxies with low gas surface density.

Ionisation of the neutral gas in a galaxy will be a significant factor in determining whether or not a dark galaxy will be detectable in a modern H I survey. Any photons with a wavelength shorter than 913 Å has the ability to ionise hydrogen. The source of these photons in a normal galaxy would come from internal sources (H II regions, supernovae, stellar winds, etc.) as well as from the hot intergalactic medium (IGM). In a dark galaxy, without stars, the only source of ionising radiation would be from the IGM, and so the question of whether or not a galaxy could remain dark depends on how good H I is at self-shielding.

Various pieces of evidence (e.g. Maloney, 1993) have shown that ionisation of hydrogen occurs within column densities of only a few $\times 10^{19}$ cm^{-2}. This ties in well with the observed truncation of galactic H I disks (van Gorkom, 1993). This leaves little room for dark galaxies to exist at all. If the gas column density is too low then the H I simply evaporates into the IGM. Conversely if it is too high, the gas collapses and forms stars. This fact is used by Taylor & Webster (2005) to conclude that all galaxies with H I will go on to form stars, which in effect rules out the possibility of a population of dark galaxies.

This is a view shared by Doyle et al. (2005) who completed a survey of the optical counterparts to all 4315 HIPASS objects and did not find a single *isolated* dark galaxy. Their search consisted of analysing optical surveys within the area defined by the main beam area of HIPASS. The mean final gridded beam in HIPASS is $\sim 15.5'$. This is a very large area compared to the resolution of optical surveys which is of the order of arcseconds. With such a large search field, it is not

surprising that coincidental objects turn up. For positive identification of optical counterparts it is necessary to match the H I object with the optical spectra.

Unfortunately optical spectra were only available for $\sim$ 1800 of the 4315 HIPASS objects which leaves a possible $\sim$ 2500 misidentifications. Doyle et al. adopt a grading system for these remaining objects to narrow down the dark galaxy candidates further. Quoting Table 3 of Doyle et al. (2005), 848 are spatially coincident – 'good guesses', and 216 have no optical counterpart within a 7.5′radius – 'blank fields'. Assuming that the good guesses are correct, that still leaves 216 possible candidates. Of these they reject those with over a magnitude of extinction in B, since faint galaxies will be obscured. This leaves only 13 objects. Of these 11 are found to be in dense stellar fields, making optical identification difficult. Of the two remaining objects, one was detected by Banks et al. (1999) as having a LSB counterpart and the final object was rejected as RFI.

Given the possibility of misidentification associated with such a large beam as that of HIPASS they are rather confident in their conclusions. Much of the optical data has been taken from the digitally scanned Schmidt survey plates available via SuperCOSMOS. None of the survey plates reach the optical surface brightness limit achieved by Minchin et al. (2005) so the rejection of the 214 objects with high extinction or that are located in regions of stellar over-crowding is not placing tight enough limits on these objects and could therefore result in the rejection of potential dark galaxies. This underlines the importance of deep optical follow up for H I surveys.

The expected amount of dark galaxies for HIPASS and all the other major H I blind surveys mentioned previously is calculated in Davies et al. (2006). They used a semi-analytical approach to simulate a population of stable disk galaxies within

dark matter haloes (Mo, Mao & White, 1998). A star formation threshold is then used to separate those galaxies that will form stars from those that will remain dark. In the prescription here, the star formation threshold used is the constant H I surface density threshold derived from Schaye (2004). This criterion has the advantage that it is simple to calculate and track.

The amount of dark galaxies produced varies according to the amount of angular momentum that is transferred from the dark matter halo into the disk. This value itself is dependent on the disk mass fraction, m_d and is difficult to estimate. One method would be to use the Universal baryonic mass density fraction: $\frac{\Omega_{baryon}}{\Omega_M} = 0.15$ (Spergel et al. 2003). This however assumes that the system is 100% efficient at transferring all the baryons into the disk. Observations of the Intra Cluster Medium in X-rays have revealed that a vast amount of baryonic matter resides in this region so this is an unlikely upper limit. Fukugita, Hogan & Peebles (1998) calculate that only 0.09% of the Universal energy density is in the form of stars in discs. It can be shown that this value leads to a disk mass fraction of 0.004. Most of the baryons, they predict, remain in a hot halo around the individual galaxies and their groups. Silk (2004) is of the opinion that only half of the baryons predicted have been detected, and of these 30 % form cold intergalactic gas. Assuming the rest goes into galactic disks leads to an absolute upper limit for the disk mass fraction of 0.05.

Taylor & Webster (2005) adopt $m_d = 0.05$ and 0.1. This seemingly insignificant difference actually produces a marked change in the production of dark galaxies. Fig. 1 of Davies et al. (2006) shows the column density distribution of the whole population of simulated galaxies, for three different values of m_d. It is clear that using higher values of m_d produces relatively smaller numbers of dark galaxies. The highest value used by Davies et al. is $m_d = 0.05$ and already this has reduced

the dark galaxy population to a tiny fraction. It is not surprising then that Taylor & Webster do not predict any dark galaxies – in their simulations all galaxies would form with gas column densities above the critical threshold for star formation.

One of the most important results to come out of Davies et al. (2006) is that the population of simulated dark galaxies is dominated by small mass ($< 10^7$ $M_\odot$), low velocity width (< 40 km s^{-1}) galaxies. This provides a natural explanation for the lack of observed dark galaxies since the H I surveys to date are either incapable of detecting small H I objects over large volumes or the velocity resolution is too coarse to pick up low velocity width objects.

Ionisation is another threat to the dark galaxy population but this turns out to be relatively benign. Only 2% of the dark galaxy population is judged to be destroyed by the extragalactic radiation field. Davies et al. go on to predict the number of galaxies that would be expected to turn up in past and future H I surveys. HIPASS is predicted to have 80 dark galaxies lurking in its data, yet there are no isolated dark galaxies in HIPASS (Doyle et al. 2006). But given that their ability to positively identify optical counterparts is limited by the lack of optical spectra and a large telescope beam, it would not be surprising to find that misidentifications have been made in the $\sim$ 850 objects that make up the 'good guesses'. The $\sim$ 200 objects 'blank field' population also requires much deeper optical observations to be able to eliminate them from the possible dark galaxy population. One option could be to use near infrared (NIR) observations which are not as affected by dust extinction like the optical bands. So it would not be too unrealistic to expect that this dark galaxy population is present in the HIPASS catalogue but is simply misidentified. Another point of contention is that Doyle et al. have imposed the restriction that the dark galaxies be isolated. This suggests that dark galaxies cluster differently to visible galaxies. Is this really expected? It is certainly true

that galaxies in dense environments like clusters and groups will suffer interactions with other galaxies and the cluster potential that make them more likely to become star-forming. However there is probably scope for dark galaxies to exist in the outskirts of groups and clusters where the effects of the cluster potential are small and/or galaxy-galaxy interactions are infrequent.

This thesis presents results of a search for dark galaxies from one of the next generation of H I surveys currently underway using the Arecibo 305 m radio telescope. Chapter 2 is an in-depth investigation into the gas morphology and kinematics of a sample of nearby LSBs, with a view to ascertaining a star formation threshold. This result is then used to justify the need for high sensitivity H I blind surveys. Chapter 3 is a description of a high sensitivity H I survey, The Arecibo Galaxy Environment Survey. In Chapter 4 the results from the survey regions around NGC 628 and NGC 1156 are presented. The results from these two regions are then combined with a third region centred on the Abell 1367 and the optical and H I properties of the H I population are presented. A demonstration of the possible uses of this data are discussed in Chapter 5. Chapter 6 presents a summary of this work.

Chapter 2

The conditions for star formation in LSBs

Based on a paper written by R. R. Auld, W. J. G. de Blok, E. Bell & J. I. Davies monthly Notices of the Royal Astronomical Society vol. 366, p. 1475

2.1 Introduction

LSBs have very little star formation going on in them, despite having large reservoirs of gas from which to form their stars (Longmore et al. 1982). This begs the question of what is the difference between LSBs and HSBs that could account for this. This is an extremely important question in the context of dark galaxies, since dark galaxies are merely the most extreme version of LSBs – they have failed to produce any stars at all!

LSBs represent a class of galaxy that is only just capable of producing stars and

this property makes them extremely good laboratories for testing star formation theories. The abrupt truncation of the stellar disk in spiral galaxies, suggests that star formation is a threshold phenomenon. Several criteria for a star formation threshold were discussed in the previous chapter. In this chapter, two of the most popular - Toomre-Q and constant H I surface density are put to the test for a sample of nearby LSBs.

2.2 History of star formation thresholds in LSBs

The low star formation rates in LSBs have been attributed to their gas surface densities being below a critical threshold for star formation (Kennicutt, 1989; van der Hulst *et al*, 1993). This prevents them from sustaining star formation on a large scale. Kennicutt (1989) found that star formation in galactic disks may be governed by gravitational (dynamical) instabilities. In particular he found that a modified version of the Toomre-Q criterion (Toomre, 1964; Quirk, 1972) for instability in the disk could describe a threshold for the gas surface density, below which star formation is strongly suppressed.

A different view of a critical surface density of H I for star formation that is apparently independent of rotation was first suggested by Gallagher & Hunter (1984). Data from spiral and irregular galaxies available at the time provided empirical evidence that there was a sharp cutoff in Hα emission and hence in recent massive star formation at around 5×10^{20} cm^{-2}. Further studies (e.g. Skillman & Bothun, 1986; Skillman, 1987; Guiderdoni, 1987) all led to a similar conclusion although the measured critical values vary between (2.6–10) $\times$ 10^{20} cm^{-2}. Modelling of star formation scenarios such as that by Elmegreen & Parravano (1994) and Schaye

Figure 2.1: False colour image of ESO-LV 0280140 showing the extent of the H I gas. B and R bands have been combined to produce 'white' light. H I is represented in orange Hα is shown in purple.

Figure 2.2: False colour image of ESO-LV 1040220 showing the extent of the H I gas. B and R bands have been combined to produce 'white' light. H I is represented in orange Hα is shown in purple.

Figure 2.3: False colour image of ESO-LV 1040440 showing the extent of the H I gas. B and R bands have been combined to produce 'white' light. H I is represented in orange Hα is shown in purple.

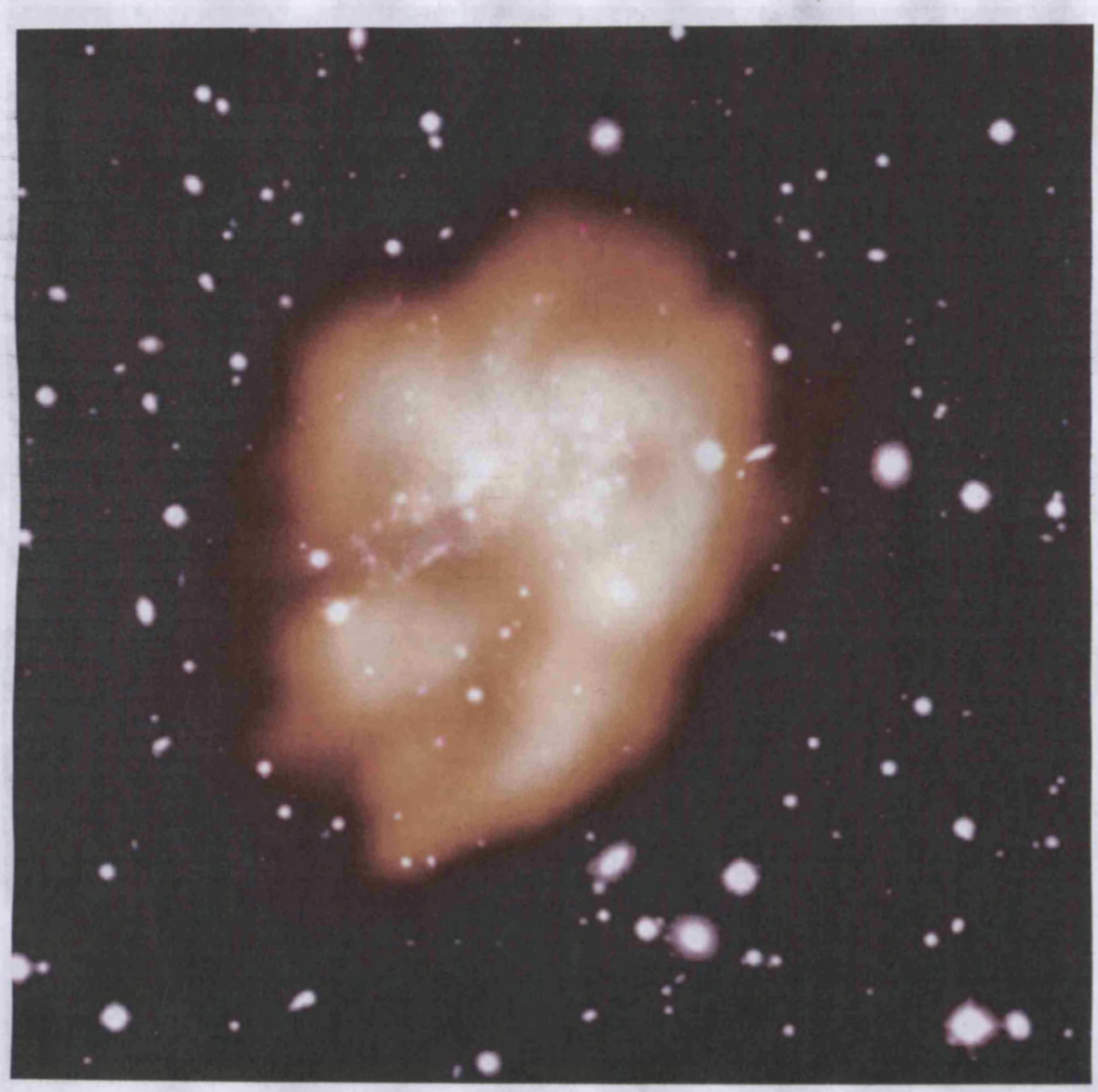

Figure 2.4: False colour image of ESO-LV 1450510 showing the extent of the H I gas. B and R bands have been combined to produce 'white' light. H I is represented in orange Hα is shown in purple.

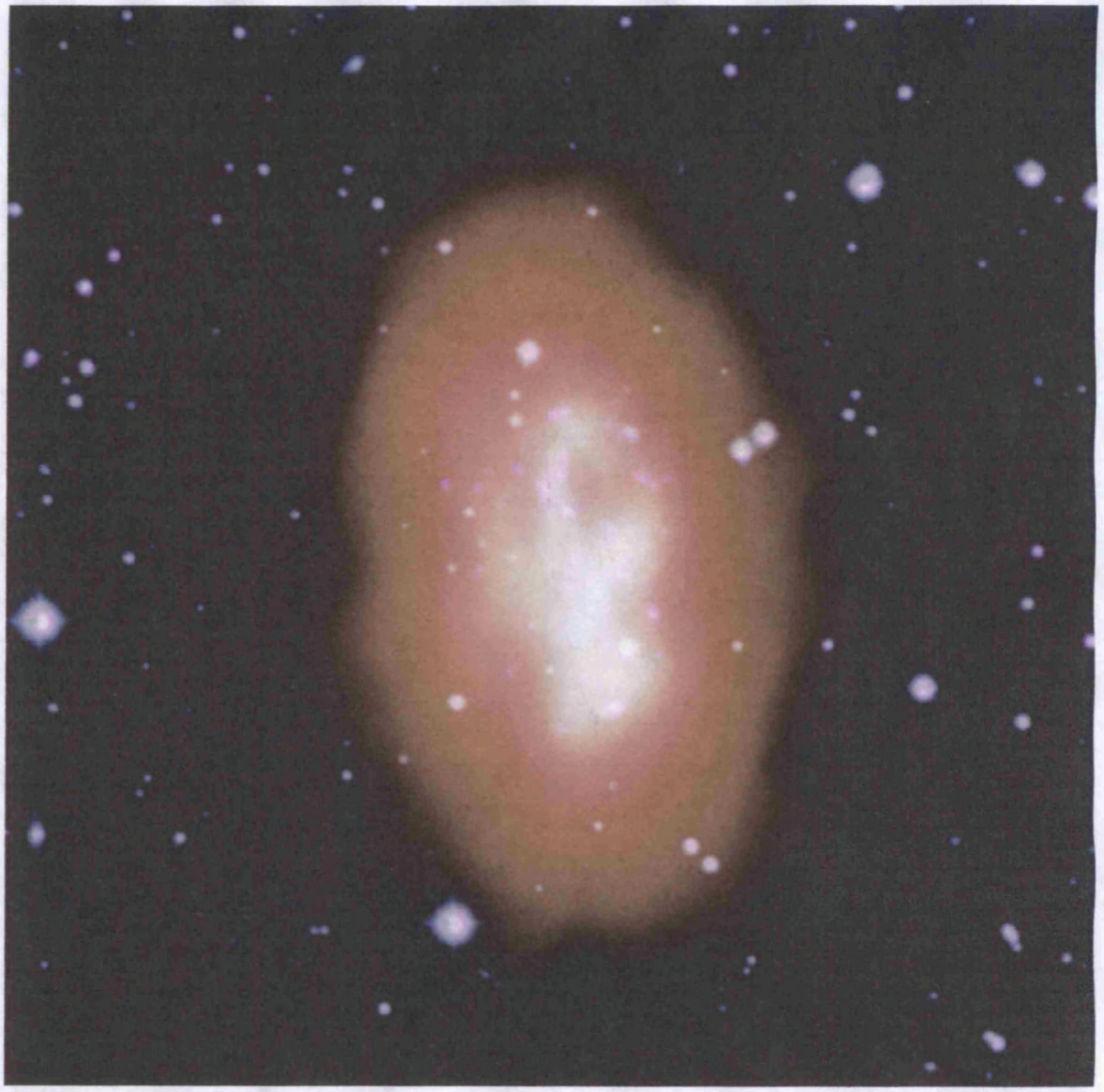

Figure 2.5: False colour image of ESO-LV 1870510 the extent of the H I gas. B and R bands have been combined to produce 'white' light. H I is represented in orange Hα is shown in purple.

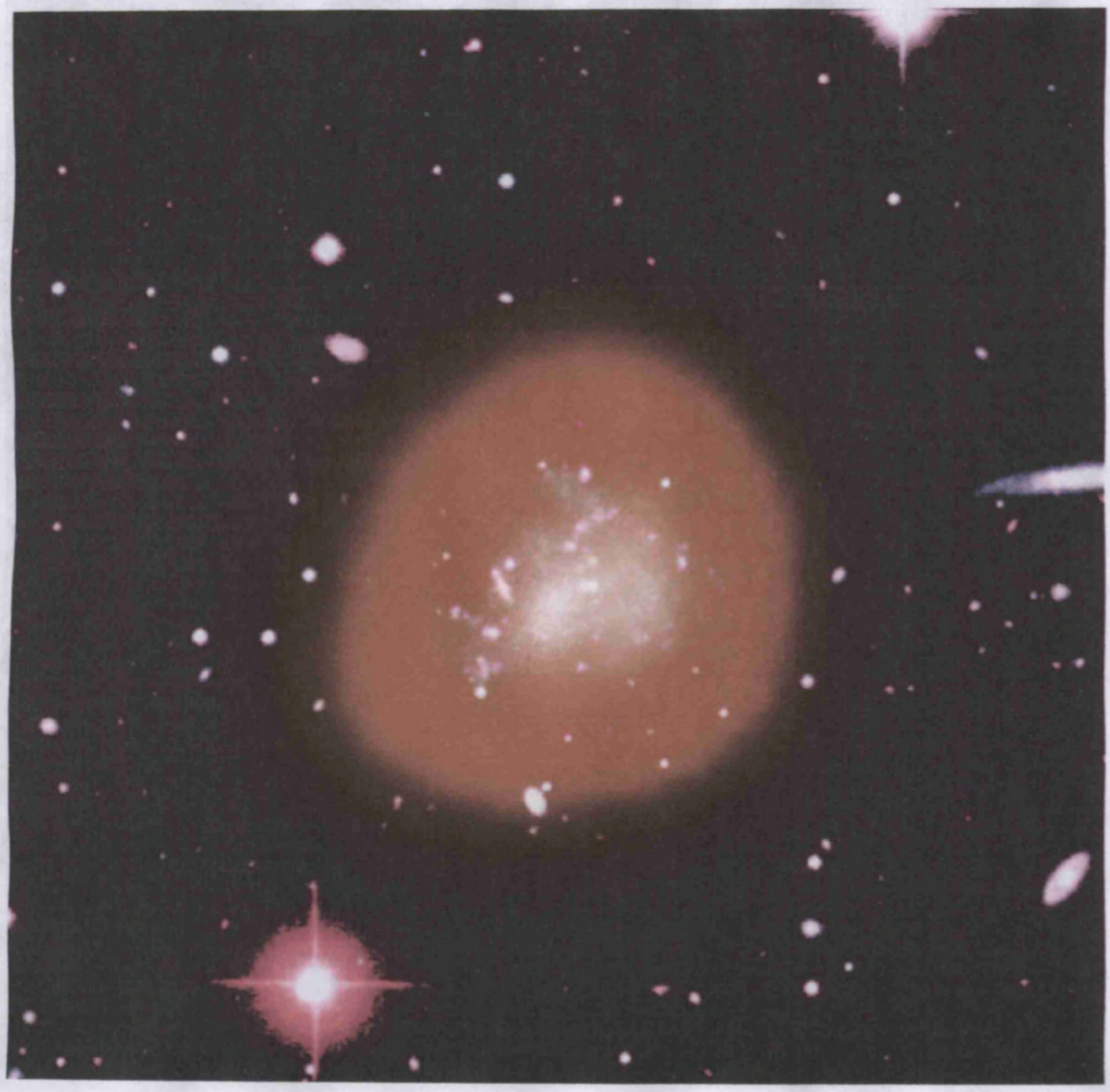

Figure 2.6: False colour image of ESO-LV 2490360 showing the extent of the H I gas. B and R bands have been combined to produce 'white' light. H I is represented in orange Hα is shown in purple.

(2004) have also supported the critical H I surface density. Elmegreen & Parravano postulated that stars form in regions where the interstellar medium (ISM) can sustain two stable phases, a warm ($\sim 10^4$ K) and a cold ($\sim 10^2$ K) phase, that are in pressure equilibrium. A constant critical gas surface density arises naturally from their models. In the case of Schaye (2004), modelling produced a critical H I surface density, $\Sigma_{HI} = 3\text{–}10 \times 10^{20}$ cm^{-2} (2.4–8 M$_\odot$pc^{-2}) below which star formation is unlikely to occur. Such a specific prediction should be relatively straightforward to test observationally.

Van der Hulst *et al.* (1993) concluded that their sample of LSBs had gas densities lower than the critical threshold as calculated by Kennicutt (1989) and it was this that was preventing them from producing widespread star formation. Hunter, Elmegreen & Baker (1998) studied the star formation properties of a sample of dwarfs and ellipticals. They found that shear in the neutral gas played a more critical rôle in stabilising the gas against gravitational collapse rather than rotation. It should be noted though that they used a different value for the velocity dispersion, 9 km s^{-1}, rather than 6 km s^{-1}as used by Kennicutt (1989). Had they adopted Kennicutt's value their results would have compared more favourably with Kennicutt's results. Later work on LSBs such as van Zee *et al.* (1997), O'Neil, Verheijen & McGaugh (2000) and Simpson & Gottesman (2000) all recognised two features of these systems: there seems to be an H I threshold column density below which star formation does not occur; also star formation is a local phenomenon not well described by global properties. Schaye (2004) compared previous observations to his galaxy models for both LSBs and HSBs based on the work of Elmegreen & Parravano (1994). He arrived at the conclusion that neither rotation nor shear could stabilise a region once the H I surface density was high enough to allow the ISM to form a cold phase.

Previous studies of star formation thresholds in LSBs have largely been based on studies of distant LSBs, with relatively poor resolution. As such, they are limited to the study of global effects. By taking higher resolution images of a sample of nearby LSBs it is also possible to examine localised effects on star formation. To test these ideas a sample of nearby LSB galaxies was required.

2.3 The galaxy sample

Bell *et al.* (2000) studied a diverse sample of 26 LSBs, originally drawn from the ESO-Uppsala Catalogue (Lauberts & Valentijn, 1989). Their aim was to model the colours, stellar metallicities and star formation histories of a wide range of LSBs. They concluded that LSBs exhibit a large range of morphologies and stellar populations. Early-type LSBs with higher K-band surface brightnesses tend to have older populations and higher metallicities. The late-types, however, exhibit lower K-band surface brightnesses and are typically dominated by younger stellar populations and lower metallicities.

They recognised two strong correlations. Stellar age is primarily correlated with gas surface density and metallicity is correlated with both gas surface density and the galaxy mass. Their interpretation was that such correlations would be observed if the star formation law depended entirely on the local gas surface density or on the local dynamical time-scale, and the mass of a galaxy determined the efficiency with which it retained its newly produced metals.

The sample comprises 6 of the nearest ($v \lesssim 2000$ kms^{-1}), late-type LSBs from the sample of Bell et al. (Figs. 2.1–2.6). The near-infrared colours of ESO-LV 1040220, ESO-LV 1040440, ESO-LV 1450250 and ESO-LV 1870510 are the bluest in the

sample of Bell *et al.* (2000). These galaxies are also among the bluest in the optical colours. The modelling presented in Bell *et al.* (2000) suggests these galaxies are unevolved with metallicities lower than 0.01 solar. Most very low metallicity galaxies in the literature are relatively high density compact dwarfs. The galaxies here offer an opportunity to study the properties of galaxies at both low gas surface density and low metallicity. The metallicity of some of these galaxies is so low that one starburst event may have been enough to produce the current metallicity values (de Blok *et al.* 1999). If that is the case, the blue colours suggest that the starburst happened recently and the galaxies are at an early stage in their evolution.

2.4 Observations and data reduction

2.4.1 *B*-band, *R*-band and Hα data

The optical data were obtained with the Cerro Tololo Interamerican Observatory (CTIO) 0.9 m. A 2048×2048 Tectronix CCD was used with a pixel size of 0.40 arcsec pixel^{-1}. Images in the *B*-band were compiled from 6 individual exposures of 600s. Images in the *R*-band used 6 individual exposures of 300s. For full details of the observing conditions and data calibration see Bell *et al.* (2000).

The Hα images were also taken at Cerro Tololo, using the 0.9 m telescope and an exposure time of 20 minutes. Unfortunately no calibration for these data is available, so the images have been used to highlight, qualitatively, the presence of HII regions as indicators of regions that have recently formed stars.

Cross-analysis of the multi-band images was used to distinguish galactic emission from foreground stellar contamination. Foreground star subtraction was performed

using the masking routine BLOT in the data reduction package GIPSY. Once star subtraction was completed, surface brightness profiles were constructed for each galaxy in each band. This was achieved using the ELLINT program within GIPSY and using ellipses of width 5″. The central pixel for each galaxy was estimated from the *R*-band images. The other ellipse parameters (inclination and position angle) were taken from Bell *et al.* (2000). As all the galaxies are situated more than 20° above the Galactic Plane, Galactic extinction was $A_B < 0.36$ and has been ignored.

2.4.2 *K*-band data

The near-infrared observations were taken with the GRIM I instrument on the 0.6 m South Pole Infrared EXplorer (SPIREX). GRIM I employed a NICMOS 1 128×128 array with a pixel scale of 4.2 arcsec pixel^{-1}. The K_{dark} filter (2.27–2.45 μm) was used in preference to the more common *K* filter. The advantage of using the K_{dark} filter is that it has been chosen to cover a portion of the *K*-band relatively free from the numerous OH lines that can be intense and highly variable between ~1.9 μm and 2.27 μm. The sky background is reduced by over 1 mag in comparison to a standard *K*-band filter.

By observing at the South Pole it was possible to take advantage of the extremely cold conditions to reduce thermal emission from the telescope and the sky. This resulted in a further reduction in the background of almost 2 mag when compared with a mid-latitude telescope. Full details of the observing run and data reduction can be found in Bell *et al.* (2000). Surface photometry was then performed on the data as for the optical data.

2.4.3 H I data

The high resolution H I data were obtained using the Australian Telescope Compact Array (ATCA) to complement the optical and infrared observations of Bell *et al.* (2000). H I observations were taken with the ATCA in 750-m and 1.5-km configurations during 1998 and 1999. Each galaxy was observed for 12 hours using a correlator configuration of 512 channels over 8 MHz bandwidth, giving a channel separation of 15.6 kHz. At the observing frequency this corresponds to a velocity width of 3.3 kms^{-1} per channel. A summary of the observational details is given in Table 2.1.

Initial data reduction to produce the datacubes was performed in MIRIAD using standard procedures. First, the data were checked for interference and Galactic emission and any bad data were omitted from further processing. The data were then flux and phase calibrated. Channels that were considered free of spectral line emission were used to define the continuum level and continuum was then subtracted. The data were Fourier-transformed using 'natural' weighting and a velocity channel width of 3.3 kms^{-1}. The data were then cleaned using the CLEAN algorithm and restored.

The zeroth moment map (integrated H I), the first moment (velocity field) map and the second moment, showing the velocity dispersion, were all produced from the datacubes using GIPSY. Each channel map in a cube was smoothed spatially to twice the original resolution and clipped at the 3σ noise level. By doing this it was possible to isolate the galaxies' H I signal from surrounding noise. This information was then used to produce a mask that was applied to the unsmoothed data. Any noise-like signals were then removed by eye from the masked, unsmoothed channel maps. The final maps produced contain only galaxy emission.

Table 2.1: Details of the H I observations taken with the ATCA

Galaxy	Date	ATCA configuration	Integration time (hrs)	Primary (flux) calibrator	Secondary (phase) calibrator
ESO-LV 0280140	02/06/1998	750E	13.00	PKSB 1934-638	PKSB 0252-712
	29/03/1999	150B	11.65	PKSB 1934-638	PKSB 0252-712
	12/04/1999	1.5C	4.44	PKSB 1934-638	PKSB 0252-712
	13/04/1999	1.5C	2.6	PKSB 0823-500	PKSB 0252-712
ESO-LV 1040220	31/05/1998	750E	11.95	PKSB 1934-638	PKSB 1934-638
	27/03/1999	150B	12.65	PKSB 1934-638	PKSB 1934-638
	13/04/1999	1.5C	8.10	PKSB 1934-638	PKSB 1934-638
ESO-LV 1040440	01/06/1998	750E	0.77	PKSB 1934-638	PKSB 1934-638
	27/06/1998	750E	1.03	PKSB 1934-638	PKSB 1934-638
	28/06/1998	750E	13.33	PKSB 1934-638	PKSB 1934-638
	26/03/1999	150B	10.02	PKSB 1934-638	PKSB 1934-638
	28/03/1999	150B	2.67	PKSB 1934-638	PKSB 1934-638
	28/04/1999	1.5C	12.5	PKSB 1934-638	PKSB 1934-638
ESO-LV 1450250	24/06/1998	750E	4.42	PKSB 1934-638	PKSB 1934-638
	26/06/1998	750E	2.23	PKSB 1934-638	PKSB 1934-638
	27/06/1998	750E	2.40	PKSB 1934-638	PKSB 1934-638
	27/03/1999	150B	1.88	PKSB 1934-638	PKSB 0008-421
	28/03/1999	150B	8.58	PKSB 1934-638	PKSB 1934-638
	11/04/1999	1.5C	12.55	PKSB 1934-638	PKSB 1934-638
ESO-LV 1870510	25/06/1998	750E	2.32	PKSB 1934-638	PKSB 0008-421
	27/06/1998	750E	11.08	PKSB 1934-638	PKSB 1934-638
	29/03/1999	150B	12.16	PKSB 1934-638	PKSB 1934-638
	12/04/1999	1.5C	12.05	PKSB 1934-638	PKSB 1934-638
ESO-LV 2490360	06/06/1998	750E	11.92	PKSB 1934-638	PKSB 0407-658
	29/03/1999	150B	4.58	PKSB 1934-638	PKSB 0407-658
	30/03/1999	150B	6.67	PKSB 1934-638	PKSB 0407-658
	12/04/1999	1.5C	5.90	PKSB 1934-638	PKSB 0407-658

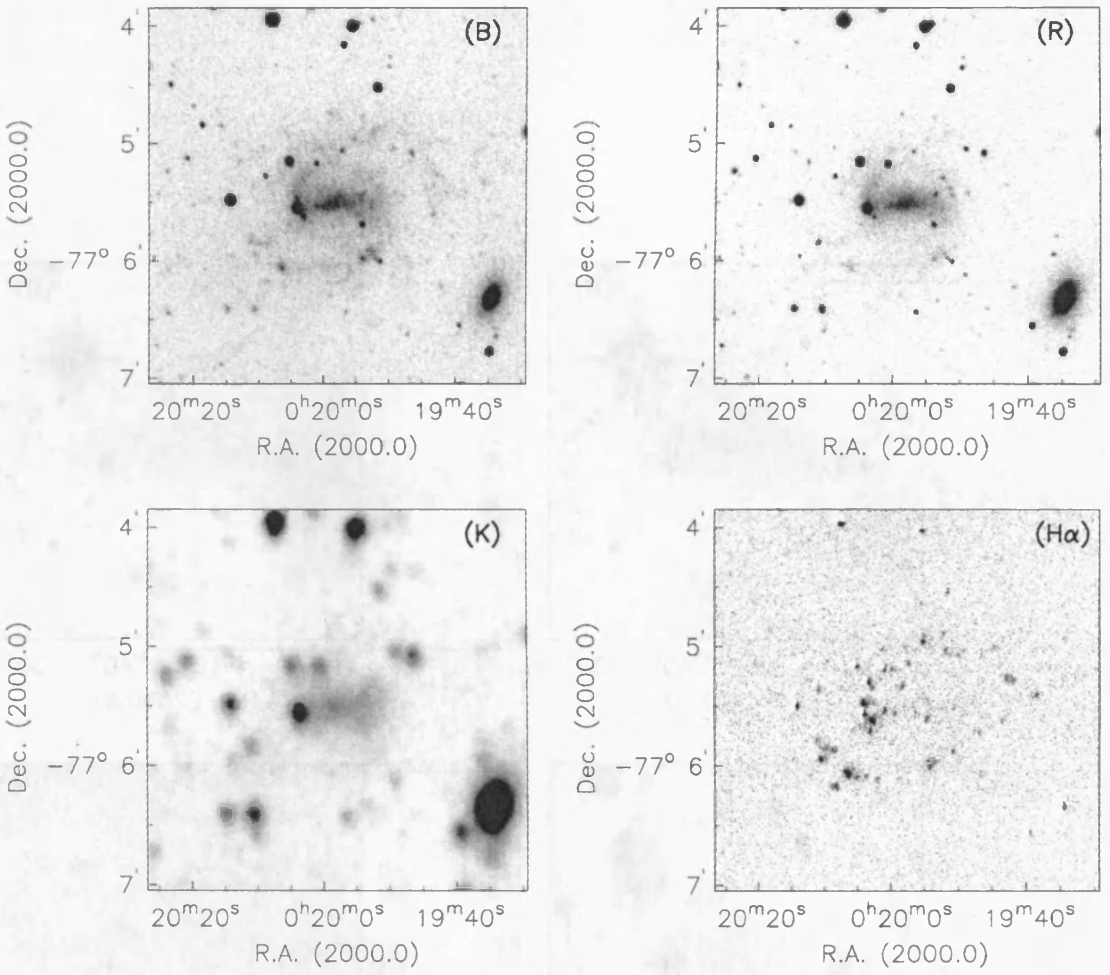

Figure 2.7: *B*,*R* and Hα images of ESO-LV 0280140 taken with the Cerro Tololo Interamerican Observatory 0.9 m telescope. *K*-band images were taken with the 0.6 m SPIREX telescope situated at the South Pole. All the images are centred on the same sky position and share the same physical scale.

2.5 Galaxy properties

2.5.1 Optical properties

Figs. 2.7–2.12 show the *B*, *R*, *K*, & Hα images before foreground star subtraction. All the images are centred on the galaxy centre as estimated in the R-band.

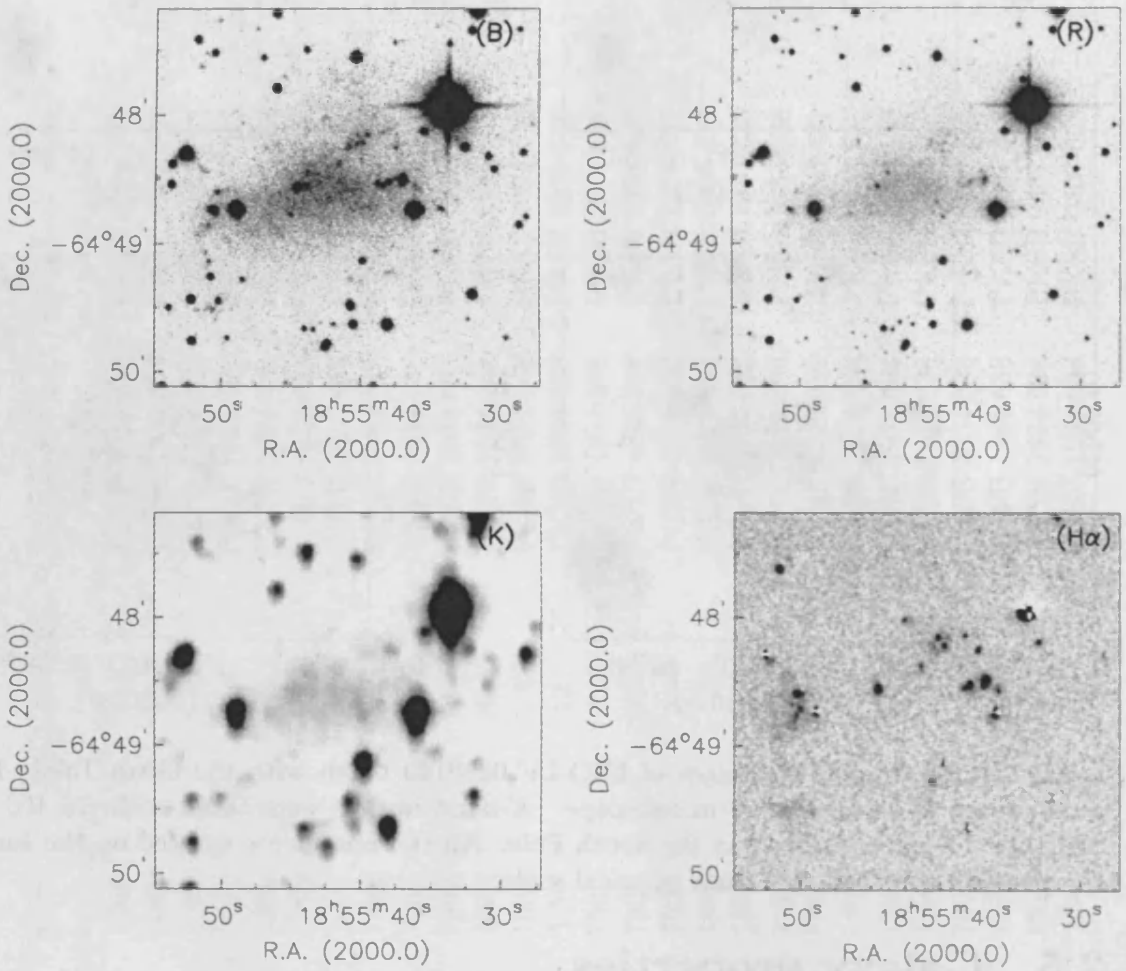

Figure 2.8: B,R and Hα images of ESO-LV 1040220 taken with the Cerro Tololo Interamerican Observatory 0.9 m telescope. K-band images were taken with the 0.6 m SPIREX telescope situated at the South Pole. All the images are centred on the same sky position and share the same physical scale.

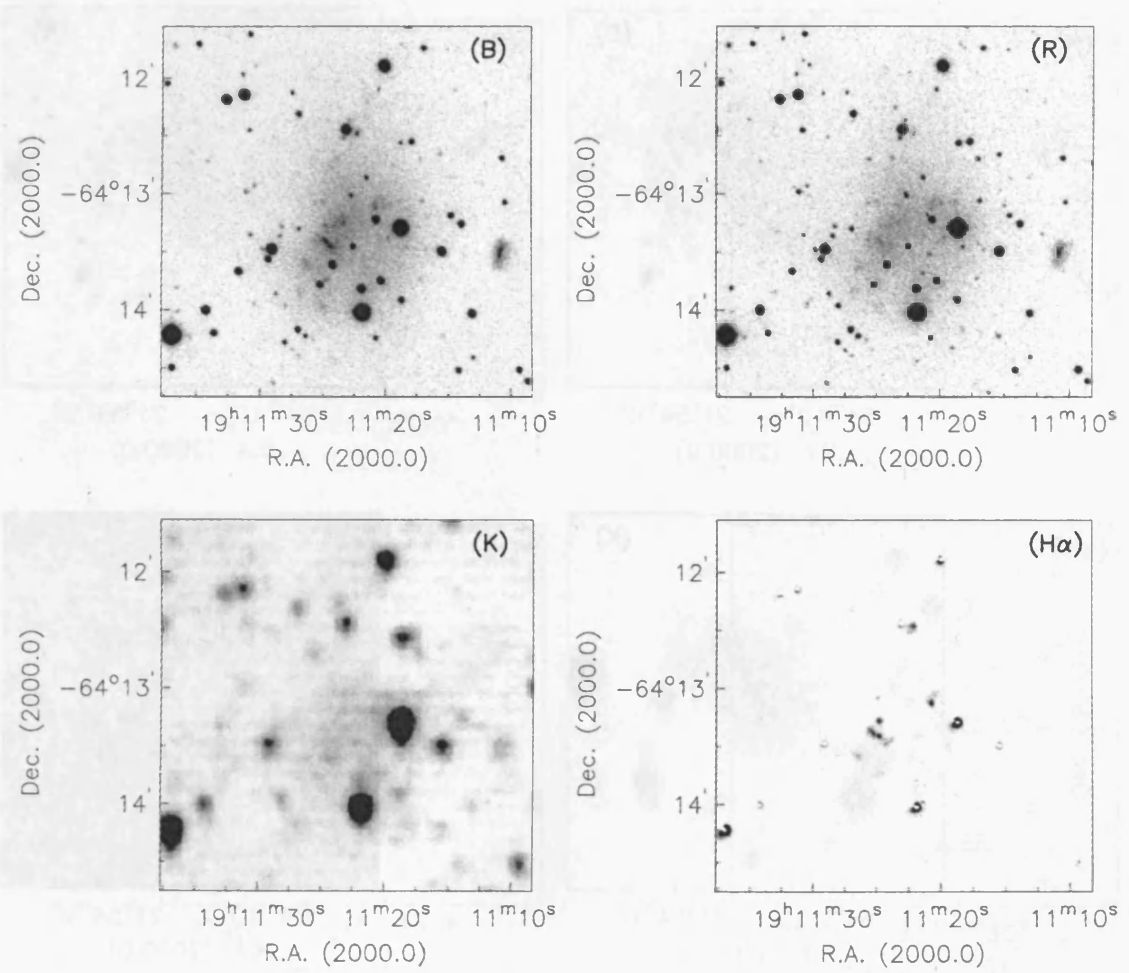

Figure 2.9: *B*,*R* and Hα images of ESO-LV 1040440 taken with the Cerro Tololo Interamerican Observatory 0.9 m telescope. *K*-band images were taken with the 0.6 m SPIREX telescope situated at the South Pole. All the images are centred on the same sky position and share the same physical scale.

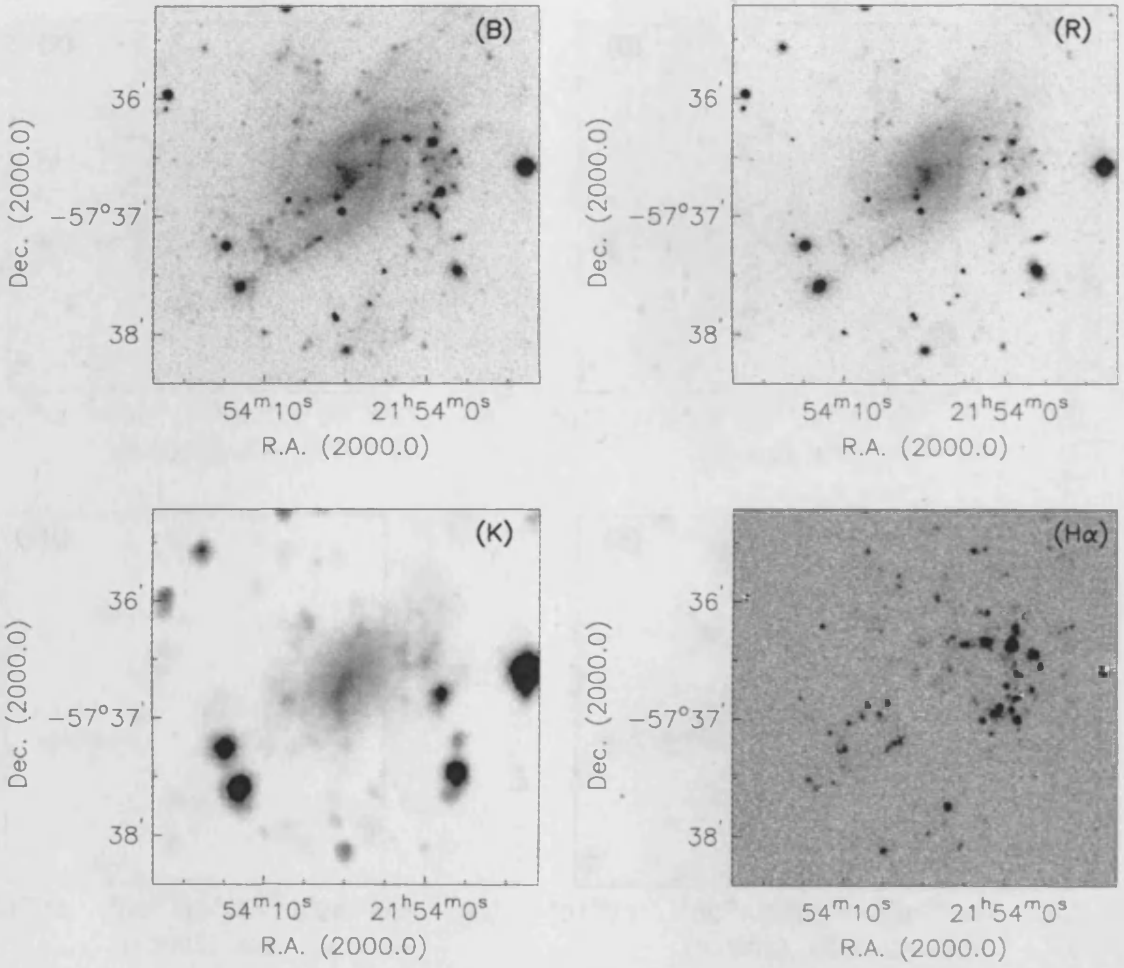

Figure 2.10: *B*,*R* and Hα images of ESO-LV 1450250 taken with the Cerro Tololo Interamerican Observatory 0.9 m telescope. *K*-band images were taken with the 0.6 m SPIREX telescope situated at the South Pole. All the images are centred on the same sky position and share the same physical scale.

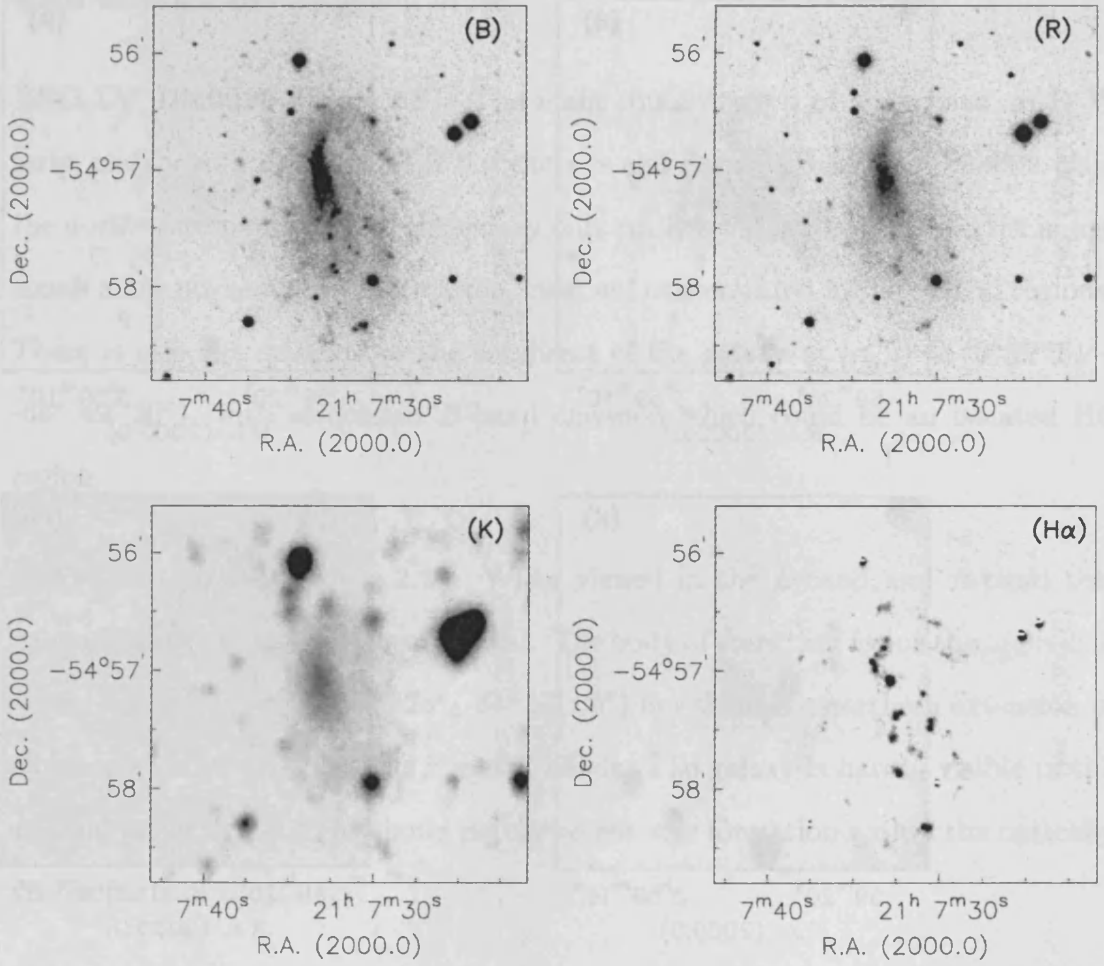

Figure 2.11: *B*,*R* and Hα images of ESO-LV 1870510 taken with the Cerro Tololo Interamerican Observatory 0.9 m telescope. *K*-band images were taken with the 0.6 m SPIREX telescope situated at the South Pole. All the images are centred on the same sky position and share the same physical scale.

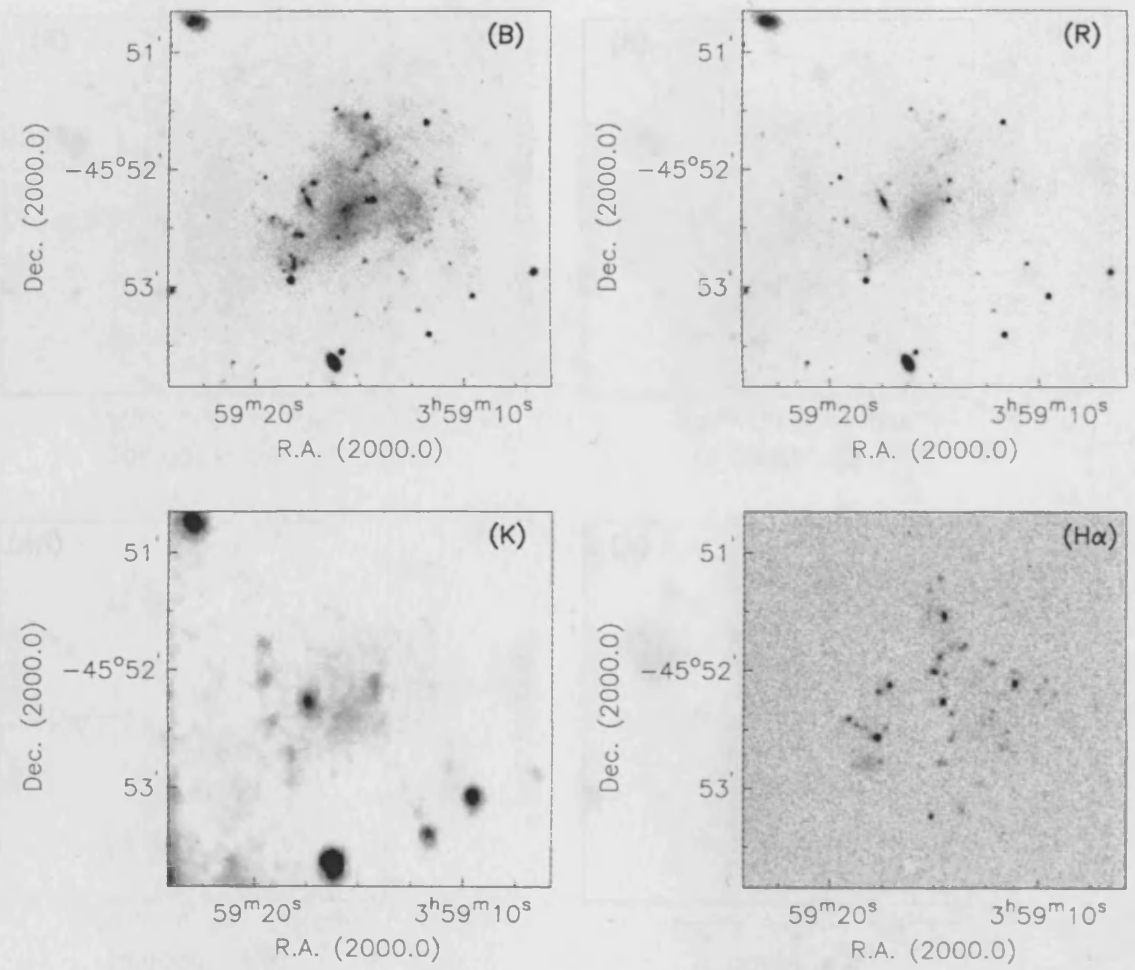

Figure 2.12: B,R and Hα images of ESO-LV 2490360 taken with the Cerro Tololo Interamerican Observatory 0.9 m telescope. K-band images were taken with the 0.6 m SPIREX telescope situated at the South Pole. All the images are centred on the same sky position and share the same physical scale.

ESO-LV 0280140 (Fig. 2.7): The B-band and R-band images clearly show a bar running E–W. There are two spiral arms, the northern arm emanating from the east side of the bar and the southern arm from the west side. In the K-band image the galaxy bar can be seen as a smudge in the centre of the image. The spiral arms are also traced out in Hα.

ESO-LV 1040220 (Fig. 2.8): The main concentration of stars form an E–W strip, clearly seen in B, R and K but there is also some LSB optical emission from the northwestern quadrant of the galaxy only really seen in B and R. The Hα image shows a few pockets of star formation, most are concentrated in the central regions. There is also Hα emission to the southeast of the galaxy at $(\alpha, \delta) = (8^h55^m51^s$– -64° 49′ 30″), with associated B-band emission which could be an isolated HII region.

ESO-LV 1040440 (Fig. 2.9): When viewed in the B-band and R-band this galaxy appears almost teardrop shaped. The body of stars that forms the main disk is centred on$(\alpha, \delta) = (19^h11^m23^s$, -64° 13′ 30″) but there is a northern extension of emission clearly visible in the B and R bands. The galaxy is hardly visible in the K-band image and the Hα shows patchy recent star formation within the optically visible parts of the galaxy.

ESO-LV 1450250 (Fig. 2.10): The spiral design is clearly visible in all wavelengths. The western spiral arm is particularly prominent in B and Hα. All the Hα emission appears to be associated with the spiral arms of the galaxy.

ESO-LV 1870510 (Fig. 2.11): This is also a spiral galaxy but the spiral arms are not as prominent as in the previous galaxy. The galaxy is particularly bright in the K-band. The bright centre of the galaxy seems to be the same position in B,

R and K at $(\alpha, \delta) = (21^h7^m33^s$,-54° 57′ 10″). The H$\alpha$ indicates that star formation is occurring uniformly throughout the visible extent of the galaxy.

ESO-LV 2490360 (Fig. 2.12): The optical images show an irregular galaxy with no clear structure. As with ESO-LV 1870510 pockets of Hα emission are evenly spread throughout the optical extent of the galaxy.

The derived surface brightness profiles are shown in Fig. 2.13. The error bars represent the uncertainty in the sky background due to the error in the sky background level, taken from many areas in the image clear of galaxy emission and contaminating objects. The error bars produced here are different to those of Bell *et al.* (2000) Fig. 1, where the standard deviation of the mean background level was used to calculate the error bars.

All the galaxies are well fit by exponential profiles without a central bulge (Bell *et al.* 2000), with central B-band surface brightnesses in the range $23.0 \lesssim \mu_{0B} \lesssim 24.0$. The profiles and morphologies of these galaxies are all typical of the LSBs observed in other surveys (e.g. de Blok *et al.* 1995, van der Hulst *et al.* 1993, Schombert *et al.* 1992).

2.5.2 H I morphology and dynamics

ESO-LV 0280140: Fig. 2.14(a) shows the integrated H I emission. There is a central depression surrounded by four emission peaks and the overall structure is rather clumpy. From this figure, the dimensions of the H I disk are 5.8′×4.1′ at a position angle of ~290°. The inclination angle, estimated from the H I distribution, is 45°. This corresponds very well with the inclination angle estimated from the optical images, 44°. In Fig. 2.14(c) the gaseous extent of the galaxy can be seen to

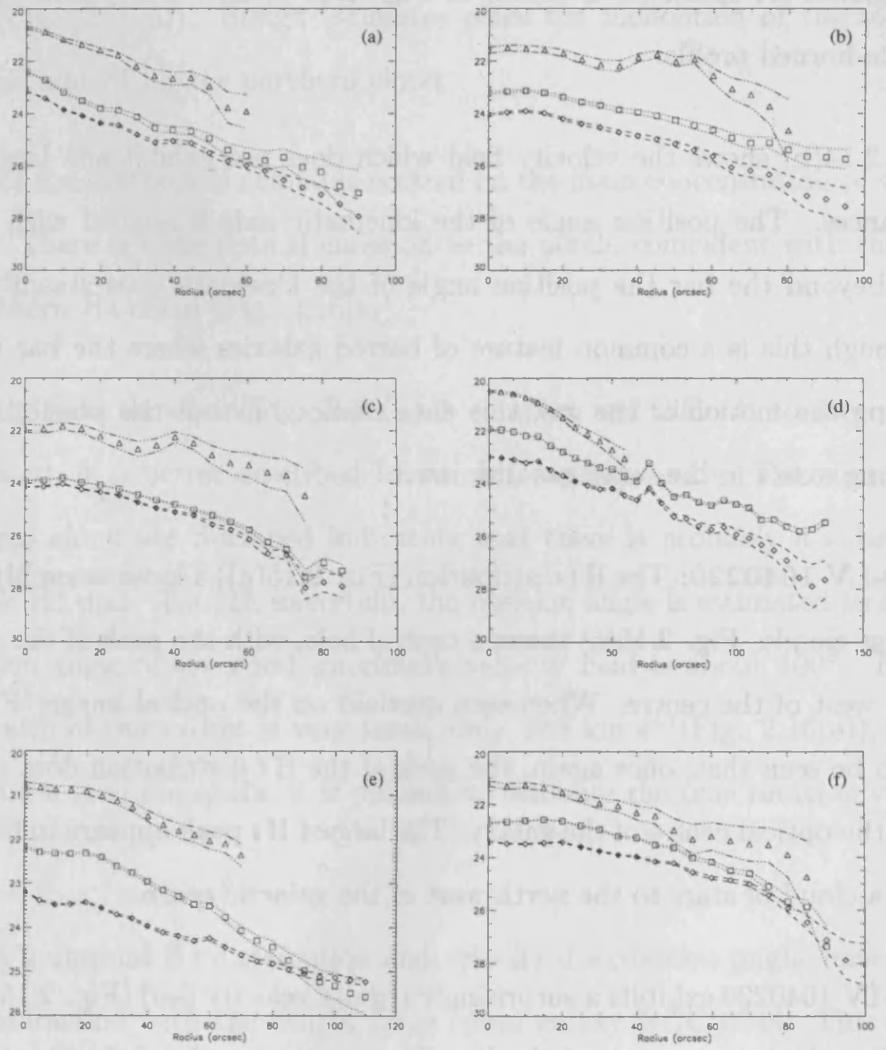

Figure 2.13: Surface brightness profiles for *B*-, *R*-, and *K*-bands. *K*-band data are denoted by triangles (errors shown with dot–dash line), *R*-band by squares (errors shown with dotted lines) and *B*-band by diamonds (errors shown with dashed line). (a) ESO-LV 0280140, (b) ESO-LV 1040220, (c) ESO-LV 1040440, (d) ESO-LV 1450250, (e) ESO-LV 1870510, (f) ESO-LV 2490360. Ellipse fitting parameters are taken from Bell *et al.* (2000).

be much greater than the optical extent, as is common in late-type galaxies. From this figure it is also clear that the peak of the H I distribution does not coincide with the optical centre of the galaxy, but lies on top of the southern spiral arm. The global H I spectrum is shown in Fig. 2.14(e) and is a typical example of a double-horned profile.

Fig. 2.14(b) shows the velocity field which does not exhibit any large scale disturbances. The position angle of the kinematic axis is aligned with the optical bar, beyond the bar the position angle of the kinematic axis steadily increases. Although this is a common feature of barred galaxies where the bar itself is disrupting the motion of the gas, this data cannot rule out the possibility that the warping exists in the outer gas disk itself.

ESO-LV 1040220: The H I distribution (Fig. 2.15(a)) a loose assembly of individual gas clouds. Fig. 2.15(a) shows a central hole, with the peak of the distribution lying west of the centre. When seen overlaid on the optical image (Fig. 2.15(c)) it can be seen that, once again, the peak of the H I distribution does not coincide with the optical centre of the galaxy. The largest H I peak appears to be associated with a cloud of stars to the north-west of the galactic centre.

ESO-LV 1040220 exhibits a surprisingly regular velocity field (Fig. 2.15(b)) despite the disturbed appearance of the H I. The position angle of the kinematic axis is different to the position angle as judged from the optical image.

The clouds in ESO-LV 0280140 and ESO-LV 1040220 could be falling in as new arrivals or as clouds that were blown out previously. If the latter is the case then the regular velocity field shows that these processes are apparently not powerful enough to affect the overall dynamics of these galaxies.

ESO-LV 1040440: A close neighbour of ESO-LV 1040220, this galaxy's neutral gas consists of two individual clouds of similar angular size. The northern cloud has around half the mass of the southern cloud as inferred from the column density contours (Fig. 2.16(a)). Rough estimates place the inclination of the southern cloud at 44° and 23°for the northern cloud.

The peak of the southern H I cloud is centred on the main concentration of stars in the south. There is some optical emission to the north, coincident with the peak of the northern H I cloud (Fig. 2.16(c)).

The velocity field shown in Fig. 2.16(b) is complex and difficult to interpret as a single cloud, it is better described by two interacting clouds. The contours in the southern cloud are S-shaped indicating that there is probably a substantial warp in the H I disk. Though uncertain, the position angle is estimated to be 45°. The position angle of the northern cloud's velocity field is about 100°. The H I velocity width of this object is very small, only 19.8 km s^{-1}(Fig. 2.16(e)), but as the inclination is so uncertain, it is difficult to estimate the true rotation velocity width.

The galaxy's unusual H I distribution and velocity distribution might have arisen from an interaction with the nearby large spiral galaxy NGC 6744. This galaxy contains about 100 times more H I than ESO-LV 1040440 and the projected separation of the galaxy centres is only 156 kpc.

ESO-LV 1450250: This galaxy has a very clumpy H I morphology that is not centrally peaked. The H I peaks follow the spiral arms somewhat loosely, apart from the south-eastern knot which appears to be unconnected with the arms (Fig 2.17(c)).

This flocculent H I actually produces a very regular velocity field as seen in Figs. 2.17(b) and (d). It suggests that the knot of H I to the south-east is a local peak that is corotating with the other gas around it.

ESO-LV 1870510: This galaxy is the most isolated of the sample and has a smooth H I distribution and also a very regular velocity field (Figs. 2.18(a) & (b)). The H I peaks coincide with the spiral arms (Fig. 2.18(c)). Fig. 2.18(d) highlights how the kinematic centre is also the optical centre of the galaxy - a property shared by all the galaxies in the sample.

ESO-LV 2490360: This galaxy has the smoothest distribution of H I (Fig. 2.19(a)) and has a very low inclination angle as estimated from the axis ratio. In the approaching half of the galaxy, the position angle of the kinematic axis is around 155°. This slowly changes to around 130° at the receding, southern tip. A clue to this feature may come from the optical image (Fig. 2.19(c)). To the west is a companion to ESO-LV 2490360: ESO-LV 2490350. ESO-LV 2490350 was also partly visible in the H I data. As well as being close in angular separation, the velocities of their H I emission differ by only 60 km s^{-1}. ESO-LV 2490350 could be affecting the dynamics of ESO-LV 2490360 but more sensitive observations would be required to confirm this scenario.

H I masses, distances, H I line flux, line widths and other measured parameters are shown in Table 2.2. The distances have been derived by assuming pure Hubble flow, with H_o=75 km $s^{-1}Mpc^{-1}$ and ignoring peculiar motions.

The velocity fields of ESO-LV 0280140, ESO-LV 1040220, ESO-LV 1450250, ESO-LV 1870510 and ESO-LV 2490360 are fairly regular and symmetric. Any large scale shearing motions would have caused kinks in the iso-velocity contours. Since there

Table 2.2: Galaxy H I properties

Galaxy	Type	v_{sys}	Distance	i	PA	W_{20}	F_{HI}	M_{HI}	semi-major axis	$\frac{M_{HI}}{L_B}$
		(kms^{-1})	(Mpc)	(°)	(°)	(km s^{-1})	(Jy km s^{-1})	($\times 10^9$ $M_\odot$)	(kpc)[a]	$\left(\frac{M_\odot}{L_\odot}\right)$
ESO-LV 0280140	SB(s)d	1780	24.1	32	290	120	14.2	2.0	18.5	2.0
ESO-LV 1040220	IB((S)m	795	10.6	10	295	48	19.8	0.5	9.5	1.7
ESO-LV 1040440[b]	SABm	843	10.4	10,5	30,305	28	4.4	0.1	5.8	0.5
ESO-LV 1450250	SAB(s)dm	1825	24.6	42	153	68	26.4	3.8	21.5	1.8
ESO-LV 1870510	SB(s)m	1383	18.1	52	11	136	13.7	1.1	12.5	1.8
ESO-LV 2490360	IB(s)m	898	12.0	15	156	65	55.7	1.9	9.8	8.4

[a]measured to column density = 2×10^{19} cm^{-2}

[b]individual values for the northern and southern clouds

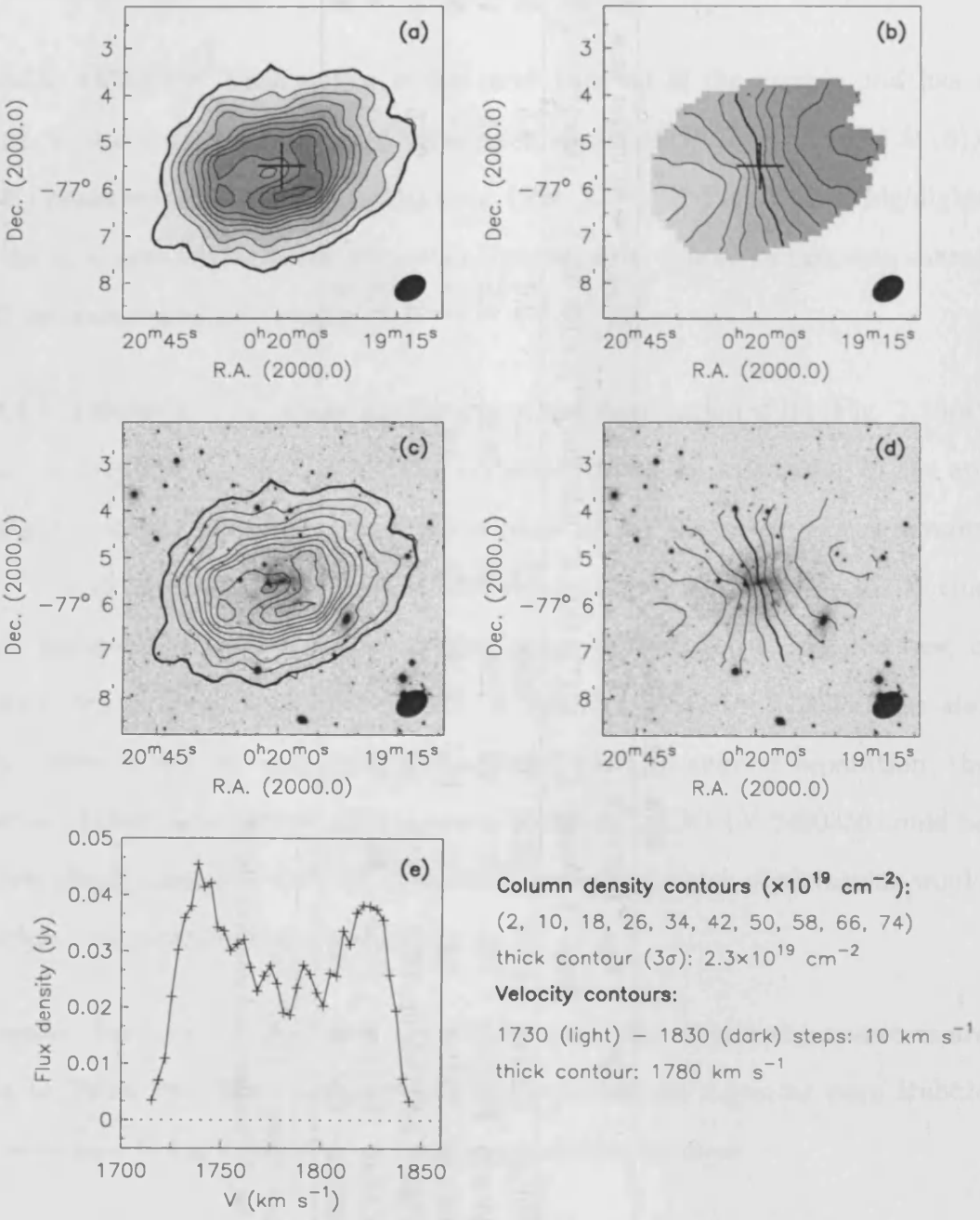

Figure 2.14: ESO-LV 0280140. (a) H I column density map. (b) H I velocity field. (c) H I column density contours overlaid on *B*-band image. (d) Velocity contours overlaid on *B*-band image. (e) H I-velocity profile. The filled ellipses indicate the size and orientation of the synthesised H I beam.

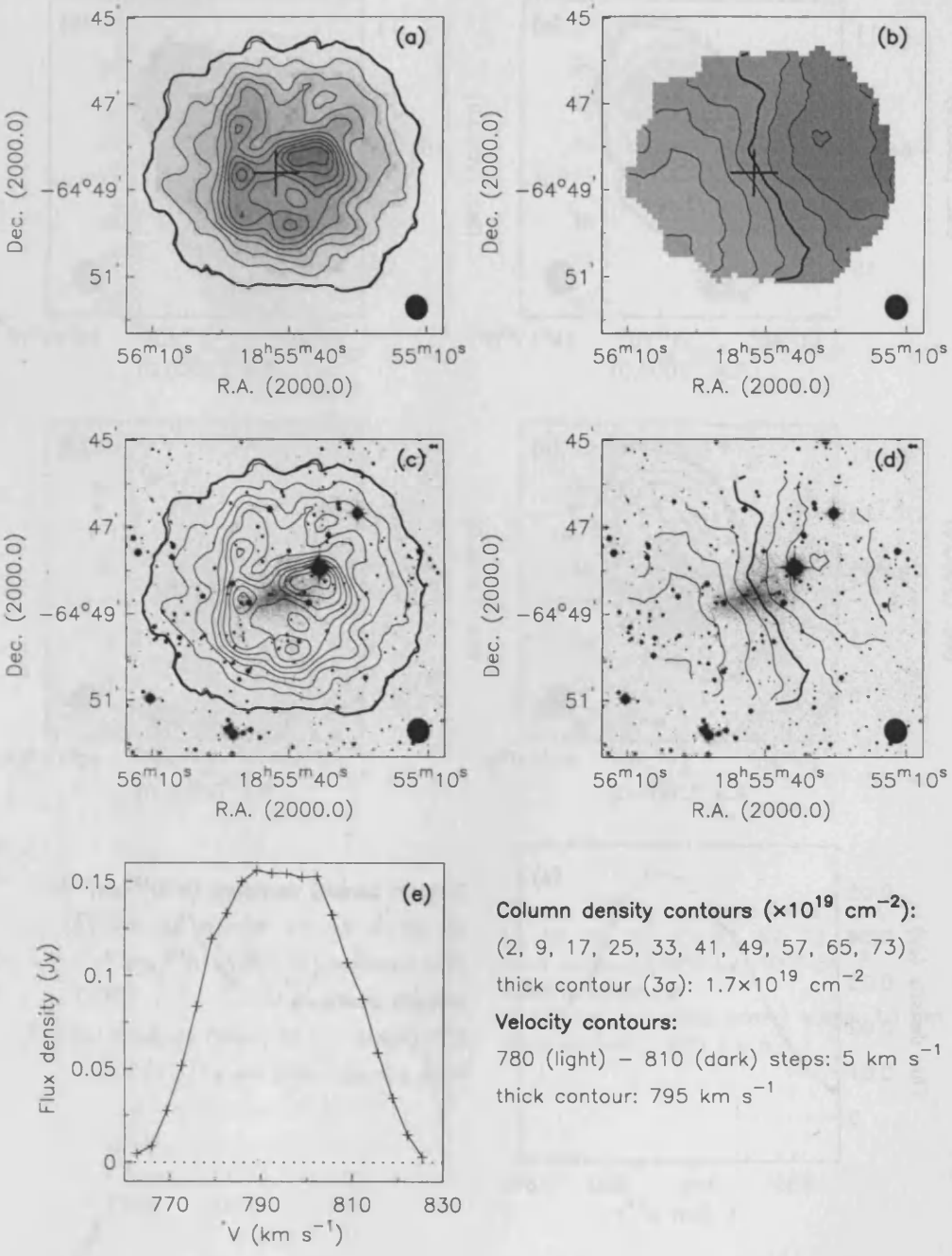

Figure 2.15: ESO-LV 1040220. (a) H I column density map. (b) H I velocity field. (c) H I column density contours overlaid on *B*-band image. (d) Velocity contours overlaid on *B*-band image. (e) H I-velocity profile. The filled ellipses indicate the size and orientation of the synthesised H I beam.

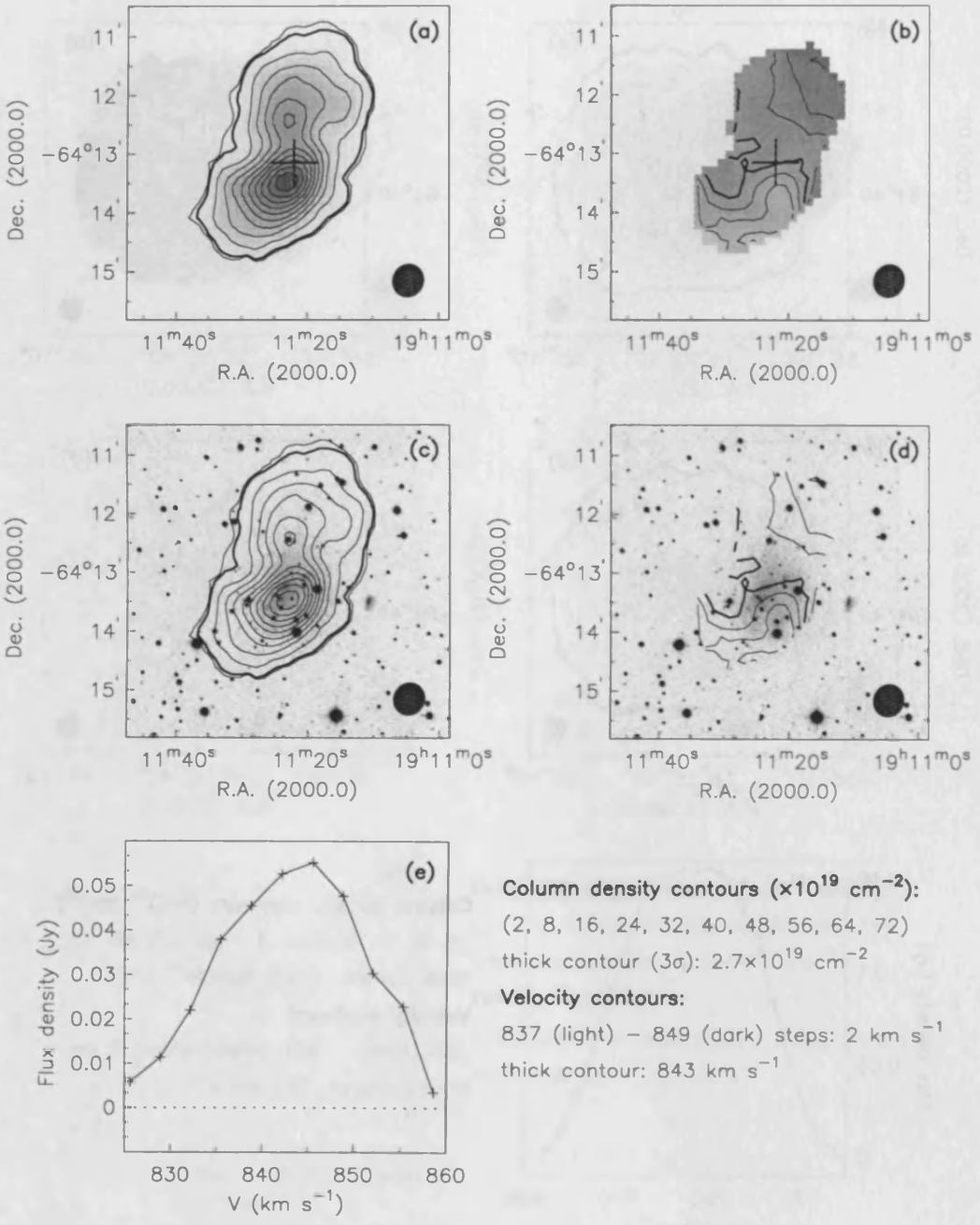

Figure 2.16: ESO-LV 1040440. (a) H I column density map. (b) H I velocity field. (c) H I column density contours overlaid on *B*-band image. (d) Velocity contours overlaid on *B*-band image. (e) H I-velocity profile. The filled ellipses indicate the size and orientation of the synthesised H I beam.

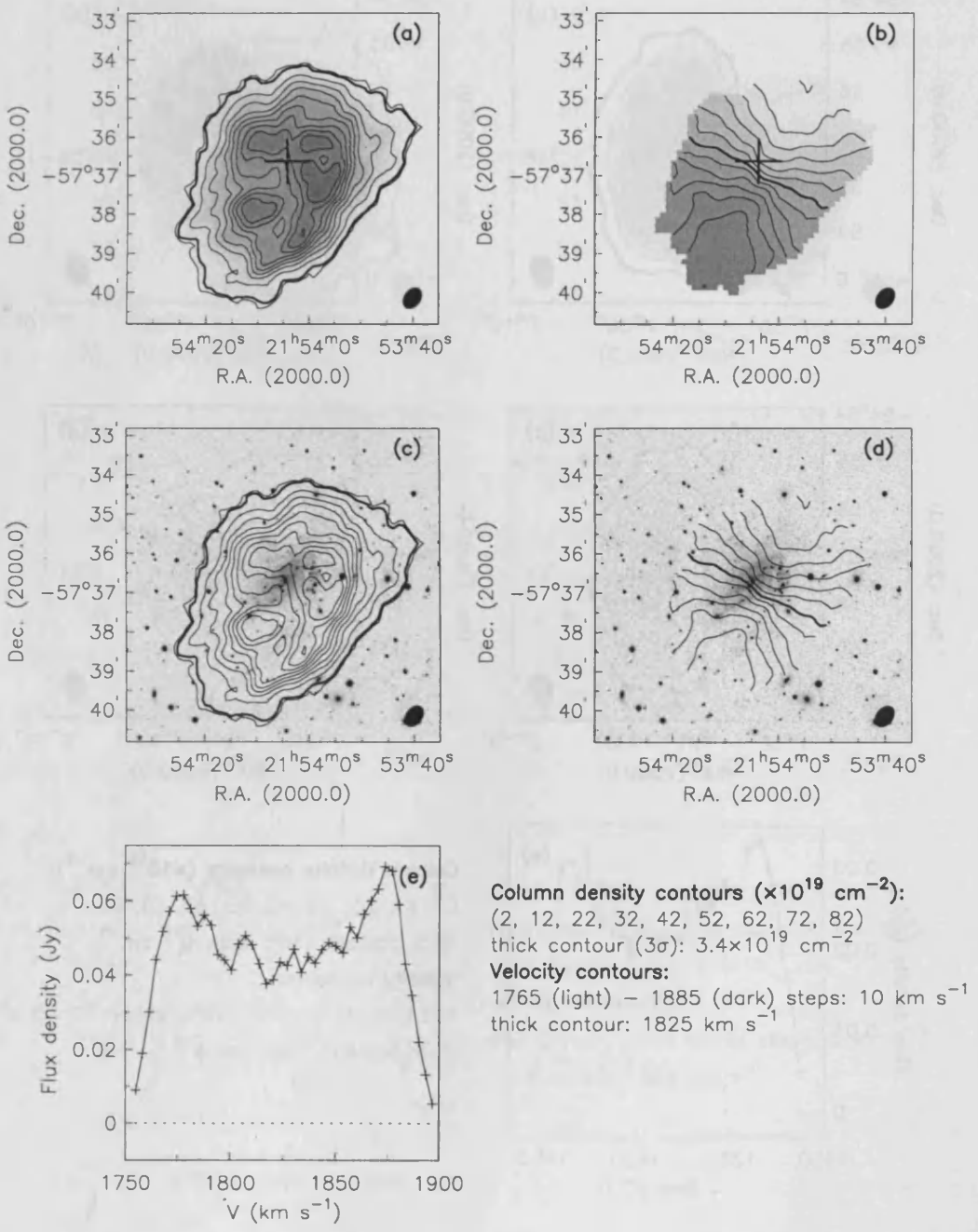

Figure 2.17: ESO-LV 1450250. (a) H I column density map. (b) H I velocity field. (c) H I column density contours overlaid on *B*-band image. (d) Velocity contours overlaid on *B*-band image. (e) HI-velocity profile. The filled ellipses indicate the size and orientation of the synthesised H I beam.

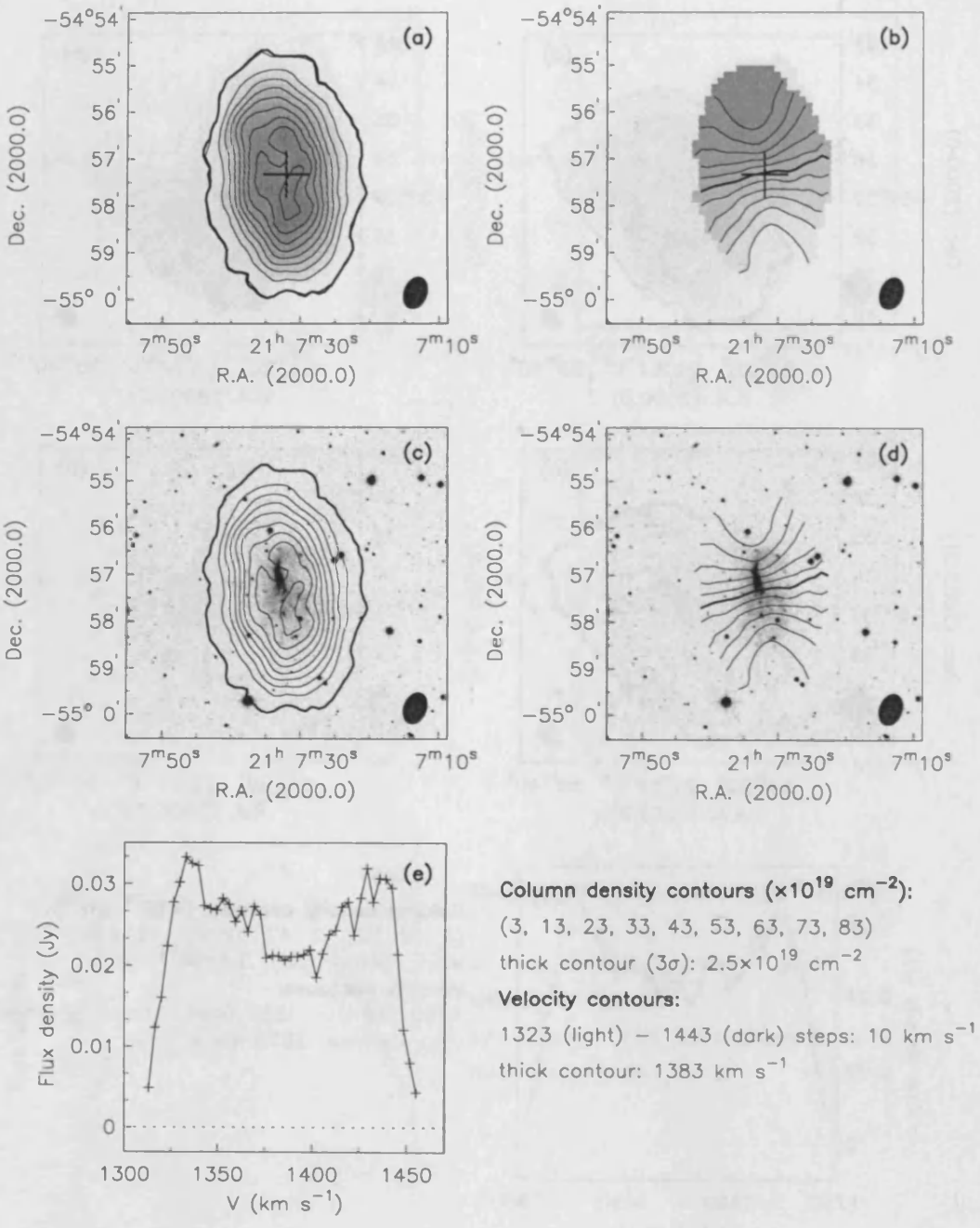

Figure 2.18: ESO-LV 1870510. (a) H I column density map. (b) H I velocity field. (c) H I column density contours overlaid on *B*-band image. (d) Velocity contours overlaid on *B*-band image. (e) HI-velocity profile. The filled ellipses indicate the size and orientation of the synthesised H I beam.

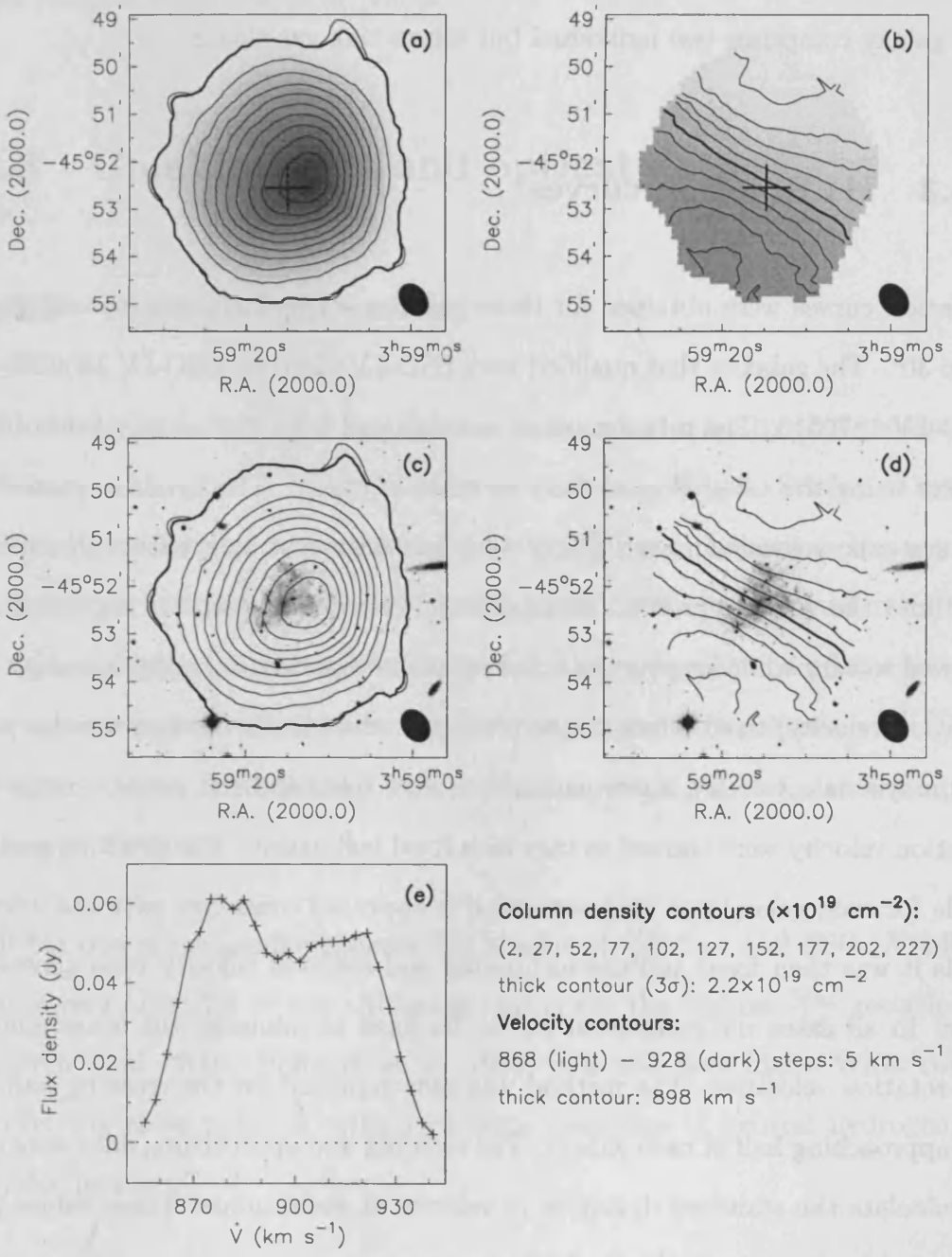

Figure 2.19: ESO-LV 2490360. (a) H I column density map. (b) H I velocity field. (c) H I column density contours overlaid on *B*-band image. (d) Velocity contours overlaid on *B*-band image. (e) HI-velocity profile. The filled ellipses indicate the size and orientation of the synthesised H I beam.

are no kinks, radial changes in the position angles are probably a sign that the H I disks for these galaxies are warped. The velocity fields are typical of late-type galaxies, the exception being ESO-LV 1040440 whose H I distribution suggests that this galaxy comprises two individual but interacting gas clouds.

2.5.3 H I Rotation curves

Rotation curves were obtained for those galaxies whose inclinations were greater than 30°. The galaxies that qualified were ESO-LV 0280140, ESO-LV 1450250 and ESO-LV 1870510. The rotation curve was obtained from the velocity field of each galaxy using the tilted ring method ROTCUR in GIPSY. The dynamic centre and the systemic velocity for each galaxy were first estimated by eye from the velocity field and the velocity profile. These parameters were fed into the algorithm and allowed to vary while keeping the other parameters (inclination, position angle and rotation velocity) fixed. Once the ROTCUR procedure had settled on a centre point and a systemic velocity, these parameters were fixed and the position angle and rotation velocity were allowed to vary for a fixed inclination. The resulting position angle for each galaxy was analysed and if it appeared consistent with the velocity fields it was then fixed and the inclination and rotation velocity were allowed to vary. In all cases the inclination had to be fixed to minimise the uncertainty in the rotation velocities. The method was then repeated for the receding half and the approaching half of each galaxy. The receding and approaching data were used to calculate the standard deviation in velocity at each radius. These values then formed the error bars in the final rotation curve.

The rotation curves for ESO-LV 0280140, ESO-LV 1450250, and ESO-LV 1870510 are shown in Fig. 2.20. The rotation curve for ESO-LV 1870510 has much larger

error bars than the other two galaxies due to the asymmetry on both sides. The three rotation curves are typical of LSBs, rising slowly in the inner regions and still rising at their outermost points.

2.6 Combined H I and optical data

2.6.1 Mass-to-light ratios

The mass-light ratio $\left(\frac{M_{HI}}{L_B}\right)$ is a distance independent quantity that measures the efficiency with which a galaxy has formed stars from its gas. Studies of optically selected galaxies have shown that most have a $\frac{M_{HI}}{L_B} < 1$ (Roberts & Haynes 1994), although such studies have been biased against LSBs. More recent results from H I selected galaxies that are not subject to the same selection effects as optical surveys have shown that in fact there is a large number of galaxies with $\frac{M_{HI}}{L_B} > 1$ (Warren, Jerjen & Koribalski, 2004). The mass-light ratios for this sample are shown in Table 2.2.

All but one of the sample galaxies has a value of $\frac{M_{HI}}{L_B} > 1$ and ESO-LV 2490360, has a very high $\frac{M_{HI}}{L_B} = 8.4$. Although this is not the highest $\frac{M_{HI}}{L_B}$ recorded (e.g. Warren *et al.* 2004, Hoffman *et al.* 1993) it is still very high. What could be preventing these galaxies, with such large reservoirs of neutral hydrogen, from producing stars?

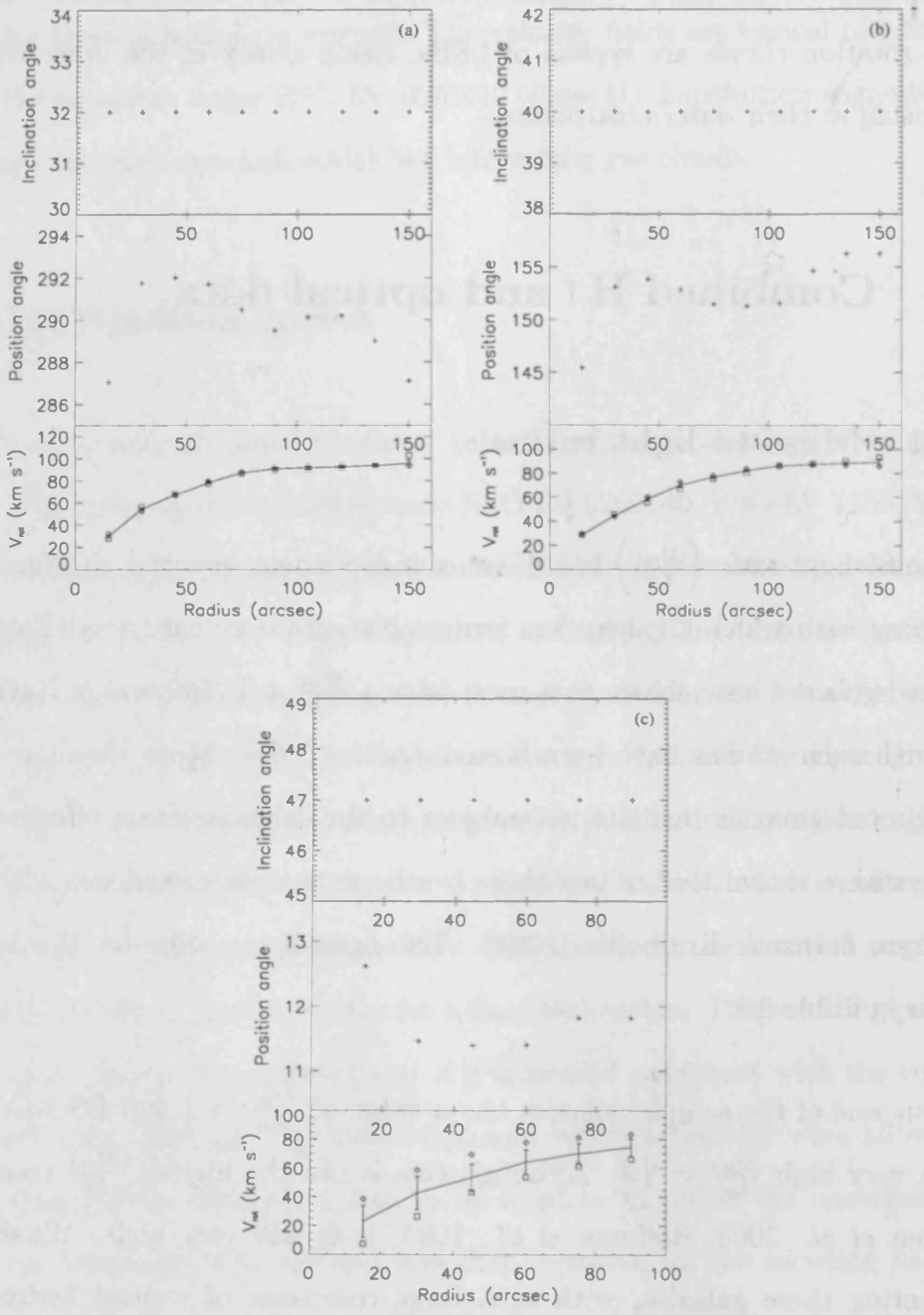

Figure 2.20: Inclination, position angle and rotation curve for (a) ESO-LV 0280140, (b) ESO-LV 1450250 and (c) ESO-LV 1870510. Analysis was restricted to galaxies whose inclination was above 30 °. The ROTCUR routine in GIPSY was used to derive the rotation curves. For each galaxy the inclination angle was fixed to derive the final rotation curve. Errors in the rotation curve represent the standard deviation of the rotation curves for the approaching and receding halves of the galaxy, evaluated at each radius.

2.6.2 The Kennicutt Star Formation Threshold

The critical gas surface density criterion for gravitational instability from Kennicutt (1989) is given by:

$$\Sigma_{crit}(r) = \alpha \frac{\sigma(r)\kappa(r)}{\pi G}, \tag{2.1}$$

where $\Sigma_{crit}(r)$ is the critical gas surface density, $\sigma(r)$ is the gas velocity dispersion, $\kappa(r)$ is the epicyclic frequency and α is a dimensionless factor, used by Kennicutt (1989) to reconcile his predictions with the observations. The epicyclic frequency, $\kappa(r)$ is given by Eqn. 1.2, reproduced here for convenience:

$$\kappa^2(r) = 2\left(\frac{V^2}{r^2} - \frac{V}{r}\frac{dV}{dr}\right),$$

where r is measured in (km) and V is the rotational velocity at r (km s^{-1}). $\kappa(r)$ can thus be calculated from the rotation curve. The derivative, was calculated using the DERIVE procedure in IDL, which uses 3-point Lagrangian interpolation.

In his original analysis Kennicutt (1989) found that a value of $\alpha = 0.63$ was sufficient to fit his observations to his predictions. In a more detailed work conducted with a larger sample, Martin & Kennicutt (2001) found that a value of $\alpha = 0.69$ produced a better fit to the data. The value of α from Martin & Kennicutt (2001) has been adopted for the analysis i.e. since LSBs are not producing stars on a large scale one would expect that the gas surface density profiles should all fall below Σ_{crit}.

Radial profiles of Σ_{crit} and Σ_{gas} have been constructed for each of the three galaxies with a rotation curve (Fig. 2.21). The gas surface density used in the Kennicutt (1989) analysis includes H I and helium using a conversion factor ($\Sigma_{gas} = 1.41\Sigma_{HI}$). Here, molecular gas has been ignored, however its contribution is likely to be

unimportant – Schombert *et al.* (1990) showed CO results indicating that LSBs do not contain significant amounts of molecular gas. A constant $\sigma(r) = 6\dot{}\text{km s}^{-1}$ has been assumed throughout to be consistent with Kennicutt (1989).

The solid lines in Fig. 2.21 show the radial gas surface density plots for each galaxy. The dashed lines represent the critical surface density threshold calculated from Eqn. (2.1) using a value of $\alpha = 0.69$. The criterion for gravitational instability and hence star formation is simple: anywhere the solid line rises above the dashed line, there should be evidence of star formation.

The Hα profiles can now be used as evidence of recent star formation to see if this prediction is observed. Each azimuthally averaged Hα surface brightness profile has been constructed using the raw counts above the sky background, and the ELLINT routine in GIPSY. This has then been scaled arbitrarily and plotted in Fig. 2.21 to highlight radii which have undergone recent star formation.

Fig. 2.21(a) shows that the Hα is fairly constant out to 9 kpc and then declines to the background level. According to the Kennicutt scenario there should be no widespread star formation in the inner 7 kpc of ESO-LV 0280140, but the Hα emission is indicating that this is precisely where it is occurring. Between 7 and 13 kpc, the gas surface density shows its closest approach to the critical level and one would expect this region to show the greatest amount of star formation. The Hα is declining in this region however and no Hα is detected beyond 10.5 kpc.

The Hα profile of ESO-LV 1450250 (Fig. 2.21(b)) increases between 2.0–7 kpc, peaking at 7 kpc where Σ_{gas} is approaching the critical value. Beyond 7 kpc the Hα declines to the background level at 18 kpc. The decline in Hα is not necessarily contradictory, but one would expect that the region with the greatest amount of

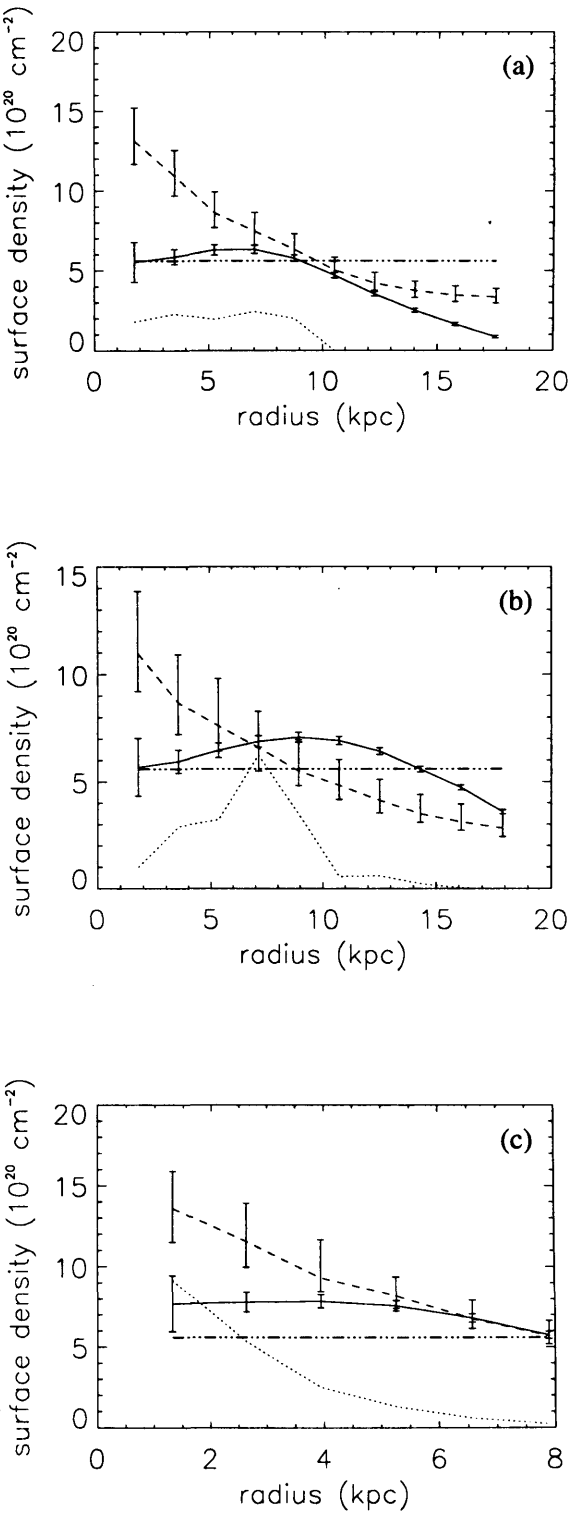

Figure 2.21: H I surface density plots, for (a) ESO-LV 0280140, (b) ESO-LV 1450250 and (c) ESO-LV 1870510. The Kennicutt-derived critical surface density is denoted by the dashed line. The solid line represents the H I surface density profile. The Schaye-derived critical surface density is represented by the dot-dash line. The azimuthally averaged Hα surface density profiles (dotted lines) have been arbitrarily scaled. They are meant only to indicate recent large scale star formation activity within each galaxy.

star formation would be where $\Sigma_{gas} > 0.69\Sigma_{crit}$. The excess H$\alpha$ emission at 7 kpc is most likely due to the western spiral arm.

ESO-LV 1870510 (Fig. 2.21(c)) shows a central peak in Hα emission and rapidly decreases out to 8 kpc. This central region shows the most star formation activity yet the gas density is well below the critical density set by Kennicutt. Kennicutt predicts that star formation should only be occurring in the outer disk between 5.5–7.8 kpc and possibly beyond. Although there is some Hα emission in this region it is relatively less than the emission from the central region of the galaxy. This is contrary to expectations – more Hα emission is expected from the regions with gas surface density above the critical value.

ESO-LV 0280140 and ESO-LV 1870510 both have gas surface density profiles that fall beneath their critical threshold profiles as calculated using Kennicutt (1989). This can explain the global absence of star formation in these LSBs. In this respect, ESO-LV 1450250 has an unusual H I profile. It rises above the critical threshold at 7 kpc and stays above it to the detectable edge of the H I disc. This ability to form stars is not reflected in the Hα profile, suggesting perhaps there are other mechanisms that are contributing to the gravitational stability of the gas. Magnetic fields may be contributing to the stability of the gas, but while these fields are important in individual regions (Kim & Ostriker, 2002), they are probably unimportant on galactic scales. Another way to reconcile the difference would be to adopt a higher value for the velocity dispersion, σ in ESO-LV 1450250. By increasing the velocity dispersion to 9 km s^{-1}, all the H I profiles would fall well below the critical surface density, explaining the lack of star formation on a galactic scale. A final possible explanation of the unusual profile in this galaxy would be to adopt a velocity dispersion that varies with radius which is one prediction of the modelling of Schaye (2004).

2.6.3 The constant density star formation threshold

Here the constant H I surface density star formation threshold scenario, described by Skillman (1987) is tested. The modelling work by Schaye (2004) builds on the work of Elmegreen & Parravano (1994) and provides a theoretical foundation for the phenomenon, and so the results of Schaye (2004) have been adopted for comparison.

The heavy dash-dot lines in Fig. 2.21 marks the 5.6×10^{20} cm^{-2} (4.5 M$_{\odot}$pc^{-2}) threshold found by Schaye (2004). If there is a constant star formation H I surface density threshold, all the galaxies in this sample should exhibit evidence of star formation where the H I gas surface density is above this threshold.

ESO-LV 0280140, shown in Fig. 2.21(a), has a Σ_{HI} density above 5.6×10^{20} cm^{-2} (4.5 M$_{\odot}$pc^{-2}) from the centre of the galaxy out to 9 kpc. Hα emission should only be expected in the inner 9 kpc. This is very close to what is seen. The Hα emission is fairly constant out to 9 kpc, then declines rapidly and there is no emission beyond 10.5 kpc. The Σ_{HI} density at this point is $\sim 5{\times}10^{20}$ cm^{-2}, well within the critical surface density limits of Schaye (2004). Fig. 2.21(b) reveals a similar result. The H I profile for ESO-LV 1450250 is above the threshold value out to 14.5 kpc and then drops below 5.6×10^{20} cm^{-2}. The Hα emission is present from the galaxy centre out to 16 kpc. ESO-LV 1870510 (Fig. 2.21(c)) also exhibits this trend. The H I surface density stays above 5.6×10^{20} cm^{-2} all the way from the centre to the detectable edge of the galaxy and Hα emission extends all the way to the edge of the disk.

Another way of visualising the constant surface density threshold is to plot the H I critical surface density from Schaye (2004) as a contour on top of the Hα images.

If the Schaye value is correct, all the H II regions within each galaxy should fall within this contour. This test can be applied to all the galaxies as the surface density is not as sensitive as the rotation curve to small changes in inclination angle, i, when i is small. The dashed line in Fig. 2.22 represents the Schaye value of 5.6×10^{20} cm^{-2}, with the upper and lower bounds shown by the dotted lines. ESO-LV 2490360 is the the only galaxy whose peak surface density rises above the upper bound of 10^{21} cm^{-2} hence Fig. 2.22(f) is the only image in which the upper bound is plotted. For most of the galaxies the H I contour that best encompasses all the HII regions is somewhere in the limits set by Schaye. The one exception is ESO-LV 2490360. The upper bound of 10^{21} cm^{-2} (8.0 M$_\odot$pc^{-2}) does not tightly constrain the distribution of HII regions as seen on the Hα image, implying this galaxy has a higher threshold value than that predicted by Schaye. The Hα images were then examined in turn to find the highest H I contour that encompassed all the HII regions visible in the image. These H I surface density threshold contour values for each galaxy are shown in Table 2.3.

The H I threshold contour for ESO-LV 0280140 (Fig. 2.22(a)) traces a fairly regular ellipse and the value of the surface density is 4.1×10^{20} cm^{-2} (3.3 M$_\odot$pc^{-2}). Fig. 2.22(b) shows the H I surface density threshold contour for ESO-LV 1040220. This contour encompasses the central, irregular distribution of HII regions extremely well. It even highlights an isolated HII region to the north-east. The threshold contour is 4.9×10^{20} cm^{-2} (3.9 M$_\odot$pc^{-2}). ESO-LV 1040440, shown in Fig. 2.22(c) has several HII regions associated with the southern cloud and a single HII region in the northern cloud. The H I contour (4.9×10^{20} cm^{-2} $\equiv$ 3.9 M$_\odot$pc^{-2}) encompasses all the HII regions in the northern and southern clouds. Fig. 2.22(d) shows the Hα image of ESO-LV 1450250. The HII regions are distributed mostly along the spiral arms of the galaxy and the H I contour, 3.6×10^{20} cm^{-2} (2.9 M$_\odot$pc^{-2}), traces this

Table 2.3: Constant star formation H I surface density thresholds.

Galaxy	Threshold Surface Density $[\times 10^{20} cm^{-2}]$ ($M_{\odot} pc^{-2}$)
ESO-LV 0280140	4.1 (3.3)
ESO-LV 1040220	4.9 (3.9)
ESO-LV 1040440	3.9 (3.1)
ESO-LV 1450250	3.6 (2.9)
ESO-LV 1870510	3.2 (2.6)
ESO-LV 2490360	12.6 (10.1)

distribution well. ESO-LV 1870510 (Fig. 2.22(e)) has a fairly elliptical distribution of HII regions in the centre of the galaxy and the elliptical H I contour (3.2×10^{20} cm^{-2} (2.6 $M_{\odot}pc^{-2}$) constrains the HII regions successfully. The final image (Fig. 2.22(f)) is of ESO-LV 2490360. The HII regions are spread evenly throughout the central regions of the galaxy and the H I contour that best traces these regions is n(H I) = 12.6×10^{20} cm^{-2} (10.1 $M_{\odot}pc^{-2}$). This value is above the upper limit for the threshold derived by Schaye (2004) of 10×10^{20} cm^{-2} (8 $M_{\odot}pc^{-2}$). Hα emission would have been expected further out from the centre of this galaxy based on the constant critical gas surface density scenario.

The H I–Hα profiles (Fig. 2.21) and the spatial distribution of HII regions (Fig. 2.22) largely support the idea of a constant surface density threshold for this sample of galaxies. The threshold H I surface densities listed in Table 2.3 are almost all in agreement with Schaye's value of $(5.6^{+4.4}_{-3.0}) \times 10^{20}$ cm^{-2} ($4.5^{+3.5}_{-3.4}$ $M_{\odot}pc^{-2}$).

2.7 Discussion

Inhibited star formation in this sample of LSBs has been inferred from their high $\frac{M_{HI}}{L_B}$. To explain this, two alternative views of star formation have been consid-

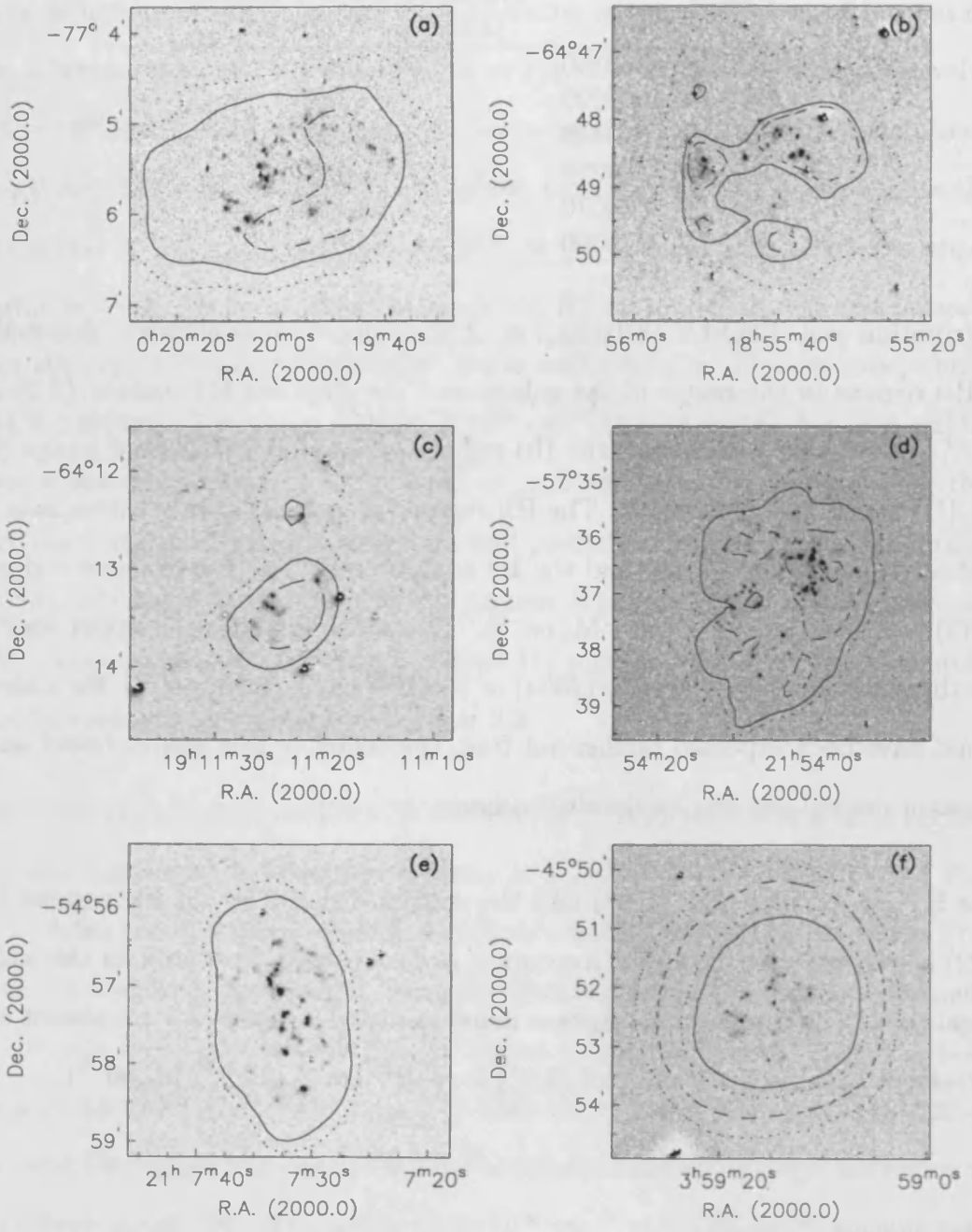

Figure 2.22: Hα images with H I surface density contours. The dashed line is the inclination corrected Schaye H I critical surface density value $(5.6^{+4.4}_{-3.0}) \times 10^{20}$ cm^{-2} $(4.5^{+3.5}_{-3.4}$ M$_\odot$pc$^{-2})$, with the dotted lines representing the upper and lower bounds. The solid lines represent the highest H I surface density contours that encompass all the H II regions within each galaxy. The values of these contours are listed in Table 2.3

ered: Kennicutt (1989) and Schaye (2004). While all of the sample comply with the ideas of Schaye (2004), only two of the three galaxies that could be used to test Kennicutt's gas threshold conform with this idea. The results from ESO-LV 1450250 seem to indicate that rotation alone is not enough to support the gas against gravitational instability.

The data presented here are subject to a number of systematic errors, some of which might have a considerable effect on the final analysis. The accuracy of the rotation curves is limited by the resolution of the H I synthesised beam, especially in the innermost parts of the galaxies. The curves are certainly subject to a certain amount of beam smearing in the central regions of each galaxy. This would have the effect of making the rotation curves appear to rise more slowly in the inner regions, ultimately making the critical surface density profile different. To assess the influence of this, a steeper inner rotation curve was simulated for each galaxy and the critical surface density re-calculated (Fig. 2.23). The change in gradient has had a dramatic effect on the critical density profile. The effect has been to increase the critical density in the inner regions but the outer regions remain largely unaffected. It should also be noted that H I does not constitute the total gas content of these galaxies. There are other constituents (helium and possibly H_2) that, once taken into account, would raise the gas surface density profile by a factor of typically 1.4. So it would seem that when beam smearing effects and chemical abundance in the ISM are taken into account, it is actually more difficult to interpret the Hα profiles in terms of the Kennicutt criterion.

Another factor to consider is that since star formation is a local phenomenon, using the azimuthally averaged H I surface density may not be appropriate for galaxies where the variation in surface density at a given radius can be large (Martin & Kennicutt, 2001). This would affect clumpy galaxies such as ESO-LV 0280140 and

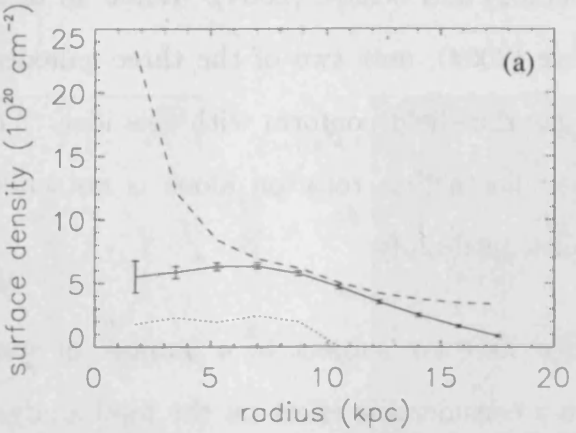

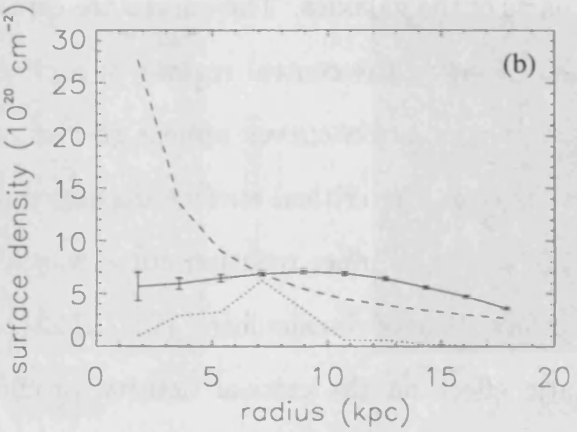

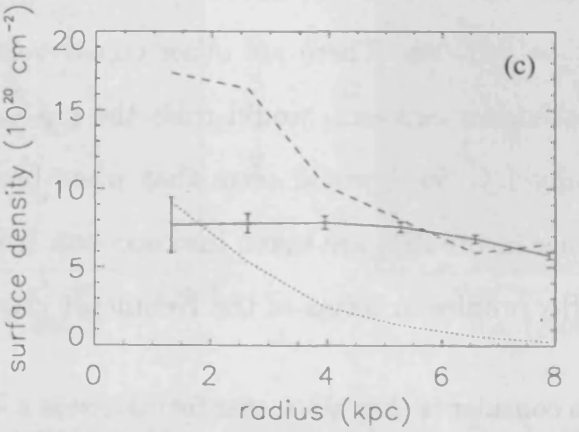

Figure 2.23: Revised critical surface density profiles for (a) ESO-LV 0280140 (b) ESO-LV 1450250 and (c) ESO-LV 1870510. In each case the rotation curve has been made steeper in the inner regions to counteract the effects of beam smearing. The most noticeable effect is that the critical density increases in the inner parts of each galaxy.

ESO-LV 1450250. Also assuming a constant velocity dispersion seems to be too simple. Schaye (2004) demonstrated that it is the sharp drop in velocity dispersion at the critical radius that is responsible for the sharp decrease in Q. Perhaps a more fitting test of the Kennicutt regime would be to construct 2-D critical surface density maps such as that performed by de Blok & Walter (2006) on NGC 6822. The results from NGC 6822 showed that star formation can be fit equally well by a constant H I surface density criterion or a Toomre-Q criterion, so long as one uses a lower velocity dispersion (4 km s^{-1}) than Kennicutt (1989). The adoption of a lower value for the velocity dispersion is also more consistent with that of a cold phase such as that predicted by Elmegreen & Parravano (1994) and Schaye (2004). Unfortunately a similar analysis on these galaxies requires higher resolution maps than are currently available.

2.8 Conclusions

B, R, K, Hα and H I data have been collated for a sample of LSBs to examine the morphology and dynamics of the stellar population and the neutral gas disk. These objects show a wide range of morphologies, H I mass, dynamic range of H I surface density, optical features and relatively large M/L ratios. Some of the unusual morphology such as that in ESO-LV 1040440 or ESO-LV 1040220 could be explained by a scenario where there has been a starburst event and the subsequent stellar winds and supernovae have driven the gas from the galaxy, causing H I holes, plumes and knots. In the case of of ESO-LV 1040440 it is likely that interactions with NGC 6744 are also contributing to the interesting morphology and dynamics.

The comparison of the star formation scenarios of Kennicutt (1989) and Schaye

(2004) have also been explored. The results from two of the three galaxies can be explained within the framework of a Kennicutt-like threshold. The entire galaxy sample supports the idea of Schaye: that there is a constant value of H I surface density below which star formation is highly suppressed. The range of values for the critical H I surface density for this sample is 2.6–12.6 $\times$ 10^{20} cm^{-2} (2.1–10.1 $M_{\odot}pc^{-2}$).

Since all dark galaxies fail to meet the star formation threshold, this result provides a simple criterion by which potential dark galaxies can be judged. This criterion, combined with the optical evidence, will be used to search for a dark galaxy population within a new sensitive blind H I survey: the Arecibo Galaxy Environment Survey (AGES).

Chapter 3

The Arecibo Galaxy Environments Survey

Based on a paper by R. R. Auld et al. Monthly Notices of the Royal Astronomical Society, vol. 371, p. 1617

3.1 Introduction

With the advent of 21cm multibeam receivers on single dish telescopes, it has become possible to carry out fully sampled surveys over large areas of sky. The H I Parkes All Sky Survey (HIPASS: Barnes et al. 2001) and its sister survey the H I Jodrell All Sky Survey (HIJASS: Lang et al. 2001) have recently completed mapping the whole sky south of δ =+25° as well as selected fields north of δ=+25°. These surveys have been used to construct H I selected catalogues of galaxies (Koribalski et al. 2004, Meyer et al. 2004), identify extended H I structures and High Velocity

Clouds (HVCs) in the Local Group (Putman et al. 2002; Putman et al. 2003), place limits on the faint end of the HIMF (Kilborn, Webster & Staveley-Smith 1999; Zwaan et al. 2005), to identify a population of gas-rich galaxies (Minchin et al. 2003), to study Galactic star forming regions through radio recombination lines (Auld, 2003), to place limits on the number of previously undetected H I clouds and extended H I features (Ryder et al. 2001; Davies et al. 2001; Ryan-Weber et al. 2004), to measure the H I properties of cluster galaxies (Waugh et al. 2002; Davies et al. 2004) and to measure the cosmic mass density of neutral gas (Zwaan et al. 2003).

Table 3.1 shows a comparison of the past, present and future blind H I surveys. Minchin et al. (2005) describe the criteria that need to be met by blind H I surveys searching for a population of LSBs, these are listed in Chapter 1. When the results of the modelling of Davies et al. (2006) is taken into account, this yields even more stringent limits. The population they predict from their simulations is dominated by a population of narrow velocity (< 40 km s^{-1}), low column density ($< 10^{19}$cm^{-2}) objects. Most of these surveys are limited in their ability to be able to detect such a population of dark galaxies. Low sensitivity limits most of the surveys, while coarse velocity resolution means that most narrow-line detections are rejected as RFI.

The H I information alone is not enough. Any H I survey which is designed with the intention of placing limits on a population of LSBs, must be accompanied by a system of deep optical follow up observations. The DSS represented a major step forward in data availability, but the survey itself is quite shallow ($\mu_B < 24.5$ mag arcsec^{-2}, so its application to a search for dark galaxies is only of use for rejecting the brightest optical counterparts.

AHISS, VIRGOHI and HIDEEP are the only H I surveys that have associated deep optical observations, leading to the rejection of all but one dark galaxy candidate – VIRGOHI21. This chapter introduces the Arecibo Galaxy Environment Survey: a survey that combines H I, optical, NIR & UV data from different galactic environments. As can be seen from Table 3.1 the H I observations have been designed to specifically probe the region in which dark galaxies are thought to exist. First a description of the Arecibo *L*-band Feed Array (ALFA) will be given. The survey, observing strategy, data reduction, and analysis techniques are also explained in this chapter.

3.2 ALFA

The installation of ALFA at Arecibo presents the opportunity to survey the sky with higher sensitivity and higher spatial resolution than has been achievable previously. In addition to the receiver array, new back-ends have been designed specifically for Galactic, extragalactic and pulsar observers. Three consortia have been formed to gain the full potential from ALFA: PALFA for Pulsar research, GALFA for Galactic science and EALFA is the extragalactic consortium. The new back-end for extragalactic astronomers provides not only increased spectral resolution but also more bandwidth than was available for previous H I surveys.

ALFA operates between 1.225 and 1.525 GHz and consists of a cluster of seven cooled dual-polarisation feed horns, with a maximum of 100 MHz available at any one time. The outer six feeds are arranged in a hexagonal pattern around the central beam. The digital back-end signal processors are Wide-band Arecibo Pulsar Processors (WAPPs) that have been upgraded to perform spectral line

Table 3.1: Parameters of previous blind H I surveys

	AHISS	**Arecibo Slice**	**Shostak (1977)**	**Henning (1995)**	**ADBS**	**HIPASS**	**HIJASS**
Telescope	Arecibo	Arecibo	NRAO 300 ft.	Arecibo	Arecibo	Parkes	Lovell
Velocity range (km s^{-1})	-700–7400	100–8340	-775–11000	-400–6800	-654–7977	-1280–12700	-3000–10000
Area coverage (sq. deg.)	13	33.6	154	183	430	30000	1152
Noise[a] (mJy)	0.75	2.0	18–105	3.4	3–4	13	14
Channel separation (km s^{-1})	16	16	11	22	33.8	13.2	13.2
FWHM (arcmin)	3.3	3.3	10.8	10.8	3.3	15.5	12
5σ M_{HI} limit ($\times 10^5$ $M_\odot d_{Mpc}^{-2}$	1	2.8	25–150	4.7	4.2-5.5	19	19
5σ N_{HI} limit ($\times 10^{18}$cm^{-2})	18	48	41–240	7.7	72–96	16	26
No. of detections	66	75	—	37	265	4315	222
	HIZOA	**HIDEEP**	**VIRGOHI**	**ALFALFA**	**AGES**	**AUDS**	
Telescope	Parkes	Parkes	Lovell	Arecibo	Arecibo	Arecibo	
Velocity range (km s^{-1})	-1280–12700	-1280–12700	-1000–10000	-1600–18000	-2200–20000	0-48000	
Area coverage (sq. deg.)	1728	32	32	7000	200	0.36	
Noise[b] (mJy)	6	3.2	4	2.5	0.9	0.05	
Channel separation (km s^{-1})	13.2	13.2	13.2	5.2	5.2	5.2	
FWHM (arcmin)	15.5	15.5	12	3.4	3.4	3.4	
5σ M_{HI} limit ($\times 10^5$ $M_\odot d_{Mpc}^{-2}$	8.3	4.4	5.5	4.8	1.2	0.7	
5σ N_{HI} limit ($\times 10^{18}$cm^{-2})	48	41–240	7.7	72–96	16	26	
No. of detections	1036	173	31	—	—	—	

[a]per channel per beam
[b]per channel per beam

observing. The WAPPs have 4096 channels, the central frequency can be tuned to any frequency within the ALFA operating range and they are capable of producing variable bandwidths and hence varying spectral resolution. For the purposes of AGES the bandwidth was set to 100 MHz giving a channel spacing of 24.4 kHz $\equiv$ 5.15 km s^{-1} at the rest frequency of H I. At 1.4 GHz the mean half power beam width is 3.4′and the mean system temperature is 30 K.

The array is mounted on the rotating feed mount at the focus of the tertiary dish, which is itself housed in the Gregorian dome at the Arecibo 305 m dish. Once in place ALFA rotates independently of the feed mount. The feed must be rotated to the correct angle to produce equidistant beams on the sky (Fig. 3.1). Unlike Parkes, Arecibo is actually a spherical dish and the feed is moved to illuminate different areas of the dish, which has the effect of looking at different areas of the sky. The spherical nature of the dish causes aberrations to appear in the data as coma lobes and varying sidelobe structure (Fig 3.2). Without correct treatment these effects would have a detrimental effect on the survey's ability to probe the low column density regime. These are studied and quantified in chapter 4. The attention now turns to the survey itself and its goals.

3.3 AGES

The Arecibo Galaxy Environment Survey (AGES) forms one of four working groups within EALFA and will study environmental effects on H I characteristics. The Arecibo Legacy Fast ALFA, ALFALFA, survey (Giovanelli et al. 2005) covers a larger area (~7000 sq. deg.) but is much shallower than AGES (T_{int} ~24s). AGES will use 2000 hours of telescope time between 2003 and 2008 and will go

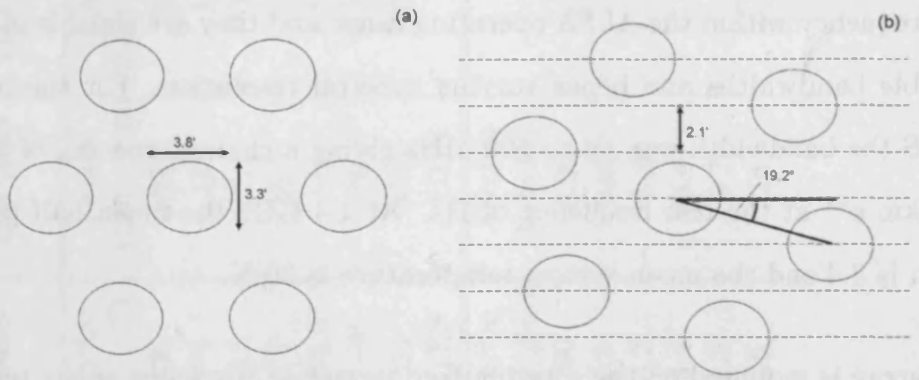

Figure 3.1: An illustration of the projected ALFA footprint, (a) unrotated with respect to the direction of the scan, and (b) rotated to produce equidistant beams of 2.1′ separation. Dotted lines indicate the individual beam tracks across the sky.

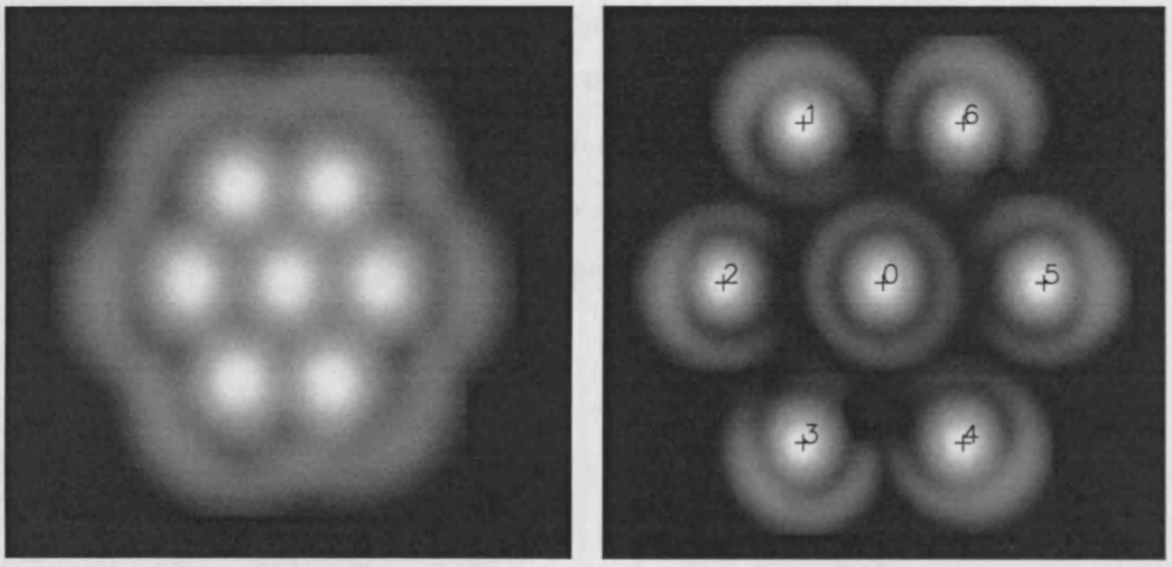

Figure 3.2: An illustration of the ALFA beam footprint to emphasise the strength and symmetry of the sidelobes. (a) A highly stretched image of the combined response of all seven ALFA beams, the image size is 32′×32′. (b) The beam separations have been stretched to 2.5 times the true separations to highlight the sidelobes of the beams. The angular scales of each beam is correct and unchanged. The image size in this case is 48′×48′. (Figures appear courtesy of Carl Heiles.)

deeper than ALFALFA to produce a much more sensitive survey (T_{int} ~300s) over a smaller area (~200 sq. deg.).

The Zone of Avoidance survey, ZOA (Henning et al. 2006) will concentrate on the low-Galactic latitude ($b < 5°$) portion of the sky visible to Arecibo. By performing commensal observations with the Galactic ALFA working group (GALFA) and the Pulsar ALFA working group (PALFA), they will reach a $T_{int} \sim 270$s.

The ALFA Ultra Deep Survey, AUDS (Freudling et al. 2005) will reach an integration time of ~75 hours, over a small area (~0.4 sq. deg.) and will search for objects more distant than the previous surveys will be able to detect.

Exploiting the improvements in sensitivity, velocity resolution and spatial resolution offered by the ALFA system, the Arecibo Galaxy Environment Survey (AGES) aims to study the atomic hydrogen properties of different galactic environments to high sensitivity limits; low H I masses ($5 \times 10^6 M_\odot$)[1] and low column densities ($3 \times 10^{18} cm^{-2}$). These environments range from apparent voids in the large scale structure of galaxies, via isolated spiral galaxies and their halos, to galaxy-rich regions associated with galaxy clusters and filamentary structures. Our intentions are: to explicitly investigate the HIMF in each environment, to measure the spatial distribution of H I selected galaxies, to identify individual low mass and low column density objects, to determine the low column density extent of large galaxies and to compare our results with expectations derived from QSO absorption line studies. In addition we aim to explore the nature of High Velocity Clouds (HVCs) and their possible link to dwarf galaxies, measure the contribution of neutral gas to the global baryonic mass density, identify gaseous tidal features as signatures of mergers and interactions and compare our results with numerical models of galaxy

[1] at the distance of the Virgo Cluster (16 Mpc)

formation.

While ALFALFA and AGES share similar goals, by going deeper AGES will be able to reach lower mass limits and column density limits than ALFALFA at any given distance. An added benefit of choosing smaller fields is that deep multi-wavelength comparison surveys become much more feasible. This is extremely important as it will allow us to study not only objects of interest but also the surrounding environment which may be influencing their evolution. This environment may stretch over length scales of degrees, particularly for nearby galaxies, requiring sensitive telescopes with large fields of view. The Hubble Space Telescope, MEGACAM on the Canada-France-Hawaii Telescope (CFHT), GALEX and UKIRT amongst others will be used for deep observations of each of the AGES fields in optical, UV, and NIR bands.

3.4 The AGES fields

Arecibo is a fixed-dish telescope so the observable sky is restricted in declination ($-1° \lesssim \delta \lesssim +38°$) and on-source time is limited to typically a 2 hour window centred on the meridian on any night. To optimise scheduling, AGES fields were chosen across a range of RAs (Fig. 3.3). Most areas comprise a 5°×4° field with an integration time of 300s per point in two polarisations. The rms noise in the final data is estimated to be between 0.5–1 mJy/beam per channel for a channel separation of 5.15 km s^{-1}. At the distance of the Virgo cluster (∼16 Mpc) this will enable us to reach an H I mass limit of $5 \times 10^6 M_\odot$ ($W_{50} = 30$ km s^{-1}), and will permit us to detect H I masses as low as $5 \times 10^7 M_\odot$ out to 3 times this distance. This is of particular significance as the HIMF is poorly constrained below $10^8 M_\odot$.

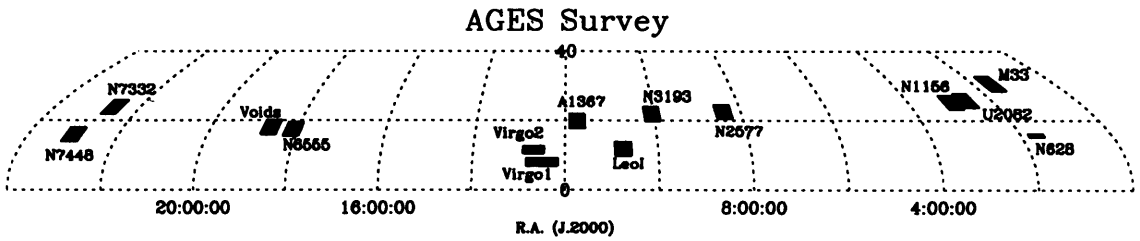

Figure 3.3: A northern sky map showing the location of the AGES fields.

3.4.1 Precursor observations: NGC 628

This galaxy group is centred around a large, face-on spiral, NGC 628 and the peculiar spiral NGC 660. NGC 628 is associated with several companions: UGC 1104, UGC 1171, UGC 1176(DDO13), UGC A20 and KDG10. NGC 660 also has a couple of companions: UGC 1195 and UGC 1200. Most of the companions are star forming dwarf irregulars and together these galaxies form a gas-rich group analogous to the Local Group (Sharina et al., 1996).

These observations were part of the AGES precursor observations to test different observing strategies, noise behaviour, data reduction etc. The group was chosen for its proximity to the Milky Way (9.3 Mpc, Hendry et al. 2005), its gas-rich nature and the presence of a low mass object: dw0137+1541 ($M_{HI} = 7 \times 10^6 M_\odot$). There are also a significant number of previous comparison measurements. These features made the group a natural target for precursor observations. The area surveyed was $5° \times 1°$.

3.4.2 The Virgo cluster

Two regions of the Virgo cluster have been selected to make a comparison of the H I properties of cluster galaxies with those in the field. Both regions avoid the

inner 1° of the cluster as the large continuum source associated with M87 limits the dynamic range in the area of about 1° around it. In any case, previous observations indicate very little H I within the cluster core (Davies et al. 2004).

The first region is 10°×2° centred on $(\alpha, \delta) = 12^h\ 30^m\ 00^s$, 8° 00′ 00″. This region will be imaged as part of the UKIDSS large area survey (Lawrence et al. in prep.) in J, H and K bands. In addition deep B-band images of the region have already been taken with the Isaac Newton Telescope, on La Palma. To complement these data, this region has also been observed by GALEX (Martin et al. 2005) in the near (2300 Å) and far ultraviolet (1500 Å) in the summer of 2006. NIR bands are less susceptible to extinction and are thus more accurate measures of stellar mass. Optical-NIR colours can also be used for studying galaxy metallicity and star formation histories. UV is a tracer of ongoing star formation and will allow comparisons of the current star formation rates with integrated star formation histories. The UV is also useful for searching for signs of star formation in tidal features.

The second region is a 5°×1° E–W strip centred on $(\alpha, \delta) = 12^h\ 48^m\ 00^s$, 11° 36′ 00″. This strip extends radially towards the cluster edge and will be used to observe changes in galaxy properties with radius from the cluster centre, expanding on the work of Sabatini et al. (2003). This strip extends through the galaxy grouping known as sub-cluster A that is associated with M87 (Binggeli, Popescu & Tammann 1993). The results of these observations will be useful for comparing with models of how the cluster environment affects galaxy evolution (tidal stripping, ram pressure stripping etc.).

The aim is to also search for low mass galaxy companions or cluster dwarf galaxies as well as previously unidentified H I clouds. Another interesting study will be to

see how baryonic material (stars, X-ray gas, neutral gas) in the cluster is distributed and compare this with the environment surrounding field galaxies.

3.4.3 The local void

A 5°×4° region centred on $(\alpha, \delta) = 18^h\ 38^m\ 00^s$, 18° 00′ 00″has been selected to search for H I signatures that might be associated with very low surface brightness galaxies or with H I clouds devoid of stars. The properties of galaxies detected will provide an interesting comparison with those in more dense environments.

3.4.4 M33 and the Perseus-Pisces filament

This will comprise a 5°×4° region centred on $(\alpha, \delta) = 01^h\ 34^m\ 00^s$, 30° 40′ 00″. The aim is to map in detail the environment of M33 to search for tidal bridges, HVCs etc. that are signatures of diffuse hydrogen in the Local Group. Westmeier, Braun & Thilker (2005) and Braun & Thilker (2005) have already observed numerous HVCs around M31 and M33, as well as an H I bridge connecting M31 and M33.

M33 will occupy about 1 sq. deg. at the centre of the field. At the distance of M33, the ALFA beam width (3.4′) will be about 0.6 kpc, providing superb spatial resolution. The H I mass sensitivity will be as low $2\times10^4 M_\odot$. The Perseus-Pisces filament will become visible behind M33 at approximately 4000–6000 km s^{-1}.

3.4.5 The cluster A1367

A1367 is a spiral-rich, dynamically young cluster at a velocity of around 6500 km s^{-1}, and is currently forming at the intersection of two large scale filaments (Cortese et al. 2004). Recent optical and X-ray observations (i.e. Gavazzi et al. 2001; Sun & Murray, 2002) suggest that ram pressure stripping and tidal interactions are strongly affecting the evolution of cluster galaxies, making this cluster the ideal place to study the environmental effects on the gas content. The whole cluster will just about fill a 5°×4° region centred on $(\alpha, \delta) = 11^h\ 44^m\ 00^s$, 19° 50′ 00″. Given the morphology of the cluster many detections are expected, including new objects that are more prominent in H I than other wavelengths. The H I mass detection limit at this distance will be approximately 2×10^8 $M_\odot$.

3.4.6 The Leo I group

This group lies at about 1000 km s^{-1} and a 5°×4° region centred on $(\alpha, \delta) = 10^h$ $45^m\ 00^s$, 11° 48′ 00″will be surveyed. The group is of particular interest because of the relatively large number of early-type galaxies (e.g. NGC 3377 & NGC 3379) and will make a good comparison with spiral rich groups. A lower H I mass limit of $\sim 2 \times 10^6$ $M_\odot$ should be possible at the adopted distance of 10 Mpc.

3.4.7 The NGC 7448 group

NGC 7448 is a Sbc spiral galaxy at a velocity of $\sim$ 2200 km s^{-1}, with a number of late and early type companions. The group will serve as a good contrast to the Leo I group. A 5°×4° area centred on $(\alpha, \delta) = 23^h\ 00^m\ 00^s$, 15° 59′ 00″will be studied.

At the distance of this group (30.6 Mpc) the H I mass limit should be 1.8×10^6 $M_\odot$.

3.4.8 The NGC 3193 group

NGC 3193, in contrast to NGC 7448, is an elliptical galaxy and there are another 9 known group members all part of a well defined galaxy filament. NGC 3193 has a velocity of 1362 km s^{-1} and the survey area will comprise a $5°\times4°$ region centred on $(\alpha, \delta) = 10^h\ 03^m\ 00^s$, $21°\ 53'\ 00''$. The lower H I mass limit at this distance (18.9 Mpc) will be approximately 7.0×10^6 $M_\odot$.

3.4.9 Individual galaxies

This will consist of observations of pairs of galaxies (principle galaxy either early or late type) and very isolated galaxies such as NGC 1156 and UGC 2082. NGC 1156 has no neighbouring galaxies within 10° (Karachentsev, 1996), UGC 2082 has no neighbour within 5 ° in the Nearby Galaxies Atlas (Tully & Fisher, 1987). Details are shown in Table 3.2.

3.4.10 AGESVOLUME

In addition to the data collected from the targets mentioned above, the large system bandwidth (100 MHz) simultaneously samples a much deeper volume of the universe. This allows for a blind search for more distant galaxies along the line of sight out to $cz \sim 19000$ km s^{-1}. The detection limit at this distance will be $M_{HI} = 1.4 \times 10^9 M_\odot$. This is the AGESVOLUME and will be a very important

part of the project, providing information on the HIMF, the baryonic mass density of neutral gas and the distribution of H I.

3.5 Observing strategy

A number of observing strategies were considered for the survey, which involved pointed observations, drift scanning, driven scanning techniques or combinations thereof. The successful observing method had to strike the right balance between data quality and observing efficiency.

Giovanelli et al. (2005) describe in detail an observing mode known as drift scanning. As the name suggests, the array is kept at a fixed azimuth and elevation while the sky drifts overhead. The benefits of this technique are that the telescope gain and sidelobe structure remains constant, while the system temperature only varies slowly over the course of a single scan. Standing waves set up between the receiver and the dish cause ripples to appear in the spectrum baseline. These waves are quasi-periodic and depend on the polarisation, the geometry of the dish and the location of continuum sources in the main beam and sidelobes. Hence each beam and polarisation will have a different baseline ripple at any given time. This baseline ripple can cause confusion with low signal sources so limiting its effect is highly desirable. The drift scan technique has the advantage that this ripple is more or less constant over the course of the scan. It is then possible to accurately estimate the ripple and remove it from the data during the data reduction. The benefits made the drift scan highly desirable for AGES.

The Earth's rotation rate governs the on-source time in a drift scan. For Arecibo this means that each point in the sky takes 12s to cross the beam at 1.4 GHz. 25

Table 3.2: H I Survey fields for individual galaxies.

Galaxy	RA ($h\ m\ s$)	dec. ($^\circ\ '\ ''$)	Type	V_{sys} (km s^{-1})	Distance (Mpc)	H I mass limit ($M_\odot$)	Comments	Survey area
NGC 6555	18 06 00	17 30 00	Sc, face-on	2225	30.9	1.9×10^7	paired with NGC 6548	5°×4°
NGC 2577	08 24 00	22 30 00	S0	2057	28.6	1.6×10^7	paired with UGC 4375	5°×4°
NGC 7332	22 36 00	23 48 00	S0 (pec)	375	5.2	5×10^5	paired with NGC 7339	2.5°×2°
UGC2082	02 36 00	25 48 00	Sc, edge-on	696	9.7	1.8×10^6	very isolated	2.5°×2°
NGC 1156	03 00 00	25 12 00	Irr	375	5.2	5×10^5	very isolated	2.5°×2°

separate scans are then required per point to reach the 300s integration time. Since the technique used in ALFALFA only allows for scans taken along the meridian (Giovanelli et al. 2005) it was necessary to adapt the method to allow scans before and after transit, and hence build up sky coverage more quickly.

In order to compensate for the change in parallactic angle, and thus achieve uniform sky coverage, ALFA must be rotated before every scan. The geometry of the Gregorian system projects a slightly elliptical beam pattern on the sky. The projected beams are also slightly elliptical (see Fig. 3.1). As a result of these effects, once the array is rotated to produce equidistant beam tracks, the beam separation is slightly larger than that required for Nyquist sampling. To attain fully sampled sky coverage it is necessary to stagger the declination of individual scans by $\sim 1'$ (half the beam separation). An IDL routine has been developed to calculate the rotation angle and the starting coordinates and LSTs in advance of every observing run. This staggering is arranged such that every beam covers the same patch of sky helping to combat variations in gain between the beams. Another benefit of this method is to reduce the impact of sidelobe contamination. This effect is discussed separately in the next section.

3.6 Data reduction

Data reduction was performed using the AIPS++ packages LIVEDATA and GRIDZILLA (Barnes et al. 2001), developed by the Australian Telescope National Facility (ATNF). These packages were originally designed for the HIPASS and HIJASS surveys but were modified to accept the Arecibo CIMAFITS file format. LIVEDATA performs bandpass estimation and removal, Doppler tracking and calibrates

the residual spectrum. It also has the ability to apply spectral smoothing if required.

Bandpass calibration can be performed using a variety of algorithms, all based around the median statistic. The median has the advantage that it is more robust to outliers than the mean statistic. This property makes the median estimated bandpass more resistant to radio frequency interference (RFI). Thanks to the sophisticated monitoring system at Arecibo, it was not necessary to process the data in real time as in HIPASS.

The process itself involves bandpass calibration and removal for each scan individually. First a calibration source (hot diode) of known temperature was fired into the beam at the beginning of every scan. From LIVEDATA the user selects the amount of data that will be used to calculate the reference bandpass and also the size of the target window. The drift scan technique ensured that the bandpass shape was constant over an entire AGES scan, which allowed for use of the whole scan as a reference bandpass. The bandpass was calibrated and estimated for each integration. The target window defined all those data to be excluded from forming the reference bandpass, i.e. all those within the beam area.

Once the bandpass was calibrated and removed from each spectrum, the user then had the option of fitting a polynomial to the residual spectrum. It is desirable to keep the order of this polynomial as low as possible to avoid removing real, physical signals from the spectrum or introducing fake ones. For AGES data it was found that a first order polynomial was sufficient to produce a flat, zero baseline for all but the brightest continuum sources.

Digital sampling produces high frequency artefacts known as Gibbs ringing for

very bright narrow sources such as Galactic H I. This has a very well defined *sinc* function shape and can extend over a large number of channels. This is easily attenuated by using an appropriate filter on the data. In LIVEDATA the user has the option of using the Hanning filter or Tukey filter. Each produces a different result – the Hanning filter is much better at removing the ringing, but at the expense of degrading your spectral resolution to twice to original channel width. The Tukey filter is not as good at suppressing ringing, but the spectral resolution is only degraded to roughly 1.6 times the original channel width. The spectral resolution of raw AGES data is so fine (5.1 km s^{-1}) that the spectral degradation caused by applying the Hanning function was considered an acceptable compromise for the improved suppression of ringing and was therefore applied.

GRIDZILLA is a gridding package that co-adds all the spectra using a suitable algorithm, to produce 3-D datacubes. The user has full control over which beams and polarisations to select, the frequency range, the image size and geometry, pixel size and data validation parameters as well as the gridding parameters themselves. Various weighting functions are available for gridding the data. The output datacube has two spatial dimensions and the spectral dimension can be chosen by the user to be frequency, wavelength or velocity (numerous conventions are available for each choice). Full details of the bandpass estimation and gridding technique are given in Barnes et al. (2001). For the AGES data 1′pixels provided a compromise between resolution and sensitivity. The data were weighted inversely to the response of the beam (which was judged to be Gaussian) over a 3′radius round each pixel. In order to conserve flux, the values were then normalised.

The sidelobes for the central beam are symmetric, while sidelobe levels for each of the outer beams are highly asymmetric, as shown in Fig. 3.2. The ability to detect low column density emission could be highly affected if they are not corrected for,

particularly near bright or very extended objects. In the final, gridded data, each beam has contributed equally to each pixel apart from at the extreme edges of the map where sky coverage is not complete. Fig. 3.2(b) highlights the radial alignment of the peaks of each of the sidelobes. When median gridding is applied this means that in order for a pixel to be significantly contaminated by sidelobe emission, the source must appear in more than three of the beams. Point sources can therefore be considered free of sidelobe contamination. It should be noted that there is likely to be some low level contamination in extended objects and we are investigating ways to reduce this.

3.7 Data analysis

The data analysis broadly falls into two parts: analysis of the target objects and analysis of background objects. For each sample, the H I was compared with the optical, NIR and any UV data that was available at the time of writing. Descriptions of the techniques used are now given.

3.7.1 H I data

For targeted objects, the H I data analysis was performed in a similar manner to that of Chapter 2. A mask was created by smoothing the original data to twice the beam size and the galactic emission was clipped at 2.5 σ. This mask was applied to the original cube to isolate all the H I emission from each member located within the target region. Correlated noise peaks were judged by eye from the masked cube and removed from further analysis using the GIPSY routine BLOT. Then moment maps were constructed for each galaxy.

Moment 0 maps represent the integrated H I flux over the velocity extent of the emission. They were constructed to illustrate the H I distribution over the channel range occupied by each galaxy. This requires the addition of typically several channels or more. The noise in each pixel of the moment 0 map depends on how many channels contributed to it. The brighter pixels are therefore more noisy. The noise contribution σ_n is proportional to $\sqrt{n}$ where n is the number of contributing channels *only* if the channels are independent of one another. This is not the case for AGES data – Hanning smoothing was applied during the data reduction process and so the noise in each channel is correlated with the adjacent channels. In this case it can be shown that the noise, σ_H increases as:

$$\sigma_H \propto \frac{4}{\sqrt{6}}(\sqrt{n - 0.75}) \tag{3.1}$$

The GIPSY routine STAT was used to find the number of pixels that contributed to each pixel in the moment 0 map and build a noise map for each galaxy. This was then used to isolate the 3σ values in the moment 0 map. The mean of these values was then taken as the representative 3σ value for the whole map. The integrated flux values were then converted into column densities using Eqn. 1.14.

Where the galaxy was resolved, moment 1 maps were also produced. These represent the intensity weighted velocity distribution of the gas – the velocity field. The contours represent lines of iso-velocity and allow measurements of the kinematics of the system. In addition to the maps, H I velocity profiles (summed flux per channel) was also constructed.

Positions were found from applying the fitting routine IMFIT within MIRIAD to the flux map integrated over the galaxy's velocity extent. Uncertainties are shown

in brackets after each measurement. Positional uncertainties for AGES data were estimated from fitting NRAO VLA Sky Survey (Condon et al., 1998) sources to a continuum map produced from our data. For AGES, positions of NVSS sources were found to be accurate to within $\pm 30''$. Uncertainties in position from the HIPASS data were taken from Zwaan et al. (2003). The AGES positions agree with HIPASS and previous measurements to within the measured uncertainties.

The uncertainties in each of the H I properties depend on the S/N of the source, the velocity width of the source, the velocity resolution and the shape of the spectrum. An excellent summary of techniques for estimating the uncertainties in these H I properties is given in Koribalski et al. (2004) and references therein. The uncertainty in the integrated flux density is given by

$$\sigma(F_{HI}) = 4 \times SN^{-1}(S_{peak} F_{HI} \delta v)^{1/2} \tag{3.2}$$

where S_{peak} is the peak flux, SN is the ratio of S_{peak} to $\sigma(S_{peak})$, the uncertainty in S_{peak}. F_{HI} is the integrated flux and δv is the velocity resolution of the data. $\sigma(S_{peak})$ is found to increase in extended sources, regions of high 20-cm continuum emission and it also increases with rising flux density values. We adopt the estimate of Koribalski et al. (2004) that $(\sigma S_{peak})^2 = \mathrm{rms}^2 + (0.05\ S_{peak})^2$, where rms is the root mean square flux value for a blank patch of sky.

The uncertainty in the systemic velocity is given by:

$$\sigma(V_{sys}) = 3 \times SN^{-1}(P \delta v)^{1/2} \tag{3.3}$$

where $P = 0.5 \times (W_{20} - W_{50})$, which is simply a measure of the steepness of the profile edges. Errors in the widths are given by $\sigma(W_{50}) = 2 \times \sigma(V_{sys})$ and

$\sigma(W_{20}) = 3 \times \sigma(V_{sys})$. Distances are based on pure Hubble flow and the associated errors arise from the errors in the integrated flux.

3.7.2 Optical data

The optical data available for analysis was varied at the time of writing. SDSS optical photometry and spectra were available for only a small fraction of the NGC 628 sample. Optical spectra were also obtained by L. Cortese for several of the galaxies for which there were no previous spectral line measurements. The data were taken using a dispersion grism on the 1.5 m telescope Loiano observatory during 2006. The frames were bias-subtracted and flat–fielded. No flux calibration was applied since only the redshift information was sought. A template spectrum from a Ar-He lamp was used to create a calibration mask for the entire frame. Once calibration had been performed, the sky was subtracted to minimise the impact of contaminating night sky lines in the region 7000–8000 Å. The final 1-D spectrum was then produced by integrating over the pixels that were judged to contain galactic emission. Standard routines in IRAF were used throughout.

In addition deep g- and r-band images were acquired from MEGACAM on the CFHT for the central square degree of NGC 1156. Data reduction was performed onsite using the ELIXIR data reduction package used for all MEGACAM data. Aperture photometry was then performed with DS9 . In the absence of other optical observations, POSSII data were used from the SuperCOSMOS website.

3.7.3 Data from other wavelengths

NIR observations are planned using the UKIRT telescope. At the time of writing these observations have not been performed and NIR analysis is limited to the fairly shallow 2MASS data. GALEX data provides both near and far UV images for the central square degree of NGC 1156, the NGC 628 field has not yet been observed.

Having established the survey, data reduction and analysis tools, the results from this search for dark galaxies are now presented for NGC 628, NGC 1156 and more briefly, Abell 1367.

Chapter 4

Results

Based in part on the results of a paper written by R. R. Auld et al. Monthly Notices of the Royal Astronomical Society, 2006, vol. 371, p. 1617

4.1 Introduction

The search for dark galaxies begins with the precursor observations of the NGC 628 group. The precursor observations had to serve several purposes. Of great importance was to show that the adopted survey strategy was providing uniform sky coverage. Uniform coverage ensures that the sensitivity is uniform throughout the data and therefore instils confidence in the calculated survey volume. The survey volume is essential for putting constraints on the number density of dark galaxies and calculating the HIMF for the data. Integration time was built up by co-adding successive survey scans. The corresponding noise should decrease as the square root of the integration time, so knowledge of how the noise was behaving

with the addition of more scans was also important.

A study of the baselines was important in ascertaining how big the impact of baseline ripples would be in the final data. Also important was an investigation into how Radio Frequency Interference (RFI) was affecting the data. All these different aspects were vital for the future performance of the survey, so some time is dedicated to them before moving on to the H I data itself.

The H I properties of galaxies found in the survey are presented in conjunction with optical data that was acquired from SDSS, from the SuperCOSMOS website, or from the 1.5 m telescope at Loiano and NIR data was collated from the 2MASS website.

The search is then expanded to include the region surrounding NGC 1156. This was the first AGES field that reached the full depth of the survey. It was also the first field to be accompanied by deep optical data from the 4 m CFHT. This search has revealed two possible dark galaxy candidates, which will be discussed in more detail. Again, H I and optical data are presented for all galaxies found.

4.2 The NGC 628 group

The derived distance for NGC 628 has been debated for some years. Early attempts using optical data gave a distance of 19.6 Mpc (Sandage & Tammann, 1974). Later analyses based on the spectral line measurements revealed that the recessional velocity of NGC 628 is ~660 km s^{-1} (Huchra, Vogeley & Geller, 1999; de Vaucouleurs et al. 1991; Kamphuis & Briggs, 1992). This places it at approximately 9 Mpc away (assuming no peculiar motion and H_o = 75 km s^{-1} Mpc^{-1}). The most re-

cent estimate using supernova measurements (Hendry et al. 2005) gives a distance measurement of 9.3±1.8 Mpc, in line with the spectral line measurements.

NGC 628 has a very narrow velocity width, $W_{50} = 56$ km s^{-1} (Kamphuis & Briggs 1992). It is close enough to allow detection of low-mass H I objects with only $M_{HI} \gtrsim 2 \times 10^6 M_\odot$ of neutral hydrogen, but separated enough from local Galactic gas to be able to detect any high velocity gas associated with the galaxy. Kamphuis & Briggs (1992) looked at this galaxy at 21cm with the VLA and discovered high velocity gas on the outskirts of NGC 628 but nothing that could be considered HVCs. A few years earlier another survey (Briggs, 1986) revealed a new, low-mass companion, dw0137+1541 ($M_{HI} = 7 \times 10^6 M_\odot$). This group has also been covered by the HIPASS northern extension (Garcia et al. 2007 in prep.). The interesting aspects of the group and the availability of comparison observations from other instruments made it a natural choice for precursor observations using a new instrument.

4.2.1 H I observations

The observations were taken using the 305 m radio telescope located at Arecibo, Puerto Rico. AGES was allocated a total of 86 hours which was split between different observing strategies, as part of a 'shared risk' strategy. The drift scan observations received 42.5 hours and the results presented here represent these observations only. The observations were taken over 22 nights between November 19th 2004 and December 18th 2004. No radar blanking was used because it was not functional at the time, leading to several sources of RFI as discussed later. System malfunctions were inevitable during a testing run such as this, but only four nights' of observing were affected. This corresponded to approximately 10

hours lost time.

A 5°×1° field was chosen centred on a position halfway between NGC 628 and the nearest dwarf UGC 1176 (Fig. 4.1). The region includes NGC 628, UGC 1176, UGC 1171, KDG010 and dw0137+1541. The observing band was centred on 1381 MHz, giving a heliocentric velocity range of -2270 km s^{-1} to $+20079$ km s^{-1}. The roll off at the edge of the bandpass due to the filter reduces the sensitivity for about 1000 km s^{-1} at either end.

The strategy consisted of two sets of scans. The first set covered the entire field on one night while the second set were offset by half a beam width as shown in Fig. 4.2. This observing strategy differs slightly from that described in the previous chapter since in this technique individual points in the sky are only covered by one or two beams. This was a necessary sacrifice since the tools that assisted in the design of the survey strategy were still in development at the time of the observations.

Observations were planned such that the central drift scan was always conducted close to the meridian. Due to the time limits imposed by the telescope schedule, this often meant only four of the five scans were completed. With the available time most of the region was covered to a uniform depth using 16 nights' data. Due to observing constraints, the region north of 16° 06′ 00″ was often omitted from the observing run, and hence this region was only observed successfully on 6 nights. This is illustrated by Fig. 4.3, which shows the number of spectra contributing to each pixel in the final, gridded data. This was reflected in the noise quality of the final data which was significantly poorer for the more sparsely covered region (above ~16°06′00″). Calibration was performed at the beginning of every scan using a high-temperature noise diode that was injected into the beam for a duration

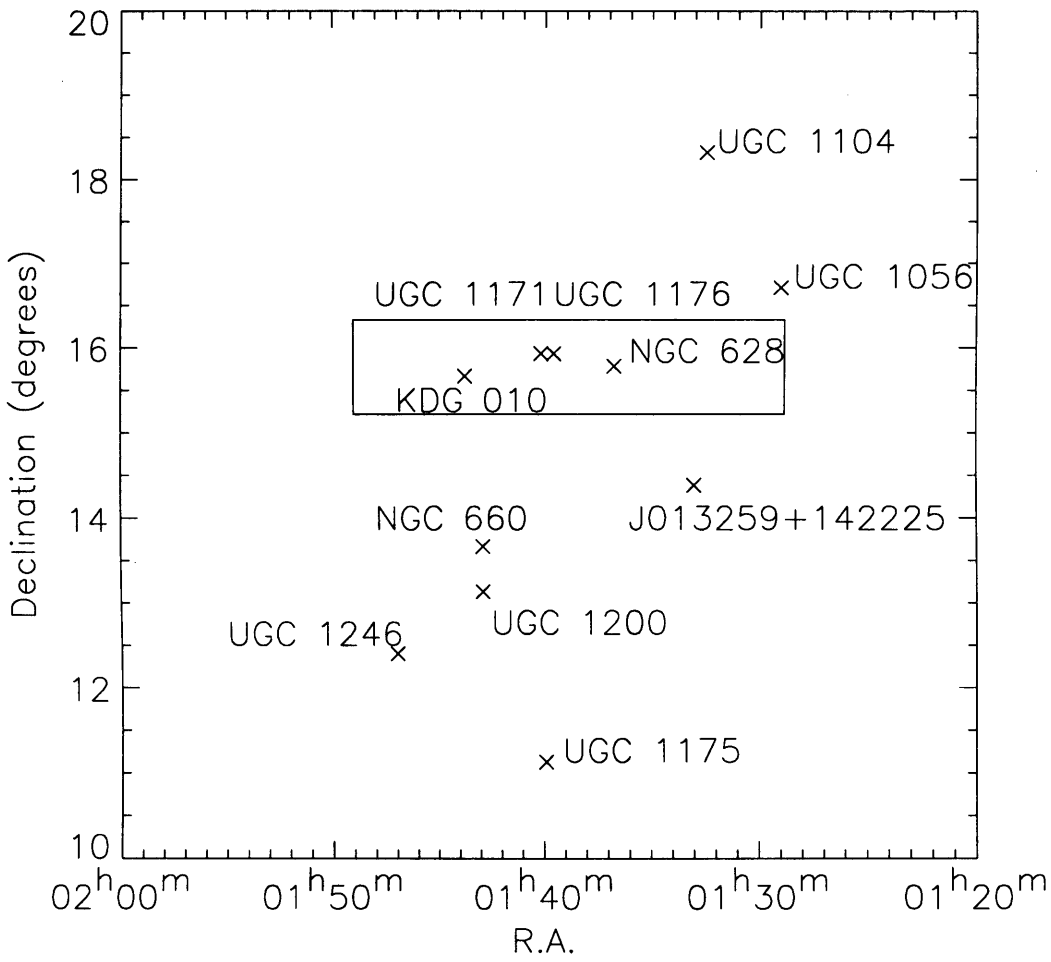

Figure 4.1: The NGC 628 group with the observed field outlined. Group members are denoted by a cross, dw0137+1541 has not been included due to its proximity to UGC 1176 and UGC 1171.

of 1s. The total power output for each of the 7 beams, both polarisations and 4096 channels was integrated every second and recorded as 4-bit floating point numbers. Over a 20 minute drift scan this equates to a total file size of ~395 Mb.

After data reduction, the resulting FITS datacube from GRIDZILLA has dimensions of RA, dec and velocity/frequency. The $5° \times 1°$ region was gridded using a median gridding technique into $1' \times 1'$ pixels, each of which contains a 4096 channel spec-

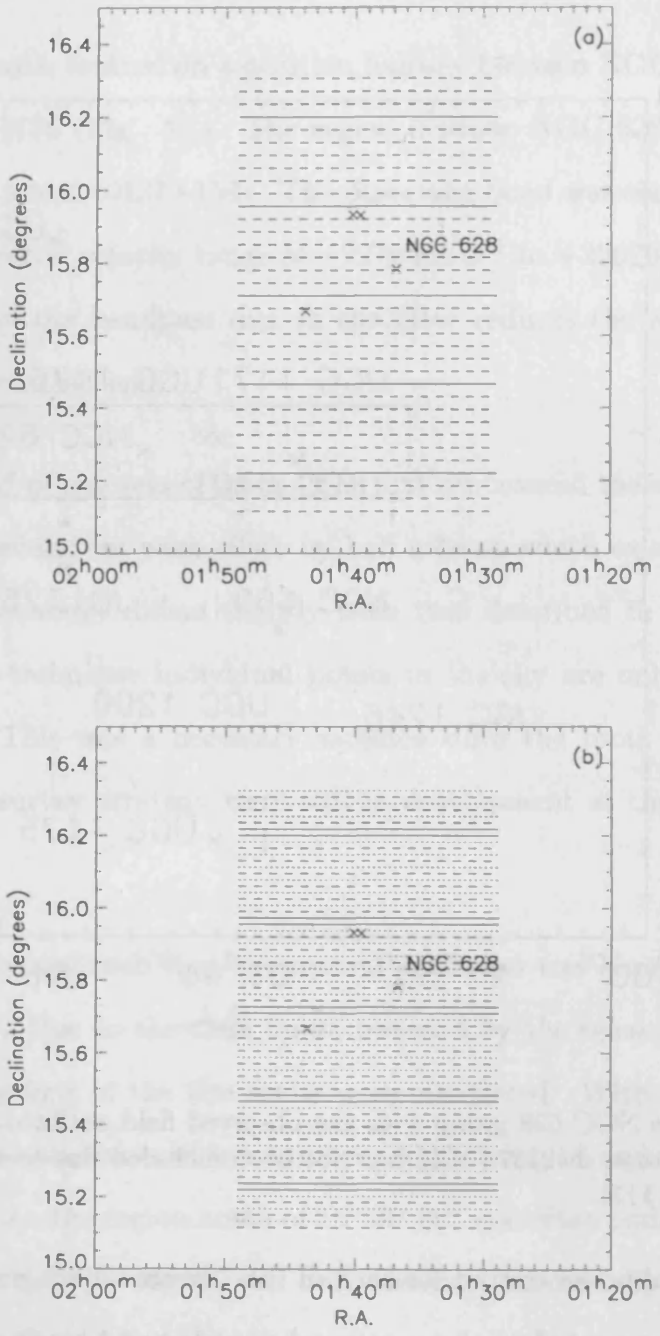

Figure 4.2: An illustration of how the sky coverage is built up over two nights of observations. The declination axis has been stretched for convenience. The solid lines represent the central beam tracks, the dashed lines mark the outer beam tracks. On the first night (a), 5 separate drift scans are performed to cover the $5° \times 1°$ area. On the second night (b), exactly the same pattern is reproduced offset by half the beam separation (the outer beams from the second night are denoted by dotted lines). On subsequent nights the two patterns are alternated to build up integration time and also maintain uniform sky coverage. Due to observation scheduling it was often necessary to drop the northern-most scan. Galaxies are marked with a cross, with NGC 628 marked for guidance. Refer to Fig. 4.1 to locate other group members.

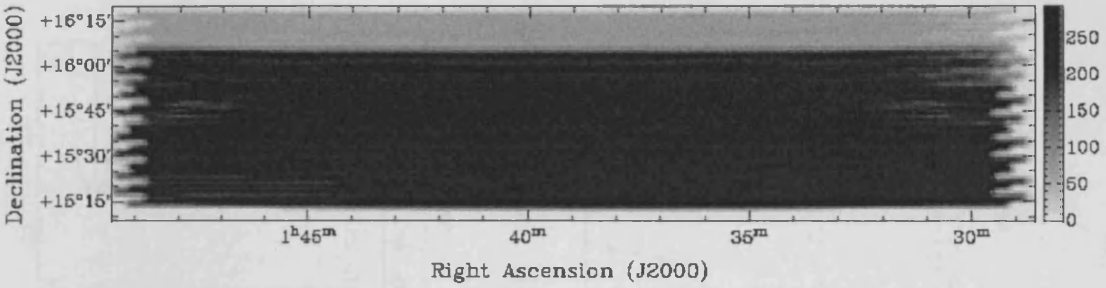

Figure 4.3: A map showing the sky coverage in the final data. The number of spectra that contributed to each pixel is shown as a grey-scale from least (light), to most (dark). The region above 16° 06′ 00″ was less well covered than the remaining region due to observing time constraints.

trum. This produced a ~365 Mb file. Initial investigations of the effects of RFI and the behaviour of noise in the data were conducted using IDL. Detailed analysis of the NGC 628 group was performed using MIRIAD, GIPSY and KARMA.

Radio Frequency Interference (RFI)

Man-made RFI is now, unfortunately, a constant source of contamination at most radio observatories. At Arecibo in the *L*-band there are a number of RFI sources. The L3 GPS satellite appears at approximately 1381 MHz. There are also several narrow contributions from aircraft radar at FAA and Punta Salinas in the range 1200–1381 MHz. While RFI from Punta Salinas was not noticed during the observations, two sources were noticed at 1350 MHz (FAA radar) and 1381 MHz (L3 GPS). These interference sources were present throughout the observing runs but other sources were only noticed occasionally. The median filtering applied by LIVEDATA and GRIDZILLA is very robust to intermittent sources of RFI but can do nothing for constant sources. As a result several channels were contaminated around 1351 MHz and 1381 MHz. These channels were included in the final data, to allow for the possibility of detecting bright sources that might still be visible.

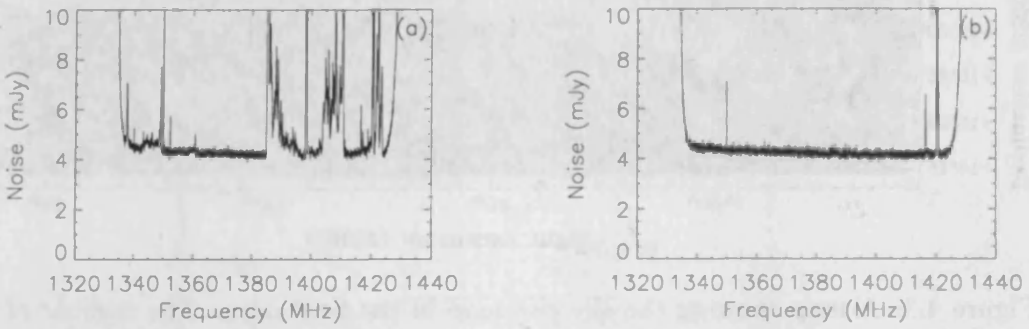

Figure 4.4: The impact of the persistent, frequency-varying RFI on the data quality. Each figure shows the rms noise per channel from observations on consecutive nights (a) with the interference present and (b) without the interference. Both datasets represents averages taken over the same source-free patch of sky.

In addition to these sources of RFI there was also a varying source. While the RFI was quite narrow, usually occupying a few channels, it would shift frequencies in a quasi-periodic fashion contaminating up to 60 MHz of the band. There was also a harmonic that would drift in an out of the observed bandwidth. Figs. 4.4(a) & 4.4(b) are two graphs showing the flux per channel of the final data, for two identical, empty regions of sky taken over two consecutive nights. The first night's data are contaminated by this transient RFI source, the second night's data are free of it. The effect on the quality of the final data is significant, causing a rise in the noise level throughout the band. The RFI source has been attributed to equipment in the focus cabin and has since been eliminated.

Noise behaviour

By combining multiple observations of the survey field it is possible to build up the effective integration time and hence increase the depth of the survey. One would expect that as more observations are taken, the noise level in the combined data

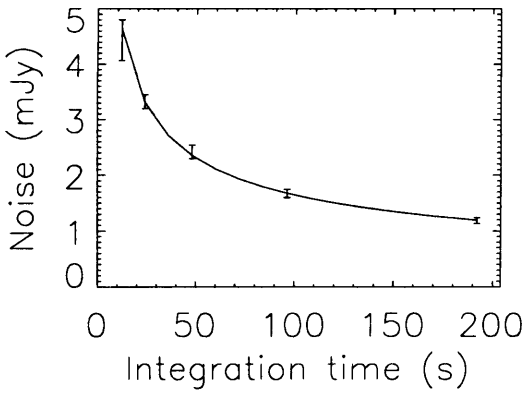

Figure 4.5: The effect of co-adding successive nights observations results in the expected reduction in the rms noise value, i.e. $\sigma \propto t^{-0.5}$.

should fall. Datacubes were produced for 1, 2, 4, 8, and 16 nights' observations. Since the integration time each night was the same (12s beam^{-1}), this was equivalent to 12, 24, 48, 96, and 192s beam^{-1}. A robust mean noise value was then calculated for each datacube, using the IDL astro library routine RESISTANT_MEAN within a large region of sky that didn't contain sources over the inner 3696 channels. The data were fitted using a least-squares fit. If the noise distribution is Gaussian, the mean level should be, $\sigma \propto t^{-0.5}$ where t is the integration time. Fig. 4.5 shows how the rms noise level varies with the integration time. The line fit indicates the noise decreases as $t^{-0.49\pm0.06}$ which is in very good agreement with the $t^{-0.5}$ dependence as predicted. This represents 16 nights' data which provided uniform coverage for most of the region. Following this predicted trend, a final noise level of 0.95 mJy beam^{-1} for a velocity resolution of 10.3 km s^{-1} could have been achieved if all 25 nights' observing (300s beam^{-1}) had been successful, which is consistent with the predicted noise level.

To investigate the Gaussianity of the noise in the final co-added data (t_{int} = 192s), a source-free region of sky was chosen and the noise in each channel for

each pixel was recorded. The values were binned into 100 equally spaced bins. The noise distribution about the mean value was then compared to a Gaussian distribution. The values lay very close to a Gaussian, distributed about zero (Fig. 4.6). From Fig. 4.6(b) there is a slight excess in noise at ~3.0 mJy ($\sim 3\sigma$) but this is statistically insignificant.

Baseline stability

The quality of the final data is highly dependent on the stability of the baselines. It is extremely important therefore to examine the baseline before any fitting is applied to it, and confirm that the drift-scanning technique is producing the stable baselines expected. Observations were chosen from a night in which there was no contamination by the persistent, variable RFI. Comparisons were then made from spectra taken at the beginning of a scan to those at the end of the scan.

Fig. 4.7 shows, for each individual beam and polarisation, the percentage difference between the first 100 spectra and the last 100 spectra within one scan. The baseline remains stable to within 0.1% over the duration of a scan.

4.3 H I results

The H I data were used to construct moment maps for each of the group galaxies using the methods described in the previous chapter. Moment 0 maps were constructed to illustrate the H I distribution over the channel range occupied by each galaxy. Where the galaxy was resolved, moment 1 maps (velocity fields) were also produced. These moment maps are shown in Figs. 4.8–4.11 and also include the

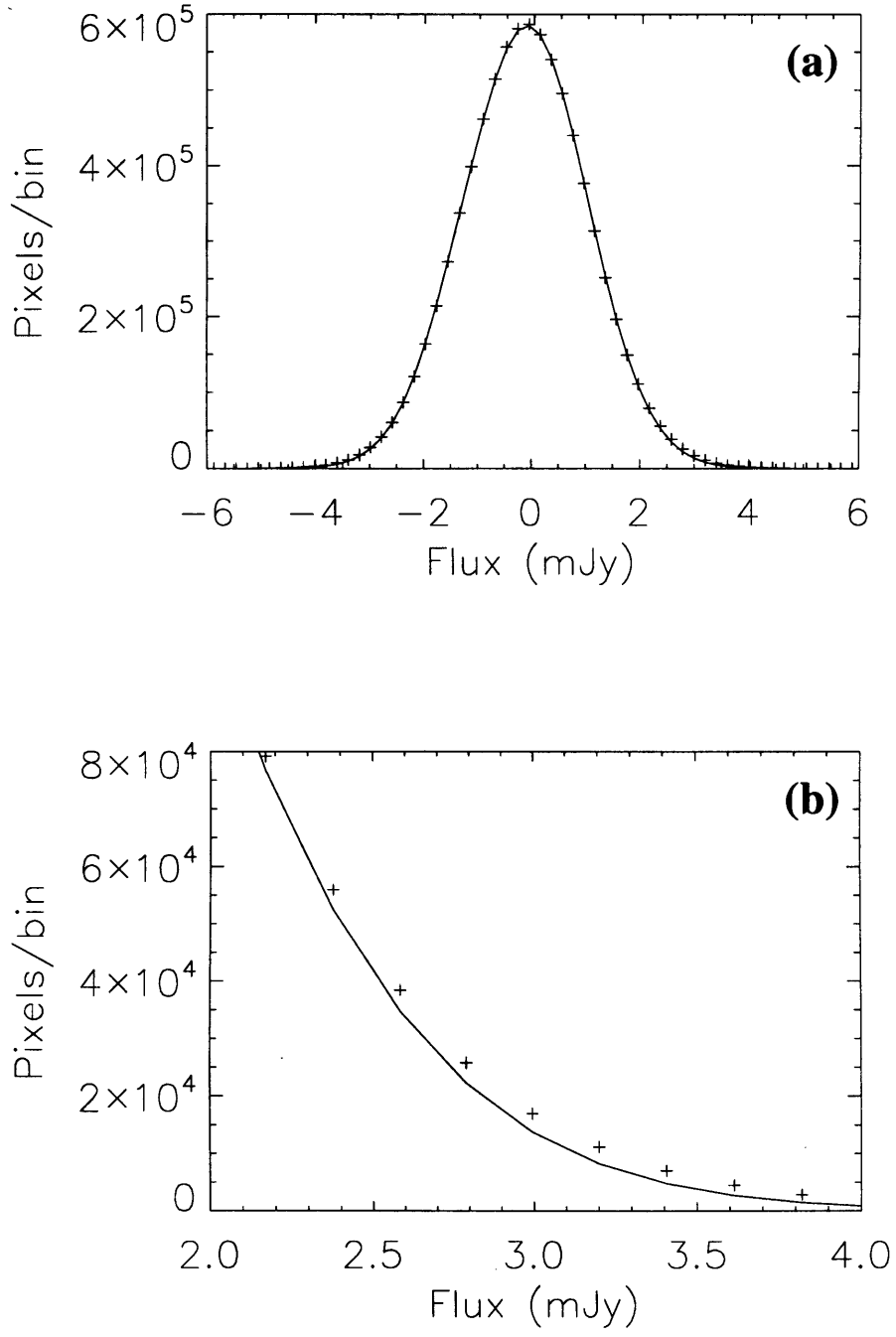

Figure 4.6: (a) The distribution of flux values within an apparently blank patch of sky in the reduced datacube is well fit by a Gaussian distribution, centred on -0.1 mJy. The data points are represented by crosses and the solid line is the Gaussian fit (b) There is a departure from Gaussianity between 2.5–4.0 mJy corresponding to 2.3–3.6σ. This is possibly due to very low-level sources within the region that were not detected by eye.

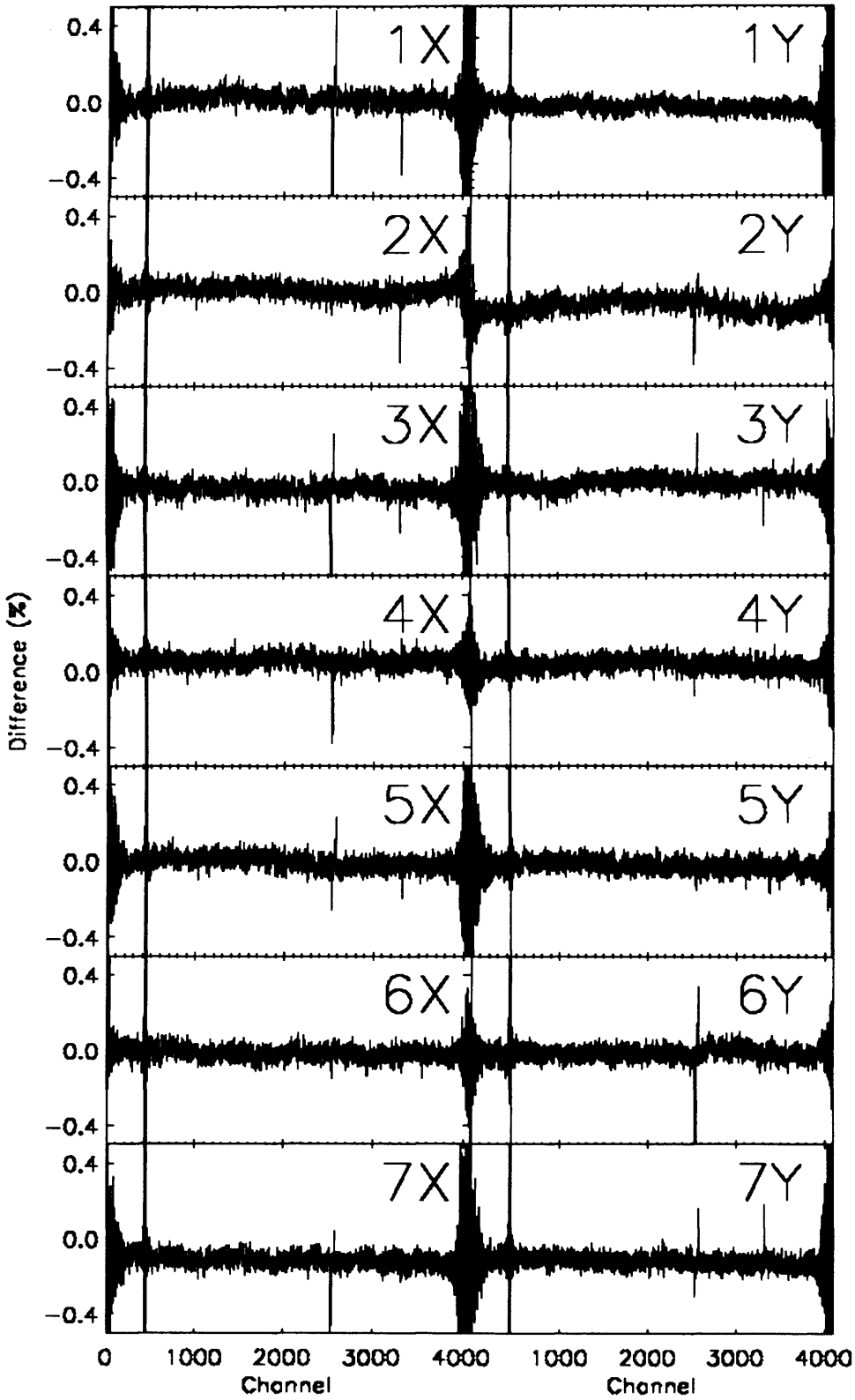

Figure 4.7: Percentage variation of the raw bandpass over a single scan for each individual beam and polarisation. Each raw bandpass remains unvarying to within ~0.1%.

velocity profile of each galaxy. An identical analysis was performed using HIPASS data from the northern extension for comparison purposes. None of the galaxies were resolved by HIPASS and so there are no velocity fields from HIPASS data.

NGC 628 was resolved by both HIPASS and AGES, UGC 1176 was resolved by only AGES. In these cases the 3σ column density limit is around 2×10^{18} cm^{-2} in the integrated H I maps for both HIPASS and the AGES precursor. The benefit of increased spectral resolution is immediately clear in the AGES velocity profiles. The improvement in spatial resolution is also highlighted by the detection of dw0137+1541. This dwarf is so close to UGC 1171 that it is indistinguishable from the larger galaxy in the HIPASS data but is clearly visible in the AGES data (Fig. 4.11b) at position $(\alpha, \delta) = 01h40m03s$, +15° 56′ 00″. Fig. 4.11(b) suggests that UGC 1171 & dw0137+1541 are embedded in a neutral gas envelope extending from northeast to southwest. This is probably the effect of beam smearing since there is no hint of extended emission in Briggs et al. (1986), but it is possible that it is real and has been resolved out by the synthesised beam of the VLA.

An important step is to compare the velocity profiles from AGES and HIPASS to see if the flux calibration is being performed correctly. From Figs. 4.8–4.11 the fluxes calculated from the AGES data are generally in agreement with the HIPASS data. The most probable reason for discrepancies is that the gridding technique responds differently to sources of different size and strength. The problem is that the gridding technique tends to overestimate the flux of extended objects (objects comparable to or larger than the beam size). This was an expected side effect of the gridding process and Barnes et al. (2001) simulated observations in the HIPASS data using sources of known flux and size to quantify the effect and calculate correction values. Another side effect of the technique is to produce larger gridded beam sizes for stronger sources (see Tables 2 & 3 in Barnes et al. 2001).

A similar analysis will need to be conducted for AGES, and is ear-marked for future work. In the absence of such analysis, the AGES fluxes were corrected as follows. First the ratio of the AGES source size to the AGES beam was found. The source size was measured from higher resolution H I data (Briggs, 1986; Kamphuis & Briggs, 1992). This ratio was multiplied by the HIPASS mean observing beam size (14.4′) to find the size of a hypothetical HIPASS source that would produce the equivalent source/beam ratio. Table 3 in Barnes et al. (2001) was then used to find the HIPASS flux-weighted beam area for this hypothetical source. The ratio of the HIPASS flux-weighted beam area to the mean observing beam area was then calculated. Finally the AGES observing beam area was then multiplied by this ratio to get the AGES flux-weighted beam area. The integrated flux was then simply the summed AGES flux from the source multiplied by the AGES pixel size divided by the AGES flux-weighted beam area.

There are other possible sources of uncertainty in the AGES data. The gain calibration did not take into account the telescope's response at different zenith angles - beyond a zenith angle of $\sim$15° the Arecibo 305 m dish is known to lose sensitivity since only part of the dish is illuminated. This effect was limited since very few scans were taken at zenith angles greater than 15°. The system temperature is also known to vary over the frequency range of the system which was not taken into account during the data reduction. Steps are underway to document these variations so that they may be included in future revisions of LIVEDATA and GRIDZILLA. As can be seen from Table 4.1 the AGES H I parameters compare well to those measured from HIPASS and also from other previous surveys (Kamphuis & Briggs, 1992; Briggs, 1986; Huchtmeier, Karachentsev & Karachentseva, 2003).

Table 4.1: H I measurements of the NGC 628 group.

Survey	RA (J2000)	DEC (J2000)	V_{sys} (km s^{-1})	W_{50} (km s^{-1})	W_{20} (km s^{-1})	F_{HI} (Jy km s^{-1})	M_{HI} ($\times 10^8 M_\odot$)
NGC 628							
AGES	1 36 41.9 (2.0)	15 47 44 (30)	657 (1)	56 (2)	73 (3)	510 (49)	130 (13)
HIPASS	1 36 42.0 (4.5)	15 47 34 (48)	654 (3)	50 (6)	75 (9)	435 (65)	111 (17)
Kamphuis & Briggs (1992)	1 36 42.0 (1.0)	15 47 12 (14)	657 (0.7)	56 (1)	—	470.1	120
KDG010							
AGES	1 43 34.9 (2.0)	15 41 48 (30)	789 (1)	34 (2)	49 (3)	3.6 (0.4)	0.9 (0.1)
HIPASS	1 43 46.5 (4.6)	15 42 48 (48)	787 (5)	27 (10)	45 (15)	2.8 (1.5)	0.7 (0.4)
Huchtmeier (2003)	1 43 37.2 (4.6)	15 41 43 (48)	788.9 (0.4)	32 (1.1)	—	2.35	0.6
UGC 1176							
AGES	1 40 06.0 (2.0)	15 54 45 (30)	630 (1)	36 (2)	54 (3)	32 (3)	8.1 (0.9)
HIPASS	1 40 08.4 (4.6)	15 55 06 (48)	628 (2)	40 (4)	58 (6)	30 (5)	7.7 (1.3)
Briggs (1986)	1 40 07.7 (1.0)	15 53 55 (14)	629 (1)	38 (1)	—	30.17	7.7
UGC 1171							
AGES	1 39 38.6 (2.0)	15 55 19 (30)	740 (1)	29 (2)	41 (3)	1.7 (0.2)	0.43 (0.06)
HIPASS	1 40 00.2 (4.6)	15 53 56 (48)	743 (2)	27 (4)	45 (6)	1.6 (1.3)	0.4 (0.3)
Briggs (1986)	1 39 44.2 (1.0)	15 54 01 (14)	740 (3)	23 (4)	—	1.80	0.5
dw0137+1541							
AGES	1 40 03.9 (2.0)	15 55 45 (30)	749 (1)	28 (2)	47 (3)	0.33 (0.09)	0.08 (0.02)
HIPASS	—	—	—	—	—	—	—
Briggs (1986)	1 40 09.2 (1.0)	15 56 16 (14)	750 (5)	23 (10)	—	0.27	0.07

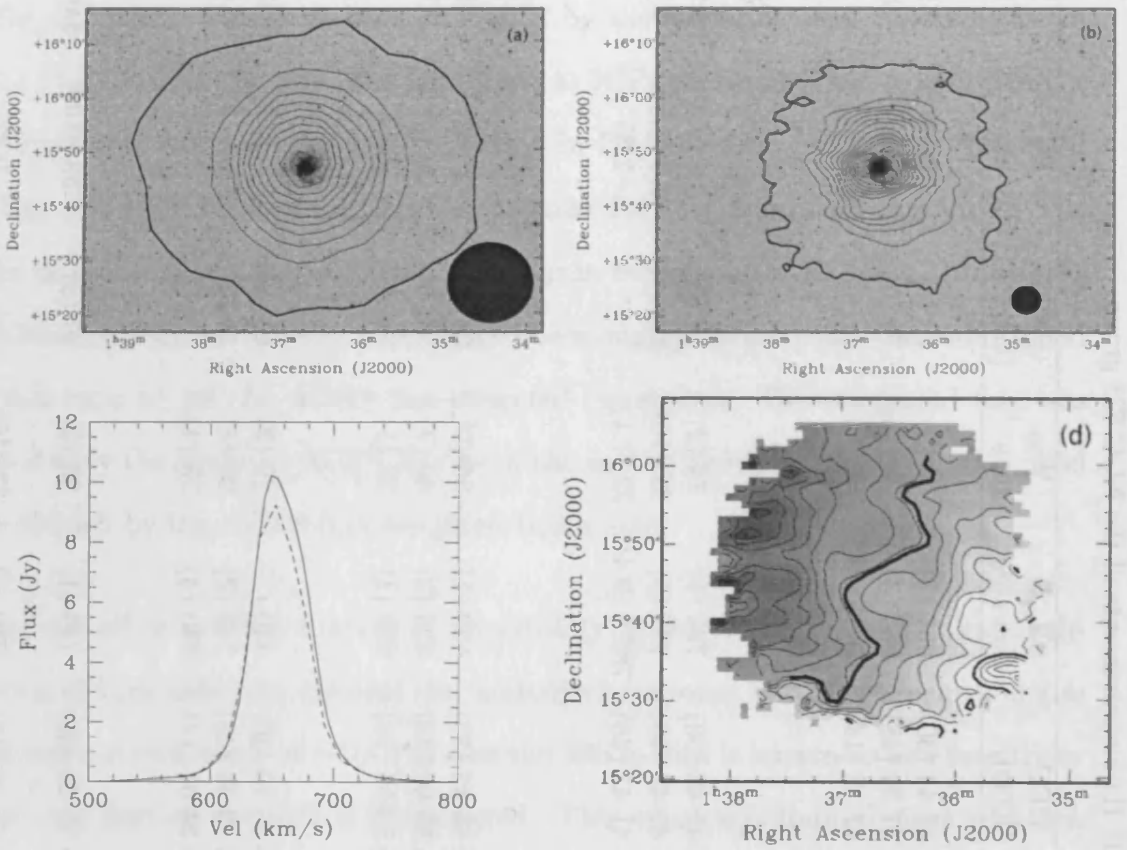

Figure 4.8: **NGC 628** (a) HIPASS H I contours overlaid on a POSS II image. Contours ($\times 10^{18}$ cm^{-2}): **2.8** (3σ), 50, 100, 150, 200, 250, 300, 350, 400, 450, 500. The solid circle illustrates the size of the HIPASS beam. (b) AGES H I contours overlaid on a POSS II image. Contours ($\times 10^{18}$ cm^{-2}): **2.2** (3σ), 100, 200, 300, 400, 500, 600, 700, 800, 900, 1000, 1100. The solid circle illustrates the size of the AGES beam.(c) H I velocity profiles: HIPASS is shown as the dashed line, AGES as the solid line. (d) Velocity field from AGES data. Iso-velocity contours increase from light to dark: 635, 640, 645, 650, 655, **659**, 660, 665, 670, 675, 680, 685, 690 km s^{-1}.

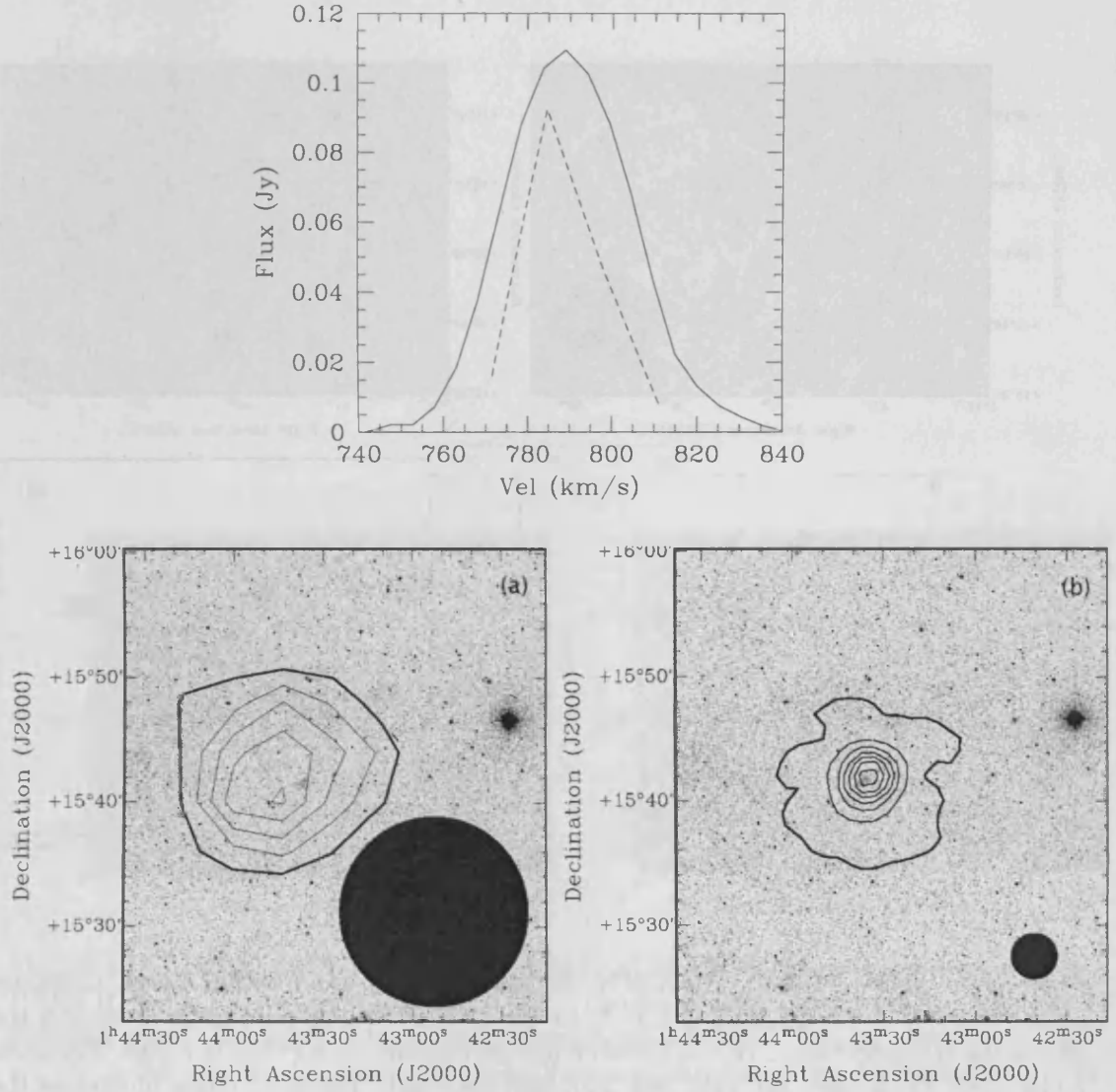

Figure 4.9: **KDG 010** (a) HIPASS H I contours overlaid on a POSS II image. Contour values (sigma): 1.5, 3, 4.5, 6, 7.5. The solid circle illustrates the size of the HIPASS beam. (b) AGES H I contours overlaid on a POSS II image. Contour values (sigma): 3, 30, 60, 90, 120. The solid circle illustrates the size of the AGES beam. (c) H I velocity profiles: HIPASS is shown as the dashed line, AGES as the solid line.

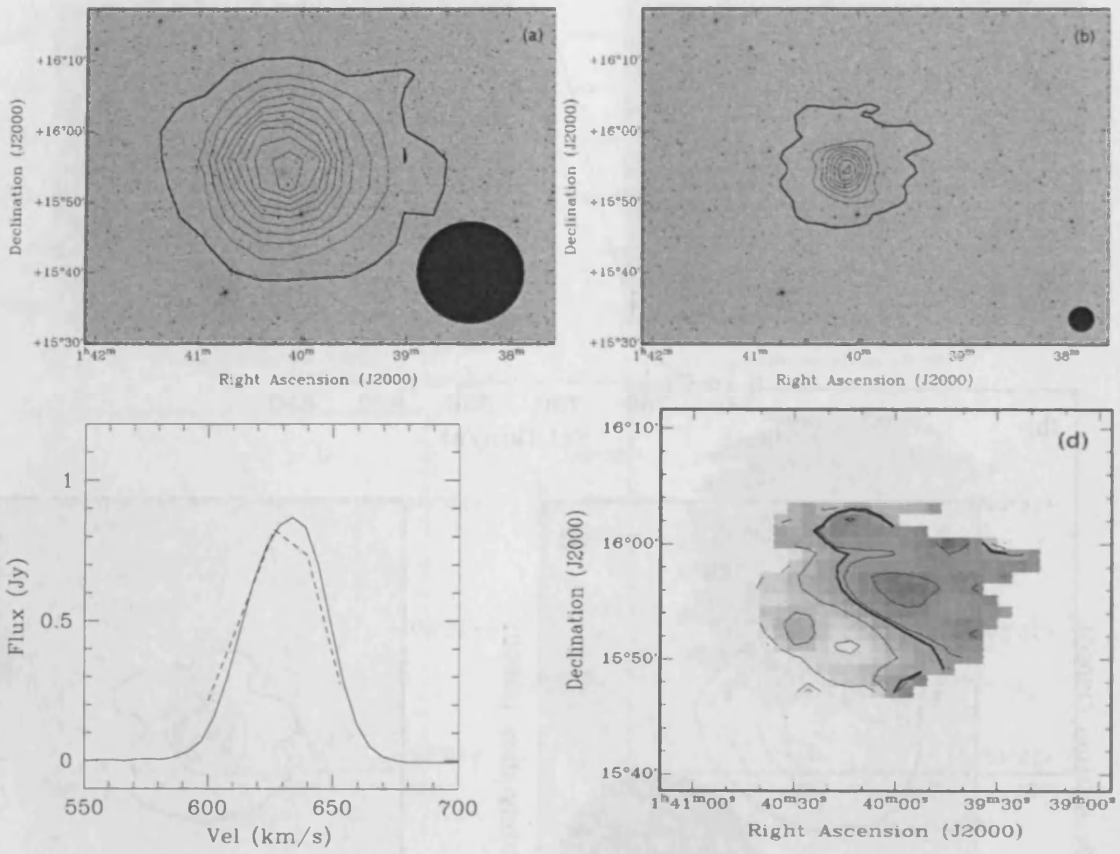

Figure 4.10: **UGC 1176** (a) HIPASS H I contours overlaid on a POSS II image. Contours ($\times 10^{18}$ cm^{-2}): 3, 7.5, 15, 22.5, 30, 37.5, 45, 52.5, 60, 67.5. The solid circle illustrates the size of the HIPASS beam. (b) AGES H I contours overlaid on a POSS II image. Contours ($\times 10^{18}$ cm^{-2}): **2** (3σ), 60, 120, 180, 240, 300, 360, 420. The solid circle illustrates the size of the AGES beam. (c) H I velocity profiles: HIPASS is shown as the dashed line, AGES as the solid line. (d) Velocity field from AGES data. Iso-velocity contours increase from light to dark: 620, 625, 630, **634**, 635, 640.

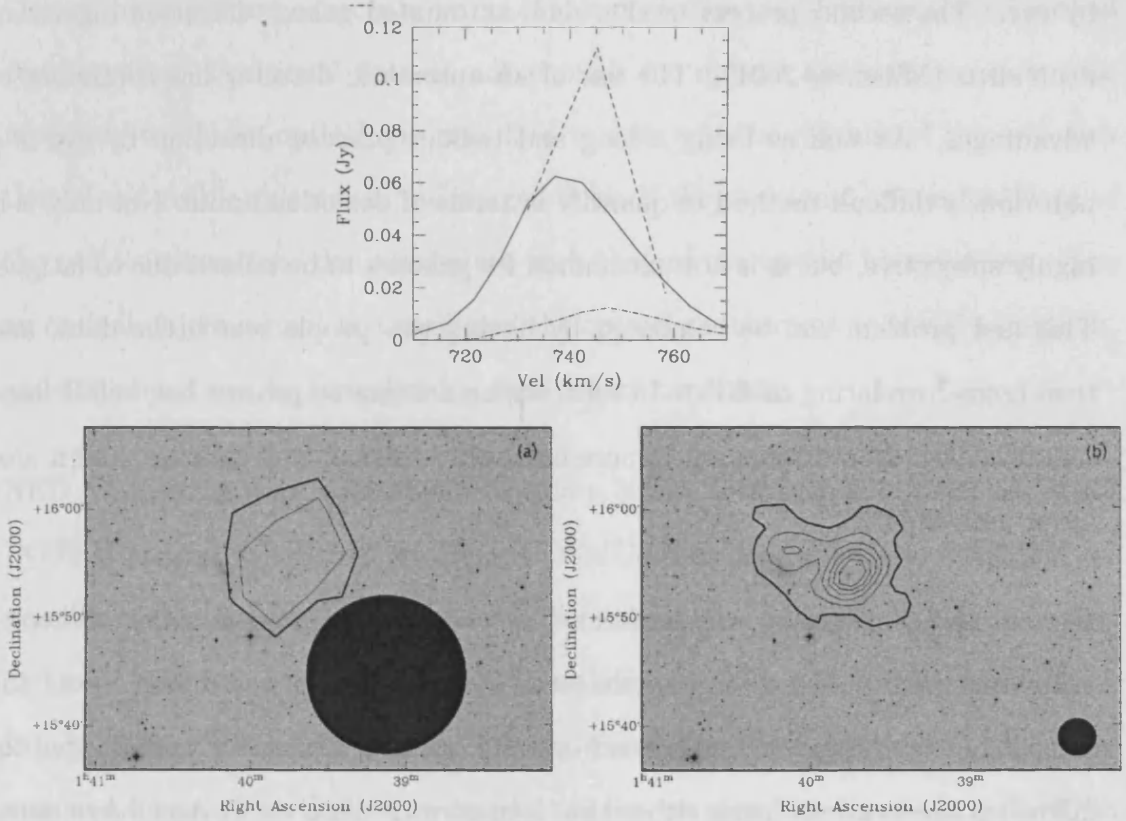

Figure 4.11: **UGC 1171 & dw0137+1541** (a) HIPASS HI contours overlaid on a POSS II image. Contours (sigma): 3, 4.5. The solid circle illustrates the size of the HIPASS beam. (b) AGES HI contours overlaid on a POSS II image. Contours ($\times 10^{18}$ cm^{-2}): 3, 7.5, 15, 30, 45. The solid circle illustrates the size of the AGES beam. (c) HI velocity profiles for UGC 1171 and dw0137+1541: HIPASS data for UGC 1171 is shown as the dashed line, AGES data for UGC 1171 is the solid line. Dw0137+1541 is shown by the dash-dot line.

4.3.1 Objects beyond the NGC 628 group

Due to the large observing bandwidth offered by the WAPPs (100 MHz) it was expected that a number of background objects would also be detected. Source detection involved two different methods. The first method involved a manual search by eye. The second process used a semi-automated galaxy detection algorithm POLYFIND (Minchin, 2001). The use of an automatic detector has a number of advantages. As well as being a long and tedious process, detection by eye is a notoriously difficult method to quantify in terms of detection limits. Not only is it highly subjective, but it is not uncommon for galaxies to be missed due to fatigue. This last problem can be combated by having two people search the data, and then cross-correlating each list. In contrast, an automated process has well defined search criteria leading to a much more homogeneous sample of galaxies, and it also never gets tired!

Manual object detection was performed by two people (R. Auld and L. Cortese) using the eye. A list of objects detected by both people was drawn up as the most likely candidates for real detections and low S/N detections were flagged for follow-up observations using either the 'L-band wide' receiver at Arecibo or using the Green Bank 110 m radio telescope. Detections that were made exclusively by each individual were cross-checked by the other and spurious signals rejected. Objects that were considered worthy of confirmatory observations were then added to the list of objects for follow-up.

In all, 22 other objects were detected by both individuals out to a velocity of cz=17500 km s^{-1}. A further 9 objects were re-observed using Arecibo or Green Bank, of which, 2 were found to be real. Including the NGC 628 group, a total of 29 galaxies were detected, this gives a detection rate of 5.8 objects deg^{-2}. This

implies that the total number of galaxies detected by AGES will be ~1200. The ALFALFA survey (Giovanelli et al. 2005) has predicted that they will detect a 20000 objects over an area of 7000 deg^2, giving an average detection rate of 2.9 deg^{-2}.

One of the important aspects in terms of this project is to identify potential optical counterparts. Positional data is not enough for optical associations, it is also necessary to obtain optical spectral data to compare the redshift of the gas with that of the visible galaxies in the imaged field. If the positional or spectral data of the radio observations don't correlate with that of the optical observations, then an optical object cannot be considered the optical counterpart to the H I emission, and the object can be considered a dark galaxy candidate.

NED was used to search for objects within a 3′ radius of each H I detection. 6′×6′ POSS II images, taken from the SuperCOSMOS database, were also examined for possible optical counterparts. Of the 22 detections, 9 are previously uncatalogued and none of the objects are listed in NED as having previous H I line measurements. In addition to NED, The Arecibo Galaxy Catalogue (Springob et al. 2005) was searched for previous H I line measurements but no matches were returned. SDSS redshift data is available for only 3 objects, and these compare favourably with the H I redshifts as described below. Additional optical spectra were obtained using the 1.5 m telescope at Loiano and were also used where available.

The H I detections are listed in Table 4.2 along with any objects listed in NED within a 3′ radius. The final column in Table 4.2 shows the angular distance between the centre of the H I detection and the NED object's position. Fig. 4.12 shows the SuperCOSMOS images for each object, centred on the H I detection, together with the H I spectra. The Arecibo beam is represented by the circle and

is to scale. Optical detections within the Arecibo beam have been identified with an arrow and previously catalogued objects have been labelled. Descriptions of the images and the corresponding spectra are given below. Although some objects coincide with the centre of the H I emission, one should bear in mind that without optical redshift data, it is impossible to say for certain whether or not these objects are associated with the gas.

J012950+152125 This marginal H I detection was confirmed by follow up observations and is not listed in prior catalogues. The optical morphology of the object near the centre of the beam is difficult to distinguish due to the size of the object and the low S/N of the H I detection. It is most likely an edge-on spiral galaxy.

AGES J013149+152353 This signal coincides with the SDSS galaxy, SDSS J013149.81+152326.5. There is an optical redshift available for this galaxy placing it at $cz = 10717$ km s^{-1}. The radio data place the galaxy at a recessional velocity of $cz = 10705$ km s^{-1}. SDSS J013149.81+152326.5 is a spiral galaxy and this morphology is reflected in the H I profile. This galaxy appears to be somewhat isolated since there are no galaxies reported in this region within 1700 km s^{-1}.

AGES J013204+152947 The SDSS galaxy, SDSS J013204.6+153001.2, falls almost in the centre of the Arecibo beam. It has an optically measured redshift of $cz = 13195$ km s^{-1} from the SDSS. The radio measurement of the recessional velocity is $cz = 13196$ km s^{-1}. The good agreement between the positional and redshift data make it almost certain that this is the source of the H I. This galaxy has a red optical colour ($g-r$ ~0.75 mag) typically observed in early type galaxies (Bernardi et al. 2003). Moreover the SDSS nuclear spectrum shows a red continuum and no sign of recent star formation (i.e. no emission lines). A similar red colour ($g-r$ ~0.84 mag) is associated with the companion, 2MASX J01320599+1529298,

AGES ID	RA (2000)	DEC (2000)	V_{sys} (km s^{-1})	Distance (Mpc)	W_{50} (km s^{-1})	W_{20} (km s^{-1})	F_{HI} (Jy km s^{-1})	M_{HI} ($\times 10^8 M_\odot$)	Previously catalogued objects	Angular separation (arcmin)	M_{HI}/L_H $M_\odot/L_\odot$
J012950+152125	01 29 50.6	15 21 25	11427 (4)	159	183 (9)	210 (13)	0.61 (0.08)	36.1	New	—	—
J013149+152353	01 31 48.9	15 23 53	10705 (3)	146	178 (6)	220 (9)	1.44 (0.11)	72.2	SDSS J01314980+1523265	0.5	0.9
J013204+152947	01 32 04.1	15 29 47	13196 (7)	178	326 (14)	400 (21)	1.01 (0.11)	75.5	SDSS J013204.6+153001.2	0.3	0.1
									2MASX J01320599+1529298	0.5	0.5
J013313+160139	01 33 12.9	16 01 39	8895 (3)	122	138 (6)	194 (9)	1.69 (0.11)	59.0	2MASXi J0133132+160125	0.2	—
J013538+154850	01 35 38.0	15 48 50	8012 (3)	110	132 (6)	153 (9)	0.61 (0.08)	17.5	New	—	—
J013718+153635	01 37 18.0	15 36 35	8174 (4)	112	144 (8)	169 (12)	0.46 (0.08)	13.7	NVSS J013714+153722	1.2	0.3
J013807+154328	01 38 07.0	15 43 28	13237 (2)	179	162 (4)	169 (6)	0.60 (0.08)	45.4	New	—	—
J013827+154728	01 38 26.8	15 47 28	8339 (2)	114	182 (3)	201 (5)	1.74 (0.11)	53.4	New	—	—
J013917+154613	01 39 17.1	15 46 13	17080 (5)	228	51 (9)	98 (14)	0.27 (0.05)	33.5	New	—	—
J013953+151955	01 39 52.7	15 19 55	16806 (6)	224	231 (12)	284 (18)	0.43 (0.07)	51.1	SDSS J013955.02+152036.7	0.9	—
J013956+153135	01 39 56.2	15 31 35	17343 (7)	231	105 (14)	214 (21)	0.42 (0.07)	53.7	New	—	—
J014013+153319	01 40 13.0	15 33 19	17052 (7)	227	535 (14)	566 (21)	1.33 (0.13)	163.0	2MASX J01401331+1533345	0.3	0.2
J014025+151903	01 40 25.2	15 19 03	16848 (5)	225	44 (9)	101 (14)	0.31 (0.06)	36.7	2MASX J01402402+1518240	0.7	0.2
J014033+160513	01 40 32.6	16 05 13	13017 (4)	176	101 (8)	152 (12)	0.59 (0.07)	42.6	2MASXi J0140360+160414	1.3	—
J014232+153921	01 42 32.6	15 39 21	10509 (5)	159	52 (11)	145 (16)	0.47 (0.05)	23.8	NVSSJ014231+153629	2.9	—
J014430+161502	01 44 30.3	16 15 02	5020 (2)	70	107 (3)	121 (5)	0.61 (0.07)	7.0	New	—	—
J014524+155923	01 45 23.7	15 59 23	5050 (4)	70	34 (7)	60 (11)	0.18 (0.04)	2.1	New	—	—
J014630+154332	01 46 30.4	15 43 32	17495 (3)	232	132 (6)	167 (9)	0.73 (0.09)	92.7	2MASX J01463012+1543250	0.1	0.4
J014644+155622	01 46 44.0	15 56 22	7063 (5)	97	27 (10)	51 (15)	0.10 (0.05)	2.2	2MASX J01465179+1557192	2.1	0.07
J014719+155603	01 47 19.1	15 56 03	5191 (3)	72	86(7)	104 (11)	0.35 (0.07)	4.3	NVSS J014722+155737	1.8	—
J014742+161317	01 47 41.7	16 13 17	4890 (3)	68	138 (6)	177 (9)	1.02 (0.09)	11.1	2MASXi J0147459+161318	1.0	—
J014752+155855	01 47 51.7	15 58 55	17514 (11)	233	450 (22)	578 (33)	1.59 (0.13)	200.0	2MASX J01475424+1558247	0.8	1.0
									2MASX J01475424+1559387	1.0	—
J014834+152756	01 48 33.7	15 27 56	12985 (4)	175	114 (8)	129 (12)	0.50 (0.07)	36.3	New	—	—

Table 4.2: H I properties of objects detected beyond the NGC 628 group.

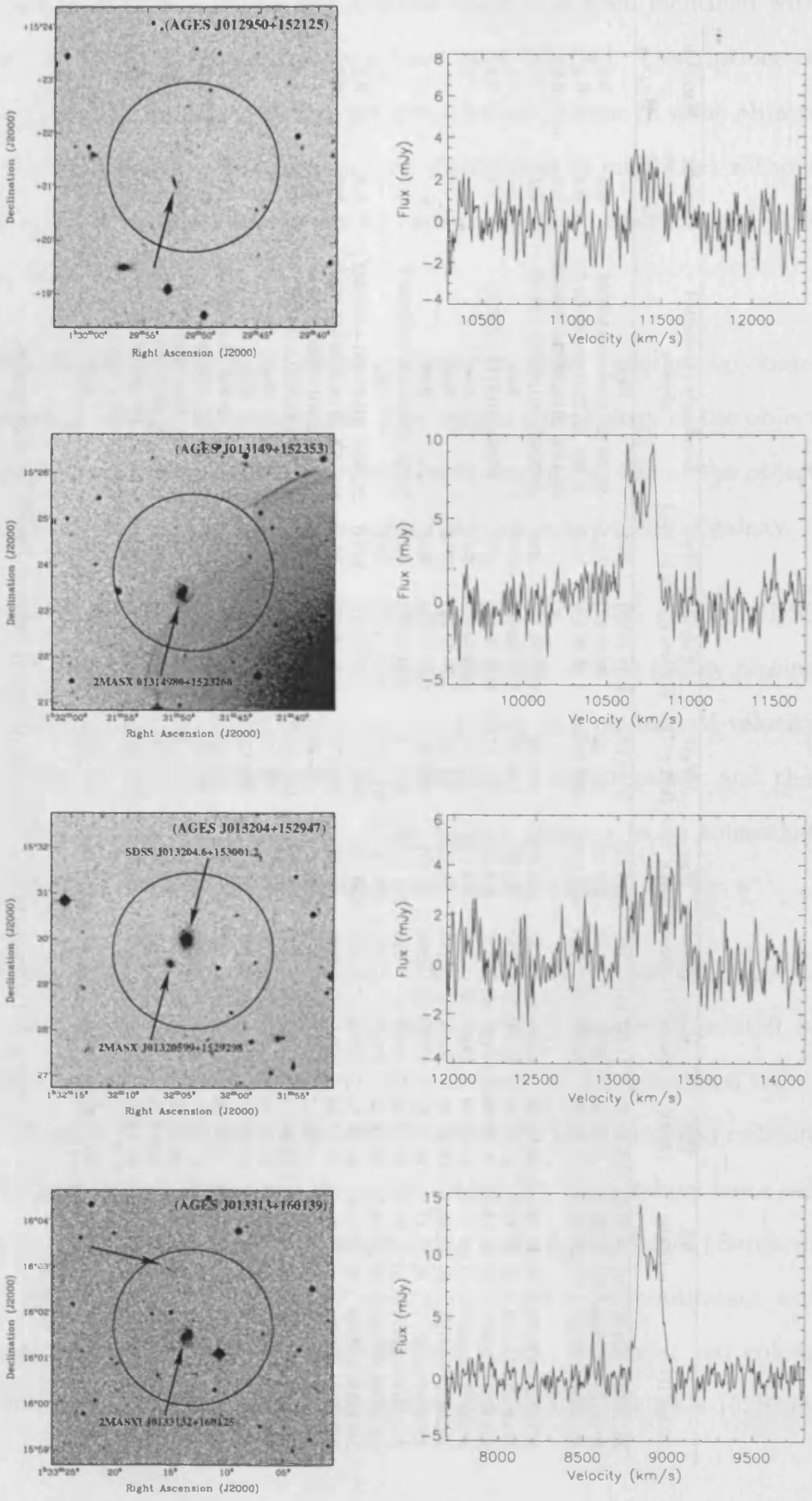

Figure 4.12: Top to bottom: B band images and accompanying H I spectra for AGES objects J012950+152125, J013149+152353, J013204+152947, J013313+160139

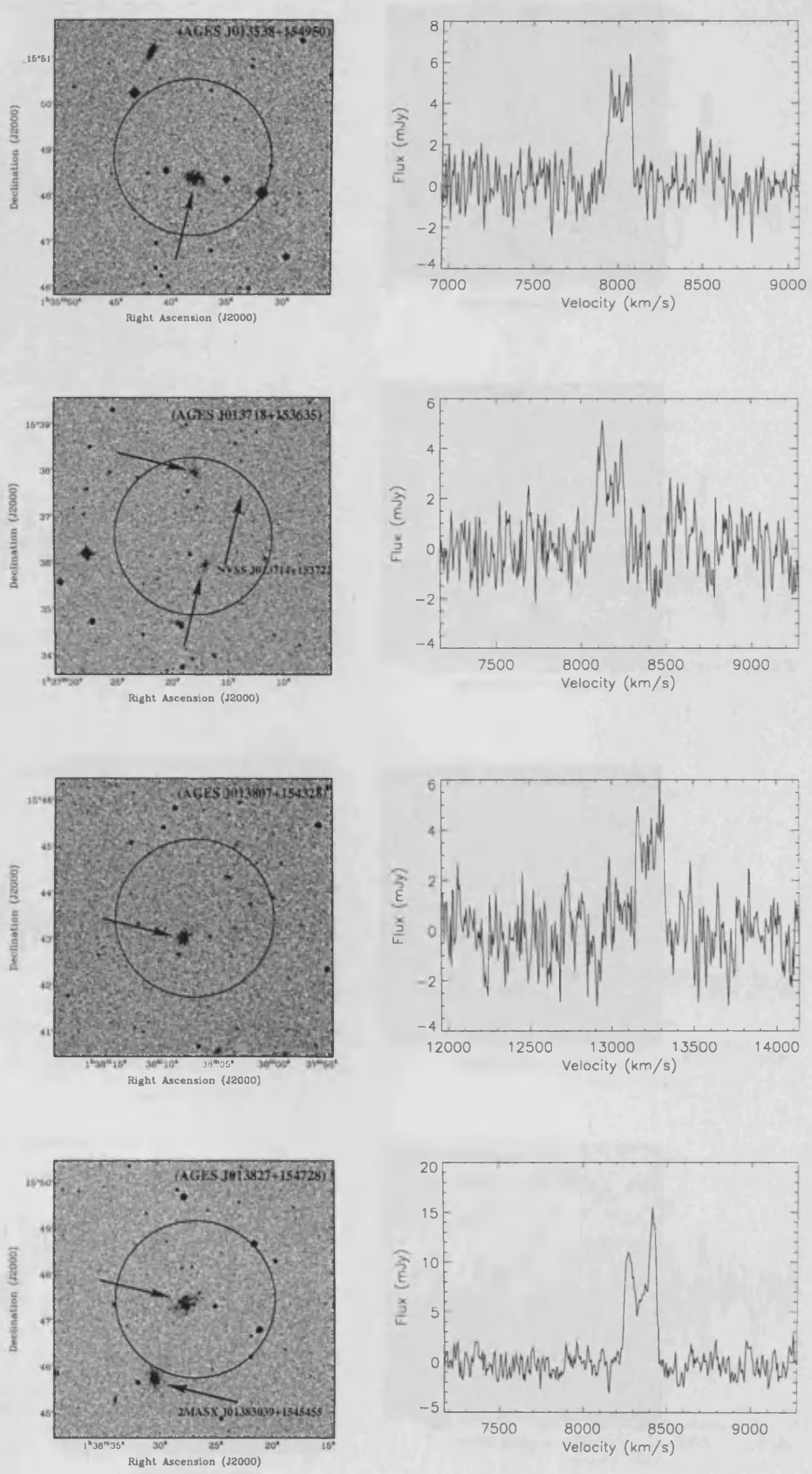

Figure 4.12: Top to bottom: B band images and accompanying H I spectra for objects J013538+154850, J013718+153635, J013807+154328, and J013827+154728

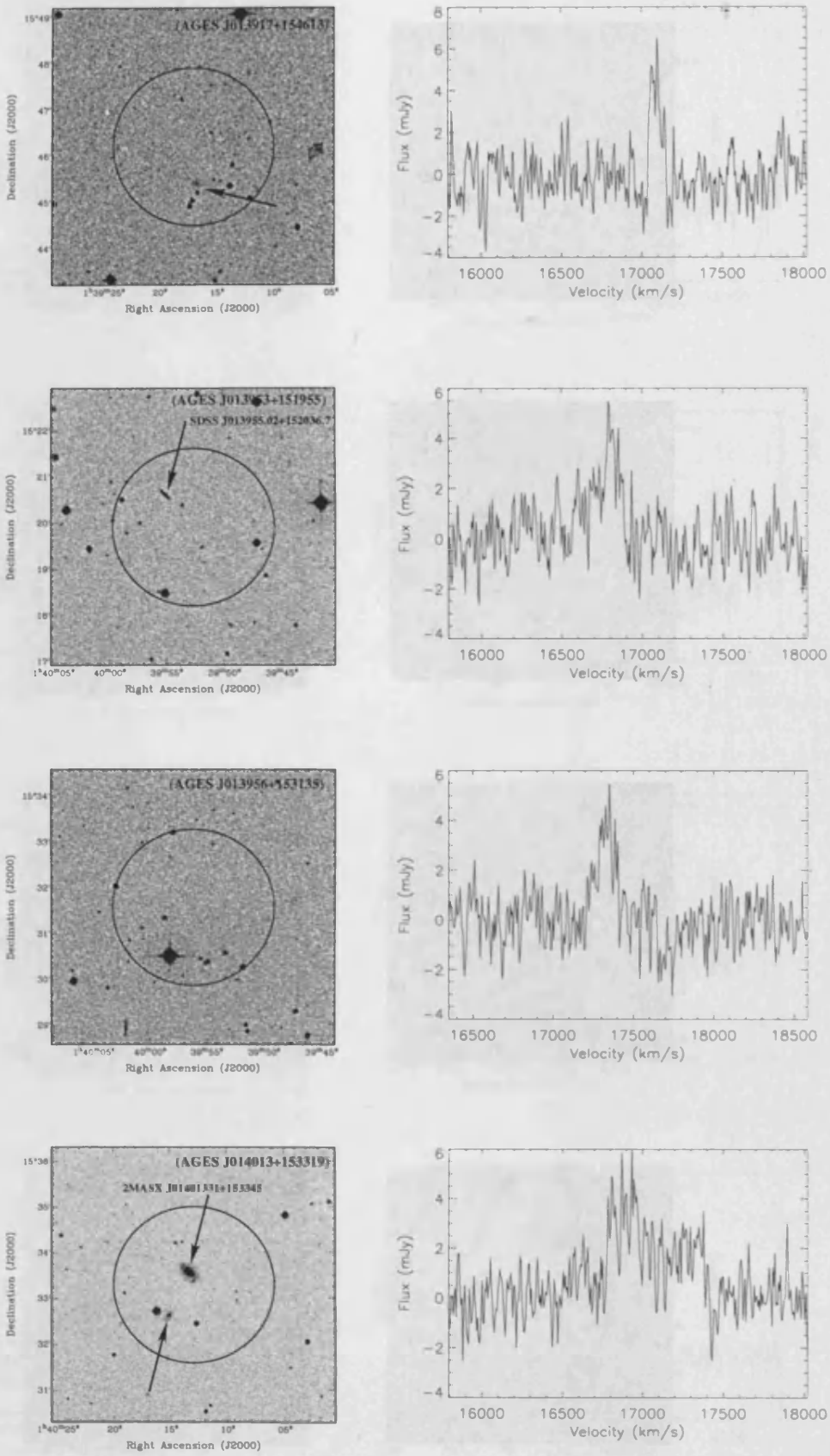

Figure 4.12: Top to bottom: *B* band images and accompanying H I spectra for objects J013917+154613, J013953+151955, J013956+153135 and J014013+153319

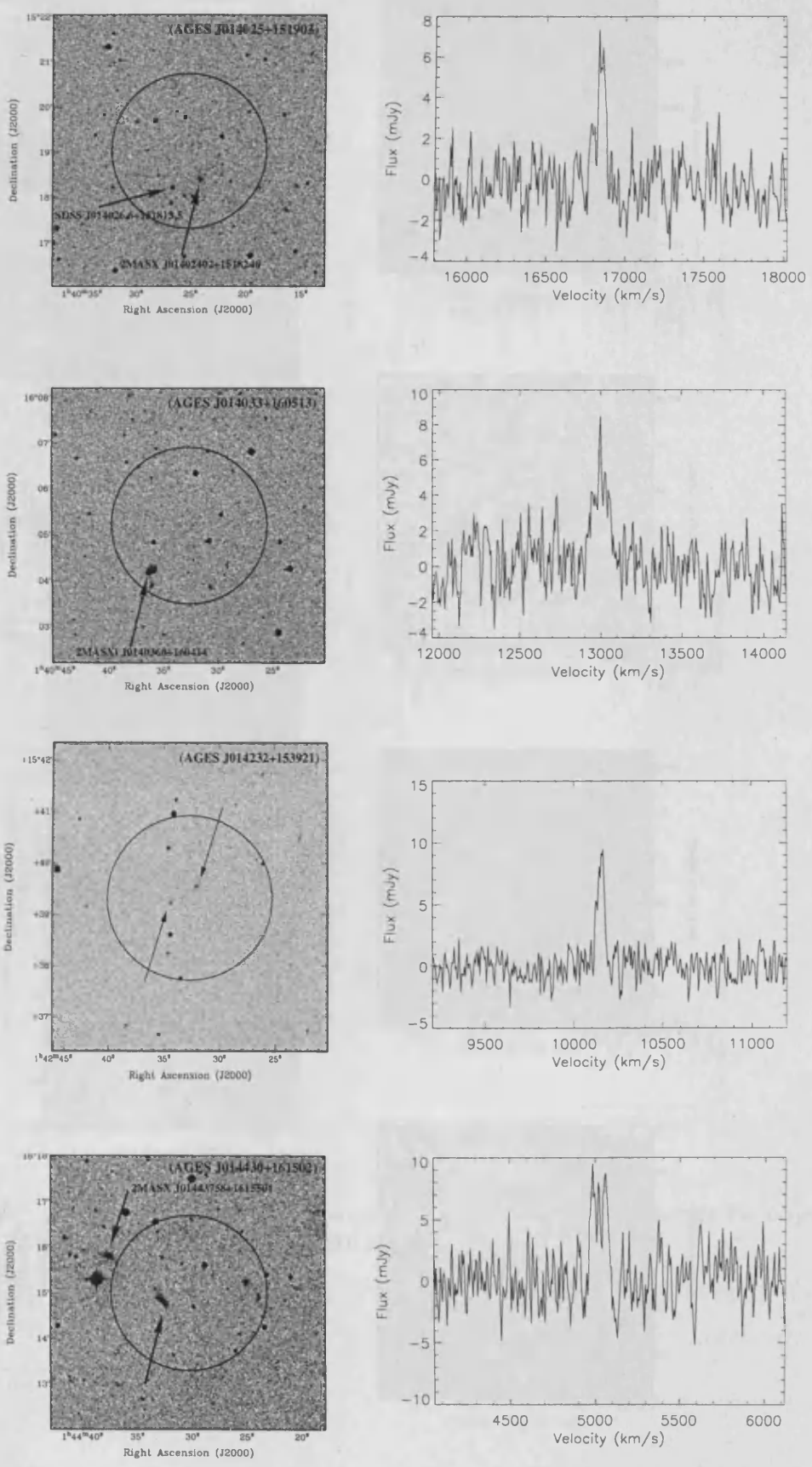

Figure 4.12: Top to bottom: B band images and accompanying HI spectra for objects J014025+151903, J014033+160513, J014232+153921 and J014430+161502

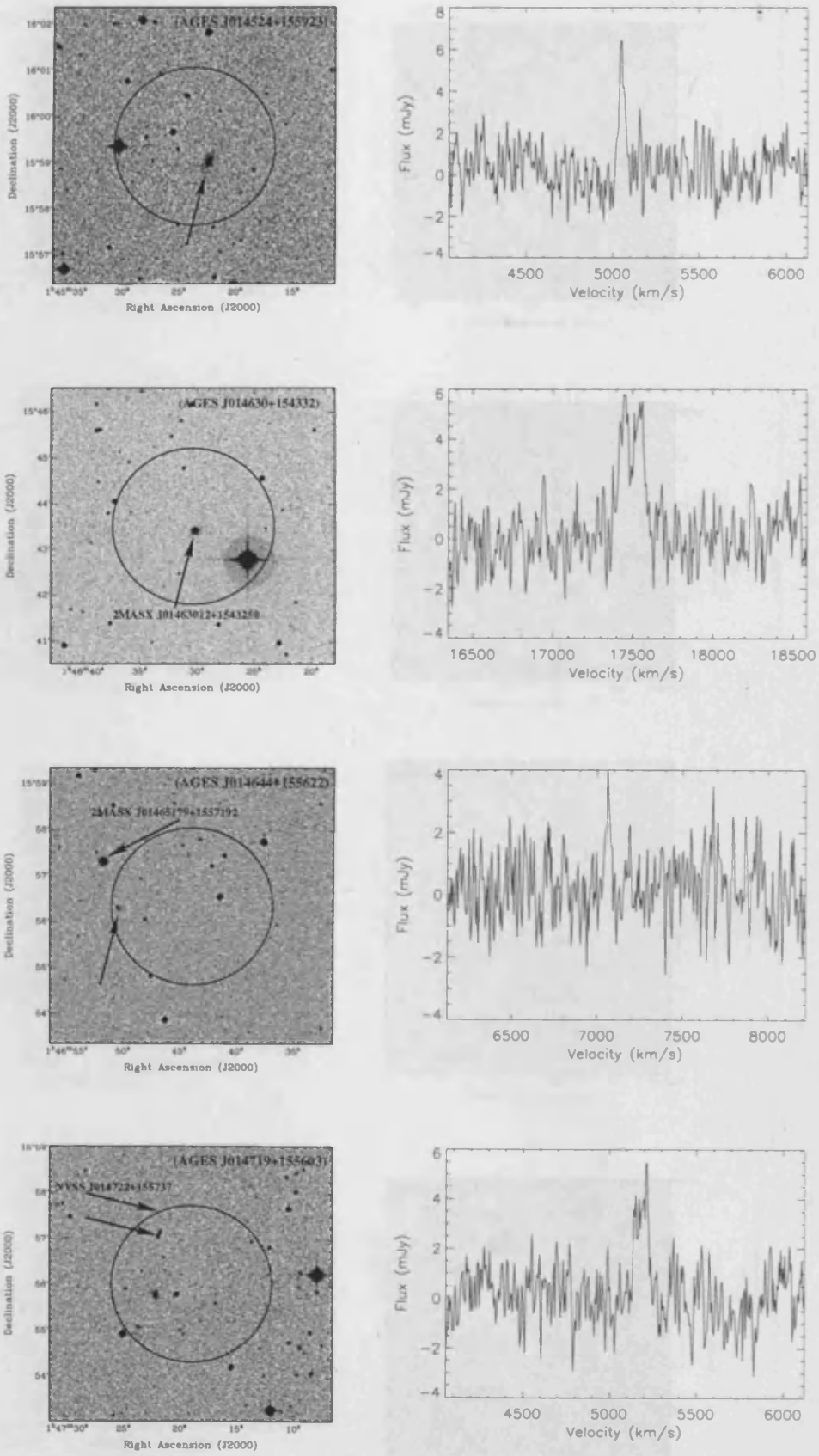

Figure 4.12: Top to bottom: *B* band images and accompanying H I spectra for objects J014524+155923, J014630+154332, J014644+155622, and J014719+155603

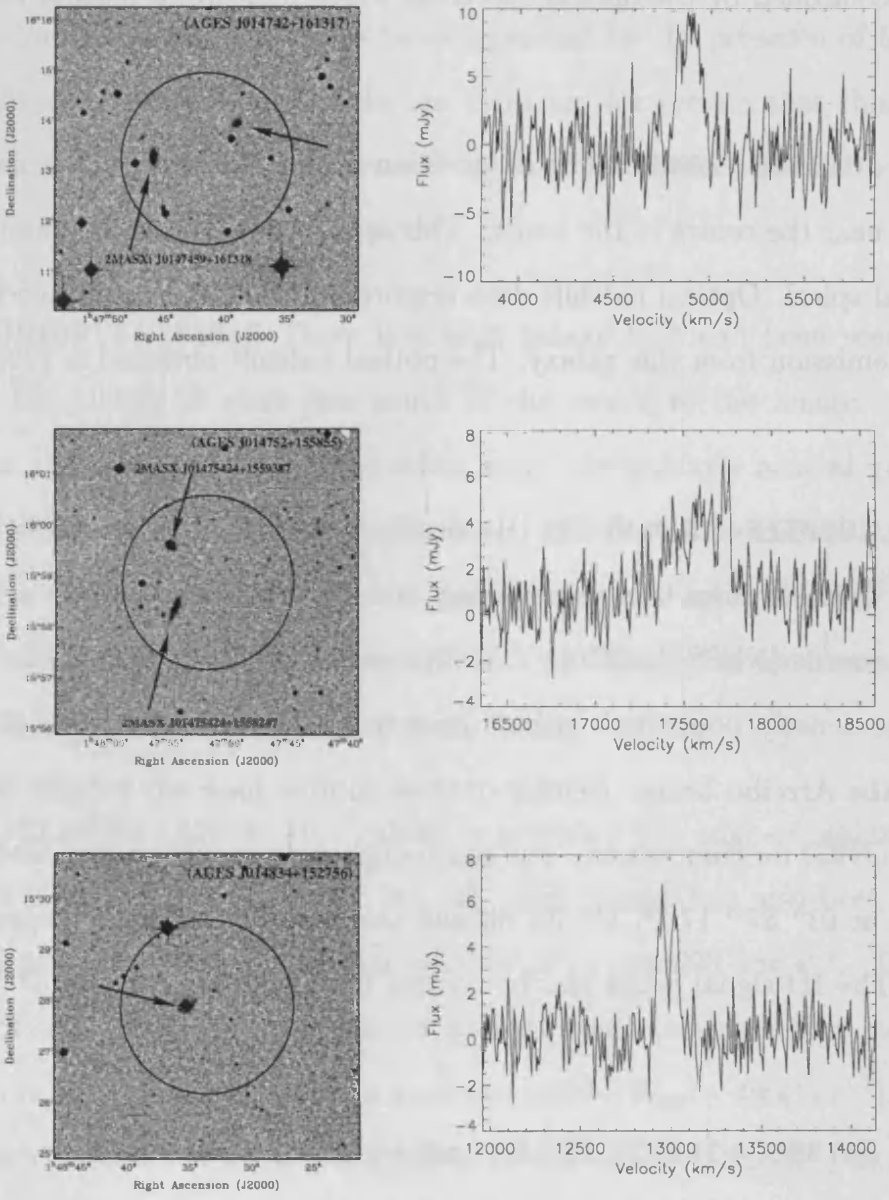

Figure 4.12: Top to bottom: *B* band images and accompanying H I spectra for objects J014742+161317, J014752+014752 and J014834+152756

which lies within the beam.

AGES J013313+160139 Rotation is clearly seen in the H I profile which is most likely coming from 2MASXi J0133132+160125 which lies in the centre of the beam. This is confirmed by the optical spectrum which indicates a redshift of 8886 ±79 km s^{-1}.

AGES J013538+154850 The H I position is likely to be coming from the spiral located near the centre of the image. This is supported by the H I profile which is a typical spiral. Optical redshift data acquired from Loiano confirmed that this is the H I emission from this galaxy. The optical redshift obtained is 7998 ±133 km s^{-1}.

AGES J013718+153635 The H I profile for this object is typical of a spiral galaxy. Tying it down to a single galaxy is difficult though. There is a 21 cm continuum source (NVSS J013714+153722) located at a distance of 1.2′. This frame is rather densely populated with at least five galaxies present, two of which fall within the Arecibo beam. Neither of these sources have any redshift information listed in NED for comparison. The continuum source could be associated with the smudge at 01^h 37^m 17.7^s, 15° 38′ 00″and this just falls within the edge of the H I beam. The H I signal could also be coming from the object at 01^h 37^m 17.0^s, 15° 39′ 50″.

AGES J013807+154328 The H I profile of this galaxy suggests a spiral galaxy of mass ~4.5 $\times 10^9 M_\odot$. The optical counterpart is probably the object located near the centre of the POSS II frame (Fig. 4.12) but this object is not listed in NED. There is a hint of spiral structure in the optical which does lend support to this being the counterpart. Optical spectroscopy would be needed to help confirm this.

AGES J013827+154728 While the bright galaxy to the south of the frame in Fig. 4.12 is identified by NED as 2MASX J01383039+1545455, the object in the centre of the frame is not listed at all. The double horn H I profile indicates a large, spiral galaxy. The optical image, however, shows a galaxy with a rather clumpy structure, although it may be exaggerated by the presence of foreground stars. Without optical redshift data one can't say for certain that this galaxy is the source of the H I emission. However the correlation between the positions of the radio and optical data is very good.

AGES J013917+154613 There is a faint galaxy that can been seen nestling amongst the cluster of stars just south of the centre of the image. Although quite dim compared with the surrounding stars, the galaxy's neutral gas content ($3.3\times10^9 M_\odot$) suggests it is a Milky Way sized galaxy that is merely far away ($\sim$ 230 Mpc). This is unusual since this galaxy also has approximately the same mass as object 2 and is at the same distance, yet nothing as obvious as 2MASX J01463012+1543250 lies within the Arecibo beam.

AGES J013953+151955 This galaxy is probably the edge-on galaxy located in Fig. 4.12 at $01^h\ 39^m\ 55.0^s$, $15°\ 20'\ 34''$. This galaxy has also been identified by SDSS with an *optical* recessional velocity of cz =16693 km s^{-1}. The AGES redshift of cz=16806 km s^{-1} compares reasonably well with this. The shape of the spectrum is fairly Gaussian and has a narrow width (W_{50} = 49 km s^{-1}). It would be highly unusual for a galaxy as massive as this one ($5.1\times10^9 M_\odot$) to have such a narrow profile unless it was being viewed face-on. SDSS J013955.02+152036.7 looks more like an edge-on galaxy, so either some of the H I flux is hidden in the noise or this galaxy is not responsible for the H I emission. More sensitive radio observations would show for certain if we are just measuring the peak of one of the double-horns that one would expect from such an edge-on system.

AGES J013956+153135 The H I signal is about a 5-σ detection with a peak of around 5.5 mJy and W_{50}=105 km s^{-1}. The optical counterpart is a little more tricky. There is a small smudge in Fig. 4.12 at 01^h 39^m 55.0^s, 15° 30′ 22″. However, the H I mass is $\sim 5 \times 10^9$ $M_\odot$, which is similar to object 2. Therefore one might expect to see a galaxy of a similar size to 2MASX J01463012+1543250. This is a very interesting detection. There are no obvious optical counterparts but the POSS II image is relatively shallow so it is possible this H I detection has a low surface brightness optical counterpart. Deep optical follow-up observations are essential to try and determine whether this object has an optical association.

AGES J014013+153319 Two objects have been identified within the beam that could be contributing to the H I emission. The H I profile shows an excess of neutral gas in the approaching half of the spectrum. This could be due to superposition of individual profiles or due to asymmetry in the gas distribution of one of the galaxies, if these galaxies are indeed responsible for the H I emission.

AGES J014025+151903 This object has a narrow velocity width (W_{50} = 44 km s^{-1}) but is a 6-σ detection. 2 objects exist in NED in this area, but one of them is a distant quasar (SDSS J014026.6+151813.5). 2MASX J01402402+1518240 falls within the Arecibo beam and shows up in the POSS II image as a faint smudge (Fig. 4.12). Follow-up optical spectroscopy and radio interferometry would determine if 2MASX J01402402+1518240 is the source of the H I emission.

AGES J014033+160513 The POSS II plate presents a particularly interesting object, 2MASXi J0140360+160414, which lies just on the edge of the beam. At first glance the optical image looks like a spiral galaxy with a spiral arm extending to the south. A closer inspection of the POSS II images has revealed that the central part of the galaxy can almost be resolved into two objects and the trailing

spiral arm looks like a tidal stream linking a third object to the south. It looks as if there is an interesting merger going on here. Further investigation would be required to ascertain the nature of this merger, and to determine whether or not these objects are responsible for the H I emission.

AGES J014430+161502 The H I signal is unmistakable but locating the optical source is not as straightforward. 2MASX J01443758+1615501 is present in the optical frame in Fig. 4.12 but its position would place it at the very edge of the beam. The H I position is more likely linked to the smudge nearer the centre of the beam at $01^h\ 44^m\ 33.5^s$, 16° 14′ 48″. Its elongated structure is pointing towards 2MASX J01443758+1615501 which may be the result of an interaction with this galaxy.

AGES J014524+155923 Although the H I detection is narrow (W_{50} = 30 km s^{-1}) the peak flux is a 6-σ detection and the source of the H I is more or less centred on the galaxy in Fig. 4.12 at $01^h\ 45^m\ 22.5^s$, 15° 59′ 00″. This is the least massive of the detected galaxies, with a H I mass of $\sim$2.1 $\times 10^8$ $M_\odot$.

AGES 014630+154332 The H I profile is double-horned with a width of 132 km s^{-1}, suggesting this object is a spiral galaxy but the galaxy located at the centre of the optical image does not reflect this. It is a very circular object, so if this object is the optical counterpart to the H I it must have a very bright bulge or very diffuse arms. It's circular nature also suggests we are looking at the galaxy face-on, but if this were the case the H I profile would look more Gaussian.

AGES J014644+155622 Although the H I signal of this object is very narrow (W_{50} = 26km s^{-1}) it persists over several channels suggesting that it is indeed real even though the peak is only a 4-σ detection. There are two objects visible on

the optical image (Fig. 4.12) that are on the edge of the beam. The first object, 2MASX J01465179+1557192, is very bright and large although it is 2.1′ away from the centre point of the H I emission. The second object is only visible as a faint smudge in the *B*-band and *R*-band images but is closer in separation (∼1.5′). The second object is not listed in NED.

AGES J014719+155603 The optical frame shows only one possible optical counterpart. The object is located at $01^h\ 47^m\ 21.5^s$, 15° 57′ 00″. NVSS J014722+155737 is listed in NED less than 30 ″away from the optical detection and is probably the source of the radio emission. The positions do not match that well, so optical spectra would help make this distinction.

AGES J014742+161317 The H I profile is fairly Gaussian with a velocity width of W_{50} = 138 km s^{-1}. The optical image shows two possible counterparts at $01^h\ 47^m\ 39.0^s$, 16° 13′ 56″ (most likely) and $01^h\ 47^m\ 46.0^s$, 16° 13′ 18″ (2MASXi 0147459+161318). Further investigation will reveal the true source of the H I emission.

AGES J014752+155855 There are 2 galaxies in the *B*-band image that fall within the beam. Both are listed as 2MASS objects and the H I emission may be coming from one, both, or neither of these objects. Without higher resolution H I images and optical spectra it is impossible to distinguish between them.

AGES J014834+152756 The double-horned H I velocity profile and the optical image both indicate the this galaxy is a spiral. On closer inspection of the optical data it seems that the galaxy may be a one-armed spiral. Again this object is not listed in NED. It would be interesting to acquire higher resolution radio data of this object to see if there is tidal debris linked to this perturbed spiral.

From the velocity information alone there appear to be four group associations at around 5000, 8000, 13000 and 17000 km s^{-1}. J013149+152353 is the one exception being the only galaxy that has no other neighbour within 1700 km s^{-1}. Fig. 4.13 is a 3D plot of the galaxies, position and redshift. From this it is possible to distinguish 3 groups: 1 group at ~5000 km s^{-1}, one at ~8000 km s^{-1} and one at ~17000 km s^{-1}. The objects at ~12500 km s^{-1} seem too scattered in RA to be considered a group, although they may be the massive tracers of a filament running at right-angles to our line of sight at this velocity.

4.3.2 Detection efficiency

It is vital to explore how well the different detection techniques performed since this will determine the best method of detection for future AGES fields. Individually, Auld identified 29 galaxies of which 22 are genuine sources. Cortese also listed 29 galaxies of which 24 turned out to be real. The semi-automatic galaxy finder, POLYFIND, returned a list of 860 possible detections of which 24 were real. POLYFIND works by convolving the data with a number of matched templates and then it returns a list of signals that have met a pre-specified set of criteria (S/N limit, noise clip threshold, channel mask). As the S/N limit is reduced, the number of returned sources obviously increases as more noise spikes meet the S/N criterion. Clearly a balance had to be reached whereby the detection efficiency is not too low, while still detecting the majority of galaxies.

In order for POLYFIND to detect the majority of sources detected by eye, it was necessary to set a rather low S/N detection threshold of 4.5σ. This in turn returned a list of 860 possible sources. These then had to be examined by eye using the MIRIAD routine, MBSPECT to judge whether or not the sources were to be judged

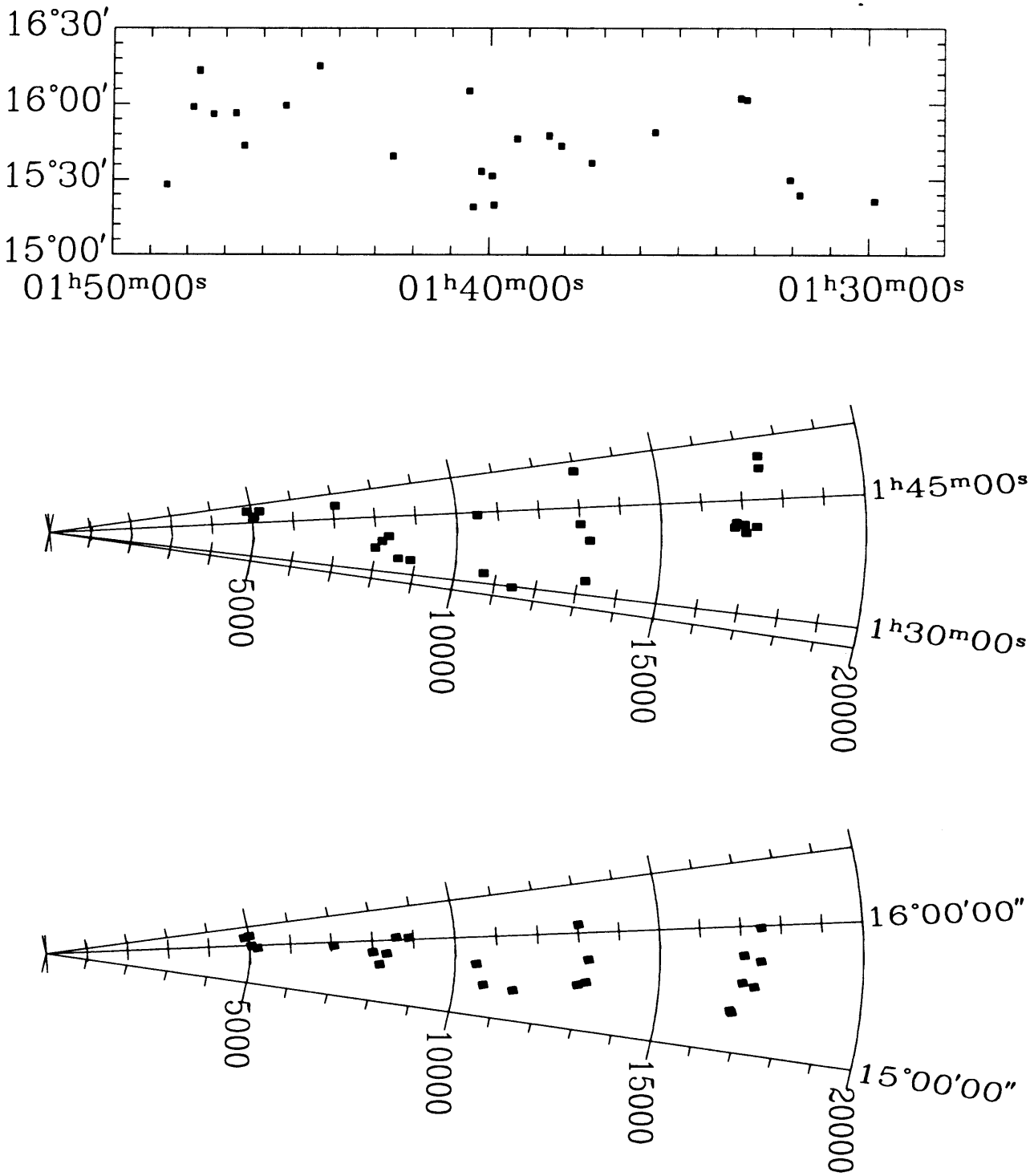

Figure 4.13: Different projections showing the 3-D layout of the detected galaxies in the NGC 628 region.Top: RA–dec projection, middle: RA–velocity projection, bottom: dec–velocity projection.

real. This does introduce a certain amount of subjectivity, but at least the sample from which the detections have been made has well defined selection criteria.

The vast majority of the spurious signals could be attributed to the aforementioned RFI sources, of which the frequency-varying RFI proved most difficult to reject. Even imposing a channel mask to cut out the sections of the bandpass contaminated by the frequency-static RFI from L3 GPS satellite or FAA radar at Punta Salinas did not fully prevent the false detection of these signals. The impact of these signals on the final number of detections could have been reduced by imposing a larger channel mask around the contaminated areas of the bandpass. However the galaxies at $v \sim 8500$ km s^{-1} would not have been detected.

Fig. 4.14 shows a comparison of the different detection methods. For each detected source the peak S/N is plotted against the total flux. It is clear that below 6 σ, each detection method is missing a number of galaxies that are picked up by the other methods. This is in agreement with the findings of Auld et al. (2006) whereby V/V_{max} analysis of the datacube populated with simulated sources implied that the 50% completeness limit was about 7σ.

It is surprising that POLYFIND required a S/N ratio threshold of 4.5 to be completely reliable to 7σ. The most recent attempt to develop a reliable galaxy detection algorithm was undertaken by Saintonge (2007) and applied to a sample of ALFALFA galaxies. The algorithm they developed was able to mimic both Gaussian shaped velocity profiles and double-horned profiles convincingly, yet the detection efficiency was not dissimilar to previous methods, improving only marginally the number of real detections below a S/N of 6. To the trained eye, it is usually trivial to distinguish between galactic signals and spurious signals, but as noted by Rosenberg & Schneider (2000), trying to describe this in terms that a computer

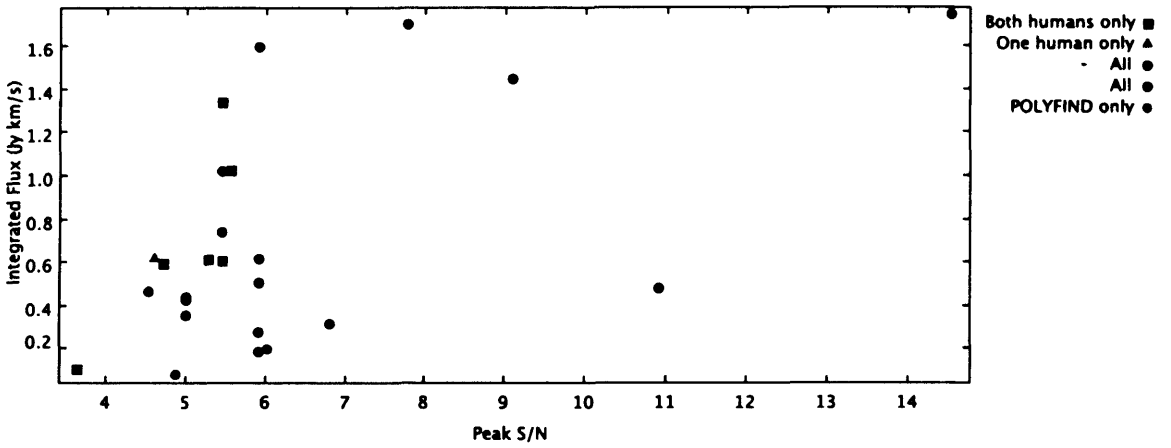

Figure 4.14: Selection criteria for NGC 628 data. Peak flux S/N is plotted against the total flux. Detections found by both humans and the algorithm are shown as solid black circles. Detections by both humans only are shown by blue squares. The galaxy that was detected by one human only is depicted as a red triangle.

can understand is tricky. Follow up observations of marginal detections (peak S/N < 5) were conducted at Arecibo during the autumn of 2006 using the '*L*-band Wide' feed and at Green Bank using the 110 m dish in the summer and autumn of 2006.

4.3.3 *H*-band properties

Despite not detecting a dark galaxy candidate it is interesting to analyse the stellar properties of this H I selected galaxy sample. This preliminary study is limited to those galaxies that were also detected by 2MASS (Skrutskie et al. 2006). Unlike the SuperCOSMOS images, the NIR data is accurately calibrated, and is also a good indicator of stellar mass (Gavazzi, Pierini & Boselli, 1996; Rosenberg, Schneider & Posson-Brown 2005), making it ideal for these purposes.

2MASS data (extracted from the extended source catalogue) were available for only 15 candidate counterparts of the 24 H I sources. Fig. 4.15 shows the distribution

of the M_{HI}/L_H ratio, of the H-band effective radius (r_e: the radius containing 50% of the light), effective surface brightness (μ_e: the mean surface brightness within r_e) and concentration index (C_{31}: the ratio of the radii containing 75% and 25% of the light.) for this sample. As a reference, Fig. 4.16 shows the same distribution for a sample of 114 galaxies belonging to the HIPASS equatorial strip (Garcia-Appadoo, 2005). The two samples occupy a similar parameter space being composed of 'normal' disk-like gas-rich galaxies. But this is not surprising since the column density limits are similar for each survey.

Any deeper analysis of the stellar content of the H I sources must be postponed to future work due to the lack of sufficiently deep near infrared and optical data. The distribution of the M_{HI}/L_H ratio shown in Fig. 4.15 has to be considered as a lower limit of the real distribution of AGES sources, since it is based on the 15 brightest H-band candidate counterparts in the sample.

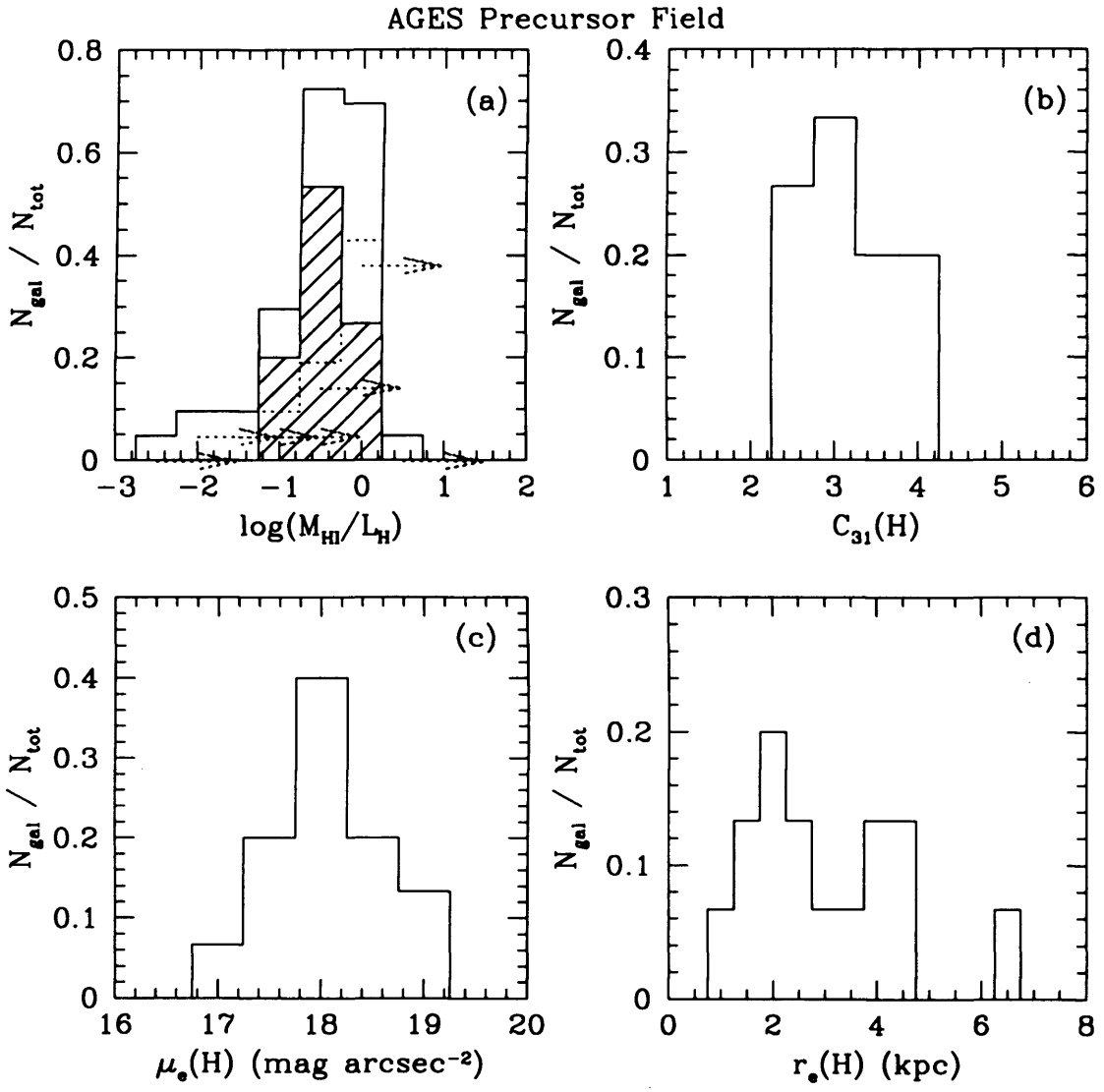

Figure 4.15: AGES precursor sample H I–H-band properties. (a) M_{HI}/L_H distribution. The shaded region represents measured values, the dotted lines represent estimated lower limits for those galaxies that were not detected in H-band. The white region is the sum of the measured values and the estimated values. (b) H-band concentration parameter distribution. Bulge galaxies are those galaxies with a value greater than 4. (c) H-band effective surface brightness distribution. (d) H-band effective radius.

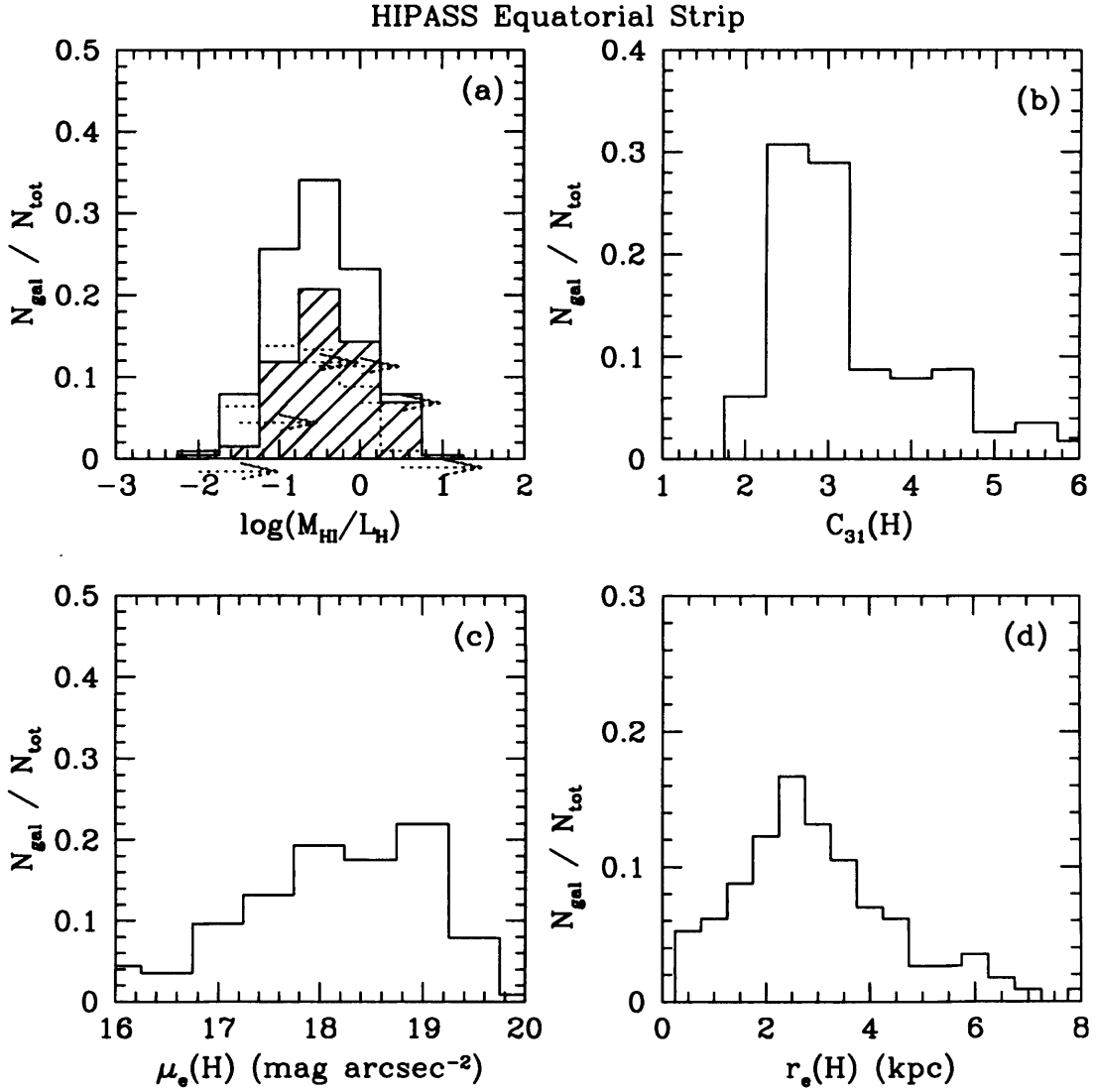

Figure 4.16: HIPASS Equatorial Strip H I–H-band properties. (a) M_{HI}/L_H distribution. The shaded region represents measured values, the dotted lines represent estimated lower limits for those galaxies that were not detected in H-band. The white region is the sum of the measured values and the estimated values. (b) H-band concentration parameter distribution. Bulge galaxies are those galaxies with a value greater than 4. (c) H-band effective surface brightness distribution. (d) H-band effective radius.

4.4 NGC 1156

4.4.1 Previous studies

NGC 1156 is a nearby, star-forming, irregular galaxy. While it has appeared in numerous catalogues (Schmidt & Boller, 1992; Prugniel et al. 1998; Martin, 1998; Broeils & Rhee, 1997) and studies of irregular galaxies (e.g. Hunter & Elmegreen, 2006; Hunter & Elmegreen, 2004; Elmegreen & Salzer, 1999) this galaxy has received little individual attention. Esipov et al. 1991 conducted $UBVR$ photometry and measured the rotation curve using Hα. In the optical bands it appears as a boxy irregular galaxy (Fig. 4.17). The galaxy shows a colour gradient, getting bluer towards the outskirts of the galaxy typical of late-type, star-forming galaxies. The rotation curve is still rising at the last point suggesting that the galaxy is dark matter dominated at all measured radii. Karachentsev et al. (1996) concentrated on the galaxy and used the brightest stars in the galaxy to estimate its distance ($\sim$ 7.8 Mpc) which is the figure that has been assumed in subsequent studies.

Early radio observations of NGC 1156 revealed a very symmetrical, undisturbed H I disk of mass $\log(M_{HI}/M_{\odot}) = 9.28$ (e.g. Broeils & van Woerden, 1994) making it similar in size to the LMC (Kim et al. 1998). More recent high resolution studies have revealed that the H I morphology is actually very clumpy, containing numerous holes and clumps especially in the outskirts. Fig. 4.18 is a reproduction from Swaters et al. (2002). The velocity field is limited by the column density sensitivity of the observations and so does not extend out much beyond the optical extent of the galaxy. Nevertheless the position angle of the galaxy exhibits signs of a warp in these central regions which could be indicative of a recent or ongoing

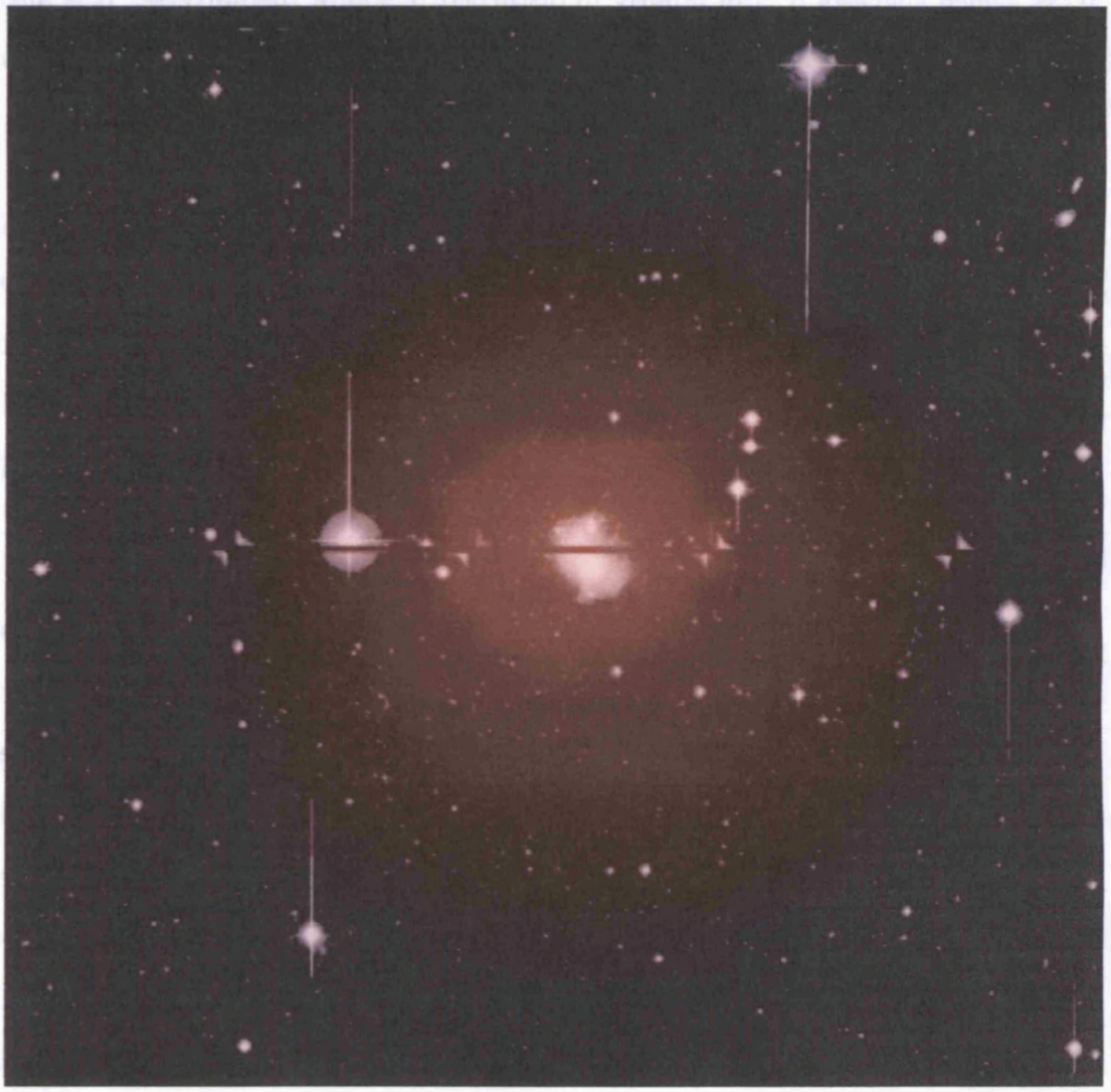

Figure 4.17: False colour image of NGC 1156. CFHT g and $r-$band data have been combined to produce 'natural' colour and H I is shown in orange.

interaction. Despite this, the velocity extent of the gas is quite symmetrical, with only a slight excess in the approaching half of the galaxy. The holes and knots in the outskirts of the galaxy could be evidence of gas accretion from the surrounding IGM, which suggests it is in a fairly undisturbed region of the universe. It is also possible that these holes could be generated from supernovae and stellar winds from massive-star clusters in the outer regions of the stellar disk.

The galaxy has B-band absolute magnitude of -18.5, which gives a $M_{HI}/L_B = 0.2$, typical of HSB galaxies, but quite low for a dwarf irregular. It has been found to be deficient in CO (Hunter & Sage, 1993; Taylor et al. 1998) which suggests a lack of molecular hydrogen. This is perhaps surprising given the abundance of neutral gas and the large amount of star formation inferred from the presence of many HII regions.

It is listed in the isolated galaxy catalogue (Karachentseva, 1973) as having no companion within 10°, making it one of the most isolated galaxies in the nearby universe. The combination of isolation, and the high degree of symmetry in the velocity extent of the gas suggest this galaxy is also one of the least disturbed galaxies in the nearby universe. This is also supported by the appearance of the gas disk. An isolated region such as this, which is free of the perturbing influences of other galaxies might prove to be an excellent place to search for dark galaxies. The chosen survey field measured 2.5°(R.A.) by 2°(dec.), equivalent to a physical region of 340×272 kpc at the distance of 7.8 Mpc.

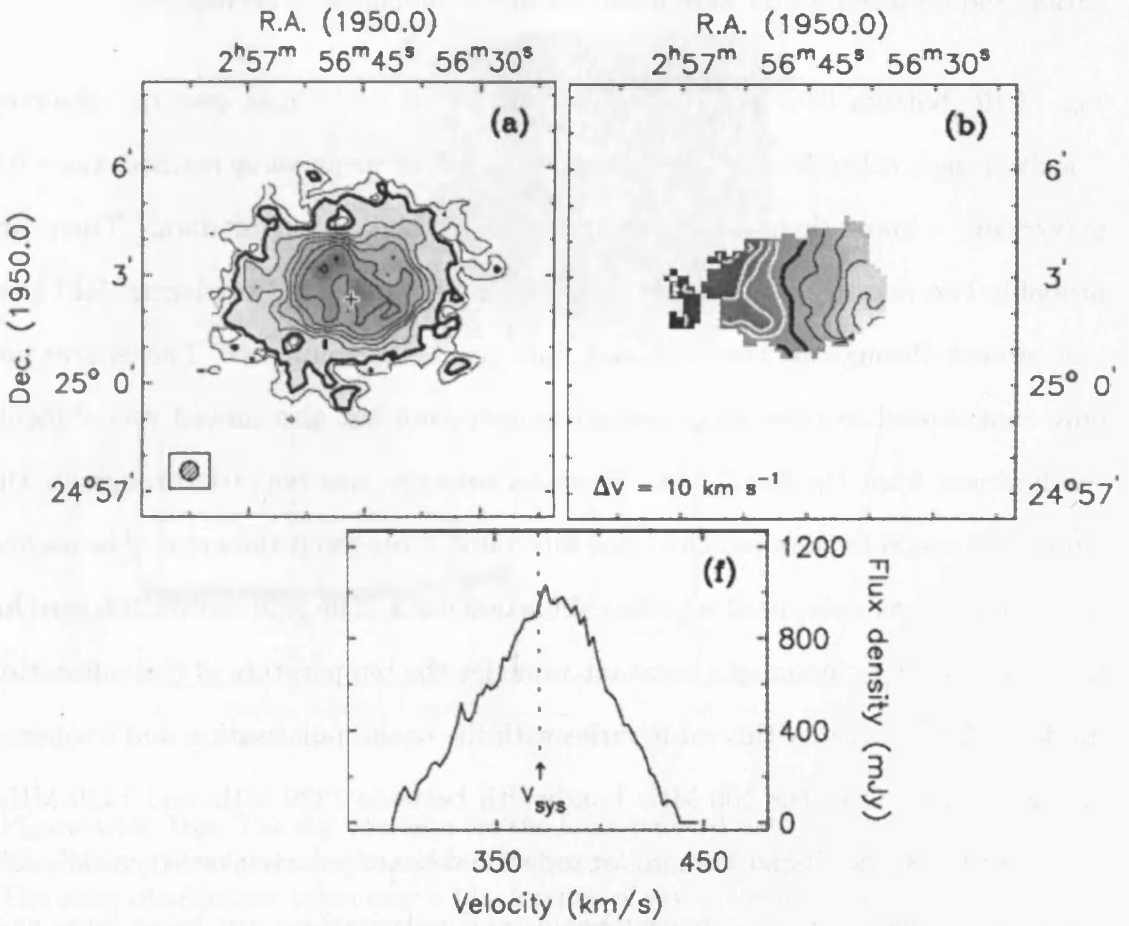

Figure 4.18: Top left: Integrated H I flux map of NGC 1156. Top right: Velocity field for NGC 1156. Bottom: Velocity profile for NGC 1156. Contours are shown at 1, 2, 5, 8, 11, 15, 20 and 30 $\times 10^{20}$ cm^{-2}. *All images reproduced from Swaters et al. (2002).*

4.4.2 H I observations

The observations were taken with the 305 m radio telescope at Arecibo, between 21/12/2005 and 2/2/2006. There were very few interruptions and the full survey depth (300s) was reached over the entire field. In contrast to the precursor observing strategy each position in the field was covered by each of the seven ALFA beams. This uniformity in sky coverage resulted in more uniform sensitivity, as shown in Fig. 4.19 (top), cutting down the effect of 'scalloping' in the final data. Aside from the slight change in the observing scan strategy, the method of obser-

vation and data reduction were identical to the precursor observations.

Fig. 4.19 (bottom left) is a plot of how the noise level varies over the observed velocity range, taken from a blank patch of sky. The mean value reached was ~0.7 mJy/beam - lower than predicted from the original precursor data. There are probably two reasons for this. The first is that the source of 'wandering' RFI that was present throughout the NGC 628 data has been eliminated. This source not only contributed to raising the system temperature but also proved very difficult to eliminate from the final data. Since its presence was noticed throughout the cube, this would have raised the r.m.s flux value throughout the cube. The second reason for a lower noise level is in the calibration itself. The gain calibration used for the NGC 628 data assumed a constant value for the temperature of the calibration diode of 12 K. In reality this value varies with the beam, polarisation and frequency of observation. Over the 100 MHz bandwidth between 1330 MHz and 1430 MHz, used by AGES, the change is small for individual beam polarisations (typically less than 1 K). The difference amongst beams and polarisations can be as large as 3 K. Data from the commissioning phase of ALFA were used to calculate an average value for the calibrator temperature taken over the whole observing bandwidth, for each of the beams and polarisations.

Fig. 4.20 (top left) shows the neutral gas extent of NGC 1156. In comparison to Fig. 4.18 (top left) the detail is not as great, but this is only to be expected due to the larger beam of the single dish, Arecibo data. The AGES data is two orders of magnitude deeper in column density and reveals a very extended H I disk. Since the beam has not yet been deconvolved from this image, the true extent of the disk is unlikely to be as great as that shown. The ellipticity of the disk is actually very small suggesting, unlike previous surveys, that the gas disk of this galaxy has a very low inclination angle (~15°). The velocity field is fairly smooth,

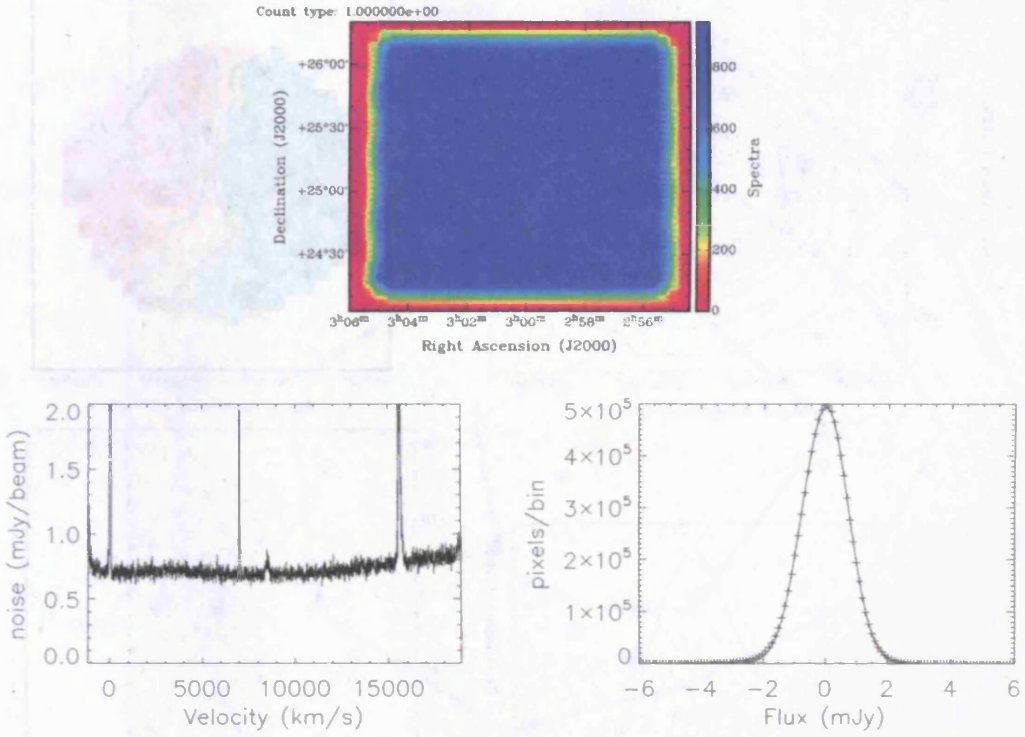

Figure 4.19: Top: The sky coverage for the final, reduced data in the NGC 1156 region. The colour scale represents the number of spectra contributing to each pixel. Bottom left: The noise distribution taken over a blank patch of sky in the final data which represents 300s integration time. RFI can be seen at 7000 (FAA radar), 8300 (L3 satellite) and 15500 km s^{-1}(FAA radar). Bottom right: A Gaussian provides a good fit to the flux distribution in a blank part of the sky. The mean value of the fit is ~ -0.0192 mJy, with a 1-$\sigma = 0.74$ mJy.

even in the outer parts of the galaxy, where the data are not as affected by beam smearing. The position angle of the axis of rotation measured from the radio data is roughly 270°over the central regions, and increases to ~300°in the receding half of the galaxy. This is in contrast to the approaching half which remains at roughly 270°. The rotation axis and the semi-major axis, as measured from the optical, do not agree, suggesting some very interesting dynamics are shaping this galaxy. The evidence for interactions with nearby objects that have thus far gone undetected, is slim. The attention now turns to the surrounding field of NGC 1156 to see what objects will be revealed.

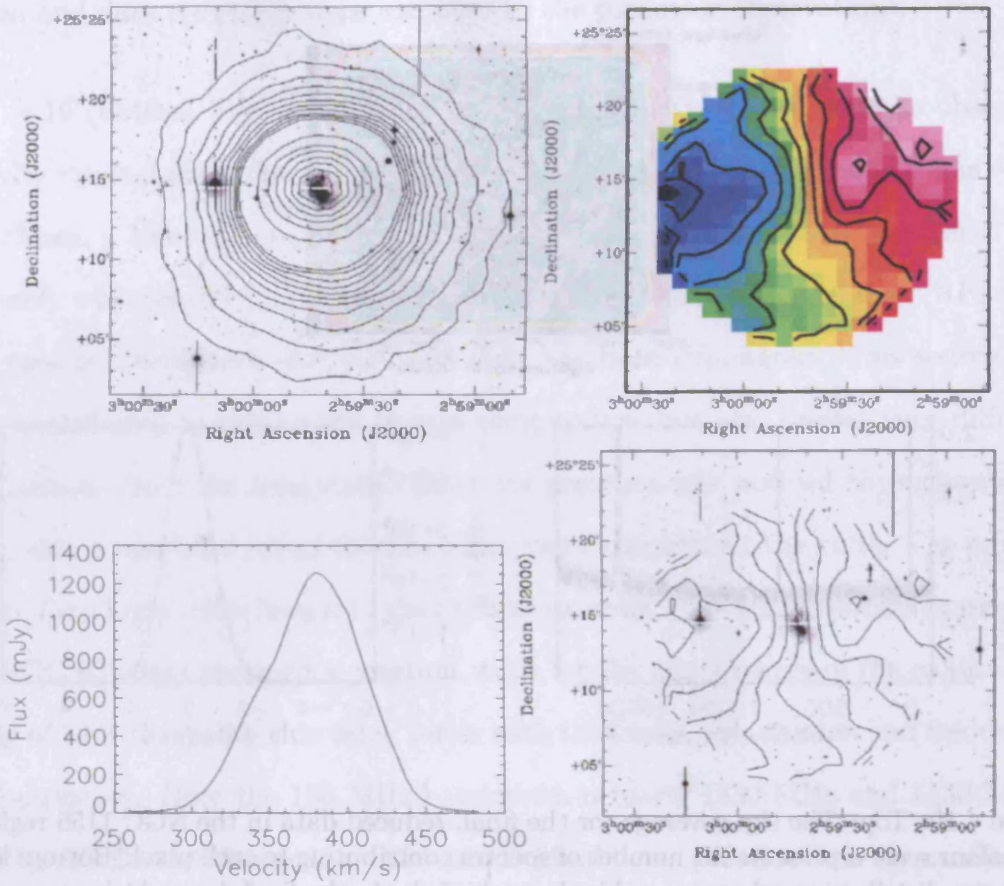

Figure 4.20: Top left: H I map integrated over the velocity extent of NGC 1156. Contour values are: 2×10^{18} (3σ), 1, 2, 3, 4, 5, 6, 7, 8, 9 ($\times10^{19}$), 1, 2, 3, 4, 5, 6, 7, 8 ($\times10^{20}$) cm^{-2}. Top right: Velocity field for NGC 1156, contours are from red to blue: 352, 357, 362, 367, 372, 377, 382, 387, 392, 397, 402 km s^{-1}. Bottom left: Velocity profile for NGC 1156. Bottom right: velocity field contours overlaid on a g-band image from the CFHT. Contour values are as for the velocity field.

4.4.3 H I Properties

One of the goals of the AGES was to discover previously undetected, low-mass companions to isolated galaxies such as NGC 1156. From this region one companion has been discovered: J030036+254707. Fig. 4.21 shows the H I distribution of the dwarf, overlaid on a SuperCOSMOS B-band image. It is impossible to make any assertions about the H I morphology since the disk is unresolved. There is definitely optical emission coincident with the centre of the H I and it is likely that

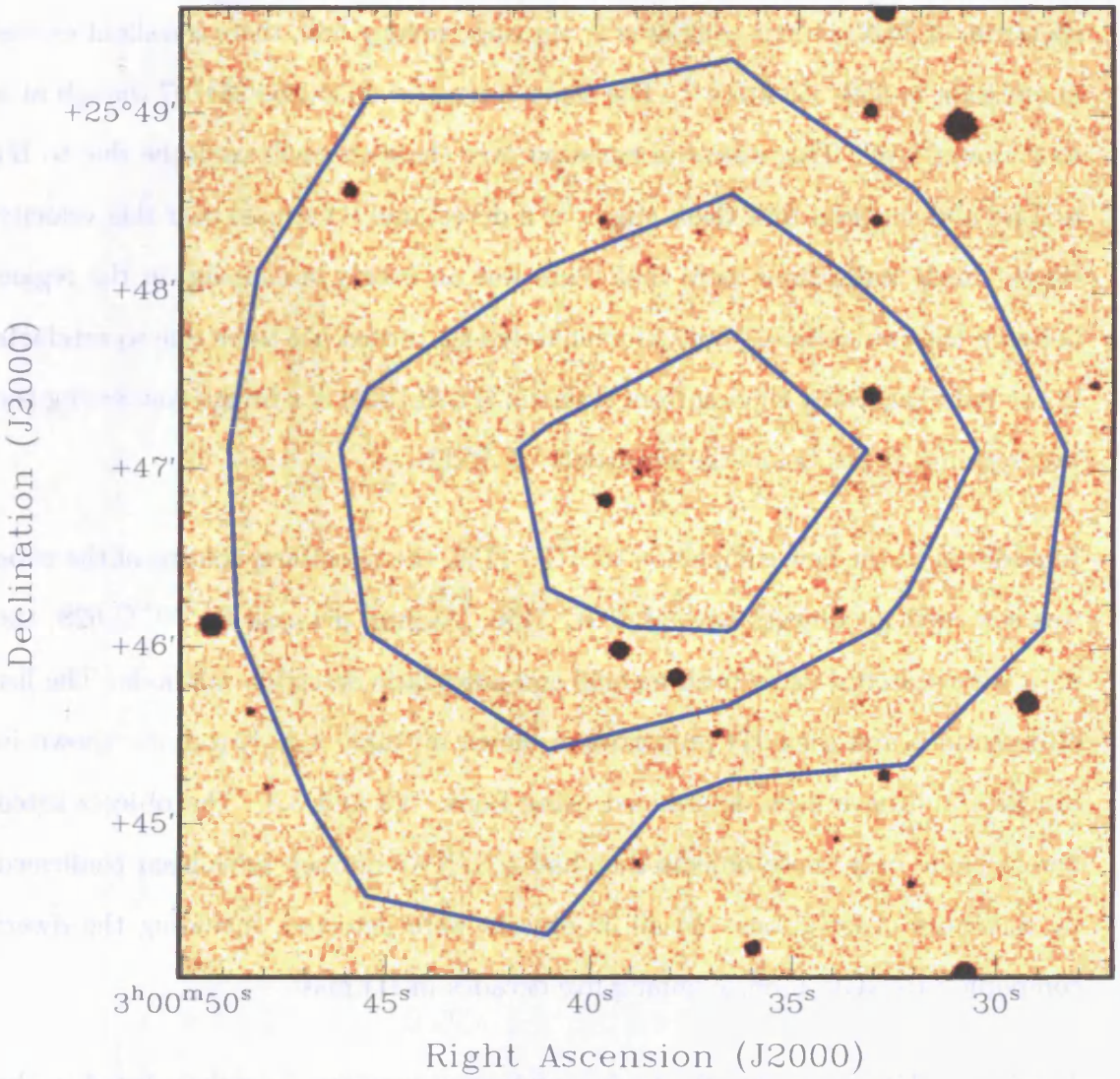

Figure 4.21: J030036+254706: A new dwarf companion to NGC 1156. H I contours are shown overlaid on a SuperCOSMOS *B*-band image. Contour values are drawn at 3, 5 and 7σ.

this is the optical counterpart. The measured H I mass, at the assumed distance of NGC 1156, is only $2\times10^6 M_\odot$ so it is not surprising that the optical emission is so low.

The dwarf is so close to NGC 1156 (2100″ ≡80 kpc separation on the sky) that it would be expected that there might be signatures of previous tidal interactions which may have stripped gas from the smaller galaxy. If the receding half of the

spectrum of NGC 1156 is compared to the approaching half, there is a slight excess in emission at 320–350 km s^{-1}. The same is true for J030036+254707 though at a much lower level. This excess in emission over these channels could be due to H I bridges and suggests that there might be a detectable H I stream over this velocity range. Early indications were that there was an excess in emission in the region between the two galaxies, but unfortunately this turned out to be due to artefacts in the data caused by ringing from Galactic H I. If there is a bridge connecting the two systems, it lies below the sensitivity of AGES.

In addition to the new companion to NGC 1156, the remaining volume of the cube was searched for objects beyond NGC 1156. As was the case for NGC 628, the data were searched using both manual and automatic detection methods. The list of detections and their H I properties is shown in Table 4.3. Errors are shown in brackets and have been determined using Eqns. 3.2 and 3.3. The objects listed here include only those objects that had a S/N>7 or they have been confirmed by follow-up observations. In all 39 objects were detected, including the dwarf companion to NGC 1156, spanning five decades in H I mass.

The NGC 1156 region benefits by having several previous detections listed in the Arecibo Galaxy Catalogue (AGC; Springob et al. 2005). Fig. 4.22 shows the measured fluxes from AGES compared with the fluxes from the AGC. The data have also been augmented by measurements from a new datacube centred on Abell 1367. This provided a further 25 fluxes. Comparison fluxes for this cube were taken from the AGC and the GOLDMINE archive (Gavazzi et al. 2003). The fluxes compare favourably with previous measurements although there is quite a large spread in measured values; the mean $F_{AGES}/F_{others} = 0.93 \pm 0.31$, which corresponds to a variation of about 14%.

AGES I.D.	RA (2000)	DEC (2000)	V_{sys} (km s^{-1})	Distance (Mpc)	W_{50} (km s^{-1})	W_{20} (km s^{-1})	F_{HI} (Jy km s^{-1})	M_{HI} ($\times 10^8 M_\odot$)	Previously catalogued objects	Angular separation (arcmin)	Optical redshift (km s^{-1})
J025511+243812	02:55:11.8	24:38:12	7017 (3.8)	97	98 (7.6)	180 (11.4)	0.2122 (0.03)	4.712	CGCG 484-024	1.4	6987
J025626+254614	02:56:26.0	25:46:14	10385 (2.8)	144	35 (5.6)	43 (8.4)	0.058 (0.02)	2.838	—	—	—
J025736+244321	02:57:36.5	24:43:21	10437 (6.9)	144	265 (13.8)	434 (20.7)	1.186 (0.08)	58.039	2MASX J02573860+2443194	0.4	—
J025742+261755	02:57:42.4	26:17:55	10384 (2.8)	144	231 (5.6)	239 (8.4)	1.368 (0.19)	66.946	—	—	—
J025753+255737	02:57:53.2	25:57:37	10424 (1.6)	144	234 (3.2)	254 (4.8)	1.255 (0.06)	61.416	2MASX J02575260+2558114	—	—
									2MASX J02575847+2559564	—	—
J025759+252143	02:57:59.7	25:21:43	6884 (7.2)	95	127 (14.4)	214 (21.6)	6.222 (0.20)	132.522	—	—	—
J025800+252556	02:58:00.6	25:25:56	6932 (2.1)	96	270 (4.2)	298 (6.3)	1.49 (0.07)	32.407	CGCG 484-026	0.4	6966
									CGCG 485-002B	2.2	6904
J025817+241737	02:58:17.0	24:17:37	10243 (2.8)	142	213 (5.6)	248 (8.4)	0.851 (0.06)	40.497	—	—	—
J025817+252711	02:58:17.6	25:27:11	10515 (1.0)	146	204 (2.0)	233 (3.0)	1.518 (0.05)	76.364	CGCG 485-004	0.9	10508
J025834+241844	02:58:34.7	24:18:44	10158 (3.0)	141	317 (6.0)	394 (9.0)	0.822 (0.05)	38.568	2MASX J02583738+2418331	1.1	—
									2MASX J02582235+2418241	2.5	—
J025835+251656	02:58:35.5	25:16:56	10457 (0.4)	145	171 (0.8)	191 (1.2)	4.535 (0.05)	225.022	UGC 02442	0.4	10463
J025842+252348	02:58:42.2	25:23:48	10436 (2.6)	144	101 (5.2)	170 (7.8)	1.01 (0.06)	49.426	V Zw 298	2.0	10383
									2MASX J02584323+2524381	3.0	—
J025842+254521	02:58:42.5	25:45:21	7222 (0.9)	100	218 (1.8)	239 (2.7)	2.365 (0.06)	55.814	UGC 02445	0.5	7210
J025903+254906	02:59:03.2	25:49:06	7161 (4.5)	99	83 (9.0)	110 (13.5)	0.126 (0.03)	2.914	—	—	—
J025903+253510	02:59:03.9	25:35:10	7116 (4.8)	98	109 (9.6)	157 (14.4)	0.4454 (0.05)	10.095	—	—	—
J025917+244756	02:59:17.0	24:47:56	4658 (1.7)	64	56 (3.4)	77 (5.1)	4.039 (0.11)	39.043	2MASX J02592467+2447363	1.8	—
J025930+255419	02:59:30.2	25:54:19	10400 (4.2)	144	221 (8.4)	306 (12.6)	1.335 (0.07)	65.331	2MASX J02593158+2554122	1.0	—
									/ NVSS J025939+255324	2.8	—
J025937+253437	02:59:37.5	25:34:37	10223 (3.0)	141	68 (6.0)	88 (9.0)	0.22 (0.04)	10.425	2MASX J02592969+2534222	1.1	—
J025952+254350	02:59:52.2	25:43:50	7197 (6.3)	99	19 (12.6)	85 (18.9)	0.1326 (0.03)	3.067	IRAS F02570+2534	2.8	—
J025954+241323	02:59:54.0	24:13:23	10226 (1.1)	142	303 (2.2)	329 (3.3)	5.328 (0.11)	253.544	2MASX J02595650+2412442	0.4	—
									/ 2MASX J02594999+2412122	1.8	—
J030008+241600	03:00:08.3	24:16:00	15091 (3.6)	209	430 (7.2)	441 (10.8)	2.107 (0.23)	217.205	2MASX J03000813+2415503	0.5	—
J030014+250315	03:00:14.0	25:03:15	11306 (1.2)	157	76 (2.4)	92 (3.6)	0.9227 (0.05)	53.675	2MASX J03001739+2504263	1.5	—
J030027+241301	03:00:27.2	24:13:01	9877 (1.7)	137	57 (3.4)	120 (5.1)	0.912 (0.05)	40.397	—	—	—
J030027+241301	03:00:27.2	24:13:01	9922 (6.1)	137	190 (12.2)	220 (18.3)	0.88 (0.13)	38.979	—	—	—

Table 4.3: H I properties of objects detected in the NGC 1156 region.

AGES I.D.	RA (2000)	DEC (2000)	V_{sys} (km s^{-1})	Distance (Mpc)	W_{50} (km s^{-1})	W_{20} (km s^{-1})	F_{HI} (Jy km s^{-1})	M_{HI} ($\times 10^8 M_\odot$)	Previously catalogued objects	Angular separation (arcmin)	Optical redshift (km s^{-1})
J030027+255407	03:00:27.6	25:54:07	10671 (12.1)	148	123 (24.2)	226 (36.3)	1.978 (0.14)	102.250	—	—	—
J030036+254707	03:00:36.5	25:47:07	310 (2.4)	7.9	20 (4.8)	46 (7.2)	0.1152 (0.02)	0.016	—	—	—
J030111+242411	03:01:11.5	24:24:11	9793 (2.2)	136	392 (4.4)	429 (6.6)	1.89 (0.08)	82.500	2MASX J03011237+2424204	0.3	—
J030136+245602	03:01:36.2	24:56:02	10396 (5.4)	144	188 (10.8)	243 (16.2)	0.6986 (0.07)	34.187	NVSS J030130+245539	1.8	—
									2MASX J03014886+2455404	2.5	—
J030139+254442	03:01:39.2	25:44:42	6733 (2.1)	93	149 (4.2)	187 (6.3)	8.712 (0.16)	177.826	2MASX J03014354+2542474	1.7	—
									MG3 J030138+2541	2.2	—
									2MASX J03012671+2544484	2.8	—
J030145+254314	03:01:45.7	25:43:14	11217 (1.7)	155	312 (3.4)	332 (5.1)	0.9201 (0.06)	52.169	2MASX J03014354+2542474	0.7	—
									MG3 J030138+2541	1.3	—
J030159+250030	03:01:59.7	25:00:30	7024 (1.2)	97	264 (2.4)	286 (3.6)	2.039 (0.06)	45.276	2MASX J03020033+2500524	1.3	—
J030204+254745	03:02:04.0	25:47:45	6784 (1.7)	94	253 (3.4)	280 (5.1)	2.294 (0.08)	47.837	FGC 0378	0.9	6786
J030234+244938	03:02:34.0	24:49:38	3260 (0.4)	45	48 (0.8)	63 (1.2)	1.166 (0.03)	5.572	NVSS J030238+244823	1.8	—
									NVSS J030232+245059	2.0	—
J030254+260028	03:02:54.2	26:00:28	10625 (0.7)	147	117 (1.4)	135 (2.1)	1.875 (0.05)	95.6	LSBC F480-V04	1.1	10613
J030308+260407	03:03:08.6	26:04:07	14007 (6.0)	194	209 (12.0)	281 (18.0)	0.3502 (0.05)	31.105	—	—	—
J030325+241510	03:03:25.2	24:15:10	14717 (5.3)	204	158 (10.6)	292 (15.9)	0.9906 (0.07)	97.291	—	—	—
J030354+241922	03:03:54.7	24:19:22	14508 (3.1)	201	102 (6.2)	135 (9.3)	6.552 (0.19)	624.709	—	—	—
J030450+260045	03:04:50.2	26:00:45	9405 (7.1)	130	134 (14.2)	183 (21.3)	0.2159 (0.05)	8.611	—	—	—
J030451+251527	03:04:51.7	25:15:27	14208 (3.5)	197	239 (7.0)	267 (10.5)	1.328 (0.10)	121.631	2MASX J03045518+2515558	1.2	—
									2MASX J03045762+2512478	2.0	—

Table 4.3: H I properties of objects detected in the NGC 1156 region.

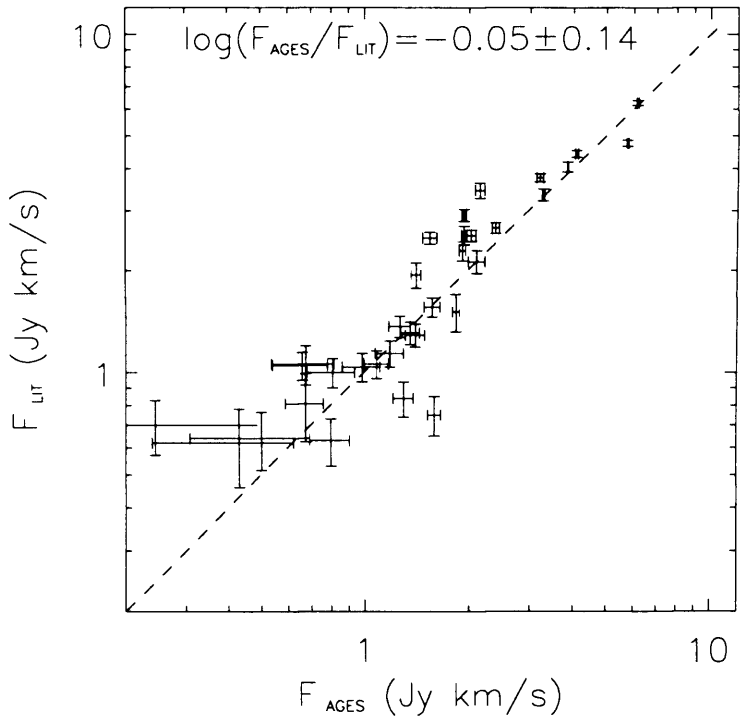

Figure 4.22: A comparison of integrated fluxes from AGES with those of previous surveys. The mean $\frac{F_{AGES}}{F_{others}}$ is 0.93±0.31. The dashed line is that expected for a one-to-one fit.

Fig. 4.23 is a comparison of the AGES systemic velocities with previous measurements. As expected the agreement is very good, with the ratio, $\mathrm{Vel}_{AGES}/\mathrm{Vel}_{others} = 1.0 \pm 0.1$. Fig. 4.24 shows a comparison of the velocity widths for the same sample. The velocity widths plotted are the mean value of the velocity width at 20% and 50%, since this is how a few of the GOLDMINE sample galaxy widths are quoted. There are only two extreme outliers; of these, one lies at the same velocity as a band of interference, which probably accounts for the difference. The other galaxy measurement is highly uncertain (Cortese, priv. comm.). Ignoring these two galaxies, $(\mathrm{Vel.\ Width})_{AGES}/(\mathrm{Vel.\ Width})_{others} = 1.02 \pm 0.02$ which is a very good agreement.

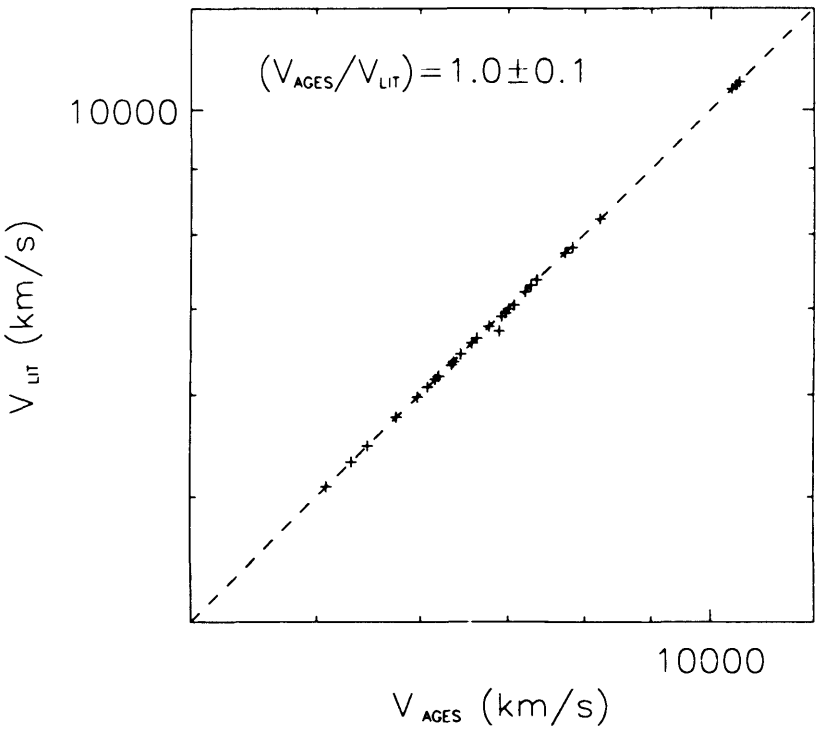

Figure 4.23: A comparison of systemic velocities from AGES with those of previous surveys. The velocity width here, is defined as the mean of the 20% and 50% widths to allow comparison with the velocity width measurements from GOLDMINE. The mean $Width_{AGES}/Width_{Lit}$ is 1.02±0.02. The dashed line is that expected for a one-to-one fit.

4.4.4 H I and optical properties of detected objects

As with the NGC 628 data, the comparison of optical data and radio data is a vital part of the analysis. The data for NGC 1156 benefit from additional optical spectra taken with the 1.5 m telescope at Loiano, and deep g and r-band data taken with the CFHT. Brief details of the observations are given in Section 3.7.2. The importance of the optical data lie in the ability to associate an optical galaxy with the H I detection. For a positive association, a coincident galaxy in the optical image is not enough. The redshift as measured in the optical bands is also required to be as sure as can be the H I and optical emission are coming from the same object.

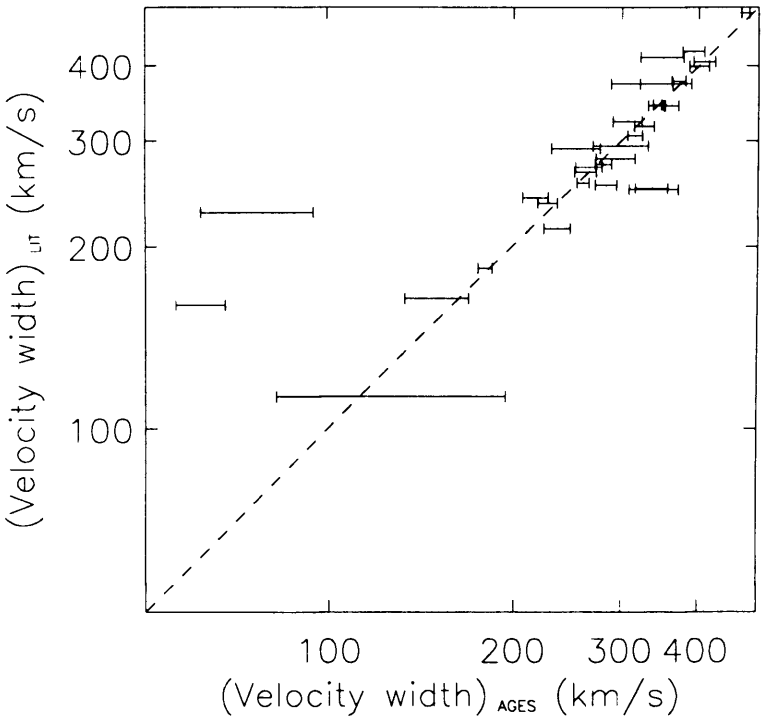

Figure 4.24: A comparison of velocity widths from AGES with those of previous surveys. The dashed line is that expected for a one-to-one fit.

The larger sample returned from the NGC 1156 data make it unwieldy to go into detail on each galaxy. Commentary here is restricted to those galaxies that show interesting characteristics. The first goal is to find galaxies with no optical emission – these are the prime candidates for dark galaxies. Two detections fall into this category: J025626+254614 and J030027+255407. Both galaxies were detected by both humans and POLYFIND. J025626+254614 was considered strong enough not to require confirmatory observations. J030027+255407 was re-observed using the L-band wide feed at Arecibo and confirmed as real after a 300s integration.

Since this field is subject to pockets of high optical extinction, it is prudent to check the B-band extinction factor, A_B, for each galaxy. NED gives values of 0.504 and 1.283 respectively for J025626+254614 and J030027+255407. If one

assumes the estimated B-band surface brightness limit of the POSS-II plates is $\sim$ 25.5 mag arcsec^{-2} then the lower limits for the central surface brightness are $\sim$ 25 and $\sim$ 24.2 mag arcsec^{-2} respectively. The H I masses of each galaxy are 2.4×10^8 $M_\odot$ and 6.3×10^8 $M_\odot$ respectively. While the central surface brightness limit on J025626+254614 is very low, it is by no means extreme for a LSB. The H I masses are typical of LSBs so it would not be surprising if deeper observations revealed two LSBs lurking behind a Galactic cloud of dust and gas. Unfortunately both galaxies fall outside of the field of view of the deep MEGACAM images and so these galaxies await further optical observations.

The rest of the objects have at least one potential optical counterpart located within the H I beam. The last column of Table 4.3 lists the optical velocities that were either available from the literature or acquired from Loiano. All the listed velocities agree well with the H I velocities, suggesting that these are indeed the optical counterparts for these objects. For those objects that have no optical spectra another method of determining a possible misassociation is to calculate the M_{HI}/L_B ratio for the potential counterpart, assuming the H I distance and see if it is reasonable.

For this investigation it is critical to have precisely calibrated optical data. Due to the uncertain nature of the SuperCOSMOS calibration (variable zero-points over different POSS-II plates, non-linear responses of the plate emulsions), the analysis is limited to the central square degree region covered by the MEGACAM images. Table 4.4 lists the H I detections in this region and the optical properties of their most likely counterparts.

Of the twelve H I detections in the MEGACAM images, none have unrealistic properties that might flag them as possible misidentifications. The object at $03^h01^m47.9^s$+25°24′25.4″has

a very high $M_{HI}/L_B = 34.31$ but this only helps reject it in favour of the bright 2MASX galaxy in this image, whose optical redshift is also in agreement. J025759+252143, J025903+253510 and J025952+254350 all have optical counterparts with $M_{HI}/L_B > 1$ which is indicative of gas-rich systems, but the values are all believable. J025903+253510 has a red colour ($g - r = 0.9$) and $M_{HI}/L_B > 5$. Normally one would expect such a gas-rich system to be relatively young and hence appear quite blue. The only object in the image is a faint smudge which may be an artefact, but given the high extinction ($A_B > 1$) it is most likely the brightest part of a red LSB that is showing.

4.5 Summary

In this chapter the results from two AGES survey regions (NGC 628 and NGC 1156) have been presented. The survey technique of co-adding successive observations results in the expected reduction in noise. The H I measurements made by AGES compare well with previous measurements in the literature, showing that the calibration and data reduction techniques are working as well as expected. Of the 69 detections made by AGES in these datacubes, 55 do not have previous H I measurements and 26 are previously uncatalogued.

The search for dark galaxies has returned two objects that are possible candidates, J025626+254614 and J030027+255407. J030027+255407 shares similar properties to VIRGOHI21 – it has a H I mass of a few $\times 10^8$ $M_\odot$ and a velocity width of $\sim$250 km s^{-1}. J025626+254614 in contrast has a narrow velocity width, but has a similar mass. The only optical data available for the regions of sky covering these two objects are the POSS-II plates and their associated digital scans. The lack of

Table 4.4: Optical properties of H I sources detected in the NGC 1156 region.

I.D.	RA (2000)	dec (2000)	m_g	μ_g mags arcsec^{-2}	A_B	M_g	m_r	μ_r mags arcsec^{-2}	A_R	$g-r$	M_{HI} $\times 10^8$ $M_\odot$	M_{HI}/L_g $M_\odot/L_\odot$
J025759+252143												
025802.8+252214.7	02 58 02.8	+25 22 14.7	20.30 (0.03)	24.95 (0.03)	0.59	-14.59	19.93 (0.03)	24.94 (0.04)	0.36	0.37 (0.05)	4.34	3.89
025759.7+252213.6	02 57 59.7	+25 22 13.6	20.79 (0.02)	24.21 (0.03)	0.58	-14.1	—	—	—	—	4.34	6.12
J025800+252556												
CGCG 484-026	02 58 04.2	+25 26 57	15.7 (0.02)	23.65 (0.03)	0.67	-19.21	15.3 (0.02)	23.34 (0.03)	0.42	0.4 (0.04)	42.35	0.54
J025817+252711												
CGCG 485-004	02 58 18.2	+25 26 57	14.52 (0.02)	22.93 (0.03)	0.74	-21.3	14.87 (0.02)	23.24 (0.04)	0.46	-0.35 (0.04)	98.45	0.18
J025835+251656												
UGC 02442	02 58 35.5	+25 16 48	15.04 (0.02)	24.29 (0.04)	0.64	-20.77	14.76 (0.02)	23.38 (0.04)	0.4	0.28 (0.04)	192.4	0.58
J025842+252348												
2MASX												
J02584322+252438	02 58 43.2	+25 24 38	16.13 (0.02)	23.73 (0.03)	0.85	-19.66	15.4 (0.02)	22.90 (0.03)	0.05	0.73 (0.04)	90.85	0.76
V Zw 298	02 58 44.5	+25 23 42	15.09 (0.02)	23.24 (0.03)	0.85	-20.7	14.59 (0.02)	22.59 (0.03)	0.53	0.51 (0.04)	90.85	0.29
J025903+253510												
025906.6+253454.1	02 59 06.6	+25 34 54.1	20.00 (0.02)	24.88 (0.03)	1.11	-14.96	19.07 (0.03)	23.74 (0.03)	0.69	0.93 (0.04)	8.31	5.43
J025917+244756												
025917.4+244843.7	02 59 17.4	+24 48 44	18.31 (0.03)	25.04 (0.04)	0.8	-15.73	18.03 (0.03)	24.60 (0.04)	0.5	0.28 (0.05)	3.38	1.07
025916.4+244829.2	02 59 16.4	+24 48 29.2	19.04 (0.03)	24.62 (0.03)	0.8	-14.99	17.92 (0.02)	23.89 (0.03)	0.5	1.12 (0.04)	3.38	2.1
025914.2+244737.3	02 59 14.2	+24 47 37.3	19.76 (0.03)	25.03 (0.04)	0.81	-14.28	19.3 (0.03)	24.8 (0.04)	0.5	0.45 (0.05)	3.38	4.06
J025937+253437												
025935.0+253502.5	02 59 35.0	+25 35 02.5	17.99 (0.02)	23.73 (0.03)	1.17	-17.75	17.76 (0.02)	23.62 (0.03)	0.72	0.24 (0.04)	8.47	0.41
025929.6+253421.6	02 59 29.6	+25 34 21.6	17.83 (0.02)	24.03 (0.03)	1.16	-17.92	17.15 (0.02)	23.38 (0.03)	0.72	0.67 (0.04)	8.47	0.35
J025952+254350												
025950.8+254400.8	02 59 50.8	+25 44 00.8	21.26 (0.04)	25.11 (0.05)	1.29	-14.82	19.21 (0.03)	24.20 (0.04)	0.8	0.95 (0.05)	2.69	1.96
J030014+250315												
030014.0+250325.0	03 00 14.0	+25 03 25.0	19.19 (0.03)	24.28 (0.03)	1.08	-16.79	18.87 (0.03)	23.87 (0.03)	0.67	0.32 (0.04)	28.63	3.37
030017.5+250426.7	03 00 17.5	+25 04 26.7	18.68 (0.02)	23.96 (0.03)	1.07	-17.29	17.6 (0.02)	23.02 (0.03)	0.66	1.08 (0.04)	28.63	2.12
J030136+245602												
030137.7+245535.6	03 01 37.7	+24 55 35.6	17.24 (0.02)	23.22 (0.03)	1.36	-18.55	16.6 (0.02)	22.77 (0.03)	0.84	0.64 (0.04)	18.01	0.42
J030145+254314												
030143.7+254247.1	03 01 43.7	+25 42 47.1	15.85 (0.02)	24.41 (0.04)	0.93	-20.1	15.37 (0.02)	23.72 (0.04)	0.57	0.48 (0.05)	78.93	0.44
030147.9+254254.0	03 01 47.9	+25 42 54.0	20.57 (0.04)	25.52 (0.05)	0.91	-15.38	19.74 (0.03)	24.16 (0.03)	0.57	0.83 (0.05)	78.93	34.31

deep optical data and the presence of high extinction in this part of the sky does not put a stringent limit on the central surface brightness of these objects, and so they are only flagged as *potential* dark galaxies.

In the next chapter, the reliability of the detections and the completeness of the survey are examined in detail. A calculation of the completeness of the survey allows a reliable calculation of the survey volume. With an accurate measurement of the survey volume it is possible to discuss the implications of these results. The HIMF is also calculated from knowledge of the survey volume. Due to the small number of galaxies, the data have been augmented with data from the Abell 1367 datacube, bringing the number of detected galaxies to 142, spanning five decades in H I mass.

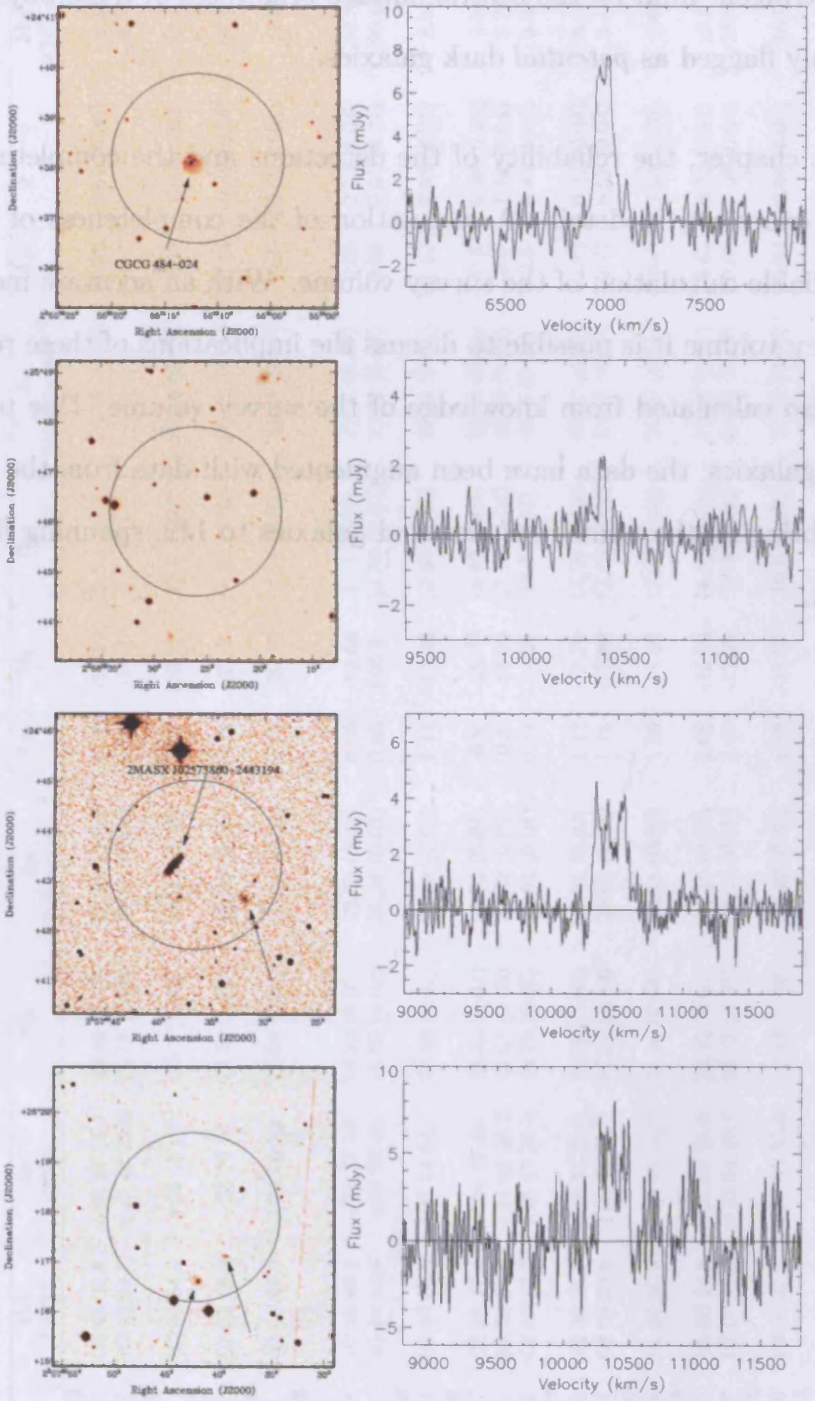

Figure 4.25: Top to bottom: SuperCOSMOS *B*-band images and accompanying H I spectra for AGES objects J025511+243812, J025626+254614, J025736+244321, J025742+261755

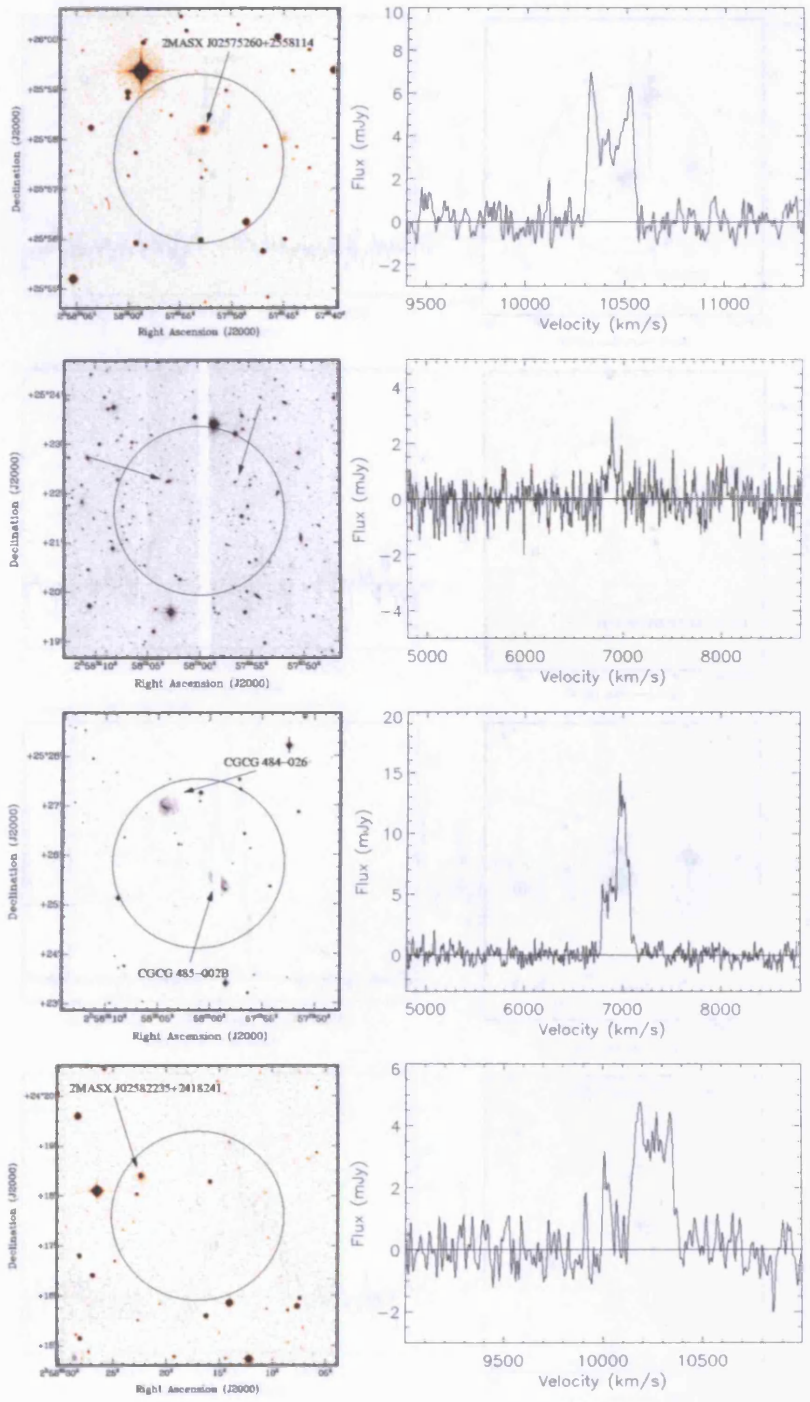

Figure 4.26: Top to bottom: SuperCOSMOS *B*-band images and accompanying H I spectra for AGES objects J025753+255737, J025759+252143, J025800+252556, J025817+241737

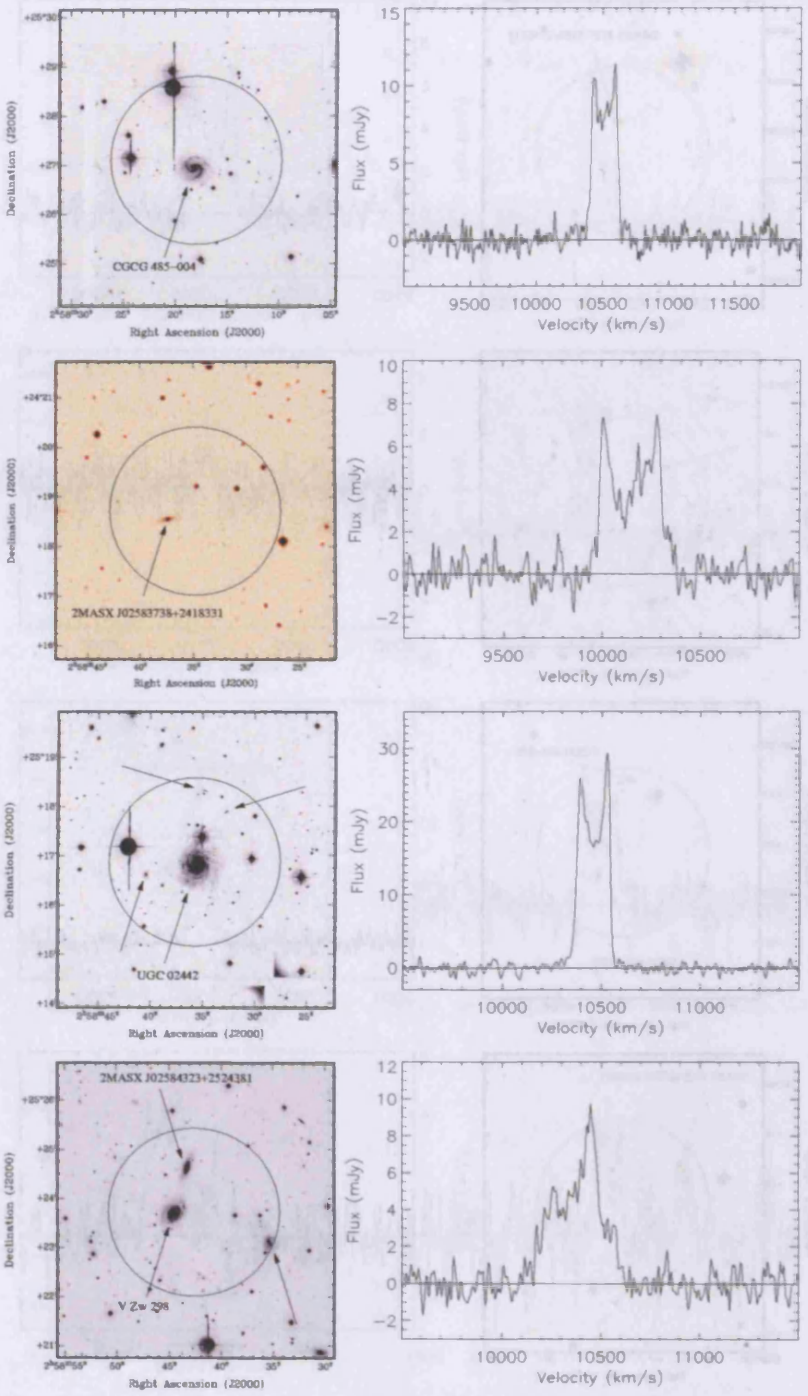

Figure 4.27: Top to bottom: SuperCOSMOS *B*-band images and accompanying H I spectra for AGES objects J025817+252711, J025834+241844, J025835+251656, J025842+252348

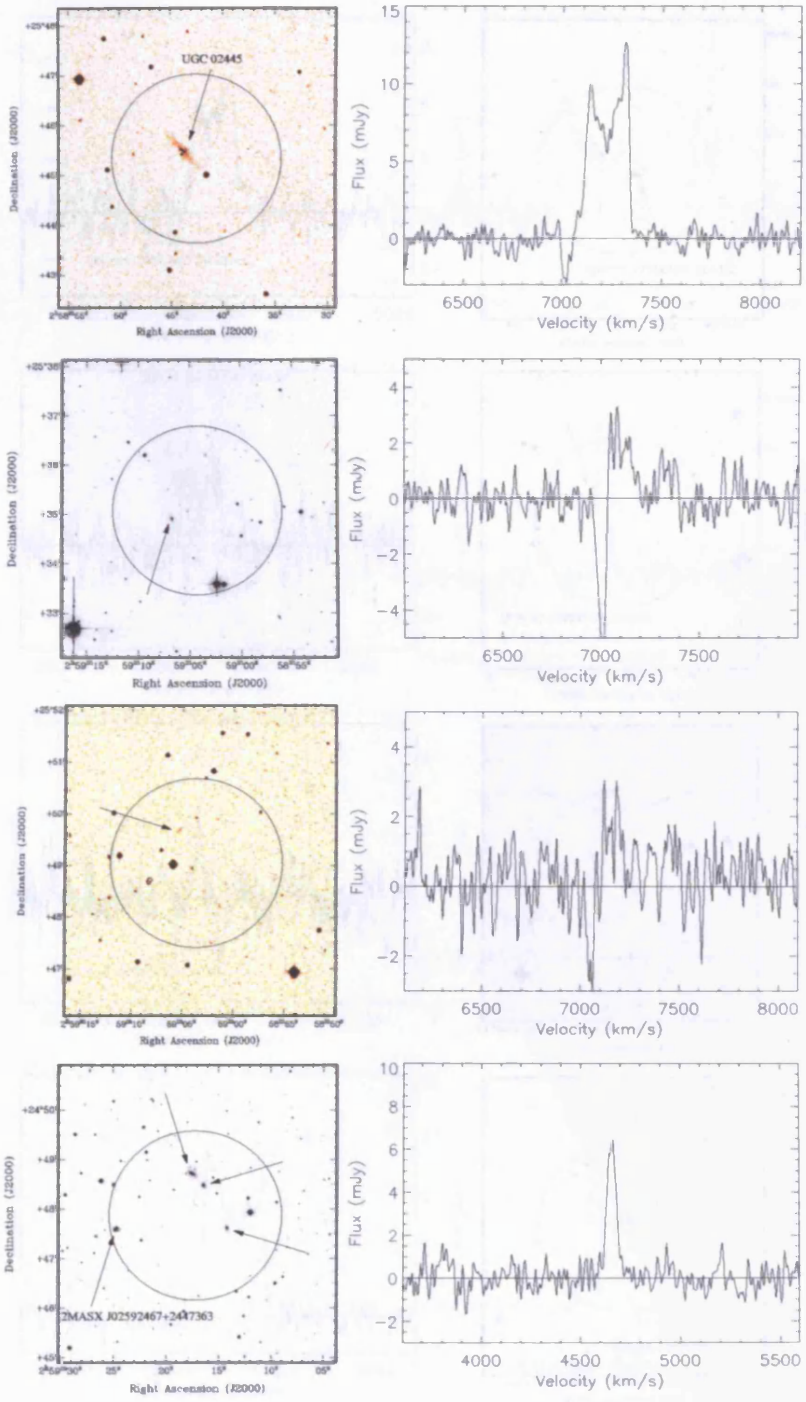

Figure 4.28: Top to bottom: SuperCOSMOS *B*-band images and accompanying H I spectra for AGES objects J025842+254521, J025903+253510, J025903+254906, J025917+244756

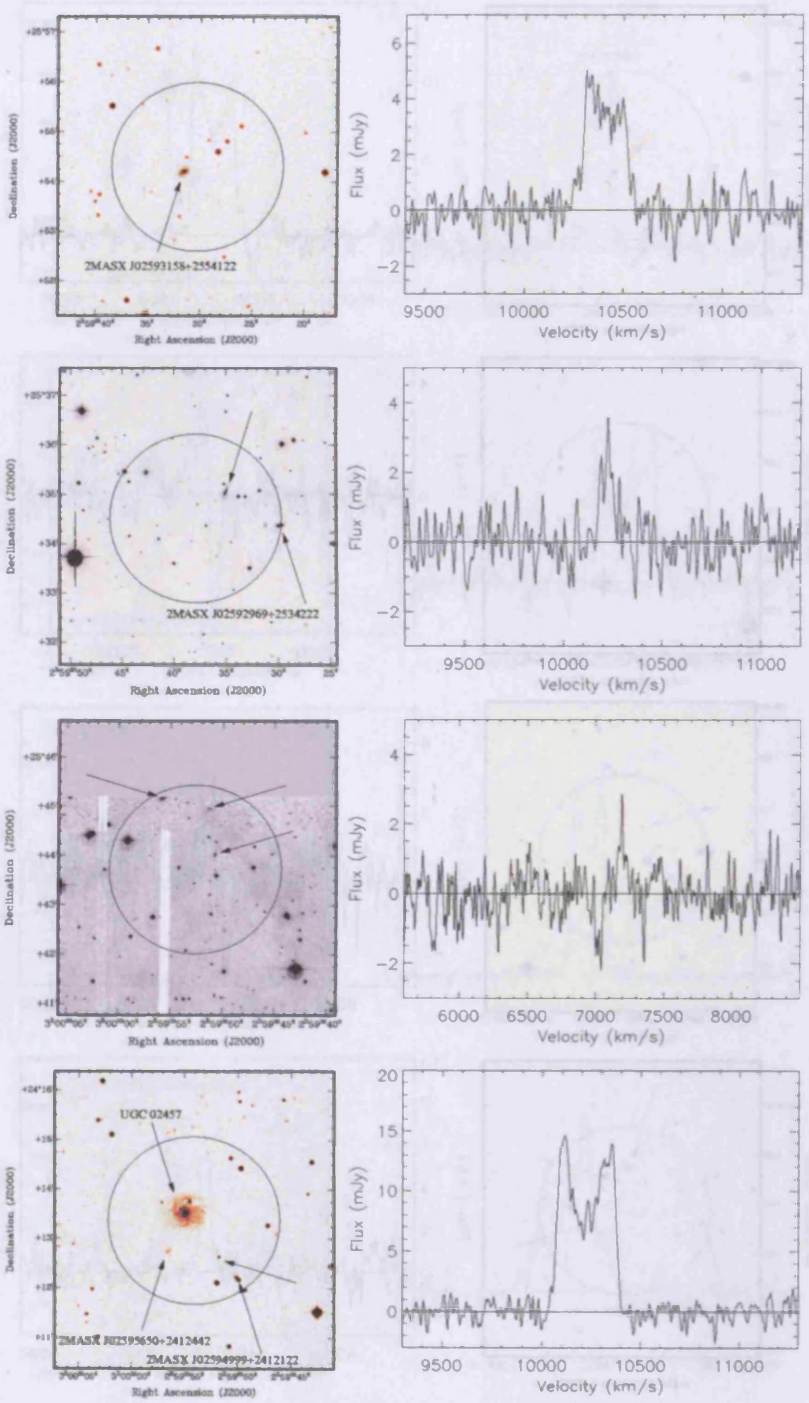

Figure 4.29: Top to bottom: SuperCOSMOS *B*-band images and accompanying H I spectra for AGES objects J025930+255419, J025937+253437, J025952+254350, J025954+241323

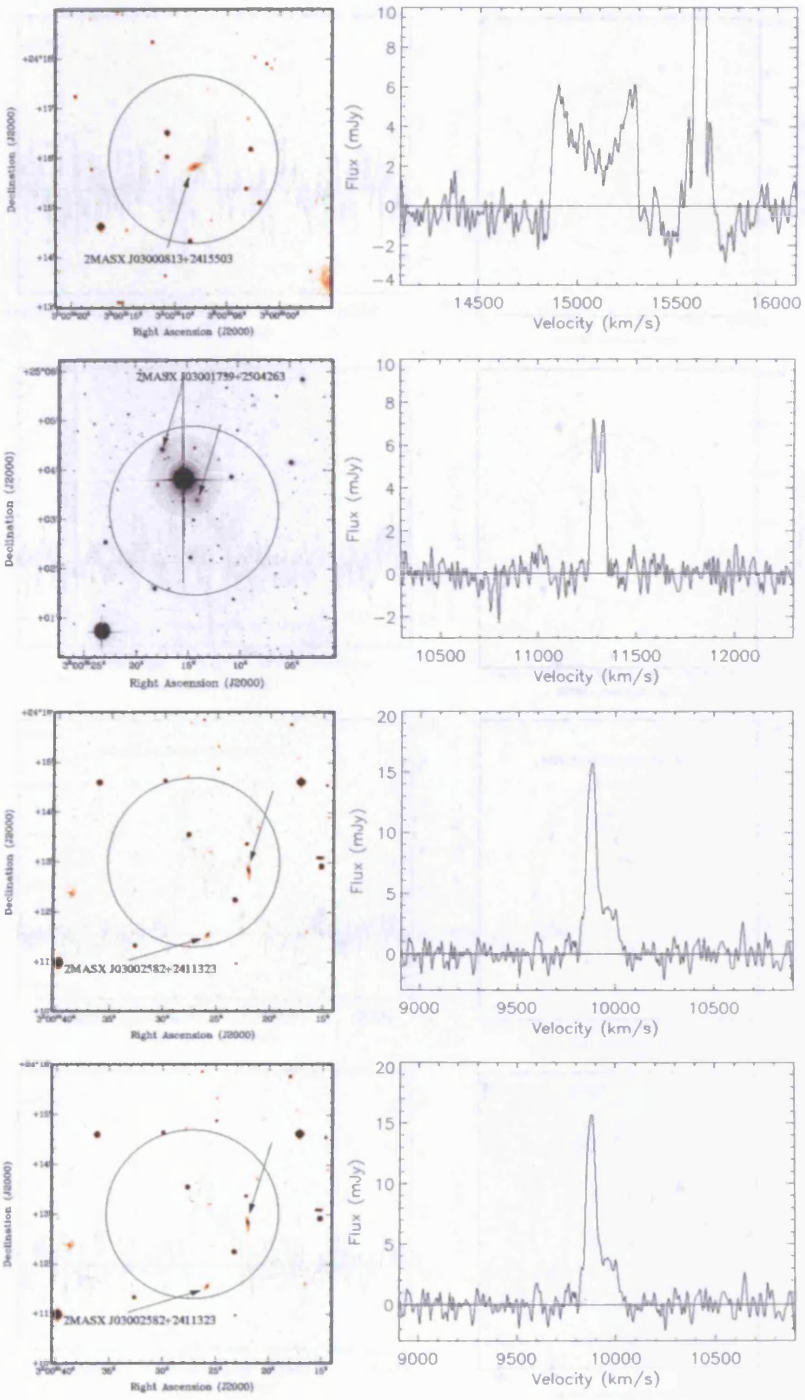

Figure 4.30: Top to bottom: SuperCOSMOS *B*-band images and accompanying H I spectra for AGES objects J030008+241600, J030014+250315, J030027+241301, J030027+241301

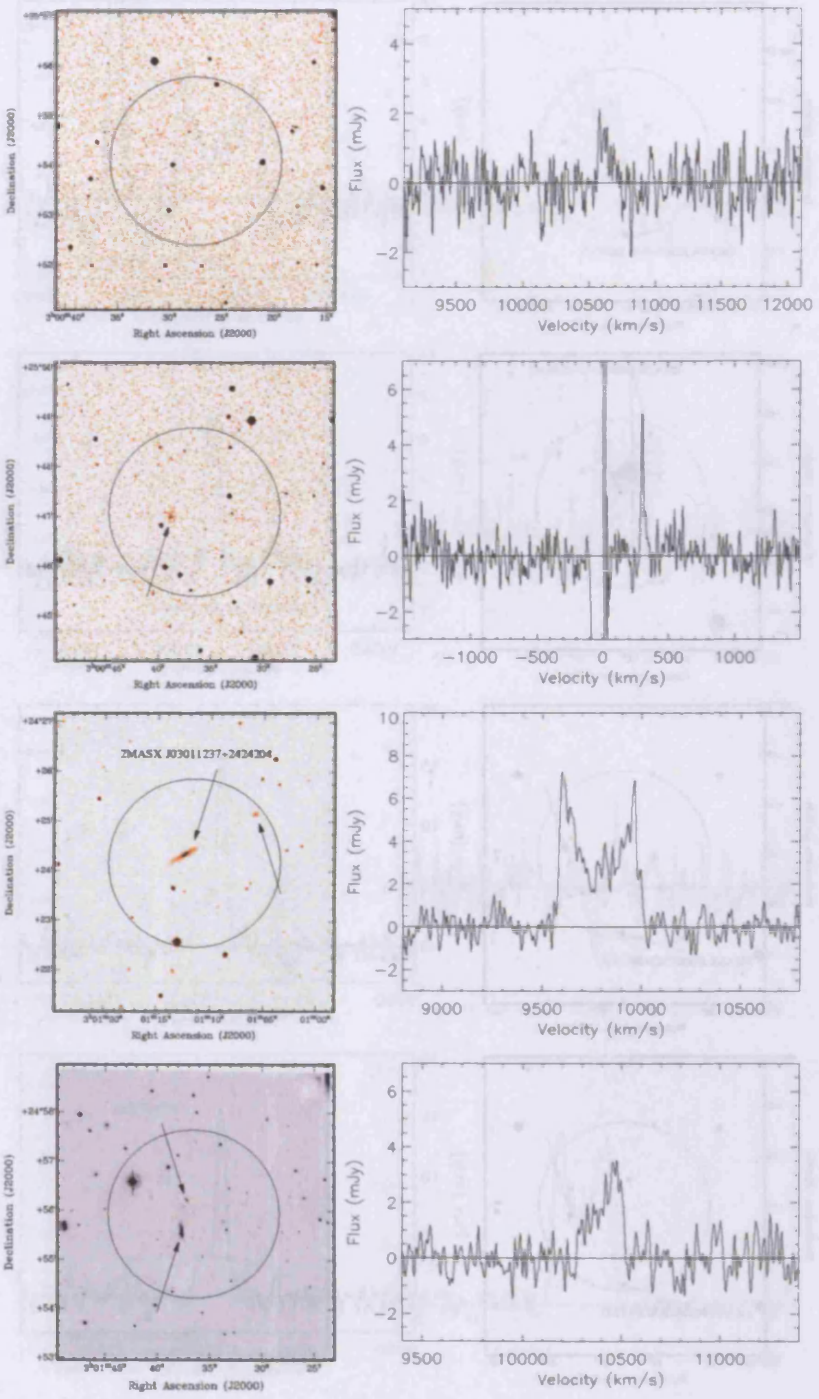

Figure 4.31: Top to bottom: SuperCOSMOS *B*-band images and accompanying H I spectra for AGES objects J030027+255407, J030036+254707, J030111+242411, J030136+245602

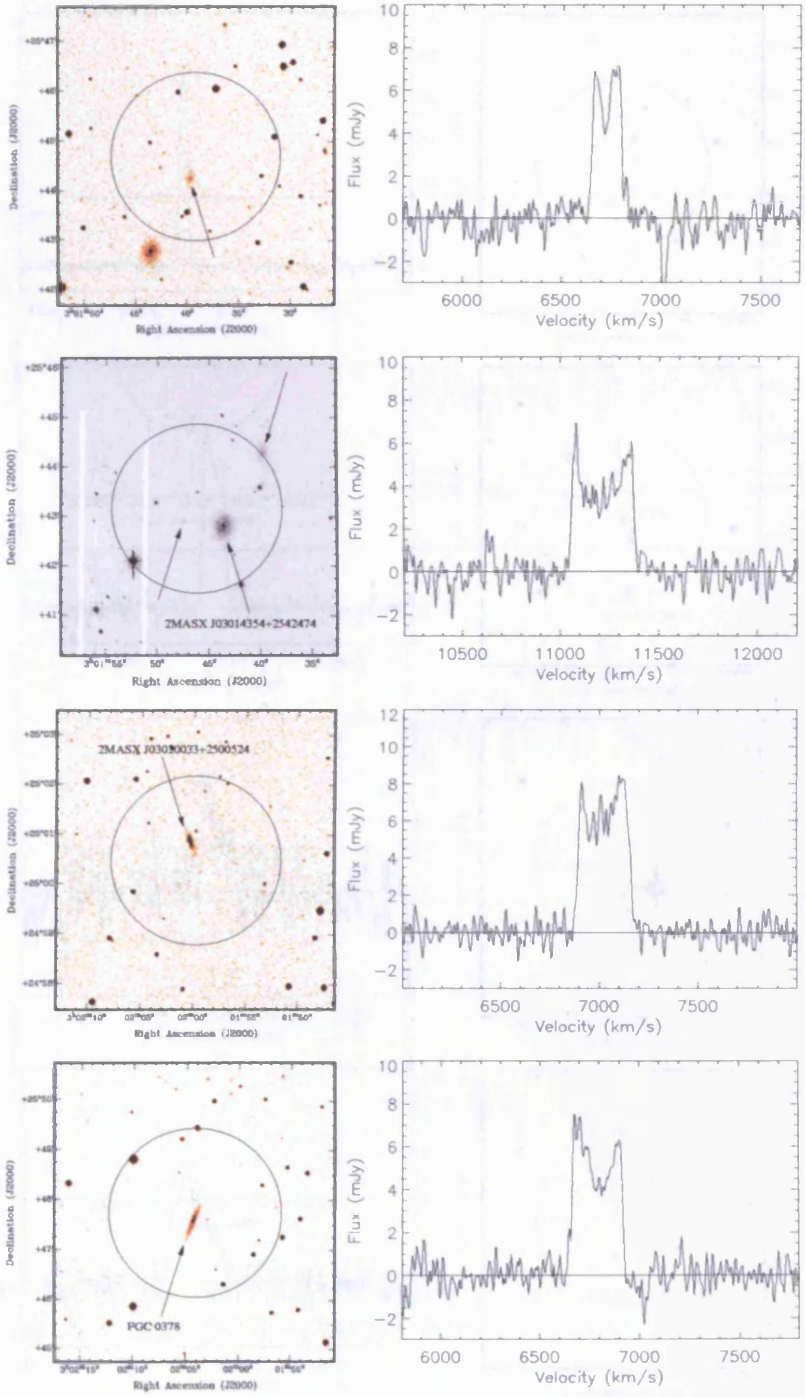

Figure 4.32: Top to bottom: SuperCOSMOS *B*-band images and accompanying H I spectra for AGES objects J030139+254442, J030145+254314, J030159+250030, J030204+254745

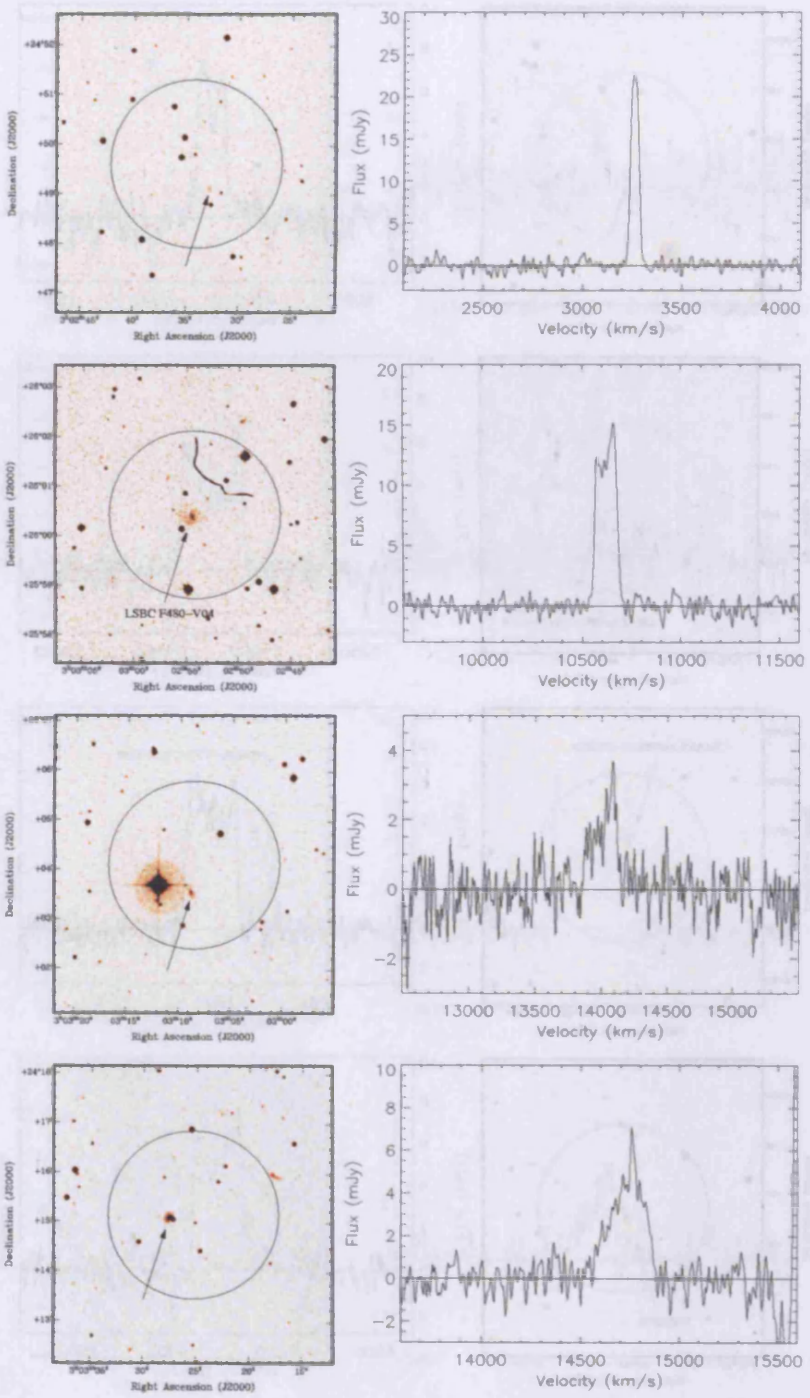

Figure 4.33: Top to bottom: SuperCOSMOS *B*-band images and accompanying H I spectra for AGES objects J030234+244938, J030254+260028, J030308+260407, J030325+241510

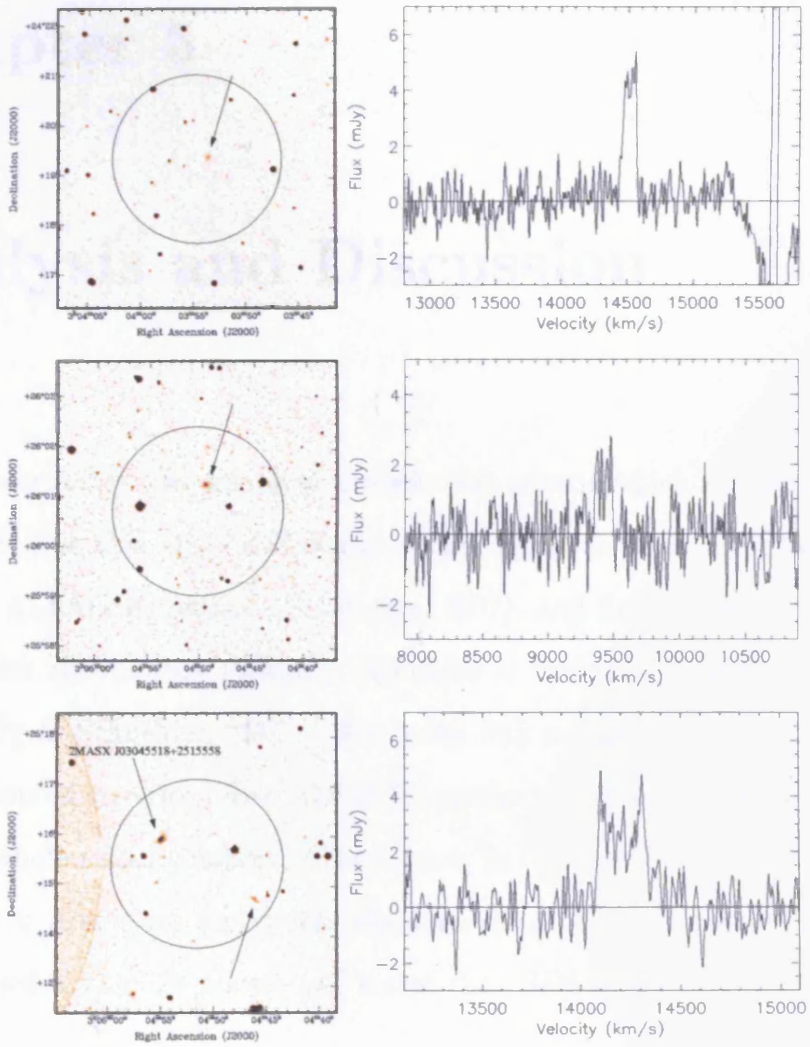

Figure 4.34: Top to bottom: SuperCOSMOS *B*-band images and accompanying H I spectra for AGES objects J030354+241922, J030450+260045, J030451+251527

Chapter 5

Analysis and Discussion

This chapter starts with a look at the selection criteria which are most appropriate for AGES. For this three definitions of the signal-to-noise are examined; peak flux, the ALFALFA method (Saintonge, 2007), and finally the method used for the Arecibo Slice Survey (Spitzak, Schneider & Rosenberg, 1998) and the ADBS (Rosenberg & Schneider, 2002). The peak flux method is historically the most widely adopted criterion. The ALFALFA method takes a mean S/N measurement over the whole velocity extent of the source. In the Arecibo Slice Survey, Spitzak, Schneider & Rosenberg found that the noise of an object increases as the velocity width raised to the 3/4 power, and scaled their S/N values accordingly.

Once these are defined, they can be used to flag which sources should be accepted, which should be followed up and which should be ignored as spurious. This should hopefully reduce the amount of time and effort spent in building future catalogues from AGES data.

The subsequent section discusses the completeness of the data presented here (NGC

628, NGC 1156 and Abell 1367). With knowledge of the completeness as a function of S/N it is possible to correct the detected number density of objects, to that expected for the true population. This information is then used to calculate the HIMF and the H I mass density function. The results of the dark galaxy search within AGES are then discussed in the context of the theoretical prediction of (Davies et al. 2006).

5.1 Selection Criteria and Reliability

This section is an investigation into which S/N formula is most appropriate for the AGES data and which search criteria prove to be the most reliable. As stated previously, detection by eye is difficult to quantify in terms of selection criteria. With an automated detection algorithm, one has a rigidly defined set of search criteria. Unfortunately it is difficult to completely eradicate using a subjective human assessment at some level of the data reduction process, whether it be to identify RFI or galaxies.

The followup observations from both NGC 1156 and NGC 628 proved vital in defining the selection criteria from this sample of AGES galaxies. They provide a direct measure of the reliability of detections for a given S/N. Reliability in this sense is simply a ratio of the number of real sources compared to the total number of sources in a particular S/N bin. The reliability function also defines the upper limit on the completeness of the survey.

Different methods of defining S/N have been employed for previous surveys. Many of the early surveys employed a simple peak flux S/N criterion. The benefit of such a simple criterion is that it is easy to implement in a search algorithm, requiring

little computing power. Unfortunately to automatically produce data with a high degree of reliability requires a large peak S/N (S/N$\gtrsim$ 10) and many low peak S/N sources are rejected that would normally appear obvious to the trained eye (usually due to their wide velocity extent).

As computer power has increased over recent years, more effort has been put into defining a more complex S/N formula that also recovers those galaxies that have a low peak S/N but a relatively large total signal. Two examples of the more recent definitions of S/N, that take into account the total flux of the object, are from the ADBS (Rosenberg & Schneider, 2000) and from ALFALFA (Saintonge, 2007).

For a source covering n independent channels, one would expect that the noise in the integrated signal should be proportional to $\sqrt{n}$, independent of the signal width. Rosenberg & Schneider noticed that the detection of their sources was highly dependent on the width of the source. Specifically, they found that wider sources were more difficult to detect. The noise dependence found by them was best fit by a $n^{0.25}$. This led to their definition of S/N as:

$$\frac{S}{N} = \frac{F(300/\delta v)^{0.25}}{\delta v \sigma (W_{20}/\delta v)^{0.75}} \tag{5.1}$$

where F is the integrated flux, measured in Jy km s^{-1}. W_{20} is the line width (in km s^{-1}) at 20% of the peak flux, σ is the rms noise and δv is the velocity *resolution* of the data, in km s^{-1}. This is the S/N normalised to a galaxy of width 300 km s^{-1}.

Saintonge (2007) uses a different definition of S/N for use in the ALFALFA survey. Her definition is simply a measure of the mean S/N across the whole signal:

$$\frac{S}{N} = \frac{F}{W_{50}\sigma}\left(\frac{W_{50}}{2\delta v}\right)^{0.5} \quad (5.2)$$

in this case W_{50} is the signal width (in km s^{-1}) at 50% of the peak flux, all other terms are as in Eqn. 5.1. Both methods take into account the total flux of an object as opposed to its peak flux. This should provide a better return on galaxies with a large velocity width but with low peak flux, while still retaining large peak S/N sources, provided they are not too narrow and thus rejected as RFI.

To assess and compare these different criteria, data were combined from the three datacubes of NGC 628, NGC 1156 and Abell 1367. For the NGC 628 and NGC 1156 datacubes, follow up observations were available in addition to the AGES data. Since follow up observations on the Abell 1367 cube have only just begun at the time of writing, only those sources that were detected by both L. Cortese, the author and POLYFIND were considered – these represent the strongest candidate detections.

Figs. 5.1–5.3 show the relationships (or lack thereof) between different H I signal properties. In each case, black dots represent sources that are considered strong source candidates. This is either because they are coincident with objects that have matching H I properties, they have been confirmed by follow up observations or the signal has been detected by eye and POLYFIND and considered too strong to be worthy of follow up observations. Red dots represent signals that have been followed up and found to be false detections.

In the top panels, S/N as calculated by the different methods is plotted against the total flux of the object. The middle panels show W_{50} plotted against the S/N and the lower panels, the W_{20} plotted against the S/N. The left hand panels represent

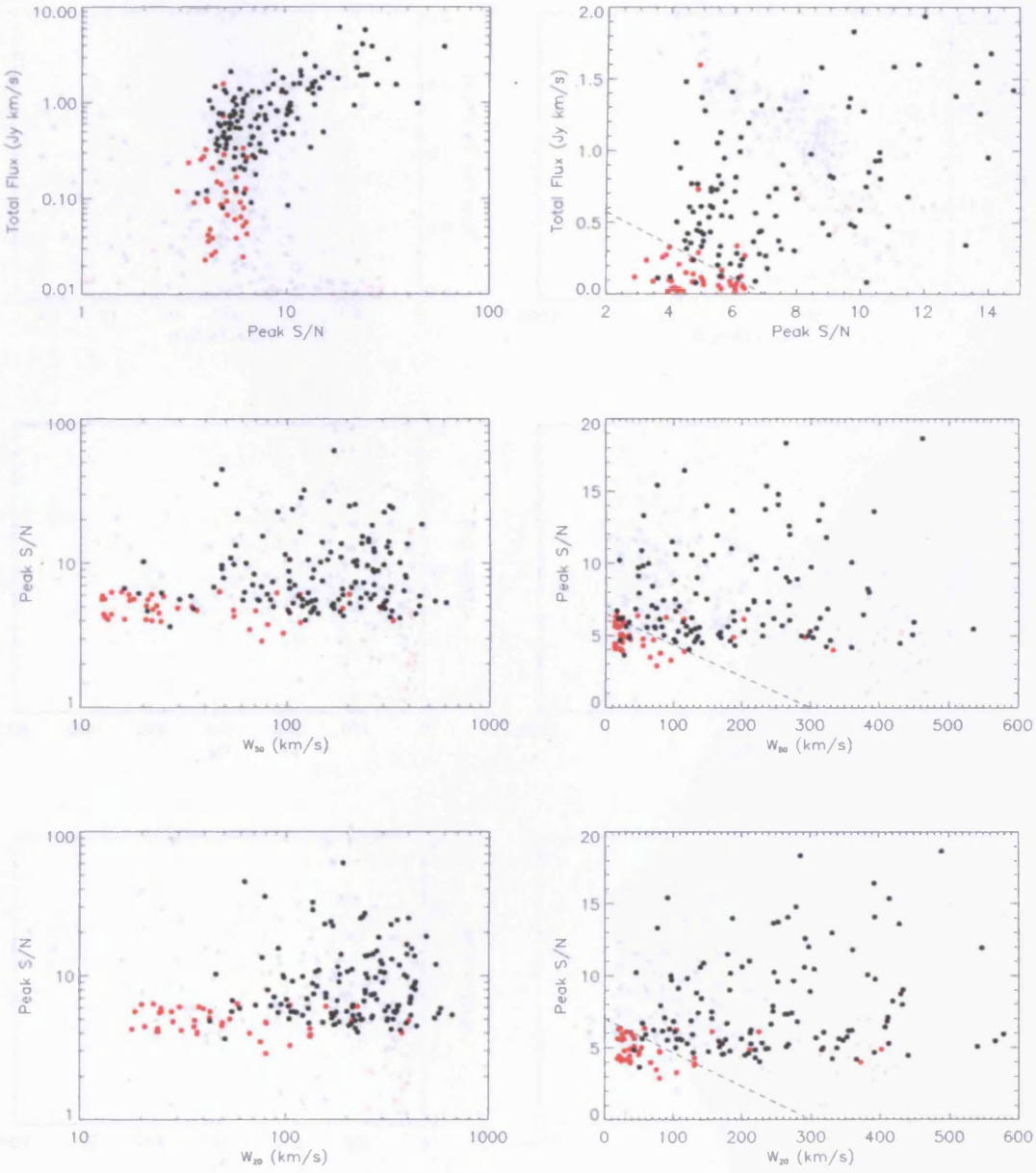

Figure 5.1: Peak S/N detection reliability. Peak S/N is plotted against the total flux, W_{50} and W_{20} for all sources (real and unreal) in the NGC 628, NGC 1156 and Abell 1367 regions. In each case, black represents detections and red represents non-detections in the follow-up observations. The right hand panels show the low S/N region expanded and dotted lines indicate suggested detection thresholds.

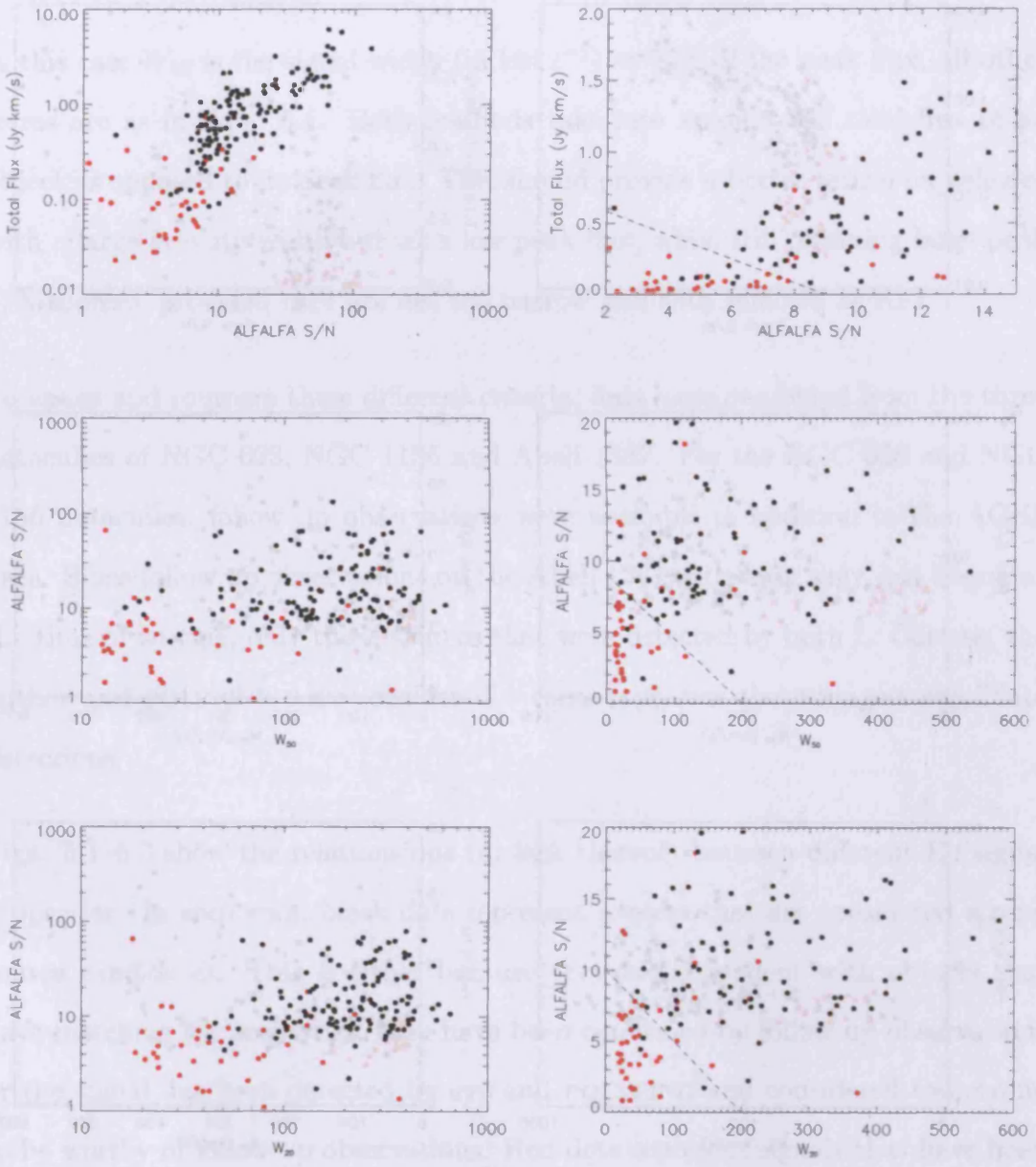

Figure 5.2: ALFALFA S/N detection reliability. ALFALFA S/N is plotted against the total flux, W_{50} and W_{20} for all sources (real and unreal) in the NGC 628, NGC 1156 and Abell 1367 regions. In each case, black represents detections and red represents non-detections. The right hand panels show the low S/N region expanded and dotted lines indicate suggested detection thresholds.

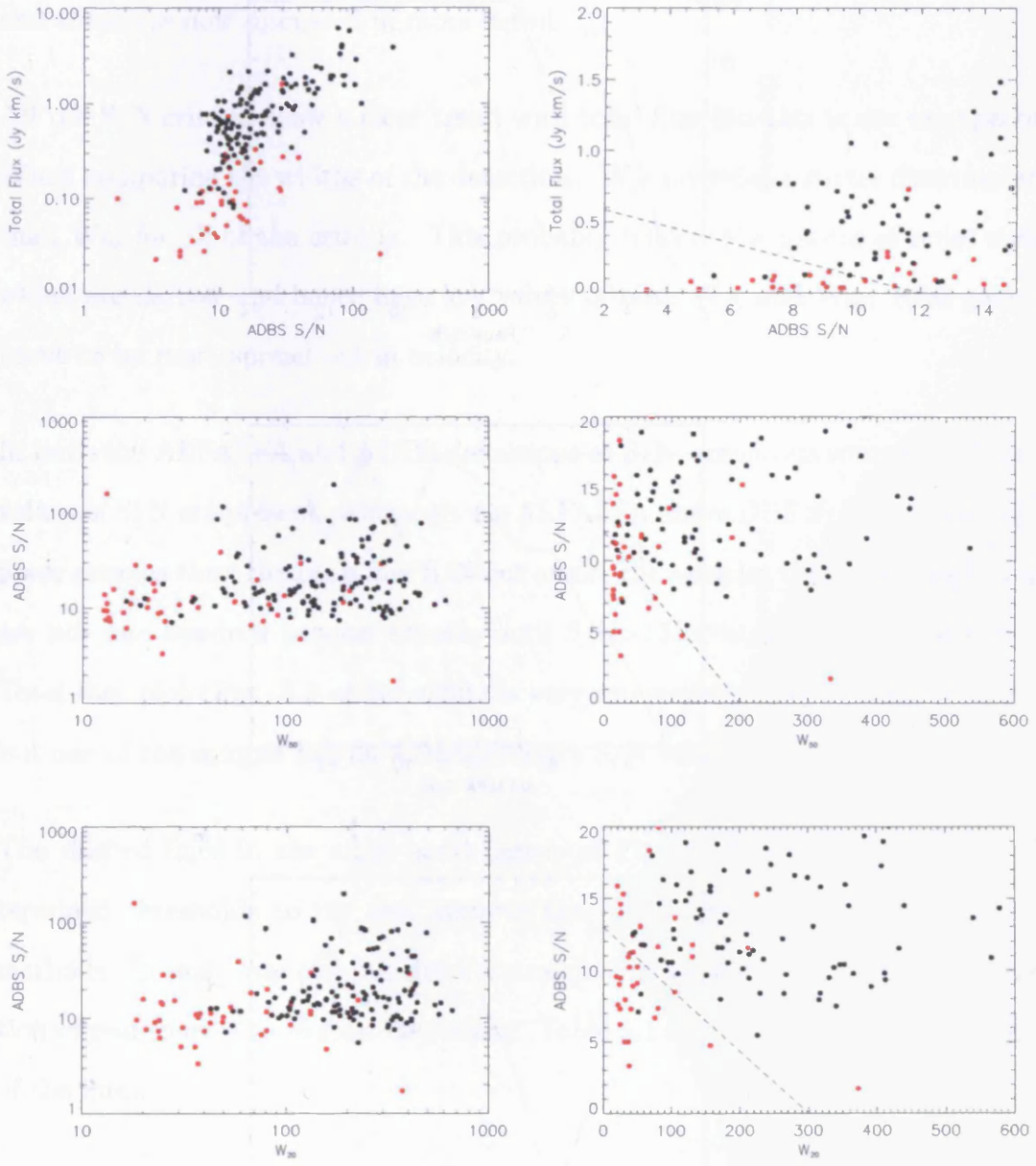

Figure 5.3: ADBS S/N detection reliability. ADBS S/N is plotted against the total flux, W_{50} and W_{20} for all sources (real and unreal) in the NGC 628, NGC 1156 and Abell 1367 regions. In each case, black represents detections and red represents non-detections. The right hand panels show the low S/N region expanded and dotted lines indicate suggested detection thresholds.

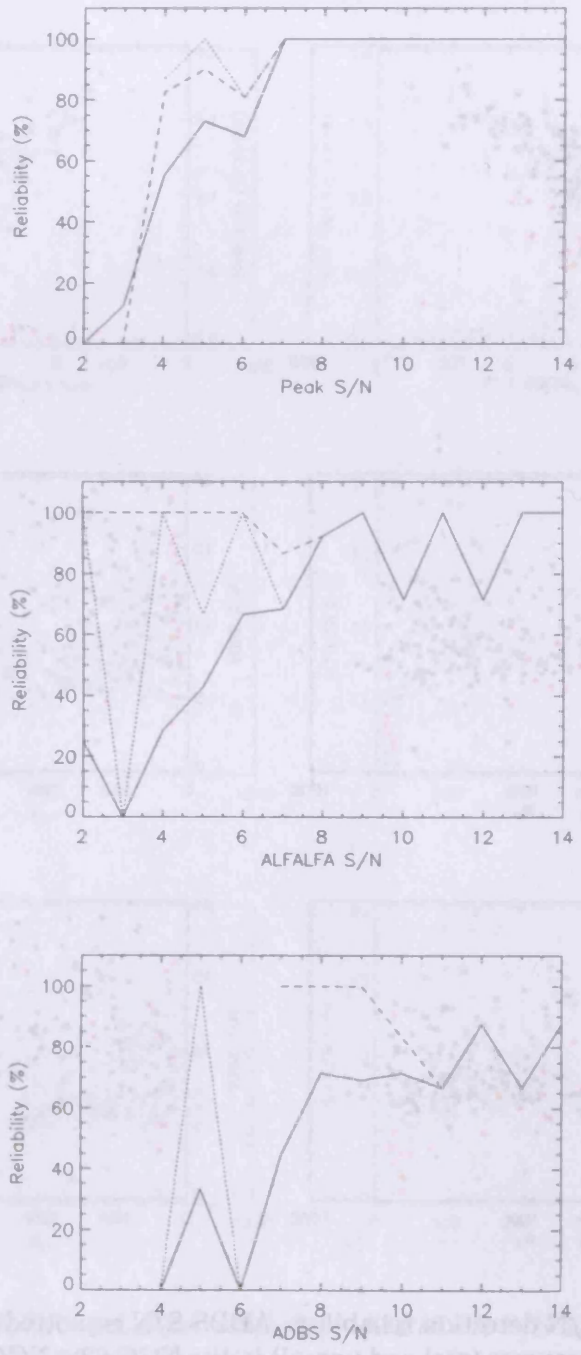

Figure 5.4: Reliability plots for each of the selection methods. From top to bottom: Peak S/N, ALFALFA S/N, ADBS S/N. For each method, the solid line is for the entire sample, the dashed line is for the S/N–W_{50} cut and the dotted line is for the S/N–W_{20} cut.

the whole sample, whereas the right hand panels focus on the region of low S/N. Overplotted on the right hand panels are dashed lines of suggested cutoff thresholds and these are now discussed in more detail.

All the S/N criteria show a clear trend with total flux but this is not unexpected. When comparing the widths of the detections, W_{20} provides a better discriminator than W_{50} for all of the criteria. This probably reflects the nature of noise spikes which are narrow and hence have low values of both W_{20} and W_{50}. Real galaxies prove to be more spread out in velocity.

In both the ALFALFA and ADBS definitions of S/N, erroneous sources with large values of S/N are present. Although the ALFALFA and ADBS S/N formulae reject fewer sources than the peak-flux S/N cut alone, the samples that meet the criteria are not one hundred percent reliable until S/N>13 or higher. The ADBS S/N–Total flux plot (Fig. 5.3 upper right) is very interesting, since it implies that all but one of the sources has an ADBS effective S/N value greater than 7.

The dashed lines in the right hand panels of Figs. 5.1–5.3 are empirically determined thresholds to try and improve the reliability of each of the detection methods. In each case one can draw a straight line that segregates the large fraction of real sources from false detections. Table 5.1 shows the parameters for each of the lines.

Imposing restrictions based on total flux, W_{20} or W_{50} give better returns. This is probably a good representation of how the by-eye detection works. Large-width, low-flux galaxies are still very noticeable to the eye when the data are searched in the RA–velocity or dec–velocity domain, often much more so than in the RA–dec plane. Conversely narrow, objects are much more noticeable in the RA–dec plane.

Table 5.1: Line parameters for different object selection criteria.

x-axis	y-axis	gradient	intercept
Peak S/N			
Peak S/N	Total Flux	-0.11	0.8
W_{50}	Peak S/N	-0.021	6.5
W_{20}	Peak S/N	-0.023	7.0
ALFALFA S/N			
ALFALFA S/N	Total Flux	-0.080	0.75
W_{50}	ALFALFA S/N	-0.045	9.0
W_{20}	ALFALFA S/N	-0.050	10.0
ADBS S/N			
ADBS S/N	Total Flux	-0.058	0.7
W_{50}	ADBS S/N	-0.060	12.0
W_{20}	ADBS S/N	-0.043	13.0

To visualise the improvement in reliability made by imposing these cuts, detection reliability has been plotted as a function of S/N in Fig. 5.4. In each case, solid lines represent the entire sample, the dashed lines are for the sample defined by the total flux–S/N cut and the dotted lines represent those defined by the S/N–W_{20} cut. It is clear that by imposing these cuts there is an improvement in reliability. At first glance it seems that the catalogue that performs best (i.e. retains a high level of reliability at low S/N) is the ALFALFA definition with the additional total flux–S/N cut applied. However since there is only one detection that meet these criteria between S/N of 2 and 6, it is most likely a misrepresentation and the real distribution is something closer to that described by the S/N–W_{20} cut over this S/N regime.

The Peak S/N criterion with an additional total flux–S/N cut performs as well as applying the S/N–W_{20} cut and rejects fewer sources. Using this method increases the reliability of detections down to 4σ. In addition the sample described by this method is 100% reliable above 7σ. It is surprising that the ADBS definition of S/N did not perform at least as reliably as the ALFALFA definition. It is also surprising that both of these definitions did not perform as well as the Peak S/N. Why should this be so?

The objects used in this investigation have been detected either manually or by the semi-automated POLYFIND. In order to make a fair comparison with the ALFALFA it would be necessary to run the data through the ALFALFA data pipeline and detection algorithm. Merely comparing the S/N criterion alone is not a true representation of how the automated galaxy finding routine by Saintonge (2007) would perform.

The overall impression is that the S/N criterion that gives the most reliable catalogue is using a peak S/N–W_{20} cut. The method rejects only three galaxies, while remaining over 80% reliable to 4σ. In practice without fore-knowledge of which sources are true sources, one would be limited to using the reliability function to decide which sources to consider for immediate analysis and which to exclude pending follow-up confirmation. With the benefit of the follow-up observations, it is possible to include all the detected objects for further analysis.

5.2 Completeness

The completeness is a measure of the survey's ability to detect all the sources that are present in the survey field and lie above the detection threshold. Calculating the survey completeness is a very important step in defining the survey volume. Completeness should not be confused with the reliability, which is a measure of how many of the detected sources are real. As one pushes the selection limit closer to the noise, the reliability decreases (as shown in the previous section) but the completeness increases, since more real sources are detected. Clearly there is a balance to be reached since one requires a highly reliable catalogue, but also one that exploits as much of the sensitivity as possible.

In early H I surveys, the assumption was that for a given peak S/N limit the survey is complete. Commonly this has been taken to be 5σ or 6σ which does not seem unreasonable. Recently however, Schneider, Spitzak & Rosenberg (1998), used a V/V_{max} analysis to show that these surveys are not complete at this level and hence are underestimating the population of sources close to the detection threshold.

Since the total population of galaxies in any part of the Universe is unknown, the only way to calculate the completeness is to insert simulated galaxies into the data and then use the selection criteria to see how many of these galaxies are detected. Since this is beyond the scope of this thesis, it is necessary to make some assumptions in order to estimate the completeness for this sample of AGES data.

The first assumption is that the completeness function exhibits a roll off as it approaches lower S/N values, as shown by Rosenberg & Schneider (2002). Saintonge (2007) shows that ALFALFA data also exhibit a roll off in completeness. The completeness function for ALFALFA differs from ADBS in two ways: it exhibits a much shallower roll off and reaches 100% completeness. This probably reflects the fact that the ADBS randomly injected their sources into real data, with RFI present and then subjected this data to the full data reduction pipeline. Saintonge (2007) uses datacubes of pure white noise, with no RFI and ensures that galaxies are spaced at least 20′ and 200 km s^{-1} apart, so it can only be seen as a best case scenario simulation.

The second assumption is that wide velocity width galaxies are harder to detect than narrow ones near the detection threshold. In particular it is assumed that the width dependence is S/N $\propto w_{20}^{-0.75}$ (Rosenberg & Schneider, 2002). Thus the ADBS S/N criterion is adopted in the absence of a more robust method. Now that the S/N has been defined, it is used to calculate the volume, V, over which each

object has been detected and also the maximum volume, V_{max}, over which each object would be detectable.

Allowing for the roll off in completeness at lower S/N, Rosenberg & Schneider (2002) calculated that the expected $\overline{V/V_{max}} = 0.61$. It is now straightforward to alter the S/N level, recalculate $\overline{V/V_{max}}$ and see which S/N returns the expected value. An analysis of the three AGES datacubes shows that in order to recover the expected value of $\overline{V/V_{max}}$, a value of S/N= 7.5 should be adopted. This is slightly higher than originally quoted in the previous chapter (S/N= 7), taken from Auld et al. (2006). The difference is probably due to the small numbers used in calculating $\overline{V/V_{max}}$ from the NGC 628 sample.

By Rosenberg & Schneider (2002) this is the S/N at which the completeness level is 50%. Only half of the number of objects are being detected at this level. Since the noise in this case is defined by Eqn. 5.1, it is entirely dependent on the width of the source and the rms noise level. Using a S/N= 7.5 it is possible to calculate the maximum distance over which that object could be detected. This distance can then be used to calculate, V. As this level of S/N corresponds to the 50% completeness level, the actual maximum search volume is half as big as the calculated volume. Thus it is possible to accurately estimate the number density of all detected objects, which is simply the HIMF.

Fig. 5.5 shows the H I mass as a function of redshift for the three AGES datacubes. Overplotted on the graphs are lines that correspond to the 50% completeness limits of different surveys for a galaxy that is 300 km s^{-1} wide. The dotted line is that of AGES, the dashed line is that of ALFALFA and the dash-dot line is that of HIPASS.

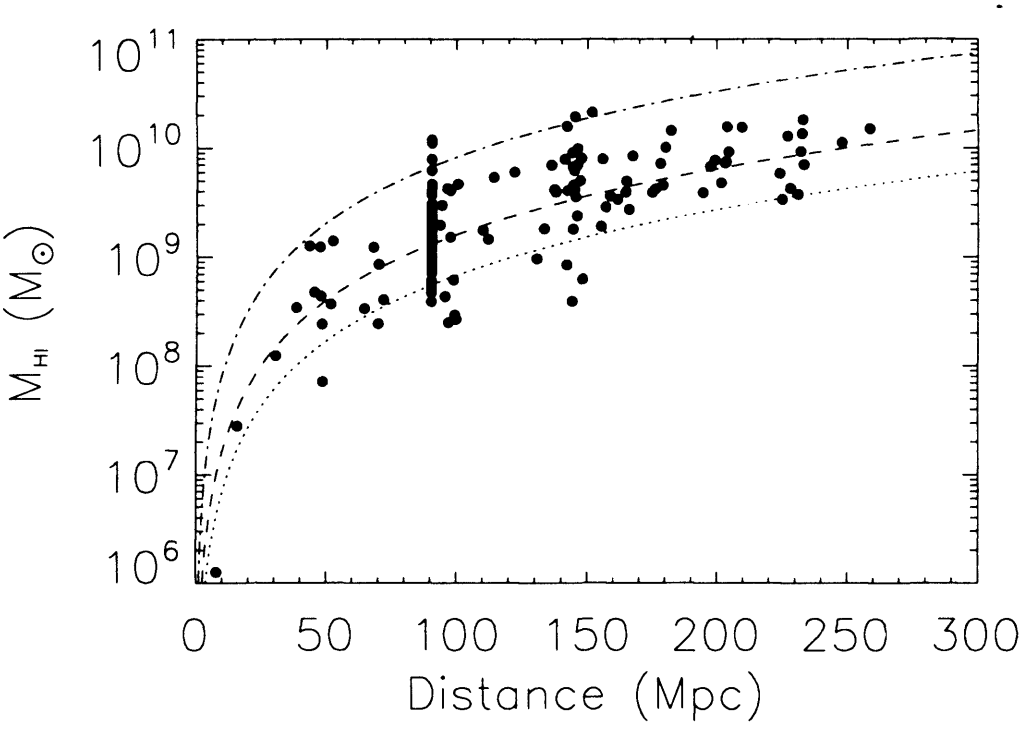

Figure 5.5: The H I mass distribution of three AGES datacubes as a function of redshift. Overplotted are 50% completeness limits of different surveys assuming a galaxy width of 300 km s^{-1}. The dotted line represents AGES, the dashed line is for ALFALFA and the dash-dot line is for HIPASS. The feature at 90 Mpc is due to the Abell 1367 cluster, for which all assumed members have been assigned the same distance.

The AGES limit uses a channel noise of 0.7 mJy and this corresponds to an integrated H I flux of 0.288 Jy km s^{-1}. In calculating the ALFALFA limit, a channel noise value of 2.2 mJy/beam is assumed and the 50% completeness S/N limit is assumed to be 4 (Saintonge, 2007). This corresponds to an integrated flux limit of 0.682 Jy km s^{-1}. As stated previously, this should be considered a lower limit, since the simulations used to derive this value are based on an ideal scenario of white noise with all simulated galaxies well separated spatially and in velocity. The HIPASS 50% completeness limit has been judged from Zwaan et al. (2004) Fig. 2. This corresponds to an integrated flux density of 3.5 Jy km s^{-1}.

The limits quoted here are not the absolute detection thresholds, this is why there

are several AGES galaxies below the dotted line, this also applies to the other surveys. Bearing this in mind, it is still true to say that HIPASS would have trouble detecting all but the brightest galaxies in this region. ALFALFA is the shallowest of the E-ALFA surveys and so is only sensitive to low-mass H I over a much smaller distance than AGES. The survey makes up for the lack of depth by covering a much greater area of sky than AGES. This implies that although ALFALFA will be able to put tight constraints on the low-mass end of the HIMF, it will be limited to the very local universe.

There is a noticeable feature at 90 Mpc, which is due to the Abell 1367 cluster. Cortese et al. (2004) have shown that the in-fall velocities of the cluster members can be as high as 2500 km s^{-1}. Therefore all galaxies in the Abell 1367 datacube between 4000 and 9000 km $s^{-1}$are assumed to be cluster members and have been assigned the same distance. The distance assumed is 90.3 Mpc (Cortese et al. 2004).

Fig. 5.6 is the mass distribution of the H I data. The Abell 1367 cluster members are overplotted with hatched shading. The mass sensitivity limit at the distance of Abell 1367 (Fig. 5.5) is a few $\times 10^8 M_\odot$ so the distribution only represents the most massive members of the cluster. This will also affect the HIMF, since there will be an overabundance of high mass objects.

5.3 The H I mass function

The survey sensitivity is well understood across each of the entire datacubes. This makes the $1/V_{TOT}$ method a simple choice for determining the HIMF. There is likely to be some contamination from the Abell 1367 cluster, but this actually offers

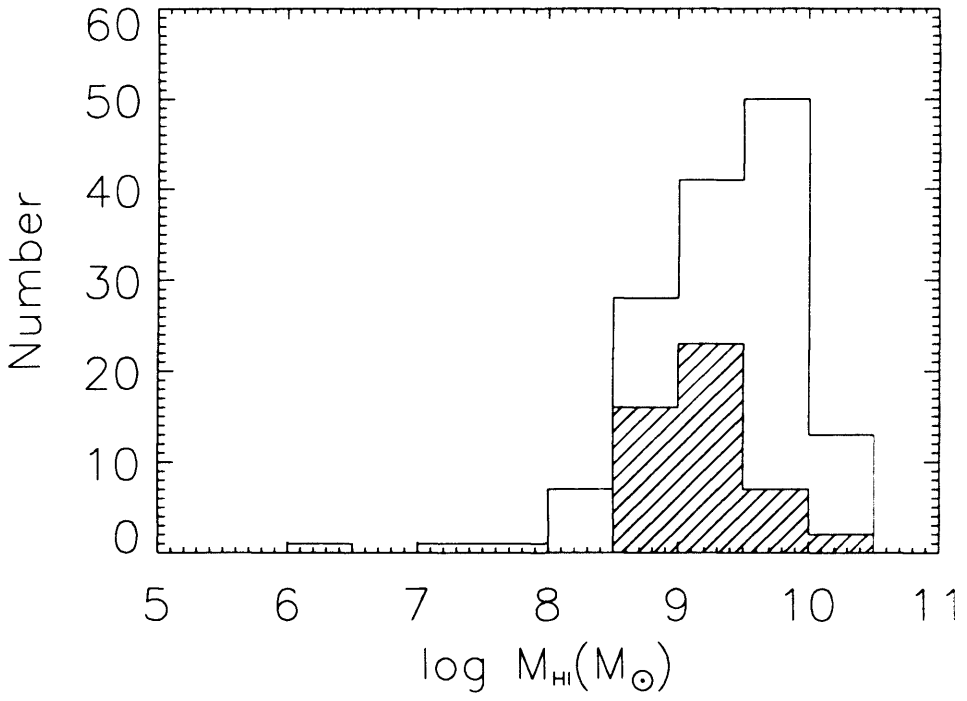

Figure 5.6: The H I mass distribution of three AGES datacubes. The Abell cluster galaxies are shown by the hatched histogram.

an opportunity to test one of the goals of AGES: the environmental dependence of the HIMF.

H I masses were first converted using $H_0 = 75\text{km s}^{-1}\text{Mpc}^{-1}$ for comparison with previous surveys. The mass bins were then determined using the median values of the mass within each bin. Mass bins were defined every half decade in mass, with the median mass value within each bin forming the ordinate. Since there is only one galaxy in the lowest mass bin, it was not used in the fitting process. A least squares fit to determine the Schechter function parameters was performed in IDL, using the MPFITFUN[1] function. The function parameters are shown in Table 5.2 along with values from previous surveys, for comparison. 1-σ error bars are shown

[1]http://cow.physics.wisc.edu/~craigm/idl/fitting.html

Table 5.2: Best fit Schechter function parameters for different H I surveys. 1-σ errors are shown in brackets where available.

Dataset	α	Φ_* (Mpc^{-3})	M_* ($\times 10^9 M_\odot$)
AGES			
Whole dataset[a]	-1.25 (0.17)	0.0098 (0.0036)	3.9 (0.9)
Whole dataset[b]	-1.28 (0.14)	0.0076 (0.0027)	7.7 (1.8)
Abell cluster	-0.07 (1.2)	0.87 (0.48)	1.7 (1.8)
Field	-1.28 (0.45)	0.004 (0.004)	5.3 (3.4)
HIPASS	-1.37 (0.08)	0.0060 (0.0014)	7.2 (0.9)
ADBS	-1.53	0.0050	7.6
AHISS	-1.2	0.0059	6.3

[a]Median mass bins
[b]Central value mass bins

in brackets.

Fig. 5.7 (Top) shows the HIMF derived from the AGES data. The parameters for this function are shown in the first row of Table 5.2. Although the faint-end slope is in agreement with HIPASS and AHISS, there is clearly a discrepancy between these and the steep mass function of the ADBS. The values of Φ_* and M_* do not agree within errors with previous surveys. This discrepancy is reduced when the mass bin values are defined by the bin centres (Fig. 5.7, Bottom). This result is a little alarming as it suggests that the Schechter parameters are dependent on the definition of the mass bins!

This could be as a result of small number statistics – the largest bin population is only 50 galaxies. The uncertainties for this data are large so while α and Φ_* have changed, the error bars are too large to judge whether the shift is significant. M_*, however, is changed significantly from 3.9 to 7.7 $\times 10^9 M_\odot$.

The AGES parameters agree with those of HIPASS and AHISS, but the steep mass function of ADBS is rejected. It is interesting to note that the lowest mass bin is significantly higher than the predicted HIMF, similar to the Arecibo Slice mass function. Since the same method for calculating the volume was used in this data,

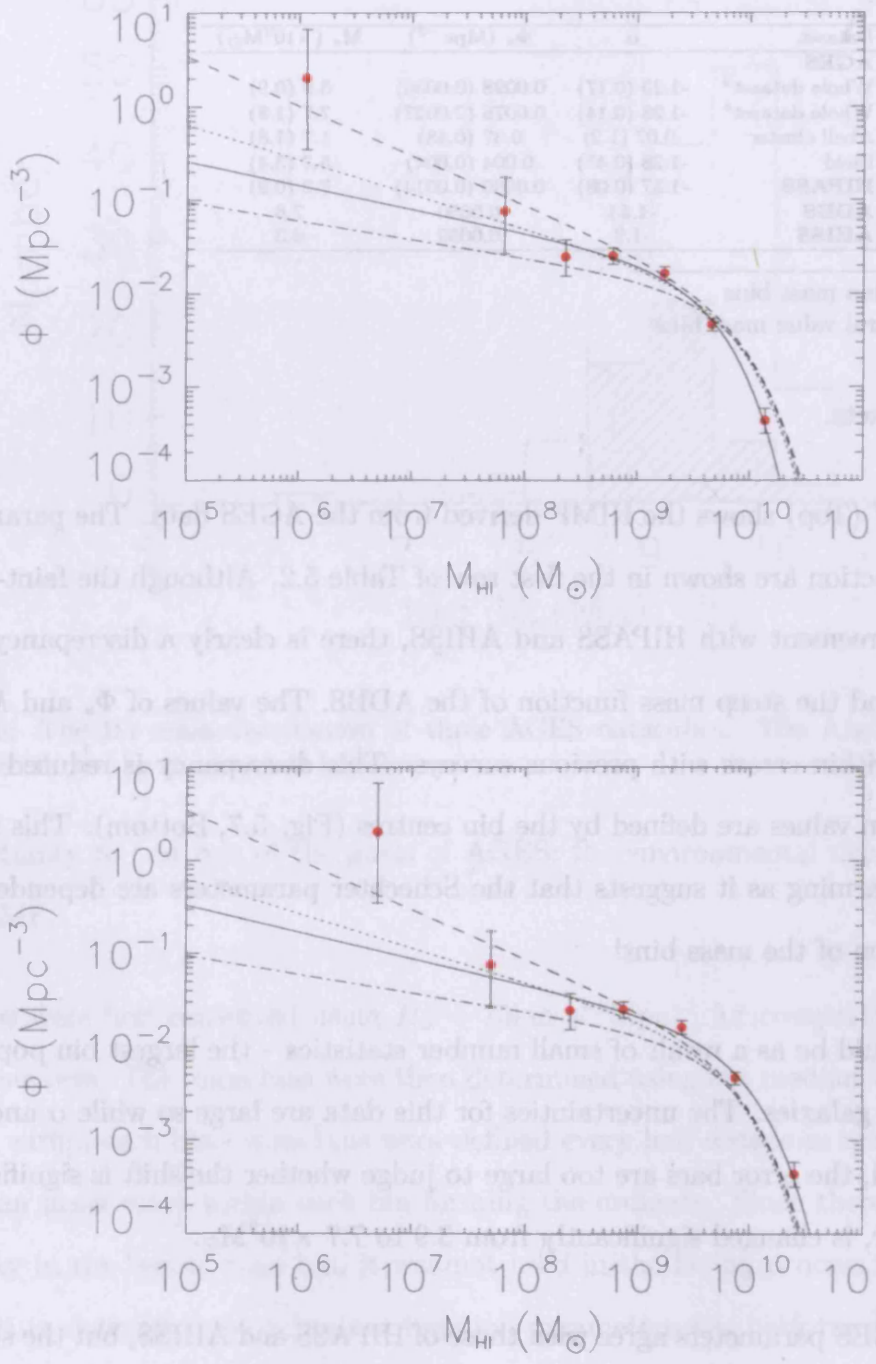

Figure 5.7: The H I mass function for 142 galaxies from AGES. Top: the bin values have been determined by the median mass within each bin. Bottom: bin values have been defined as the bin centres. The solid lines are the best fitting Schechter function in each case. Also shown are the Schechter functions from HIPASS (dotted line), ADBS (dashed line) and AHISS (Dash-dot line). Error bars are computed from Gehrels (1986).

it raises the question of whether this method over-estimates the number density for the lowest mass objects.

The analysis presented here is rather crude, no attempt has been made to account for effects that could bias the result and no other method of deriving the HIMF has been attempted for comparison. As well as deriving the HIMF using a different method, it would be necessary to quantify effects such as the presence of large-scale structure, selection bias, the Eddington effect, H I self-absorption, confusion and cosmic variance. This is work that is planned for the future as the AGES database grows larger.

5.3.1 Environmental Effects on the HIMF

Figs. 5.8 & 5.9 are attempts to measure the environmental dependence of the HIMF. The AGES mass limit at the distance of Abell 1367 means that only the high-mass end of the HIMF is constrained. This is not unexpected, most environmental effects on low mass objects from AGES will be limited to the study of nearby fields ($\lesssim$ 20 Mpc). This does mean, however, that interpretation of the HIMF for the cluster (Fig. 5.9) is severely limited.

The same cannot be said for the HIMF derived for the field. The field in this case is defined as all galaxies in all the data cubes that do not form part of Abell 1367. This is a simplistic approach since there is bound to be some influence by other large-scale structure in the data and the Abell cluster membership is overestimated. Nevertheless, the population numbers are reasonable and the spread in H I mass still covers five decades.

The derived slope for the field is $\alpha = -1.37 \pm 0.39$. This is tentative evidence that

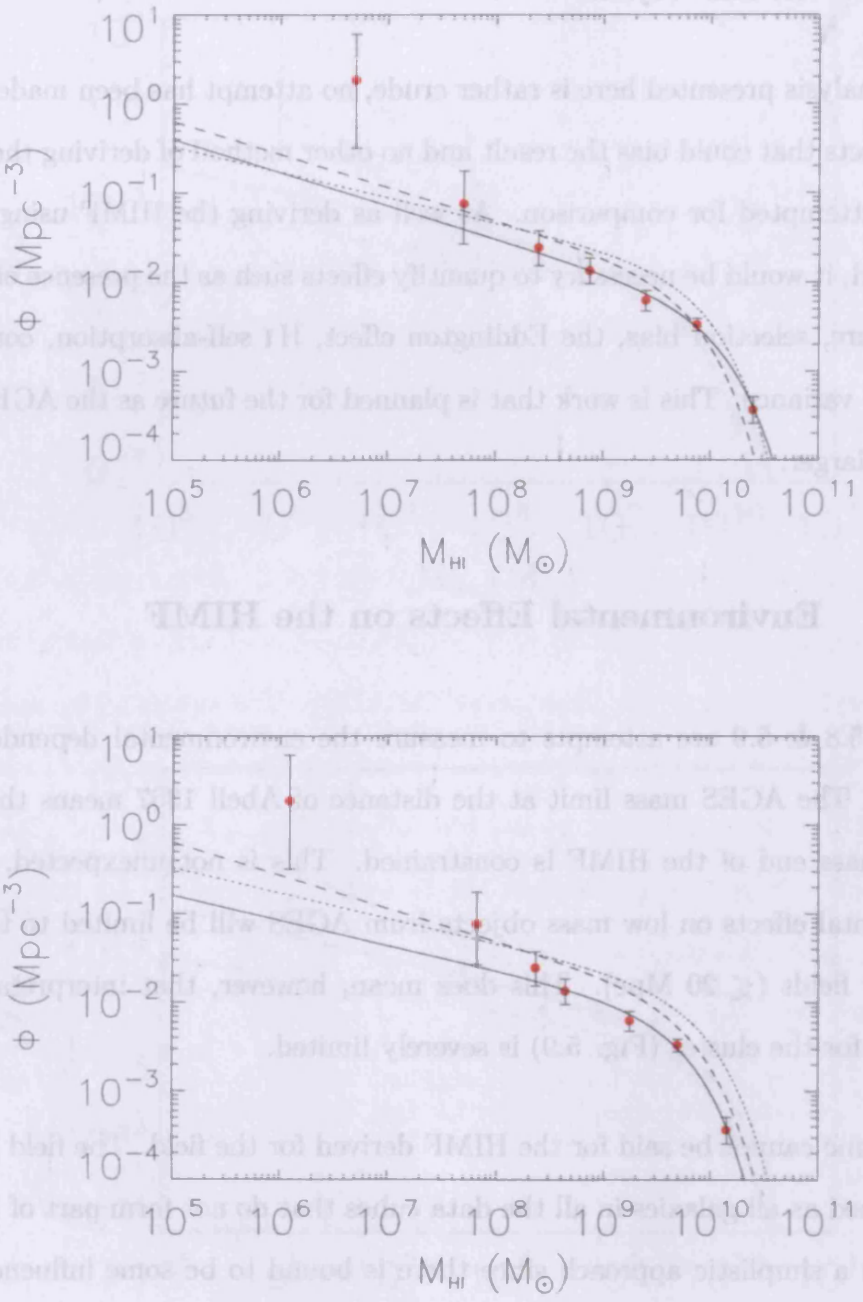

Figure 5.8: The H I mass function for 94 galaxies from AGES that are not part of the Abell 1367 cluster i.e. 'field galaxies'. Top: the bin values have been determined by the median mass within each bin. Bottom: bin values have been defined as the bin centres. The solid lines are the best fitting Schechter function in each case. Also shown are the Schechter functions from HIPASS (dotted line), ADBS (dashed line) and AHISS (Dash-dot line). Error bars are computed from Gehrels (1986).

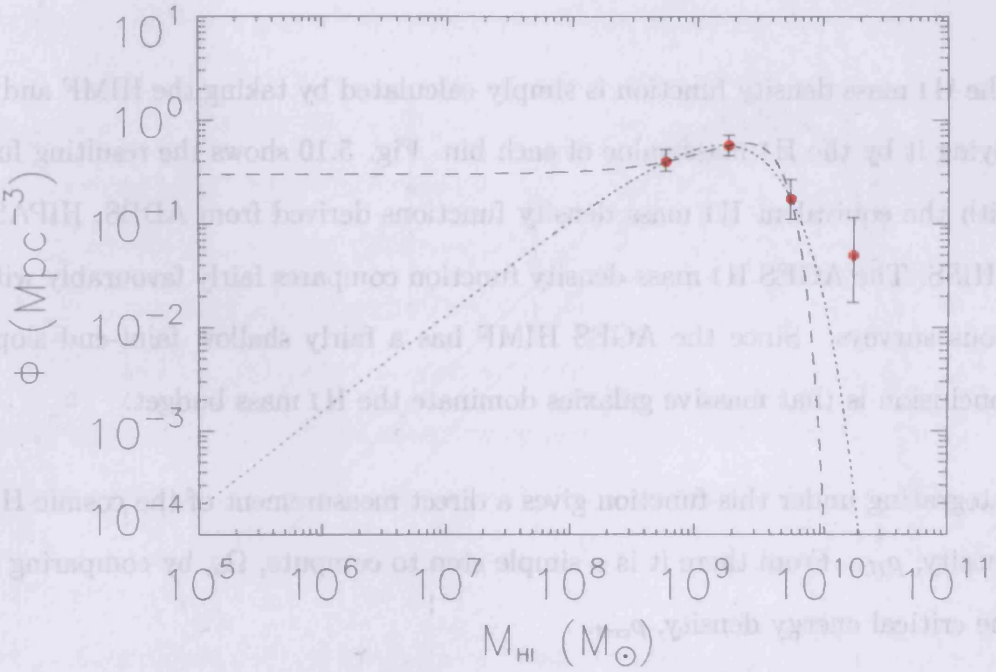

Figure 5.9: The H I mass function for 48 members of the Abell 1367 cluster detected by AGES. Each bin value has been determined by the median mass within each bin. The dotted line is a Schechter function fit to the data, the dashed line is a Gaussian fit.

the mass function is slightly steeper in the field, but the change is still within the uncertainties, so one cannot conclude that there is any dependence on environment from these data – the dataset is still too small and the cluster too distant.

Now the AGES HIMF has been derived it is possible to measure the contribution of galaxies of different mass to the Universal H I budget, and ultimately the contribution of H I to the Universal energy budget, Ω_0.

5.4 Cosmic mass density of H I

The H I mass density function is simply calculated by taking the HIMF and multiplying it by the H I mass value of each bin. Fig. 5.10 shows the resulting function with the equivalent H I mass density functions derived from ADBS, HIPASS and AHISS. The AGES H I mass density function compares fairly favourably with previous surveys. Since the AGES HIMF has a fairly shallow faint-end slope, the conclusion is that massive galaxies dominate the H I mass budget.

Integrating under this function gives a direct measurement of the cosmic H I mass density, ρ_{HI}. From there it is a simple step to compute, Ω_0, by comparing ρ_{HI} to the critical energy density, ρ_{crit}.

The derived AGES value for $\rho_{HI} = 7.5^{0.6}_{0.3} \times 10^7 M_\odot Mpc^{-3}$. This is still consistent with previous measurements, but at the high end of the scale: $\rho_{HIPASS} = 6.1 \times 10^7 M_\odot Mpc^{-3}$, $\rho_{ADBS} = 7.1 \times 10^7 M_\odot Mpc^{-3}$, $\rho_{AHISS} = 4.3 \times 10^7 M_\odot Mpc^{-3}$ (Zwaan et al. 2003) and is a result of the higher value of Φ_* for AGES. This is probably due to the presence of the Abell 1367 cluster.

The resulting $\Omega_{HI} = 4.1^{1.8}_{1.6} \times 10^{-4}$. This is also in good agreement with previous surveys, because the shallow HIMF results in the H I mass density being dominated by large mass galaxies.

5.5 The Universal contribution of dark galaxies

On of the goals of this thesis is to put constraints on the population of dark galaxies and to compare these constraints with predictions of their abundance. The results

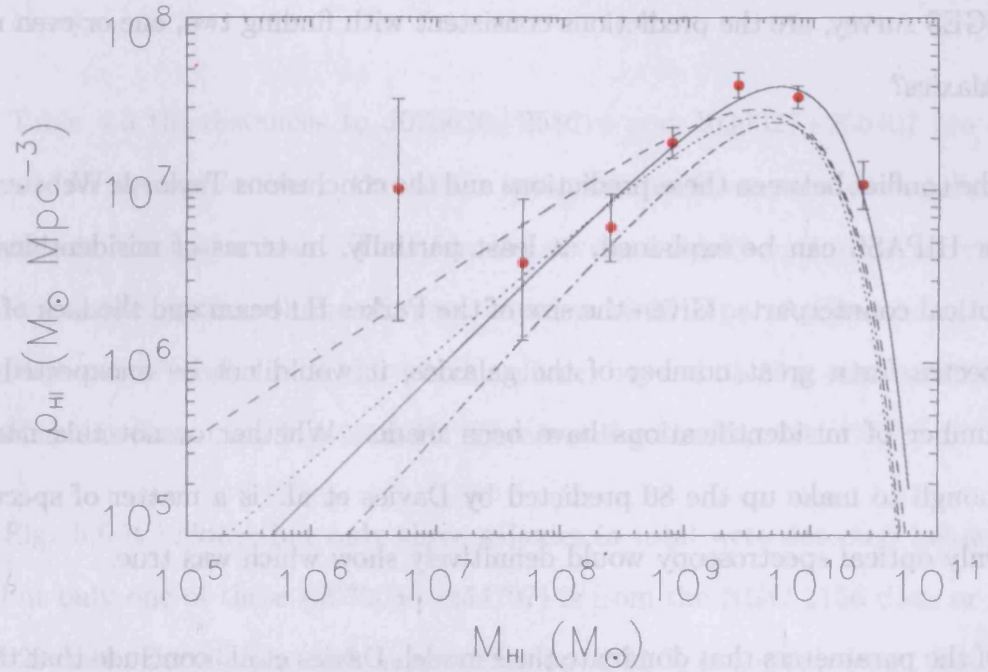

Figure 5.10: The H I mass density function derived from 142 AGES galaxies. Overplotted are the converted Schechter functions for different surveys. Solid line: AGES, dotted line: HIPASS, dashed line: ADBS, dash-dot line: AHISS.

from a search in the NGC 1156 region and the NGC 628 region has revealed 69 H I detections. Of these, two have no clear cut optical counterparts. J025626+254614 and J030027+255407 were both discovered in the NGC 1156 data cube, which contains pockets of optical extinction that rises above 1 mag. This presents a problem for confirmation of optical counterparts since the only optical information for these galaxies comes from the POSS-II plates which have a fairly shallow surface brightness limit ($\mu_B \sim 25.5$ mag arcsec^{-2}). Much deeper optical observations will be required to put tighter constraints on the lower surface brightness limits of the galaxies.

Davies et al. (2006) have already made estimates on the number of dark galaxies that can be expected from a number of H I surveys, including AGES. Given that

the data from this project represent only $\sim$ 5% of the scheduled time for the AGES survey, are the predictions consistent with finding two, one or even no dark galaxies?

The conflict between these predictions and the conclusions Taylor & Webster (2006) for HIPASS can be explained, at least partially, in terms of misidentification of optical counterparts. Given the size of the Parkes H I beam and the lack of optical spectra for a great number of the galaxies, it would not be unexpected that a number of misidentifications have been made. Whether or not this number is enough to make up the 80 predicted by Davies et al. is a matter of speculation. Only optical spectroscopy would definitively show which was true.

Of the parameters that dominate their model, Davies et al. conclude that the most crucial ones that govern the dark galaxy fraction are: the fraction of dark halo mass which goes into the galactic disk, m_d, and the faint-end slope of the HIMF, α. Reducing m_d results in an increase in the population of dark galaxies. Reducing α results in a reduction in the number of dark galaxies. In their model, Davies et al. (2006) observe a 3-fold reduction (25 % to 9 %) in the dark galaxy population when reducing α from -2.0 to -1.0. Although there is a greater dependence on m_d, this term cannot be investigated here. α on the other hand is a value that is measured directly from the HIMF. The value of $\alpha = -1.28$ from this data leads to the prediction that $\sim$ 15% of galaxies are dark.

Using the result of the previous section, it is now possible to work out an upper limit for the contribution of dark galaxies to the Universal mass budget. Two potential dark galaxies discovered in the NGC 628 and NGC 1156 data. This represents 3% of the total detections in these cubes, significantly fewer than the 23% predicted by Davies et al. (2006). It should be noted, however, that the prediction of Davies et

al. was limited to the volume of space probed at the distance of the Virgo cluster ($\sim$ 16 Mpc).

From Table 4.3 the distances to J025626+254614 and J030027+255407 are 144 Mpc and 148 Mpc respectively. Due to the low predicted H I mass of dark galaxies, completeness is a major issue. Thus far, the survey is really optimised to search for dark galaxies in the volume of space between 16-25 Mpc. At lower distances the survey area severely limits the search volume; beyond 25 Mpc, the sensitivity drop-off means that many low-mass H I sources will go unseen.

From Fig. 5.6 it follows that only three galaxies in total were detected below 30 Mpc, but only one of these (J030036+254707) is from the NGC 1156 data or the NGC 628 data. Certainly a dark galaxy fraction of 23 % is not ruled out, but the numbers are simply too low to make any kind of meaningful comparison with the prediction of Davies et al. More useful would be to calculate the upper limit on the dark galaxy fraction based on the two possible detections.

J025626+254614 is the galaxy with the narrowest velocity widths and so by Eqn. 5.1 it is detectable over a larger volume. Taking into account the variable sensitivity of the two datacubes, the volume over which both galaxies were detectable is 3008 Mpc^3. i.e. the upper limit on the number density of dark galaxies is $\sim 6.6 \times 10^{-4}$ Mpc^{-3}. This can then be converted to a mass density of $\sim 3.4 \times 10^5$ $M_\odot Mpc^{-3}$. Crudely comparing this value to the H I mass density function corresponds to a Universal contribution of at most $\sim$ 0.5% of the H I in the local Universe. One can only conclude that dark galaxies are not numerous enough to solve the 'missing haloes' problem, nor are they massive enough in total to resolve the 'missing mass' issue.

5.6 Summary

In this chapter I analysed the results of the first three AGES datasets. Different S/N definitions were assessed and it was found that a peak flux threshold with an additional constraint on the total flux provided an effective method of increasing the reliability of the data. Although not strictly relevant to the subsequent analysis in this section, this investigation will be very important for future AGES datasets.

The completeness of the AGES data was then discussed and approximated using some assumptions and $\overline{V/V_{max}}$ analysis. It was discovered that an effective S/N threshold of 7.5 recovered the expected value of $\overline{V/V_{max}}$=0.61.

Using this knowledge an HIMF was derived for the AGES data which was well fitted by a Schechter function using the parameters, $\alpha = -1.28 \pm 0.17$, $\Phi_* = 0.0076 \pm 0.0027$ and $M_* = 7.7 \pm 1.8 \times 10^9$ $M_\odot$. These parameters compare well with those measured from previous H I surveys although the uncertainties are large.

Even with this small dataset (<5% of the total AGES) the survey has demonstrated its ability to recover objects with H I masses as low as $10^6 M_\odot$. This bodes well for the full survey which should detect numerous low-mass objects and hence be able to put tighter constraints on this part of the HIMF than was previously possible. Detailed analysis of the HIMF was inconclusive in revealing an environmental dependence, due to the large uncertainties in a small dataset.

Using the HIMF it was possible to derive the H I mass density function and hence evaluate the cosmic mass density of neutral hydrogen, ρ_{HI}. The value derived here, $\rho_{HI} = 7.5^{0.6}_{0.3} \times 10^7 M_\odot$ Mpc^{-3} compares well with previous surveys as does the resulting estimate of the contribution of H I to the Universal energy budget.

$\Omega_{HI} = 4.1^{1.8}_{1.6} \times 10^{-4}$.

These values were then used to estimate the relative importance of the potential dark galaxy population, based on the two tentative detections discovered here. The relative numbers of dark galaxies in AGES as estimated from the current data agree with the predictions of Davies et al. (2006). The comparison is not robust however since the two dark galaxies are so distant and faint as to be part of an incomplete sample. J030036+254726, which was discovered in the regime where AGES is optimised to find dark galaxies, was found to have a LSB optical counterpart. The lack of dark galaxy detections in this regime is more in line with the predictions of Taylor & Webster (2005).

The two *potentially* dark galaxies contribute at most, 4% by mass to their respective bins in the H I mass density distribution. Overall this suggests that the maximum proportion of H I tied up in dark galaxies is only 0.5%. This is far short of the amount required to resolve the 'missing matter' problem. The number density of dark galaxies is also small, $n_{dark} \sim 6.6 \times 10^{-4}$ Mpc^{-3}, and so they do not represent the excess of dark matter haloes that CDM simulations predict.

Chapter 6

Conclusions

The work I have performed for this thesis has covered a number of different areas of astronomy. My work on the LSBs was an in-depth exploration of the gas morphology and kinematics of these unusual objects. The focus was on the star forming abilities of the galaxy sample, but the H I observations also revealed a rich variety of gas morphology and motion, not necessarily apparent at other wavelengths. As well as being LSB, they are neutral gas-rich objects. As such they are more suited to being detected by H I surveys than by optical surveys. The Arecibo Galaxy Environment Survey (AGES) is a survey that expects to detect a large number of this type of galaxy and a large proportion of the thesis has been dedicated to my involvement with the survey. This has included designing and implementing the observing strategy, testing the data reduction pipeline, producing the final data, testing their quality and examining the efficiency of the survey detection methods. I have demonstrated some uses the AGES data can be put to; from discovering hitherto undetected galaxies, through measuring the cosmic distribution of neutral hydrogen, to evaluating the cosmic significance of dark galaxies. The last point

has been the central theme throughout the thesis.

In the context of dark galaxies, I started by discussing some perceived outstanding problems in our current description of the Universe. Nearly all CDM simulations predict that a large number of dwarf-sized dark matter haloes should still be present around galaxies such as our Milky Way (although for proposed mechanisms to reduce this problem see Kravtsov, Gnedin & Klypin, 2004 and references therein). Despite a rapid increase in the observed number of dwarf galaxies surrounding the Milky Way in recent years, the number of satellites still falls far short of the predictions. It has been postulated that a population of galaxies containing gas and dark matter but no stars (dark galaxies) could make up the difference in the observed number of satellites surrounding massive galaxies.

In Chapter 2 it was established that there is a critical neutral gas surface density for star formation below which it is highly suppressed. This promoted the idea that dark galaxies could exist if their gas surface densities remain sufficiently low. One method of detecting this population is to search for the H I signature of the neutral gas within the galaxies. This in turn presented a problem - any H I survey hoping to detect these galaxies ought to have the ability to detect sufficiently low column density gas ($< 10^{19}$ cm^{-2}). Not only that but it was emphasised that multi-wavelength observations are critical to confirm or reject dark galaxy candidates.

One such survey is the Arecibo Galaxy Environment Survey (AGES). Among its many goals, one is to put constraints on the population of dark galaxies. The survey was described in detail in Chapter 3. The results from the first two datasets from AGES were presented in Chapter 4. The results first demonstrated that the survey strategy and the subsequent data reduction techniques were producing data which met the predefined targets; producing uniform, well calibrated data that do not

suffer from the problems (e.g. baseline ripple, low or complex sensitivity) that have dogged previous H I surveys.

To identify possible optical counterparts 2MASS and SuperCOSMOS images were examined in detail. The limitations of these shallow surveys highlighted the necessity for dedicated, deep optical and NIR follow up for the AGES H I data. One such dataset was provided from observations taken with MEGACAM on the 4 m CFHT. The image obtained proved to be a double-edged sword. While there is an obvious improvement in the ability to recover LSB objects, the images also pick up many more background objects. This creates a dilemma – to put meaningful constraints on the surface brightness of candidate dark galaxies, deep optical data are needed, but deep optical data also detect more background objects, leading to confusion. Confusion can be alleviated to some extent by taking interferometric radio observations to reduce the positional uncertainty. But it is vital to take optical spectra of all potential counterparts in a blind H I survey.

The survey has returned two candidates for dark galaxies. Based on the calculations of Davies et al. (2006) it was expected that 23% of the galaxies in AGES would be dark galaxies. It was explained, however, that this figure only applied to a simulated galaxy population at the distance of the Virgo cluster. Only one galaxy was discovered within this distance regime, and it had an optical counterpart. This result supports the predictions of Taylor & Webster (2005) that dark galaxies simply don't exist, and the dark galaxy candidates could simply be low surface brightness galaxies that are obscured by a Galactic region of high extinction. This won't be known until follow up observations are conducted.

The 23% of dark galaxies predicted by Davies et al. (2006) is not ruled out by these observations, but with a sample of only one galaxy it is fairly meaningless to

draw any conclusions. Given the low return on galaxies at such a low redshift, it's unlikely that this question will be tested until the Virgo observations themselves are completed.

The AGES data was then used to calculate a HIMF. The data were well fit by a Schechter function parameterised by $\alpha = -1.28 \pm 0.17$, $\Phi_* = 0.0076 \pm 0.0027$ and $M_* = 7.7 \pm 1.8 \times 10^9$ $M_\odot$. These values agree within the uncertainties with recent measurements from HIPASS and appear to rule out the steep faint-end slope of Schneider & Rosenberg (2002). There is a departure from the HIMF at the low-mass end of the HIMF similar to that found by Spitzak, Schneider & Rosenberg (1998). This trend, as in the Arecibo Slice Survey, was based on only a handful of objects. Since the methods of deriving the two HIMFs was the same, this suggests that the upturn is due to the analysis method, which might underestimate the search volume for these low mass objects.

The AGES HIMF was used to derive the H I mass distribution for the local Universe. The calculated value for the space density of neutral hydrogen was found to be $\rho_{HI} = 7.5^{0.6}_{0.3} \times 10^7 M_\odot$ Mpc^{-3}. This is slightly higher than some previous measurements and probably points to some contamination from the Abell 1367 cluster data which has artificially boosted the number of high mass galaxies. The overall contribution of H I to the Universal energy density was calculated from this value and found to be $\Omega_{HI} = 4.1^{1.8}_{1.6} \times 10^{-4}$, which is also in agreement with previous measurements of this value.

Assuming the two candidates are indeed optically dark, based on this value the contribution of dark galaxies was calculated to be 4% to their respective mass bins, and less than 0.5% overall. The number density was found to be $n_{dark} \sim 6.6 \times 10^{-4}$ Mpc^{-3}. Hence it would appear that dark galaxies are not numerous enough nor of

substantial mass to be able to account for the 'missing mass' or to be able to fully represent the high number of dark matter haloes produced by CDM simulations.

Herein lies a dilemma – Davies et al. (2006) developed their models based on a ΛCDM Universe, populating CDM-derived dark matter haloes with baryonic matter (gas). The resulting population of proto-galaxies are then constrained by an empirically derived star-formation law. A small but significant fraction of these objects do not meet the criteria for star formation and so remain dark. A population of dark galaxies is predicted to exist and be detectable by this and previous H I surveys.

Results from previous H I surveys and this survey have failed to convincingly discover this missing population, so questions must be raised about the model itself or the interpretation of this model which has led to this prediction. Two crucial questions are how much mass is transferred to the disk when a galaxy is forming and also can low-density H I gas survive in the IGM over sufficiently long periods of time? The answer may be simply that the baryons exist as ionised hydrogen locked in the potential wells of these dark matter haloes. H I absorption studies and recent H I emission studies (Braun & Thilker, 2006) provide evidence of low density gas. However, the timescales over which this gas can survive are still under scrutiny. If simulations to answer these questions still support a substantial population of dark galaxies then CDM has to be called into question.

Even with less than 5% of the survey complete, AGES has shown that it is capable of detecting previously uncatalogued sources (some of which appear to have no optical counterparts), constraining the low-mass end of the HIMF, and probing the cosmic impact of neutral gas at the present epoch. As the survey continues to accrue data especially in the non-radio bands, it will be possible to put even

tighter constraints on these values and further probe environmental effects on H I distribution and morphology in the local Universe.

Bibliography

Arp, H. 1965, Astrophys. J., 142, 402

Auld, R., Minchin, R. F., Davies, J. I., Catinella, B., van Driel, W., Henning, P. A., Linder, S., Momjian, E., Muller, E., O'Neil, K., Sabatini, S., Schneider, S., Bothun, G., Cortese, L., Disney, M., Hoffman, G. L., Putman, M., Rosenberg, J. L., Baes, M., de Blok, W. J. G., Boselli, A., Brinks, E., Brosch, N., Irwin, J., Karachentsev, I. D., Kilborn, V. A., Koribalski, B., & Spekkens, K. 2006, Mon. Not. R. Astr. Soc., 371, 1617

Auld, R. R. 2003, Master's thesis, Manchester University

Banks, G. D., Disney, M. J., Knezek, P. M., Jerjen, H., Barnes, D. G., Bhatal, R., de Blok, W. J. G., Boyce, P. J., Ekers, R. D., Freeman, K. C., Gibson, B. K., Henning, P. A., Kilborn, V., Koribalski, B., Kraan-Korteweg, R. C., Malin, D. F., Minchin, R. F., Mould, J. R., Oosterloo, T., Price, R. M., Putman, M. E., Ryder, S. D., Sadler, E. M., Staveley-Smith, L., Stewart, I., Stootman, F., Vaile, R. A., Webster, R. L., & Wright, A. E. 1999, Astrophys. J., 524, 612

Barnes, D. G., Staveley-Smith, L., de Blok, W. J. G., Oosterloo, T., Stewart, I. M., Wright, A. E., Banks, G. D., Bhathal, R., Boyce, P. J., Calabretta, M. R., Disney, M. J., Drinkwater, M. J., Ekers, R. D., Freeman, K. C., Gibson, B. K., Green, A. J., Haynes, R. F., te Lintel Hekkert, P., Henning, P. A., Jerjen, H.,

Juraszek, S., Kesteven, M. J., Kilborn, V. A., Knezek, P. M., Koribalski, B., Kraan-Korteweg, R. C., Malin, D. F., Marquarding, M., Minchin, R. F., Mould, J. R., Price, R. M., Putman, M. E., Ryder, S. D., Sadler, E. M., Schröder, A., Stootman, F., Webster, R. L., Wilson, W. E., & Ye, T. 2001, Mon. Not. R. Astr. Soc., 322, 486

Bekki, K., Koribalski, B. S., & Kilborn, V. A. 2005, Mon. Not. R. Astr. Soc., 363, L21

Bell, E. F., Barnaby, D., Bower, R. G., de Jong, R. S., Harper, D. A., Hereld, M., Loewenstein, R. F., & Rauscher, B. J. 2000, Mon. Not. R. Astr. Soc., 312, 470

Bennett, C. L., Halpern, M., Hinshaw, G., Jarosik, N., Kogut, A., Limon, M., Meyer, S. S., Page, L., Spergel, D. N., Tucker, G. S., Wollack, E., Wright, E. L., Barnes, C., Greason, M. R., Hill, R. S., Komatsu, E., Nolta, M. R., Odegard, N., Peiris, H. V., Verde, L., & Weiland, J. L. 2003, Astrophys. J. Suppl., 148, 1

Benson, A. J., Frenk, C. S., Baugh, C. M., Cole, S., & Lacey, C. G. 2001, Mon. Not. R. Astr. Soc., 327, 1041

Bernardi, M., Sheth, R. K., Annis, J., Burles, S., Eisenstein, D. J., Finkbeiner, D. P., Hogg, D. W., Lupton, R. H., Schlegel, D. J., SubbaRao, M., Bahcall, N. A., Blakeslee, J. P., Brinkmann, J., Castander, F. J., Connolly, A. J., Csabai, I., Doi, M., Fukugita, M., Frieman, J., Heckman, T., Hennessy, G. S., Ivezić, Ž., Knapp, G. R., Lamb, D. Q., McKay, T., Munn, J. A., Nichol, R., Okamura, S., Schneider, D. P., Thakar, A. R., & York, D. G. 2003, Astron. J., 125, 1817

Bertone, G., Sigl, G., & Silk, J. 2001, Mon. Not. R. Astr. Soc., 326, 799

Binggeli, B., Popescu, C. C., & Tammann, G. A. 1993, Astr. Astrophys. Suppl., 98, 275

Binggeli, B., Sandage, A., & Tammann, G. A. 1985, Astron. J., 90, 1681

Binney, J. & Tremaine, S. 1987, Galactic dynamics (Princeton, NJ, Princeton University Press, 1987, 747 p.)

Bothun, G. D., Impey, C. D., Malin, D. F., & Mould, J. R. 1987, Astron. J., 94, 23

Braun, R. & Thilker, D. 2004, in Astronomical Society of the Pacific Conference Series, Vol. 327, Satellites and Tidal Streams, ed. F. Prada, D. Martinez Delgado, & T. J. Mahoney, 139–+

Braun, R. & Thilker, D. A. 2005, in ASP Conf. Ser. 331: Extra-Planar Gas, ed. R. Braun, 121–+

Briggs, F. H. 1986, Astrophys. J., 300, 613

—. 1997, Astrophys. J. Letters, 484, L29+

Broeils, A. H. & Rhee, M.-H. 1997, Astron. Astrophys., 324, 877

Broeils, A. H. & van Woerden, H. 1994, Astr. Astrophys. Suppl., 107, 129

Clowe, D., Bradač, M., Gonzalez, A. H., Markevitch, M., Randall, S. W., Jones, C., & Zaritsky, D. 2006, Astrophys. J. Letters, 648, L109

Colless, M., Dalton, G., Maddox, S., Sutherland, W., Norberg, P., Cole, S., Bland-Hawthorn, J., Bridges, T., Cannon, R., Collins, C., Couch, W., Cross, N., Deeley, K., De Propris, R., Driver, S. P., Efstathiou, G., Ellis, R. S., Frenk, C. S., Glazebrook, K., Jackson, C., Lahav, O., Lewis, I., Lumsden, S., Madgwick, D., Peacock, J. A., Peterson, B. A., Price, I., Seaborne, M., & Taylor, K. 2001, Mon. Not. R. Astr. Soc., 328, 1039

Condon, J. J., Cotton, W. D., Greisen, E. W., Yin, Q. F., Perley, R. A., Taylor, G. B., & Broderick, J. J. 1998, Astron. J., 115, 1693

Cortese, L., Gavazzi, G., Boselli, A., Iglesias-Paramo, J., & Carrasco, L. 2004, Astron. Astrophys., 425, 429

Dalcanton, J. J., Spergel, D. N., Gunn, J. E., Schmidt, M., & Schneider, D. P. 1997, Astron. J., 114, 635

Davies, J., Minchin, R., Sabatini, S., van Driel, W., Baes, M., Boyce, P., de Blok, W. J. G., Disney, M., Evans, R., Kilborn, V., Lang, R., Linder, S., Roberts, S., & Smith, R. 2004, Mon. Not. R. Astr. Soc., 349, 922

Davies, J., Phillipps, S., Disney, M., Boyce, P., & Evans, R. 1994, Mon. Not. R. Astr. Soc., 268, 984

Davies, J. I., de Blok, W. J. G., Smith, R. M., Kambas, A., Sabatini, S., Linder, S. M., & Salehi-Reyhani, S. A. 2001, Mon. Not. R. Astr. Soc., 328, 1151

Davies, J. I., Disney, M. J., Minchin, R. F., Auld, R., & Smith, R. 2006, Mon. Not. R. Astr. Soc., 368, 1479

de Blok, E., Walter, F., & Bell, E. 1999, Astrophys. Space Sci., 269, 101

de Blok, W. J. G. & Bosma, A. 2002, Astron. Astrophys., 385, 816

de Blok, W. J. G. & McGaugh, S. S. 1996, Astrophys. J. Letters, 469, L89+

—. 1997a, Mon. Not. R. Astr. Soc., 290, 533

—. 1997b, Mon. Not. R. Astr. Soc., 290, 533

de Blok, W. J. G., van der Hulst, J. M., & Bothun, G. D. 1995, Mon. Not. R. Astr. Soc., 274, 235

de Blok, W. J. G. & Walter, F. 2006, Astron. J., 131, 363

de Jong, R. S. & Lacey, C. 1999, in Astronomical Society of the Pacific Conference Series, Vol. 170, The Low Surface Brightness Universe, ed. J. I. Davies, C. Impey, & S. Phillips, 52–+

de Vaucouleurs, G., de Vaucouleurs, A., Corwin, H. G., Buta, R. J., Paturel, G., & Fouque, P. 1991, Third Reference Catalogue of Bright Galaxies (Volume 1-3, XII, 2069 pp. 7 figs.. Springer-Verlag Berlin Heidelberg New York)

Disney, M. & Phillipps, S. 1983, Mon. Not. R. Astr. Soc., 205, 1253

Disney, M. J. 1976, Nature, 263, 573

Djorgovski, S., Lasker, B. M., Weir, W. N., Postman, M., Reid, I. N., & Laidler, V. G. 1992, in Bulletin of the American Astronomical Society, Vol. 24, Bulletin of the American Astronomical Society, 750–+

Djorgovski, S. & Spinrad, H. 1984, Astrophys. J. Letters, 282, L1

Donley, J. L., Koribalski, B. S., Staveley-Smith, L., Kraan-Korteweg, R. C., Schröder, A., & Henning, P. A. 2006, Mon. Not. R. Astr. Soc., 369, 1741

Doyle, M. T., Drinkwater, M. J., Rohde, D. J., Pimbblet, K. A., Read, M., Meyer, M. J., Zwaan, M. A., Ryan-Weber, E., Stevens, J., Koribalski, B. S., Webster, R. L., Staveley-Smith, L., Barnes, D. G., Howlett, M., Kilborn, V. A., Waugh, M., Pierce, M. J., Bhathal, R., de Blok, W. J. G., Disney, M. J., Ekers, R. D., Freeman, K. C., Garcia, D. A., Gibson, B. K., Harnett, J., Henning, P. A., Jerjen, H., Kesteven, M. J., Knezek, P. M., Mader, S., Marquarding, M., Minchin, R. F., O'Brien, J., Oosterloo, T., Price, R. M., Putman, M. E., Ryder, S. D., Sadler, E. M., Stewart, I. M., Stootman, F., & Wright, A. E. 2005, Mon. Not. R. Astr. Soc., 361, 34

Efstathiou, G., Ellis, R. S., & Peterson, B. A. 1988, Mon. Not. R. Astr. Soc., 232, 431

Elmegreen, B. G. 1993, Astrophys. J. Letters, 419, L29+

Elmegreen, B. G. & Parravano, A. 1994, Astrophys. J. Letters, 435, L121+

Elmegreen, D. M. & Salzer, J. J. 1999, Astron. J., 117, 764

Esipov, V. F., Kyazumov, G. A., & Jafarov, A. R. 1991, Soviet Astron., 68, 909

Ewen, H. I. & Purcell, E. M. 1951, Nature

Fall, S. M. & Efstathiou, G. 1980, Mon. Not. R. Astr. Soc., 193, 189

Ferguson, A. M. N., Wyse, R. F. G., Gallagher, J. S., & Hunter, D. A. 1998, Astrophys. J. Letters, 506, L19

Ferguson, H. C. & Sandage, A. 1988, Astron. J., 96, 1520

Fish, R. A. 1964, Astrophys. J., 139, 284

Freeman, K. C. 1970, Astrophys. J., 160, 811

Freeman, K. C. 1978, in IAU Symposium, Vol. 77, Structure and Properties of Nearby Galaxies, ed. E. M. Berkhuijsen & R. Wielebinski, 3–10

Freudling, W., Staveley-Smith, L., Calabretta, M., Catinella, B., van Driel, W., Linder, S., Minchin, R., Momjian, E., Zwaan, M., & AUDS Team. 2005, Bulletin of the American Astronomical Society, 37, 1316

Fukugita, M., Hogan, C. J., & Peebles, P. J. E. 1998, Astrophys. J., 503, 518

Gallagher, J. S. & Hunter, D. A. 1984, Ann. Rev. Astron. Astrophys., 22, 37

Garcia-Appadoo, D. A. 2005, PhD thesis, Cardiff University

Gavazzi, G., Boselli, A., Donati, A., Franzetti, P., & Scodeggio, M. 2003, Astron. Astrophys., 400, 451

Gavazzi, G., Boselli, A., Mayer, L., Iglesias-Paramo, J., Vílchez, J. M., & Carrasco, L. 2001, Astrophys. J. Letters, 563, L23

Gavazzi, G., Pierini, D., & Boselli, A. 1996, Astron. Astrophys., 312, 397

Geller, M. J. & Huchra, J. P. 1989, Science., 246, 897

Giovanelli, R., Haynes, M. P., Kent, B. R., Perillat, P., Saintonge, A., Brosch, N., Catinella, B., Hoffman, G. L., Stierwalt, S., Spekkens, K., Lerner, M. S., Masters, K. L., Momjian, E., Rosenberg, J. L., Springob, C. M., Boselli, A., Charmandaris, V., Darling, J. K., Davies, J., Lambas, D. G., Gavazzi, G., Giovanardi, C., Hardy, E., Hunt, L. K., Iovino, A., Karachentsev, I. D., Karachentseva, V. E., Koopmann, R. A., Marinoni, C., Minchin, R., Muller, E., Putman, M., Pantoja, C., Salzer, J. J., Scodeggio, M., Skillman, E., Solanes, J. M., Valotto, C., van Driel, W., & van Zee, L. 2005, Astron. J., 130, 2598

Giovanelli, R., Haynes, M. P., Kent, B. R., Saintonge, A., Stierwalt, S., Altaf, A., Balonek, T., Brosch, N., Brown, S., Catinella, B., Furniss, A., Goldstein, J., Hoffman, G. L., Koopmann, R. A., Kornreich, D. A., Mahmood, B., Martin, A. M., Masters, K. L., Mitschang, A., Momjian, E., Nair, P. H., Rosenberg, J. L., & Walsh, B. 2007, Astron. J., 133, 2569

Goldreich, P. & Lynden-Bell, D. 1965, Mon. Not. R. Astr. Soc., 130, 97

Gottesman, S. T. & Davies, R. D. 1970, Mon. Not. R. Astr. Soc., 149, 263

Guiderdoni, B. 1987, Astron. Astrophys., 172, 27

Guth, A. H. 1981, Phys. Rev. D (Particles and Fields), 23, 347

Hawkins, M. R. S. 1997, Astron. Astrophys., 328, L25

Hendry, M. A., Smartt, S. J., Maund, J. R., Pastorello, A., Zampieri, L., Benetti, S., Turatto, M., Cappellaro, E., Meikle, W. P. S., Kotak, R., Irwin, M. J., Jonker, P. G., Vermaas, L., Peletier, R. F., van Woerden, H., Exter, K. M., Pollacco, D. L., Leon, S., Verley, S., Benn, C. R., & Pignata, G. 2005, Mon. Not. R. Astr. Soc., 359, 906

Henning, P. A. 1995, Astrophys. J., 450, 578

Henning, P. A., Springob, C. M., Catinella, B., Momjian, E., Koribalski, B., Masters, K., Muller, E., Pantoja, C., Putman, M., Rosenberg, J. L., Schneider, S., & Staveley-Smith, L. 2006, American Astronomical Society Meeting Abstracts, 208, 53.04

Henning, P. A., Staveley-Smith, L., Ekers, R. D., Green, A. J., Haynes, R. F., Juraszek, S., Kesteven, M. J., Koribalski, B., Kraan-Korteweg, R. C., Price, R. M., Sadler, E. M., & Schröder, A. 2000, Astron. J., 119, 2686

Hoffman, G. L., Lu, N. Y., Salpeter, E. E., Farhat, B., Lamphier, C., & Roos, T. 1993, Astron. J., 106, 39

Hoyle, F. 1948, Mon. Not. R. Astr. Soc., 108, 372

Hubble, E. 1929, Proceedings of the National Academy of Science, 15, 168

Hubble, E. P. 1926, Astrophys. J., 64, 321

Huchra, J., Davis, M., Latham, D., & Tonry, J. 1983, Astrophys. J. Suppl., 52, 89

Huchra, J. P., Vogeley, M. S., & Geller, M. J. 1999, Astrophys. J. Suppl., 121, 287

Huchtmeier, W. K., Karachentsev, I. D., & Karachentseva, V. E. 2003, Astron. Astrophys., 401, 483

Hunter, D. A. & Elmegreen, B. G. 2004, Astron. J., 128, 2170

—. 2006, Astrophys. J. Suppl., 162, 49

Hunter, D. A., Elmegreen, B. G., & Baker, A. L. 1998, Astrophys. J., 493, 595

Hunter, D. A. & Sage, L. 1993, Publs. Astr. Soc. Pacif., 105, 374

Impey, C., Bothun, G., & Malin, D. 1988, Astrophys. J., 330, 634

Impey, C. D., Sprayberry, D., Irwin, M. J., & Bothun, G. D. 1996, Astrophys. J. Suppl., 105, 209

Jeans, J. H. 1928, Astronomy and cosmogony (Cambridge [Eng.] The University press, 1928.)

Jimenez, R., Heavens, A. F., Hawkins, M. R. S., & Padoan, P. 1997, Mon. Not. R. Astr. Soc., 292, L5

Jones, D. H., Saunders, W., Colless, M., Read, M. A., Parker, Q. A., Watson, F. G., Campbell, L. A., Burkey, D., Mauch, T., Moore, L., Hartley, M., Cass, P., James, D., Russell, K., Fiegert, K., Dawe, J., Huchra, J., Jarrett, T., Lahav, O., Lucey, J., Mamon, G. A., Proust, D., Sadler, E. M., & Wakamatsu, K.-i. 2004, Mon. Not. R. Astr. Soc., 355, 747

Kamphuis, J. & Briggs, F. 1992, Astron. Astrophys., 253, 335

Karachentsev, I., Musella, I., & Grimaldi, A. 1996, Astron. Astrophys., 310, 722

Karachentsev, I. D., Karachentseva, V. E., & Huchtmeier, W. K. 2006, Astron. Astrophys., 451, 817

Karachentseva, V. E. 1973, Astrofizicheskie Issledovaniia Izvestiya Spetsial'noj Astrofizicheskoj Observatorii, 8, 3

Kennicutt, R. C. 1989, Astrophys. J., 344, 685

Kilborn, K., Webster, R. L., & Staveley-Smith, L. 1999, Publs. Astr. Soc. Aust., 16, 8

Kim, S., Staveley-Smith, L., Dopita, M. A., Freeman, K. C., Sault, R. J., Kesteven, M. J., & McConnell, D. 1998, Astrophys. J., 503, 674

Kim, W.-T. & Ostriker, E. C. 2002, Astrophys. J., 570, 132

Klypin, A., Kravtsov, A. V., Valenzuela, O., & Prada, F. 1999, Astrophys. J., 522, 82

Koribalski, B. S., Staveley-Smith, L., Kilborn, V. A., Ryder, S. D., Kraan-Korteweg, R. C., Ryan-Weber, E. V., Ekers, R. D., Jerjen, H., Henning, P. A., Putman, M. E., Zwaan, M. A., de Blok, W. J. G., Calabretta, M. R., Disney, M. J., Minchin, R. F., Bhathal, R., Boyce, P. J., Drinkwater, M. J., Freeman, K. C., Gibson, B. K., Green, A. J., Haynes, R. F., Juraszek, S., Kesteven, M. J., Knezek, P. M., Mader, S., Marquarding, M., Meyer, M., Mould, J. R., Oosterloo, T., O'Brien, J., Price, R. M., Sadler, E. M., Schröder, A., Stewart, I. M., Stootman, F., Waugh, M., Warren, B. E., Webster, R. L., & Wright, A. E. 2004, Astron. J., 128, 16

Kormendy, J. 1977, Astrophys. J., 217, 406

Lacey, C. G. & Ostriker, J. P. 1985, Astrophys. J., 299, 633

Lang, R. H., Boyce, P. J., Kilborn, V. A., Minchin, R. F., Disney, M. J., Jordan, C. A., Grossi, M., Garcia, D. A., Freeman, K. C., Phillipps, S., & Wright, A. E. 2003, Mon. Not. R. Astr. Soc., 342, 738

Lauberts, A. & Valentijn, E. A. 1989, The surface photometry catalogue of the ESO-Uppsala galaxies (Garching: European Southern Observatory, —c1989)

Longmore, A. J., Hawarden, T. G., Goss, W. M., Mebold, U., & Webster, B. L. 1982, Mon. Not. R. Astr. Soc., 200, 325

Maccìo, A. V., B., M., J., S., & D., P. 2006, in XXVIth Astrophysics Moriond Meeting: "From dark halos to light", ed. T. L., M. S., & T. J. (Editions Frontieres)

Maloney, P. 1993, Astrophys. J., 414, 41

Martin, C. L. & Kennicutt, R. C. 2001, Astrophys. J., 555, 301

Martin, D. C., Fanson, J., Schiminovich, D., Morrissey, P., Friedman, P. G., Barlow, T. A., Conrow, T., Grange, R., Jelinsky, P. N., Milliard, B., Siegmund, O. H. W., Bianchi, L., Byun, Y.-I., Donas, J., Forster, K., Heckman, T. M., Lee, Y.-W., Madore, B. F., Malina, R. F., Neff, S. G., Rich, R. M., Small, T., Surber, F., Szalay, A. S., Welsh, B., & Wyder, T. K. 2005, Astrophys. J. Letters, 619, L1

Martin, M. C. 1998, Astr. Astrophys. Suppl., 131, 73

Martin, N. F., Ibata, R. A., Bellazzini, M., Irwin, M. J., Lewis, G. F., & Dehnen, W. 2004, Mon. Not. R. Astr. Soc., 348, 12

Marzke, R. O., da Costa, L. N., Pellegrini, P. S., Willmer, C. N. A., & Geller, M. J. 1998, Astrophys. J., 503, 617

McGaugh, S. 1999, in Astronomical Society of the Pacific Conference Series, Vol. 170, The Low Surface Brightness Universe, ed. J. I. Davies, C. Impey, & S. Phillips, 19–+

McGaugh, S. S. 1994, Astrophys. J., 426, 135

Meyer, M. J., Zwaan, M. A., Webster, R. L., Staveley-Smith, L., Ryan-Weber, E., Drinkwater, M. J., Barnes, D. G., Howlett, M., Kilborn, V. A., Stevens, J., Waugh, M., Pierce, M. J., Bhathal, R., de Blok, W. J. G., Disney, M. J., Ekers, R. D., Freeman, K. C., Garcia, D. A., Gibson, B. K., Harnett, J., Henning, P. A., Jerjen, H., Kesteven, M. J., Knezek, P. M., Koribalski, B. S., Mader, S., Marquarding, M., Minchin, R. F., O'Brien, J., Oosterloo, T., Price, R. M., Putman, M. E., Ryder, S. D., Sadler, E. M., Stewart, I. M., Stootman, F., & Wright, A. E. 2004, Mon. Not. R. Astr. Soc., 350, 1195

Miller, E. D. & Bregman, J. N. 2005, in Astronomical Society of the Pacific Conference Series, Vol. 331, Extra-Planar Gas, ed. R. Braun, 261–+

Milne, E. A. 1935, Relativity, gravitation and world-structure (Oxford, The Clarendon press, 1935.)

Minchin, R., Davies, J., Disney, M., Boyce, P., Garcia, D., Jordan, C., Kilborn, V., Lang, R., Roberts, S., Sabatini, S., & van Driel, W. 2005a, Astrophys. J. Letters, 622, L21

Minchin, R. F. 2001, PhD thesis, AA (Department of Physics and Astronomy, Cardiff University 5 The Parade, Cardiff, Glamorgan, CF24 3YB, Wales, UK

Minchin, R. F., Davies, J. I., Disney, M. J., Marble, A. R., Impey, C. D., Boyce, P. J., Garcia, D. A., Grossi, M., Jordan, C. A., Lang, R. H., Roberts, S., Sabatini, S., & van Driel, W. 2005b, ArXiv Astrophysics e-prints

Minchin, R. F., Davies, J. I., Disney, M. J., Marble, A. R., Impey, C. D., Boyce, P. J., Garcia, D. A., Grossi, M., Jordan, C. A., Lang, R. H., Roberts, S., Sabatini, S., & van Driel, W. 2005c, in baas, Vol. 37, Bull. AAS. , 1483–+

Minchin, R. F., Disney, M. J., Boyce, P. J., de Blok, W. J. G., Parker, Q. A., Banks, G. D., Freeman, K. C., Garcia, D. A., Gibson, B. K., Grossi, M., Haynes, R. F.,

Knezek, P. M., Lang, R. H., Malin, D. F., Price, R. M., Stewart, I. M., & Wright, A. E. 2003, Mon. Not. R. Astr. Soc., 346, 787

Mo, H. J., Mao, S., & White, S. D. M. 1998, Mon. Not. R. Astr. Soc., 295, 319

Moore, B., Ghigna, S., Governato, F., Lake, G., Quinn, T., Stadel, J., & Tozzi, P. 1999, Astrophys. J. Letters, 524, L19

Nilson, P. 1973, Uppsala general catalogue of galaxies (Acta Universitatis Upsaliensis. Nova Acta Regiae Societatis Scientiarum Upsaliensis - Uppsala Astronomiska Observatoriums Annaler, Uppsala: Astronomiska Observatorium, 1973)

O'Neil, K. & Bothun, G. 2000, Astrophys. J., 529, 811

O'Neil, K., Verheijen, M. A. W., & McGaugh, S. S. 2000, Astron. J., 119, 2154

Oosterloo, T. & van Gorkom, J. 2005, Astron. Astrophys., 437, L19

Penzias, A. A. & Wilson, R. W. 1965, Astrophys. J., 142, 419

Perlmutter, S., Aldering, G., Goldhaber, G., Knop, R. A., Nugent, P., Castro, P. G., Deustua, S., Fabbro, S., Goobar, A., Groom, D. E., Hook, I. M., Kim, A. G., Kim, M. Y., Lee, J. C., Nunes, N. J., Pain, R., Pennypacker, C. R., Quimby, R., Lidman, C., Ellis, R. S., Irwin, M., McMahon, R. G., Ruiz-Lapuente, P., Walton, N., Schaefer, B., Boyle, B. J., Filippenko, A. V., Matheson, T., Fruchter, A. S., Panagia, N., Newberg, H. J. M., Couch, W. J., & The Supernova Cosmology Project. 1999, Astrophys. J., 517, 565

Phillipps, S., Disney, M. J., Kibblewhite, E. J., & Cawson, M. G. M. 1987, Mon. Not. R. Astr. Soc., 229, 505

Prugniel, P. & Heraudeau, P. 1998, Astr. Astrophys. Suppl., 128, 299

Putman, M. E., de Heij, V., Staveley-Smith, L., Braun, R., Freeman, K. C., Gibson, B. K., Burton, W. B., Barnes, D. G., Banks, G. D., Bhathal, R., de Blok, W. J. G., Boyce, P. J., Disney, M. J., Drinkwater, M. J., Ekers, R. D., Henning, P. A., Jerjen, H., Kilborn, V. A., Knezek, P. M., Koribalski, B., Malin, D. F., Marquarding, M., Minchin, R. F., Mould, J. R., Oosterloo, T., Price, R. M., Ryder, S. D., Sadler, E. M., Stewart, I., Stootman, F., Webster, R. L., & Wright, A. E. 2002, Astron. J., 123, 873

Putman, M. E., Gibson, B. K., Staveley-Smith, L., Banks, G., Barnes, D. G., Bhatal, R., Disney, M. J., Ekers, R. D., Freeman, K. C., Haynes, R. F., Henning, P., Jerjen, H., Kilborn, V., Koribalski, B., Knezek, P., Malin, D. F., Mould, J. R., Oosterloo, T., Price, R. M., Ryder, S. D., Sadler, E. M., Stewart, I., Stootman, F., Vaile, R. A., Webster, R. L., & Wright, A. E. 1998, Nature, 394, 752

Putman, M. E., Staveley-Smith, L., Freeman, K. C., Gibson, B. K., & Barnes, D. G. 2003, Astrophys. J., 586, 170

Quirk, W. J. 1972, Astrophys. J. Letters, 176, L9+

Riess, A. G., Filippenko, A. V., Challis, P., Clocchiatti, A., Diercks, A., Garnavich, P. M., Gilliland, R. L., Hogan, C. J., Jha, S., Kirshner, R. P., Leibundgut, B., Phillips, M. M., Reiss, D., Schmidt, B. P., Schommer, R. A., Smith, R. C., Spyromilio, J., Stubbs, C., Suntzeff, N. B., & Tonry, J. 1998, Astron. J., 116, 1009

Roberts, M. S. & Haynes, M. P. 1994, Ann. Rev. Astron. Astrophys., 32, 115

Roberts, M. S. & Rots, A. H. 1973, Astron. Astrophys., 26, 483

Rosenberg, J. L. & Schneider, S. E. 2000, Astrophys. J. Suppl., 130, 177

—. 2002, Astrophys. J., 567, 247

Rosenberg, J. L., Schneider, S. E., & Posson-Brown, J. 2005, Astron. J., 129, 1311

Rubin, V. C. & Ford, W. K. J. 1970, Astrophys. J., 159, 379

Ryan-Weber, E. V., Meurer, G. R., Freeman, K. C., Putman, M. E., Webster, R. L., Drinkwater, M. J., Ferguson, H. C., Hanish, D., Heckman, T. M., Kennicutt, R. C., Kilborn, V. A., Knezek, P. M., Koribalski, B. S., Meyer, M. J., Oey, M. S., Smith, R. C., Staveley-Smith, L., & Zwaan, M. A. 2004, Astron. J., 127, 1431

Ryder, S. D., Koribalski, B., Staveley-Smith, L., Kilborn, V. A., Malin, D. F., Banks, G. D., Barnes, D. G., Bhatal, R., de Blok, W. J. G., Boyce, P. J., Disney, M. J., Drinkwater, M. J., Ekers, R. D., Freeman, K. C., Gibson, B. K., Henning, P. A., Jerjen, H., Knezek, P. M., Marquarding, M., Minchin, R. F., Mould, J. R., Oosterloo, T., Price, R. M., Putman, M. E., Sadler, E. M., Stewart, I., Stootman, F., Webster, R. L., & Wright, A. E. 2001, Astrophys. J., 555, 232

Sabatini, S., Davies, J., Scaramella, R., Smith, R., Baes, M., Linder, S. M., Roberts, S., & Testa, V. 2003, Mon. Not. R. Astr. Soc., 341, 981

Saintonge, A. 2007, Astron. J., 133, 2087

Sandage, A. 1961, Astrophys. J., 133, 355

Sandage, A. & Tammann, G. A. 1974, Astrophys. J., 194, 559

Sandage, A., Tammann, G. A., & Yahil, A. 1979, Astrophys. J., 232, 352

Sanders, R. H., van Albada, T. S., & Oosterloo, T. A. 1984, Astrophys. J. Letters, 278, L91

Schaye, J. 2004, Astrophys. J., 609, 667

Schechter, P. 1976, Astrophys. J., 203, 297

Schmidt, K.-H. & Boller, T. 1992, Astronomische Nachrichten, 313, 189

Schmidt, M. 1968, Astrophys. J., 151, 393

Schneider, S. E., Spitzak, J. G., & Rosenberg, J. L. 1998, Astrophys. J. Letters, 507, L9

Schombert, J. M., Bothun, G. D., Impey, C. D., & Mundy, L. G. 1990, Astron. J., 100, 1523

Schombert, J. M., Bothun, G. D., Schneider, S. E., & McGaugh, S. S. 1992, Astron. J., 103, 1107

Shapiro, P. R. & Field, G. B. 1976, Astrophys. J., 205, 762

Sharina, M. E., Karachentsev, I. D., & Tikhonov, N. A. 1996, Astr. Astrophys. Suppl., 119, 499

Shostak, G. S. 1977, Astron. Astrophys., 54, 919

Shull, J. M. & Thronson, H. A., eds. 1993, The evolution of galaxies and their environment

Silk, J. 2004, in American Institute of Physics Conference Series, Vol. 743, The New Cosmology: Conference on Strings and Cosmology, ed. R. E. Allen, D. V. Nanopoulos, & C. N. Pope, 33–40

Simpson, C. E. & Gottesman, S. T. 2000, Astron. J., 120, 2975

Skillman, E. D. 1987, in Star Formation in Galaxies, 263–266

Skillman, E. D. & Bothun, G. D. 1986, Astron. Astrophys., 165, 45

Skrutskie, M. F., Cutri, R. M., Stiening, R., Weinberg, M. D., Schneider, S., Carpenter, J. M., Beichman, C., Capps, R., Chester, T., Elias, J., Huchra,

J., Liebert, J., Lonsdale, C., Monet, D. G., Price, S., Seitzer, P., Jarrett, T., Kirkpatrick, J. D., Gizis, J. E., Howard, E., Evans, T., Fowler, J., Fullmer, L., Hurt, R., Light, R., Kopan, E. L., Marsh, K. A., McCallon, H. L., Tam, R., Van Dyk, S., & Wheelock, S. 2006, Astron. J., 131, 1163

Slipher, V. M. 1913, Lowell Observatory Bulletin, 2, 56

Smoot, G. F., Bennett, C. L., Kogut, A., Aymon, J., Backus, C., de Amici, G., Galuk, K., Jackson, P. D., Keegstra, P., Rokke, L., Tenorio, L., Torres, S., Gulkis, S., Hauser, M. G., Janssen, M. A., Mather, J. C., Weiss, R., Wilkinson, D. T., Wright, E. L., Boggess, N. W., Cheng, E. S., Kelsall, T., Lubin, P., Meyer, S., Moseley, S. H., Murdock, T. L., Shafer, R. A., & Silverberg, R. F. 1991, Astrophys. J. Letters, 371, L1

Spergel, D. N., Verde, L., Peiris, H. V., Komatsu, E., Nolta, M. R., Bennett, C. L., Halpern, M., Hinshaw, G., Jarosik, N., Kogut, A., Limon, M., Meyer, S. S., Page, L., Tucker, G. S., Weiland, J. L., Wollack, E., & Wright, E. L. 2003, Astrophys. J. Suppl., 148, 175

Spitzak, J. G. & Schneider, S. E. 1998, Astrophys. J. Suppl., 119, 159

Springel, V., White, S. D. M., Jenkins, A., Frenk, C. S., Yoshida, N., Gao, L., Navarro, J., Thacker, R., Croton, D., Helly, J., Peacock, J. A., Cole, S., Thomas, P., Couchman, H., Evrard, A., Colberg, J., & Pearce, F. 2005, Nature, 435, 629

Springob, C. M., Haynes, M. P., Giovanelli, R., & Kent, B. R. 2005, Astrophys. J. Suppl., 160, 149

Staveley-Smith, L., Juraszek, S., Henning, P. A., Koribalski, B. S., & Kraan-Korteweg, R. C. 2000, in Astronomical Society of the Pacific Conference Series, Vol. 218, Mapping the Hidden Universe: The Universe behind the Milky Way -

The Universe in HI, ed. R. C. Kraan-Korteweg, P. A. Henning, & H. Andernach, 207–+

Stoughton, C., Lupton, R. H., Bernardi, M., Blanton, M. R., Burles, S., Castander, F. J., Connolly, A. J., Eisenstein, D. J., Frieman, J. A., Hennessy, G. S., Hindsley, R. B., Ivezić, Ž., Kent, S., Kunszt, P. Z., Lee, B. C., Meiksin, A., Munn, J. A., Newberg, H. J., Nichol, R. C., Nicinski, T., Pier, J. R., Richards, G. T., Richmond, M. W., Schlegel, D. J., Smith, J. A., Strauss, M. A., SubbaRao, M., Szalay, A. S., Thakar, A. R., Tucker, D. L., Vanden Berk, D. E., Yanny, B., Adelman, J. K., Anderson, Jr., J. E., Anderson, S. F., Annis, J., Bahcall, N. A., Bakken, J. A., Bartelmann, M., Bastian, S., Bauer, A., Berman, E., Böhringer, H., Boroski, W. N., Bracker, S., Briegel, C., Briggs, J. W., Brinkmann, J., Brunner, R., Carey, L., Carr, M. A., Chen, B., Christian, D., Colestock, P. L., Crocker, J. H., Csabai, I., Czarapata, P. C., Dalcanton, J., Davidsen, A. F., Davis, J. E., Dehnen, W., Dodelson, S., Doi, M., Dombeck, T., Donahue, M., Ellman, N., Elms, B. R., Evans, M. L., Eyer, L., Fan, X., Federwitz, G. R., Friedman, S., Fukugita, M., Gal, R., Gillespie, B., Glazebrook, K., Gray, J., Grebel, E. K., Greenawalt, B., Greene, G., Gunn, J. E., de Haas, E., Haiman, Z., Haldeman, M., Hall, P. B., Hamabe, M., Hansen, B., Harris, F. H., Harris, H., Harvanek, M., Hawley, S. L., Hayes, J. J. E., Heckman, T. M., Helmi, A., Henden, A., Hogan, C. J., Hogg, D. W., Holmgren, D. J., Holtzman, J., Huang, C.-H., Hull, C., Ichikawa, S.-I., Ichikawa, T., Johnston, D. E., Kauffmann, G., Kim, R. S. J., Kimball, T., Kinney, E., Klaene, M., Kleinman, S. J., Klypin, A., Knapp, G. R., Korienek, J., Krolik, J., Kron, R. G., Krzesiński, J., Lamb, D. Q., Leger, R. F., Limmongkol, S., Lindenmeyer, C., Long, D. C., Loomis, C., Loveday, J., MacKinnon, B., Mannery, E. J., Mantsch, P. M., Margon, B., McGehee, P., McKay, T. A., McLean, B., Menou, K., Merelli, A., Mo, H. J., Monet, D. G., Nakamura, O., Narayanan, V. K., Nash, T., Neilsen, Jr., E. H.,

Newman, P. R., Nitta, A., Odenkirchen, M., Okada, N., Okamura, S., Ostriker, J. P., Owen, R., Pauls, A. G., Peoples, J., Peterson, R. S., Petravick, D., Pope, A., Pordes, R., Postman, M., Prosapio, A., Quinn, T. R., Rechenmacher, R., Rivetta, C. H., Rix, H.-W., Rockosi, C. M., Rosner, R., Ruthmansdorfer, K., Sandford, D., Schneider, D. P., Scranton, R., Sekiguchi, M., Sergey, G., Sheth, R., Shimasaku, K., Smee, S., Snedden, S. A., Stebbins, A., Stubbs, C., Szapudi, I., Szkody, P., Szokoly, G. P., Tabachnik, S., Tsvetanov, Z., Uomoto, A., Vogeley, M. S., Voges, W., Waddell, P., Walterbos, R., Wang, S.-i., Watanabe, M., Weinberg, D. H., White, R. L., White, S. D. M., Wilhite, B., Wolfe, D., Yasuda, N., York, D. G., Zehavi, I., & Zheng, W. 2002, Astron. J., 123, 485

Sun, M. & Murray, S. S. 2002, Astrophys. J., 576, 708

Swaters, R. A. & Balcells, M. 2002, Astron. Astrophys., 390, 863

Taylor, C. L., Kobulnicky, H. A., & Skillman, E. D. 1998, Astron. J., 116, 2746

Taylor, E. N. & Webster, R. L. 2005, Astrophys. J., 634, 1067

Toomre, A. 1964, Astrophys. J., 139, 1217

Trimble, V. 1987, Ann. Rev. Astron. Astrophys., 25, 425

Tully, R. B. & Fisher, J. R. 1987, Nearby galaxies Atlas (Cambridge: University Press, 1987)

van den Hoek, L. B., de Blok, W. J. G., van der Hulst, J. M., & de Jong, T. 2000, Astron. Astrophys., 357, 397

van der Hulst, J. M., Skillman, E. D., Smith, T. R., Bothun, G. D., McGaugh, S. S., & de Blok, W. J. G. 1993, Astron. J., 106, 548

van der Kruit, P. C. 1987, Astron. Astrophys., 173, 59

van Zee, L., Haynes, M. P., Salzer, J. J., & Broeils, A. H. 1997, Astron. J., 113, 1618

Verde, L., Oh, S. P., & Jimenez, R. 2002, Mon. Not. R. Astr. Soc., 336, 541

Warren, B. E., Jerjen, H., & Koribalski, B. S. 2004, Astron. J., 128, 1152

Waugh, M., Drinkwater, M. J., Webster, R. L., Staveley-Smith, L., Kilborn, V. A., Barnes, D. G., Bhathal, R., de Blok, W. J. G., Boyce, P. J., Disney, M. J., Ekers, R. D., Freeman, K. C., Gibson, B. K., Henning, P. A., Jerjen, H., Knezek, P. M., Koribalski, B., Marquarding, M., Minchin, R. F., Price, R. M., Putman, M. E., Ryder, S. D., Sadler, E. M., Stootman, F., & Zwaan, M. A. 2002, Mon. Not. R. Astr. Soc., 337, 641

Weedman, D. W., Weymann, R. J., Green, R. F., & Heckman, T. M. 1982, Astrophys. J. Letters, 255, L5

Westmeier, T., Braun, R., & Thilker, D. 2005, Astron. Astrophys., 436, 101

White, P. M., Bothun, G., Guerrero, M. A., West, M. J., & Barkhouse, W. A. 2003, Astrophys. J., 585, 739

Whitford, A. E. 1954, Astron. J., 59, 194

Wong, O. I., Ryan-Weber, E. V., Garcia-Appadoo, D. A., Webster, R. L., Staveley-Smith, L., Zwaan, M. A., Meyer, M. J., Barnes, D. G., Kilborn, V. A., Bhathal, R., de Blok, W. J. G., Disney, M. J., Doyle, M. T., Drinkwater, M. J., Ekers, R. D., Freeman, K. C., Gibson, B. K., Gurovich, S., Harnett, J., Henning, P. A., Jerjen, H., Kesteven, M. J., Knezek, P. M., Koribalski, B. S., Mader, S., Marquarding, M., Minchin, R. F., O'Brien, J., Putman, M. E., Ryder, S. D., Sadler, E. M., Stevens, J., Stewart, I. M., Stootman, F., & Waugh, M. 2006, Mon. Not. R. Astr. Soc., 371, 1855

Zwaan, M. A., Briggs, F. H., Sprayberry, D., & Sorar, E. 1997, Astrophys. J., 490, 173

Zwaan, M. A., Meyer, M. J., Staveley-Smith, L., & Webster, R. L. 2005, Mon. Not. R. Astr. Soc., 359, L30

Zwaan, M. A., Meyer, M. J., Webster, R. L., Staveley-Smith, L., Drinkwater, M. J., Barnes, D. G., Bhathal, R., de Blok, W. J. G., Disney, M. J., Ekers, R. D., Freeman, K. C., Garcia, D. A., Gibson, B. K., Harnett, J., Henning, P. A., Howlett, M., Jerjen, H., Kesteven, M. J., Kilborn, V. A., Knezek, P. M., Koribalski, B. S., Mader, S., Marquarding, M., Minchin, R. F., O'Brien, J., Oosterloo, T., Pierce, M. J., Price, R. M., Putman, M. E., Ryan-Weber, E., Ryder, S. D., Sadler, E. M., Stevens, J., Stewart, I. M., Stootman, F., Waugh, M., & Wright, A. E. 2004, Mon. Not. R. Astr. Soc., 350, 1210

Zwaan, M. A., Staveley-Smith, L., Koribalski, B. S., Henning, P. A., Kilborn, V. A., Ryder, S. D., Barnes, D. G., Bhathal, R., Boyce, P. J., de Blok, W. J. G., Disney, M. J., Drinkwater, M. J., Ekers, R. D., Freeman, K. C., Gibson, B. K., Green, A. J., Haynes, R. F., Jerjen, H., Juraszek, S., Kesteven, M. J., Knezek, P. M., Kraan-Korteweg, R. C., Mader, S., Marquarding, M., Meyer, M., Minchin, R. F., Mould, J. R., O'Brien, J., Oosterloo, T., Price, R. M., Putman, M. E., Ryan-Weber, E., Sadler, E. M., Schröder, A., Stewart, I. M., Stootman, F., Warren, B., Waugh, M., Webster, R. L., & Wright, A. E. 2003, Astron. J., 125, 2842

Zwicky, F. 1929, Proceedings of the National Academy of Science, 15, 773

—. 1937, Astrophys. J., 86, 217

—. 1957, Morphological astronomy (Berlin: Springer, 1957)

Appendix A

Derivation of the Toomre Criterion

Adapted and expanded from Binney & Tremaine (1987)

A.1 The Epicyclic Frequency

Consider a disc of objects in orbit about a central point, at position, $\mathbf{r}$ and disc thickness, z. Working in cylindrical coordinates (R, θ, z) the equation of motion for a given object can be written:

$$\ddot{\mathbf{r}} = -\nabla\Phi(R, z) \tag{A.1}$$

where Φ is the gravitational potential, and:

$$\mathbf{r} = R\hat{\mathbf{R}} + z\hat{\mathbf{z}} \tag{A.2}$$

and

$$\nabla\Phi = \frac{\partial\Phi}{\partial R}\hat{\mathbf{R}} + \frac{\partial\Phi}{\partial z}\hat{\mathbf{z}} \tag{A.3}$$

Clearly in an axisymmetric system there is no dependence of these properties on the azimuthal angle, θ. The conservaton of the angular momentum of the system can be expressed as:

$$\frac{\mathrm{d}}{\mathrm{d}t}\left(R^2\dot{\theta}\right) = 0 \tag{A.4}$$

The motion in the R-θ plane can be written:

$$\ddot{R} - R\dot{\theta}^2 = -\frac{\partial\Phi}{\partial R} \tag{A.5}$$

and the motion in the z-direction can be written:

$$\ddot{z} = -\frac{\partial\Phi}{\partial z} \tag{A.6}$$

The equations can be further simplified by using the substitution, $L_z = R^2\dot{\theta}$. Where L_z is the z-component of the angular momentum. Hence Eqn A.5 can be re-written:

$$\ddot{R} - \frac{L_z^2}{R^3} = -\frac{\partial\Phi}{\partial R} \tag{A.7}$$

Now let:

$$\Phi' \equiv \Phi(R,z) + \frac{L_z^2}{2R^2} \tag{A.8}$$

Hence Eqns. A.6 and A.7 become:

$$\ddot{R} = -\frac{\partial\Phi'}{\partial R} \tag{A.9}$$

and

$$\ddot{z} = -\frac{\partial\Phi'}{\partial z} \tag{A.10}$$

In doing so, the problem has been reduced to motion in the rotating (R,z) plane. Minimising Eqns. A.9 and A.10:

$$\frac{\partial \Phi'}{\partial R} = \frac{\partial \Phi}{\partial R} - \frac{L_z^2}{R^3} = 0 \tag{A.11}$$

and

$$\frac{\partial \Phi'}{\partial z} = 0 \tag{A.12}$$

If the problem is confined to the equatorial plane, $z = 0$, then Eqn. A.12 is satisfied. Eqn. A.11 is satisfied when:

$$\left[\frac{\partial \Phi'}{\partial R}\right]_{(R',0)} = \frac{L_z^2}{R'^3} = R'\dot{\theta}^2 \tag{A.13}$$

Eqn. A.13 is simply the condition for a circular orbit, radius, R', angular speed, $\dot{\theta}$ and angular momentum, L_z. Since most stars or gas clouds are not on precisely circular orbits, it makes sense to find approximate solutions to Eqns. A.9 and A.10. Let a small radial change, x, be defined such that:

$$x \equiv R - R' \tag{A.14}$$

Hence the minimum of Φ' occurs at $(x, z) = (0,0)$. By expanding Φ' in a Taylor expansion about this point one obtains:

$$\begin{aligned}\Phi' = \Phi'(0,0) + \frac{L_z^2}{2R'^2} + \frac{\partial \Phi'}{\partial R}x + \frac{\partial \Phi'}{\partial z}z + \\ + \tfrac{1}{2!}\left[\left(\tfrac{\partial^2 \Phi'}{\partial R^2}\right)_{(R',0)}x^2 + \left(\tfrac{\partial^2 \Phi'}{\partial z^2}\right)_{(R',0)}z^2 + \left(\tfrac{\partial^2 \Phi'}{\partial R \partial z}\right)_{(R',0)}xz\right] + \cdots\end{aligned} \tag{A.15}$$

The x, z and xz terms both drop out due to Eqn's. A.11 and A.12. The *epicycle approximation* is that in which all terms higher than 2nd order are ignored. The

epicyclic frequency, κ, is defined as:

$$\kappa^2 = \left(\frac{\partial^2 \Phi'}{\partial R^2}\right)_{(R',0)} \tag{A.16}$$

Partially differentiating Eqn. A.8 twice with respect to R, and evaluating at (R',0) yields:

$$\left(\frac{\partial^2 \Phi'}{\partial R^2}\right)_{(R',0)} = \left(\frac{\partial^2 \Phi}{\partial R^2}\right)_{(R',0)} + \frac{3L_z^2}{R'^4} \tag{A.17}$$

Comparison of Eqns. A.17 and A.16 further yields:

$$\kappa^2 = \left(\frac{\partial^2 \Phi}{\partial R^2}\right)_{(R',0)} + \frac{3L_z^2}{R'^4} \tag{A.18}$$

The orbital frequency, Ω, is given by:

$$\Omega = \frac{V}{R} = \frac{L_z}{R^2} \tag{A.19}$$

where V is the circular speed. Hence:

$$\Omega^2 = \frac{V^2}{R^2} = \frac{L_z^2}{R^4} = \frac{1}{R}\left(\frac{\partial \Phi}{\partial R}\right) \tag{A.20}$$

differentiating:

$$\frac{d\Omega^2}{dR} = \frac{1}{R}\left(\frac{\partial^2 \Phi}{\partial R^2}\right) - \frac{1}{R^2}\left(\frac{\partial \Phi}{\partial R}\right) = \frac{2V}{R^2}\frac{dV}{dR} - \frac{2V^2}{R^3}$$

$$= \left(\frac{\partial^2 \Phi}{\partial R^2}\right) - \frac{1}{R}\left(\frac{\partial \Phi}{\partial R}\right) = 2\left(\frac{V}{R}\frac{dV}{dR} - \frac{V^2}{R^2}\right)$$

$$= \left(\frac{\partial^2 \Phi}{\partial R^2}\right) - \Omega^2 = 2\left(\frac{V}{R}\frac{dV}{dR} - \frac{V^2}{R^2}\right)$$

$$= \left(\frac{\partial^2 \Phi}{\partial R^2}\right) - \frac{V^2}{R^2} = 2\left(\frac{V}{R}\frac{dV}{dR} - \frac{V^2}{R^2}\right)$$

$$\Rightarrow \left(\frac{\partial^2 \Phi}{\partial R^2}\right) + \frac{3V^2}{R^2} = 2\left(\frac{V}{R}\frac{dV}{dR} + \frac{V^2}{R^2}\right)$$

$$\equiv \left(\frac{\partial^2 \Phi}{\partial R^2}\right) + \frac{3L_z}{R^4} = 2\left(\frac{V}{R}\frac{dV}{dR} + \frac{V^2}{R^2}\right)$$

$$\Rightarrow \kappa^2 = 2\left(\frac{V}{R}\frac{dV}{dR} + \frac{V^2}{R^2}\right) \tag{A.21}$$

Eq'n (A.21) describes how κ can be calculated from measurable quantities, under the assumption that the stars (or gas) are travelling in circular orbits. Using galactic rotation curves it is possible to measure V, R and $\frac{dV}{dR}$ and hence calculate κ as a function of radius. It is then possible to examine the radial dependence of the star formation threshold as defined by the Toomre criterion.

A.2 The dispersion relation for a gaseous disk

Once again the thickness of the disk is neglected. Assuming that the pressure, P, acts only in the plane of the disk and that the denisty is replaced by the surface density, Σ, Euler's equation in cylindrical coordinates take the form:

$$\frac{\partial v_R}{\partial t} + v_R\frac{\partial v_R}{\partial R} + \frac{v_\theta}{R}\frac{\partial v_R}{\partial \theta} - \frac{v_\theta^2}{R} = -\frac{\partial \Phi}{\partial R} - \frac{1}{\Sigma}\frac{\partial P}{\partial R} \tag{A.22}$$

and

$$\frac{\partial v_\theta}{\partial t} + v_\theta\frac{\partial v_\theta}{\partial R} + \frac{v_\theta}{R}\frac{\partial v_\theta}{\partial \theta} - \frac{v_\theta v_R}{R} = -\frac{1}{R}\frac{\partial \Phi}{\partial R} - \frac{1}{\Sigma}\frac{\partial P}{\partial R} \tag{A.23}$$

A simple equation of state is assumed:

$$P = K\Sigma^\gamma \tag{A.24}$$

Given this equation of state it is possible to derive the sound speed for the medium:

$$\begin{aligned} c_s^2 &= \frac{dP}{d\Sigma} \\ &= \gamma K \Sigma^{\gamma-1} \end{aligned} \tag{A.25}$$

Introducing the specific enthalpy, h, as:

$$h = \frac{\gamma}{\gamma - 1} K \Sigma^{\gamma-1} \tag{A.26}$$

The RHS of Eqn. A.22 then becomes:

$$\begin{aligned} -\frac{\partial \Phi}{\partial R} - \frac{1}{\Sigma}\frac{\partial P}{\partial R} &= -\frac{\partial \Phi}{\partial R} - \gamma K \Sigma^{\gamma-2}\frac{\partial \Sigma}{\partial R} \\ &= -\frac{\partial}{\partial R}(\Phi + h) \end{aligned} \tag{A.27}$$

The unperturbed axisymmetric state yields the conditions, $v_{R0} = 0$, $\frac{\partial \Phi_0}{\partial \theta} = 0$, and, $\frac{\partial P_0}{\partial \theta} = 0$, hence terms containing these drop out and Eqn. (A.22) in the unperturbed disk reduces to:

$$\frac{v_{\theta 0}^2}{R} = \frac{d}{dR}(\Phi_0 + h_0) \tag{A.28}$$

This equation shows the centrifugal forces on the left of the equation are balanced by gravity and pressure forces on the right. The sound speed in interstellar gas is of the order of 1/20th of the rotational speed, hence the gravitational force dominates in A.28 and it is possible to use the approximation:

$$v_{\theta 0} = \left(R \frac{d\Phi}{dR} \right)^{\frac{1}{2}} \tag{A.29}$$

Making use of Eqn. A.20:

$$v_{\theta 0} = R\Omega. \tag{A.30}$$

Now introduce a small perturbation in the system such that:

$$\begin{aligned} v_R &= v_{R1}, \\ v_\theta &= v_{\theta 0} + v_{\theta 1}, \\ h &= h_0 + h_1 and \\ \Phi &= \Phi_0 + \Phi_1 \end{aligned} \tag{A.31}$$

Substituting these values into the equations of motion (Eqn's. A.22 & A.23) and keeping only those terms that are linear in the perturbed quantities yields:

$$\frac{\partial v_{R1}}{\partial t} + \Omega\frac{\partial v_{R1}}{\partial \theta} - 2\Omega v_{\theta 1} = -\frac{\partial}{\partial R}(\Phi_1 + h_1) \tag{A.32}$$

and

$$\frac{\partial v_{\theta 1}}{\partial t}\left(\frac{d(\Omega R)}{dR} + \Omega\right) v_{R1} + \Omega\frac{\partial v_{\theta 1}}{\partial \theta} = -\frac{1}{R}\frac{\partial}{\partial \theta}(\Phi_1 + h_1) \tag{A.33}$$

It is useful to introduce a new variable, B, such that:

$$B(R) = -\frac{1}{2}\left(\frac{d(\Omega R)}{dR} + \Omega\right) = -\Omega - \frac{1}{2}R\frac{d\Omega}{dR} \tag{A.34}$$

It is also useful to the epicyclic frequency, Eqn. (A.21), transformed using Eqn (A.19) to yield:

$$\kappa^2 = R\frac{d\Omega^2}{dR} = 4\Omega^2 = -4B\Omega \tag{A.35}$$

Any solutions of Eqns. (A.32) & (A.33) can be written as a sum of terms:

$$\begin{aligned} v_{R1} &= Re[v_{Ra}(R)e^{i(m\theta-\omega t)}] \\ \Phi_1 &= Re[\Phi_a(R)e^{i(m\theta-\omega t)}] \\ \Sigma_1 &= Re[\Sigma_a(R)e^{i(m\theta-\omega t)}] \\ v_{\theta 1} &= Re[v_{\theta a}(R)e^{i(m\theta-\omega t)}] \\ h_1 &= Re[h_a(R)e^{i(m\theta-\omega t)}]. \end{aligned} \tag{A.36}$$

m is an integer that determines the mode of the perturbation. Axisymmetric perturbations represent the special case when $m = 0$. It is then possible to substitute Eqn. (A.36) into Eqns. A.32 & A.33 and solve for v_{Ra} and $v_{\theta a}$ to get:

$$v_{Ra} = \frac{-i}{(\kappa^2 - \omega^2)}\left[-\omega\frac{d}{dR}(\Phi_a + h_a)\right] \tag{A.37}$$

and

$$v_{\theta a} = \frac{-1}{(\kappa^2 - \omega^2)}\left[-2B\frac{d}{dR}(\Phi_a + h_a)\right] \tag{A.38}$$

Using Eqns. (A.25) and (A.26) the linearised version of the equation of state becomes:

$$\begin{aligned} h_a &= \gamma K \Sigma_0^{\gamma-2}\Sigma_a \\ &= c_s^2\frac{\Sigma_a}{\Sigma_0} \end{aligned} \tag{A.39}$$

The perturbed surface density, Σ_1 is related to the perturbed velocity, v_1 by the equation of continuity:

$$\frac{\partial\Sigma}{\partial t} + \Sigma\nabla.\mathbf{v} = 0 \tag{A.40}$$

Eqn. A.40 can be rewritten in cylindrical coordinates. Keeping only those terms that are proportional to perturbed quantities yields:

$$\frac{\partial \Sigma_1}{\partial t} = \frac{1}{R}\frac{\partial}{\partial R}(R\Sigma_0 v_{R1}) + \Omega\frac{\partial \Sigma}{\partial \theta} + \frac{\Sigma_0}{R}\frac{\partial v_{\theta 1}}{\partial \theta} = 0 \tag{A.41}$$

Using the solutions from Eqn. (A.31) this becomes:

$$-i\omega\Sigma_a + \frac{1}{R}\frac{d}{dR}(R\Sigma_0 v_{Ra}) = 0 \tag{A.42}$$

Eqn's. A.37, A.38, A.39 and A.41 determine the response Σ_a, to an imposed potential, $\mathbf{\Phi_a}$. The perturbation can be thought of as a plane-density wave, whose potential can be described by:

$$\Phi_a(R) = F(R)e^{if(R)} \tag{A.43}$$

The potential and the surface density are related by Poisson's equation:

$$\Phi_1(R,\theta,t) \simeq \Phi_a e^{ik(R_0,t)(R-R_0)}, \tag{A.44}$$

where

$$\Phi_a = -\frac{2\pi G\Sigma_a}{|k|} \tag{A.45}$$

and k is the amplitude of the wavevector.

The approximation holds within the fractional error, of order $|kR|^{-1}$. This allows further approximations to be made, within the confines of this error. It is possible to write $\frac{d}{dR}(\Phi_a + h_a) = ik(\Phi_a + h_a)$ within this accuracy. Hence it is possible to

simplify Eqns. A.37 & A.38:

$$\begin{aligned} v_{Ra} &= \frac{-i\omega}{(\kappa^2-\omega^2)}\left[ik(\Phi_a+h_a)\right] \\ &= \frac{\omega k}{(\kappa^2-\omega^2)}(\Phi_a+h_a) \end{aligned} \tag{A.46}$$

and

$$v_{\theta a} = \frac{-2Bik(\Phi_a+h_a)}{(\kappa^2-\omega^2)} \tag{A.47}$$

Now substituting in for Φ_a and h_a using Eqns. A.39 & A.45:

$$v_{Ra} = \frac{-i\omega k}{(\kappa^2-\omega^2)}\left(\frac{-2\pi G\Sigma_a}{|k|}+\frac{\Sigma_a}{\Sigma_0}c_s^2\right) \tag{A.48}$$

Now it is possible to replace $\frac{d}{dR}(R\Sigma_0 v_{Ra})$ with $ikR\Sigma_0 v_{Ra}$, without increasing the error further. Thus Eqn. A.42 becomes:

$$\omega\Sigma_a + \frac{1}{R}ikR\Sigma_0 v_{Ra} = 0 \tag{A.49}$$

Now substituting in for v_{Ra} using Eqn. A.48:

$$\omega\Sigma_a + \frac{1}{R}ikR\Sigma_0\left[\frac{-i\omega k}{(\kappa^2-\omega^2)}\left(\frac{-2\pi G\Sigma_a}{|k|}+\frac{\Sigma_a}{\Sigma_0}c_s^2\right)\right] = 0 \tag{A.50}$$

Cancelling common terms yields the dispersion relation for a gaseous disk subject to an axisymmetric disturbance:

$$\omega^2 = \kappa^2 - 2\pi G\Sigma_0|k| + k^2c_s^2 \tag{A.51}$$

A.3 The Toomre criterion for a gaseous disk

Since all the terms on the right hand side of Eqn. A.51 are all real quantities, ω^2 must also be a real quantity. If $\omega^2 > 0$ then the disk is stable. If $\omega^2 < 0$ then there is a perturbation whose amplitude grows exponentially and the disk is unstable. This defines the critical condition as:

$$\kappa^2 - 2\pi G\Sigma_0|k| + k^2c_s^2 = 0 \tag{A.52}$$

This is simply a quadratic in k. Stability is achieved then if there is no solution to Eqn. A.52 for any positive values of k, i.e.

$$\begin{aligned} (2\pi G\Sigma_0)^2 &< 4(c_s^2\kappa^2) \\ \Rightarrow Q \equiv \frac{c_s\kappa}{\pi G\Sigma_0} &> 1 \end{aligned} \tag{A.53}$$

where Q is a dimensionless quantity called the Toomre-Q.